The Effect of Strain and Temperature on the Critical Current Density of High-Field Superconductors

Hamidi A Hamid

University of Durham

A thesis submitted in partial fulfilment of the requirements for the Degree of Doctor of Philosophy

Department of Physics, University of Durham

1997

Abstract

A J(B,ϵ) probe has been designed and built to measure the critical current density, J_c, versus strain on short superconducting wires and tapes. Measurements can be made from 2K to 4.2K in high magnetic fields in our 17T magnet system and at 77K for strains up to $\pm 1.0\%$.

The effect of strain on J_c has been measured on a 0.37mm diameter Nb_3Sn wire at 4.2K and 2.9K from 10T up to 14T. The compressive pre-strain of the wire measured at 4.2K is found to be about 0.3%. At 4.2K, the value of B_{c2} maximum is 19.6T and at 2.9K is 21.2T. The functional form of the flux pinning of the sample at 4.2K can be expressed as $F_P = 4.20 \pm 0.57 \times 10^8 [B_{c2}(\epsilon)]^{1.67 \pm 0.7} b^{1/2}(1-b)^2$; and for the sample at 2.9K it is $F_P = 1.37 \pm 0.05 \times 10^{10} [B_{c2}(\epsilon)]^{0.54 \pm 0.16} b^{1/2}(1-b)^2$. From temperature scaling, the functional form is $F_P = 3.63 \pm 0.62 \times 10^8 [B_{c2}(T)]^{1.72 \pm 1.3} b^{1/2}(1-b)^2$. The difference in the values of n between strain scaling and temperature scaling shows that n only parameterises the change in J_c with change in strain or temperature.

The effect of strain on J_c has been measured on five short sections of an Ag-sheathed BSCCO(2223) tape at 4.2K and in magnetic fields up to 12T. J_c degradation starts to occur between 0.18%-0.25% strain. The appearance of secondary peaks in the critical current distribution is attributed to inter-grain J_c and intra-grain J_c.

J_c measurements have been made on bulk $PbMo_6S_8$(PMS) samples. J_c increased by a factor of ≈ 7 when the sample was hot isostatically pressed(HIP). Measurements have also been made on series of HIP'ed gadolinium(Gd) doped $Pb_{1-x}Gd_xMo_6S_8$ samples. The highest T_c value is 14.55K when x=0.1. The highest J_c is when x=0.2. The irreversibility field $B_{irr}(0)$ from J_c measurements has been calculated to be 53.9T, 45.5T, 34.1T and 33.5T for the x=0, 0.1,0.2 and 0.3 samples, respectively.

Copyright

I hereby declare that the work contained within this thesis is my own work and nothing that is a result of collaboration unless otherwise stated. No part of this work has been submitted for a degree or other qualification at this or any other university.

Hamidi A Hamid
August 1997

Acknowledgements

My thanks and appreciation go to the following:

Institut Teknologi MARA(ITM) and the Government of Malaysia(JPA) for giving me the opportunity and financial support to further my studies; my supervisor Dr D. P. Hampshire for his valuable help, advice, guidance and encouragement during the course of this work; Professors B.K. Tanner and D. Bloor for allowing me to use the Department of Physics facilities; the Science and Engineering Research Council for their support for the group.

The non-academic staff at the Department of Physics: T.C. Doloughan(Dept. Superintendent); P. Armstrong, M. Greener(now at Nissan, Sunderland), P. Luke and G. Teasdale (Student Workshop); M. W Hogg and staff(Main workshop); T. Jackson and C. Mullaney(electronics workshop); D. Stockdale(computing); M. Lee, V. Greener and P.A Russell for helping me with the drawings (audio visual); N. Thompson(for taking the SEM pictures), J. Dobson and D. Pattison(technical staff); and the secretarial staff of the Dept. of Physics..

To those who have assisted me at various stages: Dr B. t. Haken(Univ. of Twente), Dr R. Jenkins, P. Richens(Univ of Oxford),M Dietrich(Vacuumschmelze), Ken Scott (Measurements Group UK Ltd.), Dr R. Scott(Enginnering Dept., Univ. of Durham), Dr I. Terry, Dr K Durose(Physics Dept., Univ. of Durham), Dr Le Lay, Dr C Friend(BICC) and Dr H. Ramsbottom who helped me in computing, Dr D. N. Zheng , Dr N. Cheggour and I. Daniel for useful discussions and T. Hase, Dr C. Moore, C. Leighton, Dr I. Pape and A. Horsfall as office fellows, and many others.

To my parents who always remembered me in their prayers and for their support. To my wife Suhara Salim, son Aiman, and daughters Maisarah and Hanis Samira for their sacrifice, love and encouragement.

Above all, I thank Allah(God) for the life He has given me.

Table of contents

Variables

The following is a list of the variables used in the thesis with a brief description of their meaning:

$\mathbf{A}$	vector potential
A	cross-sectional area
a_0	flux-line lattice spacing
α	microstructural constant
α	tangential displacement
B	magnetic flux density
B_0	constant in field dependent J_C
B_{int}	internal field
B_{ext}	external field
B_C	thermodynamic critical field
B_{C1}	lower critical field
B_{C2}	upper critical field
B_{C3}	the 3rd critical field
B^*_{C2}	the effective upper critical field
B_{C2m}	maximum B_{C2}
B_{irr}	irreversibility field
b	reduced magnetic field
C_P	specific heat
C_S	superconducting specific heat
C_{44}	tilt modulus of the FLL
C_{66}	shear modulus of the FLL
χ	susceptibility
δ	thermal pre-strain
Δ	energy gap
E	electric field strength

E	Young's modulus
E_F	Fermi energy
e	electronic charge
ξ_{GL}	Ginzburg-Landau coherence length
ξ_0	BCS coherence length
ϵ	linear strain
ϵ_{irr}	irreversible strain
F_L	Lorentz force
F_P	volume pinning force
F_{Pmax}	maximum volume pinning force
f_n	free energy of normal state
f_S	free energy of superconducting state
γ	Sommerfield constant
γ	shear strain
G	shear modulus
H	magnetic field strength
$\hbar$	Planck's constant
I	current
J	angular momentum
J	current density
J_C	critical current density
j_S	supercurrent
K	bulk modulus
k	wave vector
k_F	Fermi wave vector
k_B	Boltzman's constant
κ_{GL}	Ginzburg-Landau parameter
λ_L	London penetration depth
L	length
m	magnetic moment
m_e	mass of electron
M	magnetisation

M	atomic mass
μ	magnetic dipole moment
μ_0	permeability of free space
μ_B	Bohr magneton
N(E)	density of electron states
n	index for temperature dependence of pinning
n_p	density of pinning centres
n_S	fraction of superelectrons
ω	angular frequency
ω_D	Debye frequency
ρ	resistivity
ϕ	flux
ϕ_0	the flux quantum
ϕ_T	total flux
$\psi(r)$	Ginzburg-Landau parameter
q	wave vector of virtual phonon
σ	stress
θ	bulk strain
T	temperature
T_C	critical temperature
t	reduced temperature
τ	shear stress
u	vector function
V	voltage
V	volume
V_f	volume fraction of filament
V_m	volume fraction of matrix
V_{ep}	electron-phonon coupling constant
v_S	velocity of superelectron
v_F	Fermi velocity

Chapter 1

Introduction

1.1 Motivation

When superconductivity was discovered in 1911, it remained for a long time a scientific curiosity. Since then superconductivity has been observed in large number of elemental elements and alloys. In 1960s these materials have found their way to practical applications. The discovery of type II superconductors and the fabrication of materials with high critical current densities were important factors leading to practical applications. Superconductors were primarily used for making magnets to be used in areas such as accelerators and Magnetic Resonance Imaging. For the detection of small magnetic fields, SQUIDS(Superconducting Quantum Interference Detectors) were built. However, the overall practical applications of these materials were limited because they required liquid helium as a coolant. This is because liquid helium is expensive and the associated refrigeration system complex. The discovery of high temperature superconductors(HTS) in the late 1980's has started new efforts to search for practical applications. These HTS materials become superconducting at temperatures above that of liquid nitrogen(77K). Liquid nitrogen is relatively cheap and its associated refrigeration is easier to handle. The ongoing research and interest generated by these new discoveries also lead to new applications for low temperature superconductors(LTS) as well.

For practical applications, the most important parameter is the critical current density(J_C). The J_C of these materials must be high and should not degrade if the superconductors are subjected to mechanical strain. Thus it is important to understand the effect of mechanical strain on J_C of superconductors in order to set safe limits for mechanical designs.

1.2 Summary of chapters

This thesis basically consists of two parts. The first part is about the effect of strain on J_C and the second part is about J(B,T) measurements on LTS Chevrel phase superconductor.

Chapter 2 is about the elementary properties of superconductivity. It includes a brief historical introduction and a discussion on both the phenomenological and microscopic theories of superconductivity. Chapter 3 is about the critical current. It begins with the definition of the critical current followed by a discussion on flux pinning and the effect of mechanical strain on the critical current. Chapter 4 describes the design and operation of the J(B,ϵ) probe. This probe is designed such that both tensile and compressive measurements can be done on the samples. A section on sample mounting is also described in this chapter.

Chapter 5 presents measurements made on a commercial Nb_3Sn at 4.2K and 2.9K. Nb_3Sn is widely used for making magnets above 11T. The results are used to determine its compressive pre-strain and the effect of strain on the upper critical field, B_{C2}. In chapter 6 measurements are made on a commercial HTS Ag-sheathed BiSCCO tape. The critical current distribution of these samples under applied strain and magnetic fields is described.

The next two chapters present J(B,T) measurements on the Chevrel phase superconductor $PbMo_6S_8$(PMS). PMS are promising candidates for making magnets that can generate high magnetic fields. Chapter 7 presents data on the effect of hot isostatic pressing (HIP'ing) on PMS. The results are compared to those of an unHIP'ed PMS. The effects of doping PMS with gadolinium is presented in chapter 8. Transport, resistivity and ac susceptibility measurements were made on a set of PMS with different levels of gadolinium doping.

The main conclusions of this work is summarised in chapter 9 which also includes suggestions for further work.

Chapter 2

Superconductivity- Elementary Properties

2.1 Introduction

Superconductivity is an exciting phenomena of scientific interest and useful for technical applications. Certain materials when cooled down below a certain temperature, called the transition temperature T_C, show unusual electromagnetic properties. But the practical application of superconductors requires considerable effort.

This chapter outlines the basic ideas of superconductivity. Section 2.2 is an introduction to superconductivity. Two classes of superconductors, type I and type II, based upon their behaviour in the magnetic field are described in section 2.3. Section 2.4 describes the BCS microscopic theory. The phenomenological theory is explained in section 2.5. This section includes the London model and the Ginzburg-Landau theory. Section 2.6 lists some important superconducting parameters for some selected materials. Since part of this thesis is on strain measurements , a short description of the effect of strain and technological requirements is given in section 2.7. Section 2.8 concludes this chapter.

2.2 Introduction to superconductivity

2.2.1 Brief history of Superconductivity

In 1911 Heike Kammerlingh Onnes first observed that the resistance of mercury dropped sharply at 4.15 K to an unmeasurably small value. This new phenomena was named by Onnes as superconductivity[1, 2]. In 1913 Onnes was awarded the Nobel prize in physics for the study of matter at low temperature and his success in liquefying helium

at the turn of the century. More elemental metals were found to exhibit this superconducting phenomena.

In April 1986, J. Benordz and Karl Alex Muller discovered evidence for superconductivity at about 30 K in the ceramic Lanthanum-Barium Copper Oxide[3]. This was the beginning of the new era of high temperature superconductivity. In Jan. 1987 Wu and his co-workers reported a T_C of 92 K in the ceramic Yttrium-Barium Copper Oxide[4]. It was considered as a major breakthrough since the superconducting state can be achieved by using liquid nitrogen, a coolant that is readily available, simple to handle and less expensive than helium.

In 1988 Maeda *et al* reported a T_C of 110 K in the BiSCCO series[5]. This was followed by the Tl-series which has a T_C of 125 K [6]. The Hg-series having a T_C of 133 K at normal pressure [7] and above 150 K [8] at 150 kbar pressure were reported in 1993. Figure 2.1 represents the evolution of the superconducting transition temperature. Notice the abrupt change in 1986.

2.2.2 Zero Resistance and Meissner -Ochsenfeld effect

Below their critical temperatures all superconductors exhibit zero-resistance and can expel a magnetic field. Once a current is set up in the superconductor it will persist without any applied voltage. The persistent current, or supercurrents, have been observed to last for over two-and half years with no measurable decay[9].

In 1933 W. Hans Meissner and Robert Ochsenfeld observed that when superconductors are cooled down from the normal state to below their critical temperature in the presence of a magnetic field, the magnetic flux is expelled from the interior of the superconductor[10]. A superconductor will lose its superconductive behaviour if the applied field is above a certain critical field, B_C. The Meissner-Ochsenfeld effect, or simply the Meissner effect, is an intrinsic property of the superconductor.

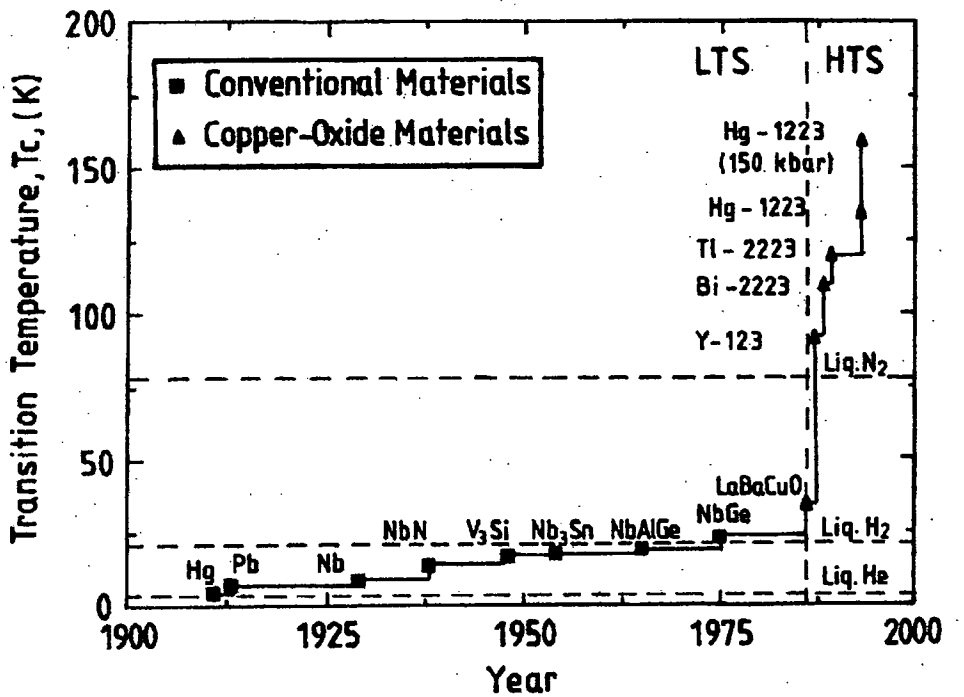

Figure 2.1: The evolution of the superconducting transition temperature (1911-93).

From Maxwell's equation, $\nabla \times E = \nabla \times (\rho J) = - dB/dt$, zero resistivity would imply that $dB/dt=0$. But the Meissner effect always occurs whether the superconductor is cooled in a magnetic field or the field was applied after cooling. Thus the superconducting state is a thermodynamic equilibrium state showing perfect diamagnetism.

2.3 Type I and type II superconductors

2.3.1 Definition of type I and type II

Superconductors can be divided into two classes depending on how the magnetic field penetrates the sample. If a magnetic field is applied to a type I superconductor the

magnetic flux is completely excluded up to the thermodynamic critical field, B_C. Once the critical field is reached the flux penetrates completely into the material and it returns back to the normal state.

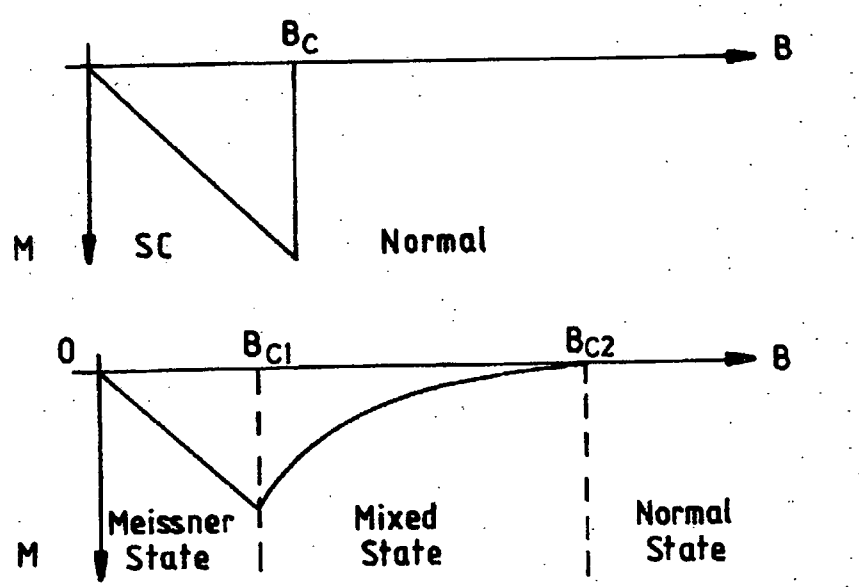

Figure 2.2: Magnetisation curves for type I and type II superconductors.

For a type II superconductor, the magnetic flux is excluded up to a lower critical field B_{C1}. Above this point magnetic flux starts to penetrate in the form of quantised flux lines. This state is known as the vortex or mixed state and the superconductor is still superconducting. Complete flux penetration occurs up to the upper critical field, B_{C2}. Above this field, superconductivity is destroyed. Figure 2.2 represents the magnetisation versus applied field for type-I and type-II superconductors.

2.4 The microscopic theory (BCS)

2.4.1 The electron-phonon interaction

In 1957 Bardeen, Cooper and Schrieffer presented a microscopic theory of

superconductivity which has had good success in explaining the various features of superconductivity[11]. The central idea of this BCS theory is that two electrons in the superconductor can bind together to form Cooper pairs if they experience an attractive interaction[12]. This can be explained by considering the interaction of the electron with the crystal lattice.

When the electron moves across the lattice it attracts the positive ions of the lattice. The result is a slight increase of positive charge in this region. A second electron travelling along the same path is then attracted to this region before the positive ions have a chance to return to their equilibrium position. The net effect is an attractive force between the two electrons. The distance over which the pair is correlated is known as the BCS coherence length, ξ_0. The attractive force between the two electrons of the Cooper pair is an electron-lattice-electron interaction. Since the quantised lattice vibrations are called phonons the attractive force between the electrons can be described as electron-phonon interaction.

2.4.2 The important predictions of BCS theory

BCS theory considers the Cooper pair as a system with two electrons with equal but opposite momenta and spin(or wave vectors $\mathbf{k}\uparrow$ and $-\mathbf{k}\downarrow$). The BCS coherence length ξ_0 over which the Cooper pair interacts is given by,

$$\xi_0 = 0.18\frac{\hbar v_F}{k_B T_C} \qquad (2.1)$$

where $\hbar$ is Planck's constant, k_B is Boltzmann's constant and v_F is the Fermi velocity.

In BCS theory the ground state can be expressed in terms of the states ($\mathbf{k}\uparrow$, $-\mathbf{k}\downarrow$) in which all electrons form bound pairs. In the normal phase all states are filled up to the Fermi wave vector $\mathbf{k_F}$. Several superconducting parameters that can be predicted from the BCS theory are as follows:

a. The energy gap

The energy gap, 2Δ, is the energy required to break a Cooper pair. At T=0 the energy is proportional T_C and is given by the relation

$$2\Delta(0) = 3.52k_BT_C \tag{2.2}$$

and near T_C ,

$$\frac{\Delta(T)}{\Delta(0)} = 1.74\left[1 - \frac{T}{T_C}\right]^{\frac{1}{2}} \tag{2.3}$$

b. The critical temperature

The superconducting transition temperature in zero applied magnetic field is given by,

$$T_C = 1.13\frac{\hbar\omega_D}{k_B}\exp\left[-\frac{1}{N(E_F)(V_{ep})}\right] \tag{2.4}$$

where ω_D is the Debye frequency, $N(E_F)$ is the density of normal-states electrons at the Fermi energy and V_{ep} is the electron-phonon coupling parameter.

c. Thermodynamic critical field

The temperature dependence of the thermodynamic critical field for all temperatures up to T_C is predicted to be

$$B_C(T) = B_C(0)(1 - t^2) \tag{2.5}$$

where t is the reduced temperature, T/T_C.

d. Temperature dependence of specific heat

As T→0 , the temperature dependence of the specific heat is

$$C_S \propto \gamma \exp\left[\frac{\Delta(0)}{k_B T}\right] \tag{2.6}$$

where γ is the electronic specific heat coefficient (also known as the Sommerfield constant) and $\Delta(0)$ is the energy gap at 0 K.

e. The isotope effect

The transition temperatures of different isotopes of the same element were observed to decrease with increasing atomic mass. Assuming V(coupling parameter) is constant, then $\omega_D \propto M^{-1/2}$ and so

$$T_C \propto M^{-1/2} \tag{2.7}$$

Here M is the atomic mass of the isotope.

2.5 The phenomenological theory

2.5.1 The London Model

In 1935 F. London and H. London proposed their famous phenomenological equations based on the two-fluid model to describe infinite conductivity and the Meissner effect[13, 14].

The two-fluid model assumes that the total current flowing in the superconductor is

$$J = J_s + J_n \tag{2.8}$$

where J_s is the superconducting current and J_n is the normal current.

The supercurrent can be written as $J_s = n_s e v_s$ and together with $m_e(dv_s/dt)=eE$ leads to

$$\frac{\partial J_s}{\partial t}=\frac{n_s e^2}{m_e}E \tag{2.9}$$

m_e is mass of electron, n_s is the total number of superelectrons per unit volume, v_s is velocity of the superconducting electrons and E is the electric-field strength.

Combining with Maxwell equation $\nabla \times \mathbf{E} = -\partial \mathbf{B}/dt$ and integrating, the following relationship is obtained

$$\nabla x J_s=\left(\frac{n_s e^2}{m_e}\right)B \tag{2.10}$$

Equations (2.9) and (2.10) are the two London equations. Equation (2.9) describes zero resistance and equation (2.10) describes the Meissner effect.

Applying Maxwell equation $\nabla \times \mathbf{B} = \mu_0 \mathbf{J}_S$ to equation (2.10) for a simple one dimensional case, one then obtains the characteristic length called the London penetration depth, λ_L,

$$\lambda_L=\left(\frac{m_e}{\mu_0 n_s e^2}\right)^{\frac{1}{2}} \tag{2.11}$$

λ_L describes the range over which the field extends inside the superconductor.
$\nabla \times \mathbf{B} = \mu_0 \mathbf{J}$ may also be combined with equation (2.10) to yield

$$\nabla^2 B = \lambda_L^{-2} B \tag{2.12}$$

Solving this equation for fields parallel to the surface gives

$$B(x) = B_0 \exp\left(\frac{-x}{\lambda_L}\right) \tag{2.13}$$

This result shows that the magnetic field is confined to the surface and decays exponentially with λ_L .

2.5.2 The Ginzburg-Landau Theory

In 1950 Ginzburg and Landau proposed a theory that represents a generalization of London's theory to allow for spatial variations in n_s [15]. They introduced a wave function for the superconducting electrons as $\psi(r,\phi) = \psi(r)e^{i\phi}$ where ϕ is the phase. ψ is defined to be zero in a normal region. The density of the paired superelectrons per unit volume in a superconducting region is

$$n_S(r) = |\psi(r)|^2 \tag{2.14}$$

Assuming a second-order transition , the expression for the superconducting free energy in a magnetic field is

$$F_s = F_n + \alpha|\psi|^2 + \frac{1}{2}\beta|\psi|^4 + \frac{1}{2\mu_0}|B_{ext} - B_i|^2 + \frac{1}{2m_e}|(-i\hbar\nabla - 2eA)\psi|^2 \tag{2.15}$$

where F_n is the free energy of the normal state, B_{ext} is the external magnetic field, B_i is the internal magnetic field and α , β are coefficients.

The first three terms are from Landau's own theory of second-order phase transition[16]. Minimizing the free energy with respect to ψ and **A** (vector potential of the magnetic field) gives the two Ginzburg-Landau equations:

$$\alpha\psi+\beta\psi|\psi|^2+\frac{1}{2m_e}(i\hbar\nabla-2eA)^2\psi=0 \tag{2.16}$$

$$J_s=\frac{ie\hbar}{m_e}(\psi^*\nabla\psi \quad \psi\nabla\psi^*) \quad \frac{4e^2}{m_e}\psi^*\psi A \tag{2.17}$$

Near T_C the Ginzburg-Landau (GL) coherence length ξ_{GL} is

$$\xi_{GL} \propto (1- t)^{-1/2} \tag{2.18}$$

where t is the reduced temperature, T/T_C . Near T_C the GL penetration depth varies in the same way as λ_L and ξ_0. The GL theory can also be described using the Ginzburg-Landau parameter

$$\kappa_{GL}=\frac{\lambda_{GL}}{\xi_{GL}} \tag{2.19}$$

Physically, at a superconducting-normal boundary the value $\kappa_{GL}= 1/\sqrt{2}$ describes the point where the surface energy goes from positive to negative. For $\kappa < 1/\sqrt{2}$ there is a positive surface energy (Type I) and for $\kappa_{GL} > 1/\sqrt{2}$ there is a negative surface energy(Type II).

From GL theory Abrikosov showed that flux penetrates the superconductor as tubes of flux, or fluxons[17]. Each fluxon contains one flux quantum,

$$\phi_0=\frac{h}{2e}=2.07x10^{-15}\ Wb \tag{2.20}$$

Each flux line is surrounded by a circulating supercurrent of radius λ_L. Kleiner et al showed that the shape of the lattice is normally a hexagonal(or triangular) configuration[18]. Figure 2.3 gives the structure of an isolated Abrikosov flux vortex. The spatial variation of $|\psi|^2$ in a type-II superconductor showing the hexagonal flux line lattice is given in figure 2.4.

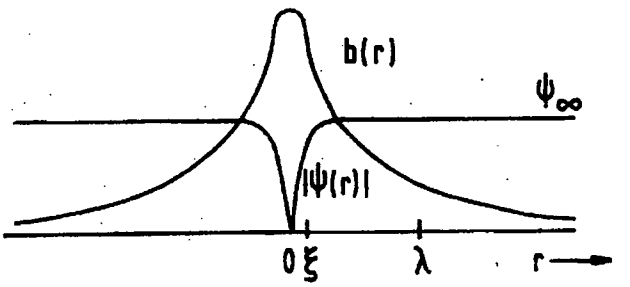

Figure 2.3: The structure of an isolated Abrikosov flux vortex.
The value of b(r) is approximately $2B_{c1}$.

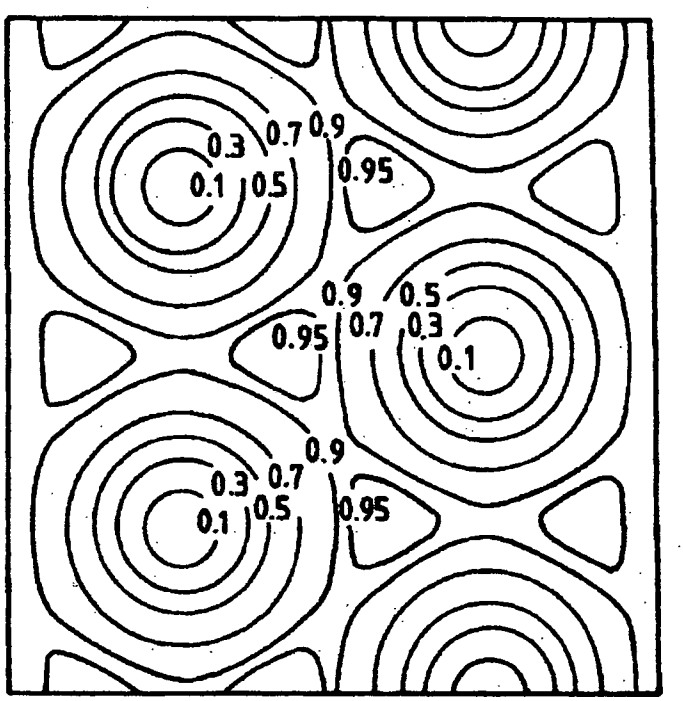

Figure 2.4: The spatial variation of $|\psi|^2$ type II superconductor showing the hexagonal flux line lattice.

2.6 Superconducting Materials

2.6.1 Some important parameters for low and high temperature superconductors

Since the discovery of superconductivity in 1911 many superconducting materials have been discovered. Table 2.1 lists important parameters for some materials. The first two, BiSCCO and YBCO, are the new high-T_C superconductors. The elemental, conventional low-T_C and Chevrel Phase (CPS) superconductors are also included in the list.

Material	T_C (K)	$B_{C2}(0)$ (T)	$B_{C1}(0)$ (mT)	κ_{GL}	ξ_{GL} (nm)	λ_{GL} (nm)
Bi-2223 (// ab-plane)	110	1200	2	1500	0.5	780
Bi-2223 (// c-axis)	110	40	0.2	810	3.0	2350
Y-123 (// ab-plane)	92	670	85	140	1	100
Y-123 (// c-axis)	92	120	25	100	2	175
Nb_3Sn	18.6	23	17	55	4	200
$PbMo_6S_8$ (CPS)	14	56	6.4	150	2.5	360
NbTi	9.8	12	60	20	5	90
Pb	7.2	0.08	80	0.5	65	30

Table 2.1 The important parameters for some superconducting materials are compiled from refs.[19 - 23].

The $PbMo_6S_8$ Chevrel Phase material is included because it is a promising candidate for technological high field application. At 4.2 K its B_{C2} its greater than 50 Tesla[24]. Figure 2.5 highlights its high field performance and compares it to other technological superconductors.

2.7 Strain and Technological Requirements

2.7.1 Superconductivity and Strain

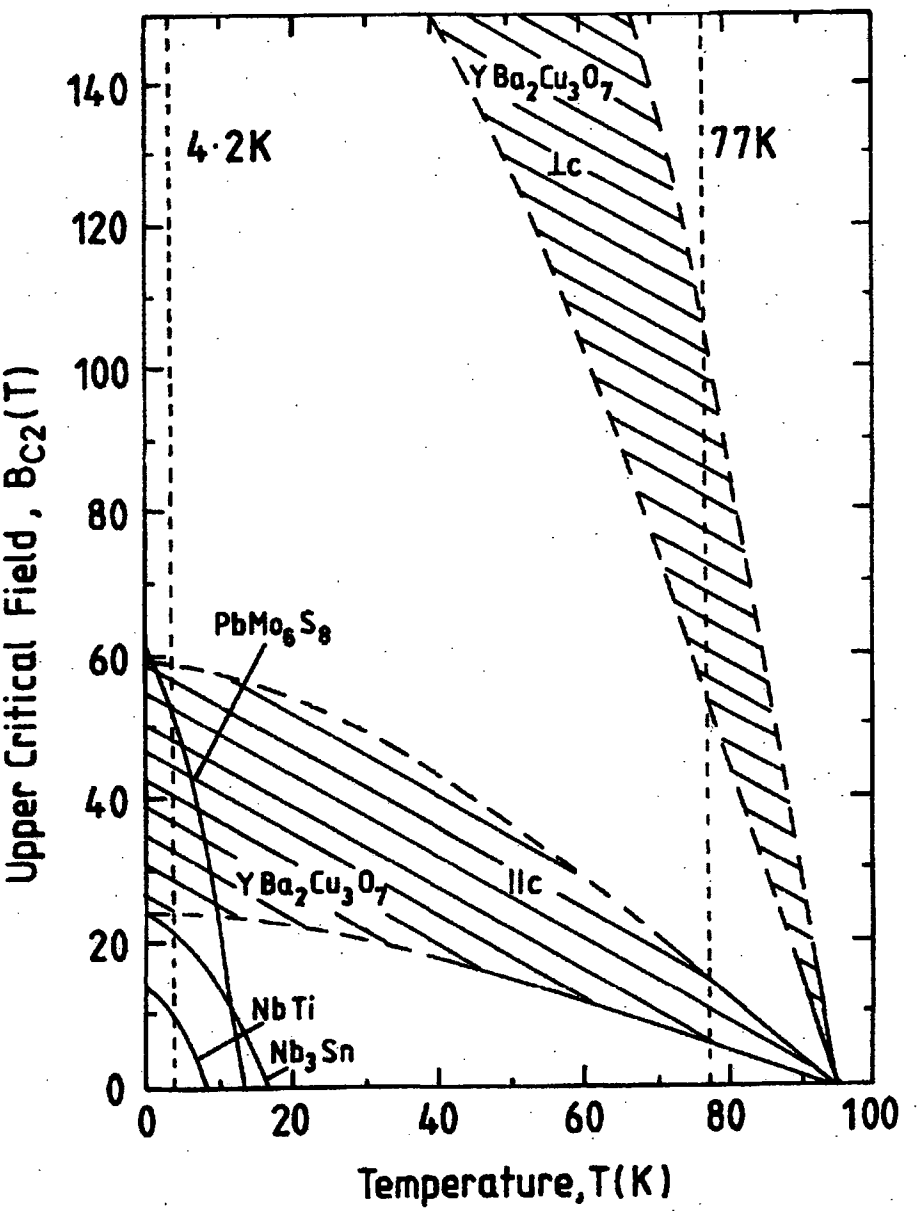

Figure 2.5: The temperature dependence of the upper critical field of $PbMo_6S_8$ compared with both LTS and HTS.

The application of superconducting wires and tapes will require not only high critical current densities in long lengths but also good mechanical properties. In practical applications these superconducting materials are subjected to strain and its influence on the critical current density, J_C , is important [25]. There is also scientific interest in understanding the relation between strain and the fundamental properties.

A simple definition of strain, ϵ, is the change of volume and/or shape of a body , or part of the body , due to applied forces[26]. The exact definition of strain depends on how deformation is produced. Generally, there are three kinds of strain [27]:

(i) Linear strain, ϵ, is the elongation ΔL divided by its original length, L ,

$$\epsilon = \Delta L/L \tag{2.21}$$

(ii) Shear strain, γ, is when stress (σ = force/area) is applied tangentially to the body,

$$\gamma = \tan \alpha \tag{2.22}$$

where the angle α is the tangential displacement of two planes unit distance apart.

(iii) Bulk strain, θ, is when hydrostatic stress acts on the body and is defined as

$$\theta = -\Delta V/V \tag{2.23}$$

where ΔV is the change in volume and V its original volume.

The modulus of elasticity associated with each type of strain are as follows:

(i) For linear strain, the Young's modulus, E, is defined as

$$E = \sigma/\epsilon \tag{2.24}$$

(ii) For shear strain, the shear modulus , G, is

$$G = \tau/\gamma \tag{2.25}$$

where τ is shear stress.

(iii) For bulk strain , the bulk modulus K, is defined as

$$K = \sigma/\theta \tag{2.26}$$

Actually, deformation is a three-dimensional case of relative points that vary continuously as functions of initial positions. Let **u** be a vector function of the coordinates which describes the displacement of the points of a body as a function of their initial positions. Then each of its scalar components $[u_1\ u_2\ u_3]$ is a scalar function of the coordinates, and each may then be differentiated partially with respect to each of the three coordinates. In a 3D-Cartesian co-ordinate system, the linear strains can be defined as follows:

$$\epsilon_{11} = \partial u_1/\partial x_1 = \partial u_{11} \quad ; \quad \epsilon_{22} = \partial u_2/\partial x_2 = \partial u_{22} \quad ; \quad \epsilon_{33} = \partial u_3/\partial x_3 = \partial u_{33} \tag{2.27}$$

The shear strains are:

$$\gamma_{12} = \partial u_{12} + \partial u_{21} \quad ; \quad \gamma_{13} = \partial u_{13} + \partial u_{31} \quad ; \quad \gamma_{23} = \partial u_{23} + \partial u_{32} \tag{2.28}$$

A rigorous treatment on stress-strain relationship may be found in books on continuum mechanics[28,29].

Figure 2.6 shows a typical stress-strain curve of a composite with brittle filaments and a ductile matrix[30]. The subscripts f and m denotes filaments and matrix, respectively. The curve shows three stages: (I) elastic-matrix-elastic filament, (II) plastic-matrix-elastic filament, (III) plastic matrix-filament fracture. The σ-ϵ curve will begin at stage

(II) if the matrix has already yielded due to residual stress.

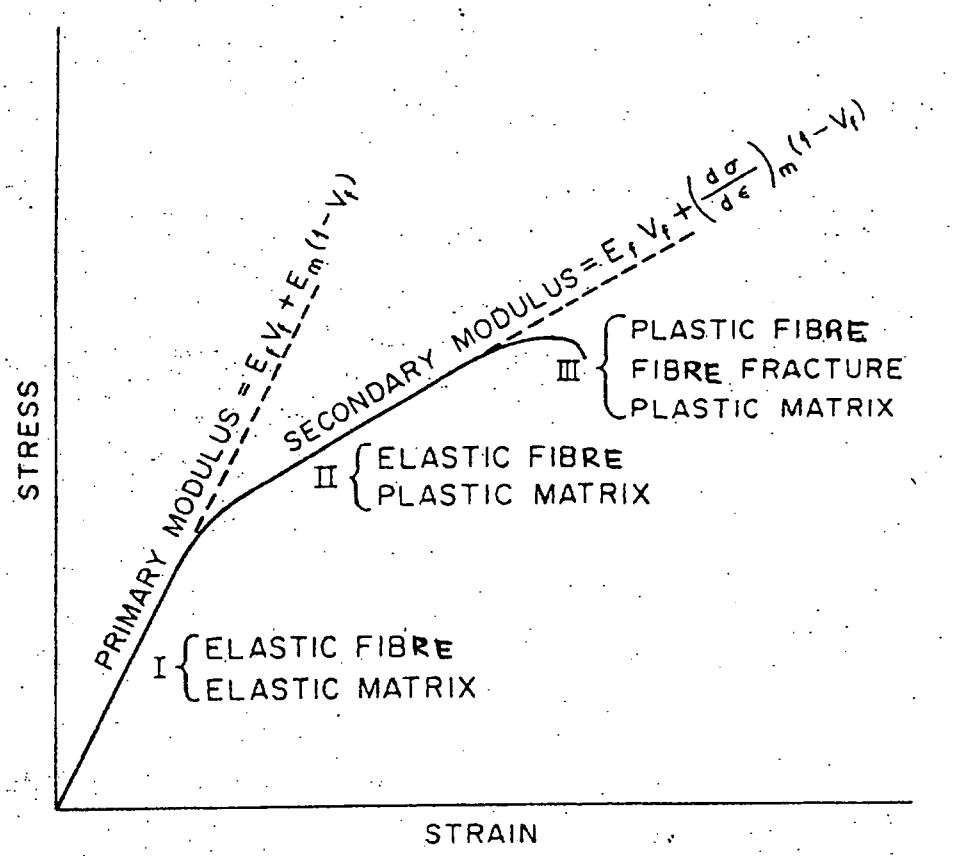

Figure 2.6: Three stages in the stress-strain curve of composite.
(E: Young's modulus; σ: stress and V: volume fraction)

Strain induced in a superconductor has three important consequences:

(a) Critical current degradation.

A tensile strain of 0.5 % can degrade J_C of Nb_3Sn at 12 Tesla by 50%. Similar strain effects have been observed for other A15 superconductors such as Nb_3Ge, Nb_3Al and V_3Ga[31]. For an Ag-sheath BiSCCO superconductor a strain of only 0.36% can degrade J_C by 50%[32].

(b) Matrix degradation.

In magnet applications, the cyclic strain generated by the magnetic stress can degrade the stability of the superconducting wire. When materials are stressed repeatedly at loads below their ultimate tensile strength, failure due to fatigue occurs. Fatigue is the gradual change of a certain property as a result of repeated cycles of stress. Fatigue at low temperatures can cause significant increases in the residual resistivity of the material. A cyclic strain of only 0.4% can halve the stability of the matrix material[33].

(c) Training

When a superconducting magnet is first charged it usually does not reach its full operating field. Thermal runaway occurs below the maximum field. After several trials, or training, the thermal runaway point will increase until the designed operating field is reached. This process is simply a relief of stress concentration points in the magnet arising in the epoxy and heating from wire movements. To avoid severe damage to the epoxy at low temperatures a strain limit of about 0.2% is usually taken as a safe limit[33].

2.7.2 Sources of stress and strain

In magnet applications the sources of stress and strain may include the following:

(a) Fabrication stress

Stresses in the superconducting solenoids can originate from wire tension during fabrication. This includes bending strain when the superconducting wire is wound into a magnet and uniaxial strain from pre-tensioning of the wire during winding[34].

(b). Differential thermal contraction stress

Another source of strain is the difference in thermal contraction between different materials within the composite as the superconducting wire is cooled from heat-treatment temperature to liquid helium temperature. Because of this the magnet can

experience severe strain during cool down.

(c). Magnetic stress

When the magnet is energised the magnetic forces generated produce orthogonal stress components in the conductor. These include axial tensile stress and transverse compressive stress. Figure 2.7 shows the effect of transverse and axial stress on the upper critical field of Nb_3Sn. The transverse stress has a large effect on upper critical field[35].

The magnetic hoop stress, σ_{hoop} , on a wire in a solenoid is related to the current carrying capacity, J, by :

$$\sigma_{hoop} = JBR \qquad (2.29)$$

where B is the magnetic field strength and R is the radius of the coil[33]. Figure 2.8 represents the magnetic hoop stress on a wire and its relation to the current carrying capacity. If the magnetic hoop stress is too large, about 1 GPa, σ_{hoop} can exceed the mechanical strength of conventional superconductors.

2.8 Summary of chapter

The discovery by Kammerlingh Onnes in 1911 was a major milestone that lead to a totally new branch of science. In 1933 Meissner and Ochsenfeld showed that magnetic field was excluded from a superconductor. This phenomena is used to distinguish between a superconductor and a perfect conductor. Superconductors can also be divided into two groups, type I and type II, depending on how magnetic field penetrates into the material. In 1935 the London brothers introduced their famous phenomenological equations based on the two-fluid model. Ginzburg and Landau later proposed a theory that represents a generalisation of the London model to allow for spatial variation. The microscopic BCS theory forwarded by Bardeen, Cooper and Schreiffer in 1957 has had success in explaining the various features of superconductivity. This theory was able

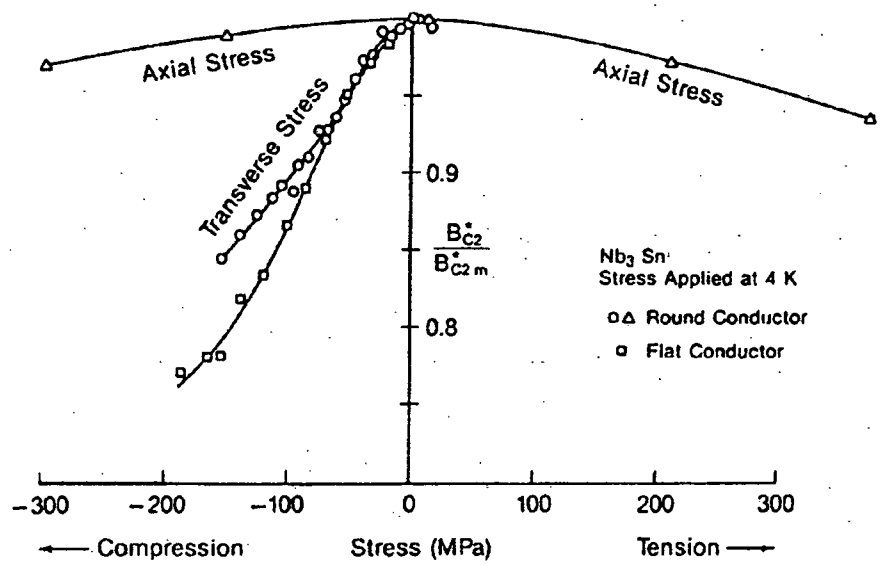

Figure 2.7: Intrinsic effect of transverse and axial stress on the upper critical field of Nb_3Sn.

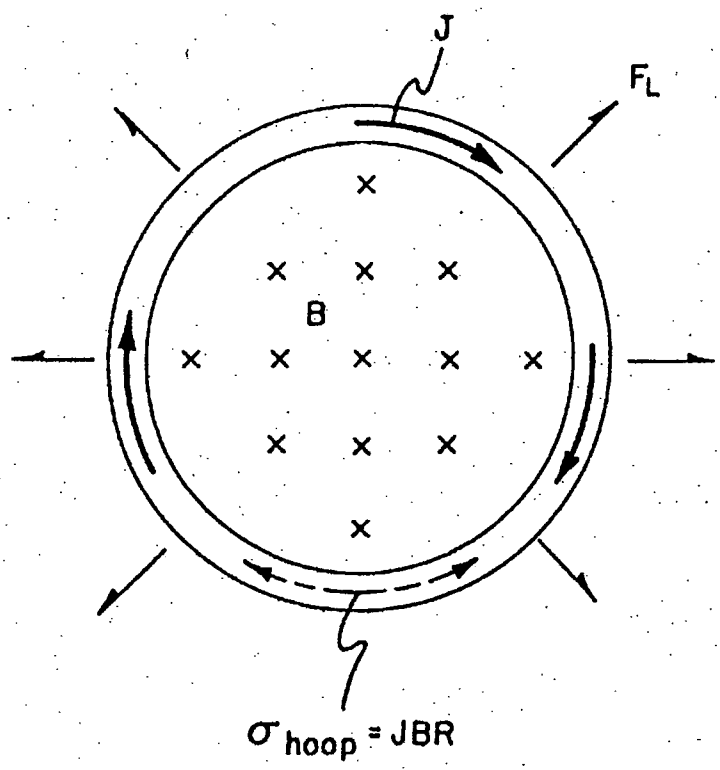

Figure 2.8: A current-carrying loop showing the transport density, J, the magnetic field, B, and the resultant hoop stress, σ_{hoop}, generated by the Lorentz force, F_L, acting on the winding.

to predict several important superconducting parameters such as the energy gap, the critical temperature, the thermodynamic critical field, the temperature dependence of specific heat and the isotope effect.

As time has progressed more materials were discovered to be superconducting. The newly discovered high temperature superconductors allows researchers to conduct experiments using liquid nitrogen instead of the more expensive liquid helium. For industrial applications there is a technical requirement that these materials have good mechanical properties. This is an important component of the work in this thesis.

Reference

1. Onnes H K., *Comm. Leiden* **120b** (1911).
2. Onnes H K., *Comm. Leiden Suppl. Nr* **34** (1913).
3. Bednorz J G and Muller., *Z Phys. B* **64** 189 (1986).
4. Wu M K, Ashburn J R, Torng C J, Hor P H, Meng R L, Gao L, Huang Z J, Wang Y Q and Chu C W., *Phys. Rev. Lett.* **58** 908 (1987).
5. Maeda H, Tanaka Y, Fukutomi M and Asano T *Jap. J. Appl. Phys.* **27** 4209 (1988).
6. Parkin S P, Lee V Y, Engler E M, Nazzal A I, Huang T C, Gorman G, Savoy R and Beyers R., *Phys. Rev. Lett.* **60** 2539 (1988).
7. Schilling A, Cantoni M, Guo J D and Ott H R., *Nature* **363** 56 (1993).
8. Chu C W, Gao L, Chen F, Huang Z J, Meng P L and Xue Y Y., *Nature* **365** 323 (1993).
9. Quinn D J and Ittner W B., *J. Appl. Phys.* **33** 748 (1962).
10. Meissner W and Ochsenfeld R., *Naturwissenschaften* **21** 787 (1933).
11. Bardeen J L, Cooper N and Schrieffer., *Phys. Rev.* **108**(5) 1175 (1957).
12. Cooper L N., *Phys. Rev.* **104** 1189 (1956).
13. London F and London H., *Proc. Royal Soc. (London)* **A149** 71 (1935).
14. Gorter C J and Casimir H B G., *Physica* **1** 305 (1934).
15. Ginzburg V L and Landau L D., *Zh. Eksp. Teor. Fiz.* **20** 1064 (1950).
16. Landau L D and Lifshitz E M., *Course of Theoretical Physics* **5** 430 Pergamon Press (1959).
17. Abrikosov A A ., *Sov. Phys. **JETP** 5* 1174 (1957). [Translation of *Zh. Eksp. Teor. Fiz.* 32 1442 (1957)].
18. Kleiner W H, Roth L M and Autler S H., *Phys. Rev.* **133** A1266 (1964).
19. Weast R C ed., *CRC Handbook of Physics and Chemistry* **73rd** Ed (CRC press Inc, Florida) (1992).
20. Collings E W., *Applied Superconductivity: Metallurgy and Physics of Titanium Alloys* (Plenum Press, New York) (1986).
21. Burns G., *High temperature Superconductivity: An introduction* (Academic Press, UK) (1992).

22. Matsubara I, Tanigawa H, Ogura T, Yamashita H and Kinoshita M., *Phys. Rev. B* **45** (13) 7414 (1992).

23. Zheng D N, Ramsbottom H D and Hampshire D P., *Phys. Rev. B* **52** (17) 12931 (1995).

24. Fisher Ø, Odermatt R, Bongi G, Jones H, Chevrel R and Sergent M., *Phys. Lett.* **45A** 87 (1973).

25. Savvides N and Yau J., *Physica C* **235** 3457 (1994).

26. Valerie H P., *The Penguin Dictionary of Physics* (Longman UK) (1979).

27. Colliue A M and Powney D J, The Mechanical and Thermal Properties of Materials (Edward Arnold, London) (1973).

28. Edmunds H G., *Mechanical Foundations of Engineering Science* (Ellis Horwood Ltd. UK) (1981).

29. Timoshenko S and Goodier J N., *Theory of Elasticity* (McGraw Hill USA) (1951).

30. Easton D S, Kroeger D M, Specking W and Koch C C., *J. Appl. Phys.* **51**(5) (1980).

31. Ekin J W., *IEEE Trans. Magn.* **MAG-19** 900 (1982).

32. Ekin J W, Bray S L, Miller T A, Finnemore D K and Tenbrink J., *Advances in Cryogenic Engineering(Materials)* **28** 1041 (1992).

33. Reed R P and Clark A F., *Materials at Low Temperatures* (American Society for Metals, Ohio) (1983).

34. Arp V., *J Appl. Phys* **48**(5) 2026 (1977).

35. Ekin J W., *J. Appl. Phys.* **62** (12) (1987).

Chapter 3

The Critical Current

3.1 Introduction

Since the discovery of superconductivity attempts were made to construct superconducting coils for practical applications. However, it was realised that when the current density, J, exceeded a certain value the superconducting material becomes resistive. Besides the critical temperature, T_C , and the upper critical field, B_{C2} , it is the value of the current density of the material in high fields that determine the practical prospects for industrial applications. Thus understanding the current carrying capacity of the material is essential in order to fabricate better materials for applications.

The critical current is a broad subject and this chapter touches only some of its important aspects. Section 3.2 gives the definition of the critical current, the critical current density and the different criteria used in determining the value of the critical current from V-I characteristics. Section 3.3 is about critical current in type I and type II superconductors. The idea of flux pinning, the volume pinning force, the irreversibility line and the scaling law of Feitz and Webb is discussed in section 3.4. Section 3.5 discusses the critical current distribution (CCD) which includes the distribution function and methods of getting the distribution. The effect of strain on the critical current and the strain scaling law is described in section 3.6. This chapter concludes with a short summary.

3.2 Defining the critical current

The critical current, I_C, is the upper limit to the current that a superconductor can carry. Below this value an ideal superconductor may exist in the superconducting state at a

specified temperature, magnetic field and other specified external conditions[1]. The critical current density , J_C , is I_C divided by the cross-sectional area of the conductor. The critical current density is an extrinsic property of the material and is measured in Am^{-2}. For commercial use a J_C of about $10^8\ Am^{-2}$ is required. The critical current density is strongly affected by the applied field and temperature. Figure 3.1 shows a typical J-B-T surface of a superconductor(eg. Nb_3Sn and NbTi)[2]. The material is superconducting in the region between the origin and the critical J-B-T surface. Above this surface the superconductor is normal. The temperature dependence of the critical current density can be described by the following equation[3]:

$$J_C = J_0\left[1-\left(\frac{T}{T_C}\right)^2\right] \qquad (3.1)$$

where J_0 is the critical current density at 0 K.

The critical current is usually determined by measuring the voltage-current (V-I) characteristics using the standard four terminal technique. Transport current is passed through the superconductor via the current terminals and its corresponding voltage detected by the voltage terminals placed between the current terminals. Unlike T_C which corresponds to a thermodynamic transition, the critical current represents the point at which dissipation is first detected. The V-I characteristics of most practical superconductors is not a step function but exhibits a curved transition. Thus the critical current is not uniquely defined but depends on the criterion used for its measurement[4]. The different kinds of criteria used to determine I_C are:

a. Superconducting-to- normal transition criterion

This is actually the point of thermal runaway where the superconductor is driven into the normal state.

b. Voltage criterion

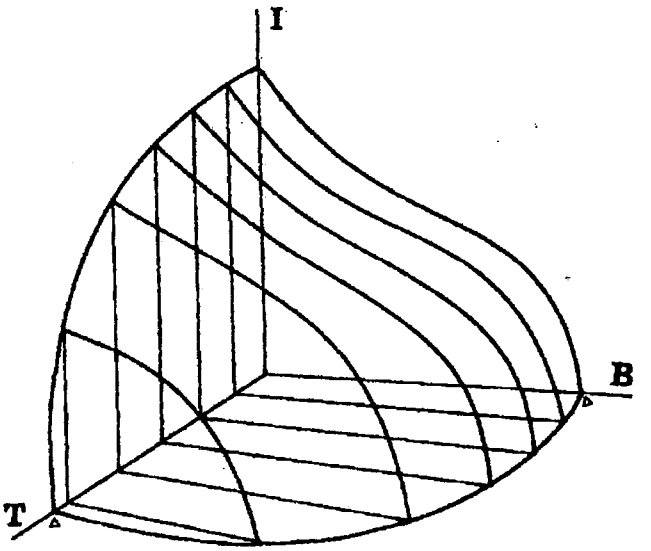

Figure 3.1: A typical J-B-T surface of a superconductor. The triangular symbols on the horizontal axes mark T_c(critical temperature) and B_{c2}(upper critical field) at zero transport current[2].

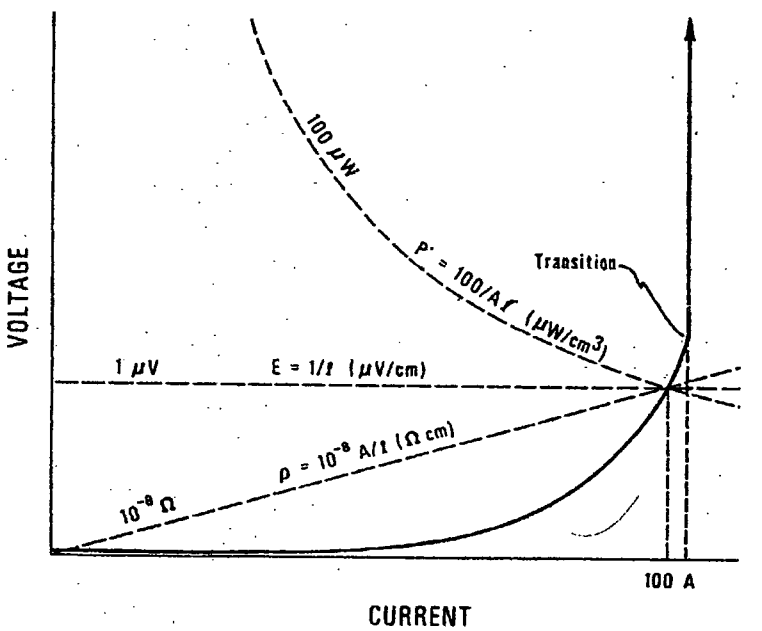

Figure 3.2: The voltage-current characteristics of a practical superconductor with different criteria used to determine the critical current[4].

This is when a minimum detectable voltage is observed. If the minimum detectable voltage is, say 0.5 μV, then the critical current is defined at 0.5 μV.

c. Electric field criterion

Instead of using the voltage criterion the electric field (E), or voltage per unit length, criterion is used. The critical current is the current at which the electric field criteria reaches a certain value. Typically the E field values used is between 1 - 10μVcm^{-1}.

d. Resistivity criterion

The critical current is when the resistivity(ρ), or resistance x (area/length), reaches a certain value. Typical ρ values used is between 1 - 100 pΩ-cm.

e. Power criterion

The critical current is defined as when power, current x voltage, reaches a given value. A typical value would be 100 μW.

The voltage and electric field criteria are often used in literature. This thesis uses the electric field criteria. Figure 3.2 shows the voltage-current characteristics of a practical superconductor with different criteria used to determine the critical current.

At the transition the voltage is related to current by the relation,

$$V=KI^{n} \tag{3.2}$$

where K is a constant of proportionality. The symbol n is known as the index of transition and is a measure of `sharpness' of the transition.

3.3 Critical current in type I and type II superconductors

3.3.1 Critical current in type I superconductor

When current passes through a type I superconductor it generates a magnetic self-field at the surface of the wire. Silsbee showed that the critical current is the current at which the self-field equals the critical field, B_C [5]. The critical current is a direct result of the existence of the critical field. If an external field is applied to the superconductor the critical current is the current at which the sum of the applied field and the self-field equals the critical field.

3.3.2 Critical current in type II superconductor

When current passes through a type II superconductor the critical current is affected by flux motion before the self-field reaches B_{C2}. In the mixed state each flux line, ϕ_0 , experiences a Lorentz force per unit length, $\mathbf{F_L}$

$$F_L = J \times \phi_0 \tag{3.3}$$

where J is the current density. The Lorentz force moves the flux lines perpendicular to both the applied current and field. The flux-line movement also generates energy which heats the superconductor. This heating can drive the superconductor to its normal state. Flux-line movement can be stopped by pinning the flux lines. This can be done by introducing pinning sites such as metallurgical defects into the superconductor. This enables the superconductor to carry higher current densities. The critical current in a type II superconductor is the current at which the Lorentz force equals the maximum pinning force which holds the flux lines in place, given by

$$f_P = J_C \times \phi_0 \tag{3.4}$$

where f_P is the pinning force per unit length of flux line.

Multiplying equation 3.4 by n, the number of flux lines per unit area, gives the maximum pinning force per unit volume of the superconductor, F_P ,[6,7]

$$F_P = J_C \times B \tag{3.5}$$

There are several phenomenological theories that attempt to describe the dependence of J_C on the pinning force. Some of the important ones are discussed in section 3.4.

Defects introduced into the superconductor may include point defects, line defects, surface defects and volume defects[8]. These defects are classified according to the defect's dimensions when compared with the flux-line lattice spacing.

3.4 Flux Pinning

3.4.1 Types of pinning interactions

In the mixed state the flux-line lattice is assumed to be pinned by interaction with pinning centres. The different types of pinning centres gives rise to different types of pinning interactions. For single flux lines in a material with a large value of κ_{GL}, the two main pinning interactions are:

a. Magnetic interaction.

The distribution of the local magnetic fields and currents is altered because of material inhomogeneities. This creates changes in line energy and leads to magnetic pinning. In other words, if both the size and the spacing of the pinning centres is large compared to the penetration depth, λ, the magnetic field is able to adjust everywhere to its equilibrium value [9]. These pinning centres can be large normal inclusions, voids or boundaries between superconductors with different κ_{GL}. The range of interaction is approximately the penetration depth.

b. Core interaction

The magnetic field cannot adjust to the local equilibrium value when either the size or the spacing of the pinning centres is less than the penetration depth[9]. The field thus adjusts to some average value. The order parameter drops to zero at the centre of a flux line. This type of pinning occurs with normal inclusions smaller than the core radius

ξ_0.

In materials with large κ_{GL} magnetic interaction is small and is often dominated by core interaction. The magnetic interaction generally disappears with increasing magnetic field. A detailed discussion on pinning interactions is given by Campbell and Evetts[10].

3.4.2 Collective pinning

In optimised pinning systems the concentration of pinning centres can be very dense. This suggests that a collective treatment of the pinning forces is more reasonable. The theory of collective pinning was first formulated by Larkin and Ochninnikov[11]. Assuming a random array of pinning centres they studied its effect on the deformation of the flux-line lattice (FLL). In a volume V_C there is short range order and the lattice is periodic. For an infinitely large system the order breaks down in the directions both parallel and perpendicular to the field[12]. Larkin and Ochninnikov calculated the critical current density as

$$J_c \propto \frac{n_P^2 f_P^4}{B a_0^3 C_{44} C_{66}^2} \tag{3.6}$$

where n_P is the density of the pinning centres, f_P is the pinning force of an individual centre, a_0 is the spacing of the FLL, B is the magnetic field , C_{44} and C_{66} are the shear and tilt moduli, respectively.

3.4.3 The scaling laws

The critical current density is strongly affected by the applied magnetic field and its value varies for different materials. The characteristics of this field dependence can also be obtained from the field dependence of the volume pinning force, F_p. Fietz and Webb showed that for most materials the volume pinning force can be represented by a single

universal curve at all temperatures[13]. This curve has the form

$$F_P = J_C x B = \alpha [B_{C2}(T)]^a f(b) \tag{3.7}$$

where α is a constant depending on sample microstructure, $B_{C2}(T)$ is the upper critical field, the index n is a constant which determines the temperature dependence of the pinning and f(b) is a function of the reduced magnetic field ($b = B/B_{C2}(T)$). A graph of F_P/F_{Pmax} against the reduced field b causes the pinning curves to lie on a single curve.

Various models have been developed to explain the function F_P and the observed pinning curves. If a shearing pinning mechanism limits J_C , such as in Nb_3Sn , then the expression for F_P proposed is[14]:

$$F_P = J_C x B = \alpha B_{C2}^n(T) b^{\frac{1}{2}} (1-b)^2 \tag{3.8}$$

Kramer showed that the onset of flux motion below F_{pmax} is from breakage of line pins and above F_{pmax} the FLL shears around pins too strong to be broken[14]. However, the functional form that describes pinning in NbTi is described by Hampshire and Taylor to be of the form[15]:

$$F_P = JxB = \alpha B_{C2}^n(T) b(1-b) \tag{3.9}$$

Here they assumed that this force is independent from the relationship between the vortex separation and the pinning-centre separation. A more general treatment of flux pinning is given Dew-Hughes who considered many types of geometrical pinning sites and whether the interaction is core or magnetic in nature. He obtained a series of pinning curves and successfully predicted the scaling law for many materials[9]. The dominant pinning mechanism can be deduced from the shape of the curve. However Dew-Hughes assumed that the FLL is fluid thus neglecting any elastic effects.

3.4.4 The irreversibility line

The B-T characteristics of a type II superconductor has two regions; a low-field 'Meissner' region where the magnetic flux is completely excluded from the superconductor, and a 'mixed' state where the magnetic flux penetrates the superconductor as quantised tubes. The critical current density of the superconductor is also defined by its ability to resist the motion of these flux lines under an applied field and current. Early magnetic measurements on single crystals of oxide materials showed that at certain fields and temperature, below B_{C2} and T_C , the magnetisation became reversible[16]. The boundary between the reversible region and the irreversible region is separated by what is known as the irreversibility line, B_{irr} . At this line the critical current drops to zero and the flux lines can move easily. Although at fields between B_{C2} and B_{irr} the superconductor is still in the superconducting phase it is technologically useless. For conventional superconductors such as NbTi the irreversibility line lies close to B_{C2}[17,18,19,20]. Many experimental techniques, such as AC susceptibility, transport J_C and DC magnetization, have been used to investigate the irreversibility lines and each method gives slightly different values for B_{irr} . This is probably due to the different time scales involved in each technique[21]. Figure 3.3 is a schematic B-T phase diagram showing the various regions. The irreversibility lines can be altered by doping, varying the oxygen content and neutron irradiation[22, 23,24].

3.5 The critical current distribution

3.5.1 The distribution function

In a high current density superconductor the transition to normal state is seldom abrupt but has a broad transition over a current range. Therefore, the critical current cannot be uniquely defined by a single value. If I_C or J_C is to be compared with the microstructural distribution of the pinning centres then a measurement of the distribution of the critical current is desirable[25,26]. Baixeras and Fournet had shown that the voltage across the superconductor can be written as

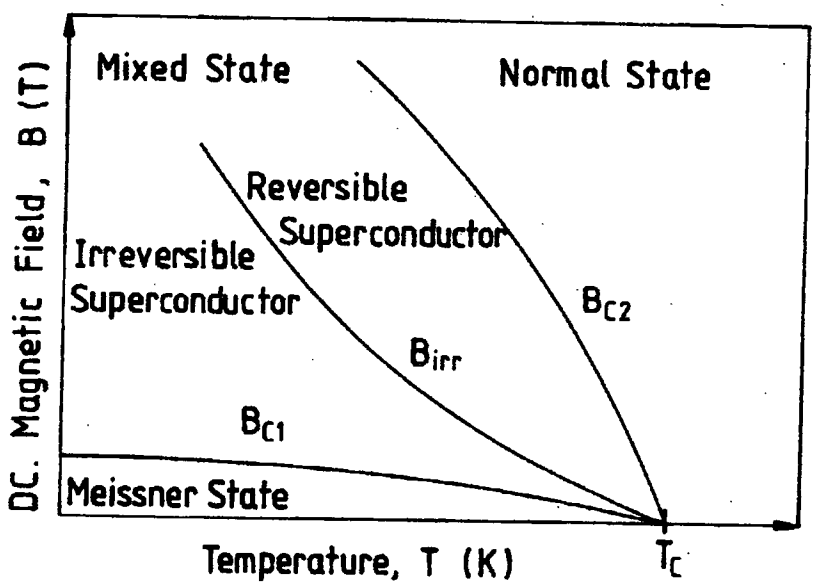

Figure 3.3: A schematic B-T phase diagram for a HTS. For a conventional LTS $B_{irr}(T)$ is very close to $B_{c2}(T)$.

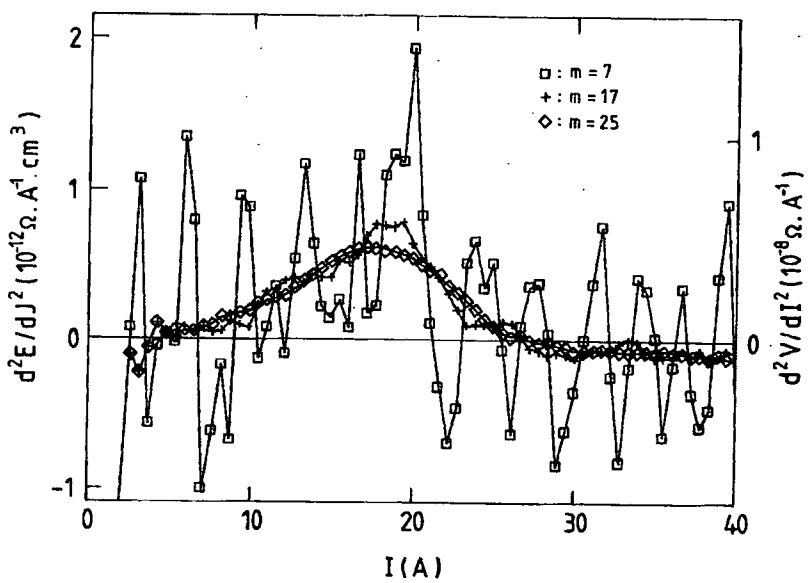

Figure 3.4: An example of the critical current distribution of a 7-core Ag-sheathed BSCCO(2223) measured at 4.2 K and 8 Tesla.

$$V(I) = A\int_0^I (I - I')f(I')dI' \tag{3.10}$$

where A is a constant describing the flux-flow process or other dissipative flow process, I is the transport current, I' is the local current density and f(I') is the distribution of critical currents in the sample[27]. The distribution of critical currents, f(I) is defined such that

$$\int_0^\infty f(I)dI = 1 \tag{3.11}$$

Differentiating equation (3.9) twice with respect to the current I gives the distribution of critical currents along the length of the sample:

$$\frac{d^2V}{dI^2} = Af(I) \tag{3.12}$$

3.5.2 Methods for getting the critical current distribution

Early methods of obtaining the critical current distribution from the resistive transition was by postulating a normal distribution for f(I). Hampshire and Jones and Plummer and Evetts applied this method to NbTi and Nb_3Sn, respectively[26,28,29,30]. They assumed a Gaussian distribution of J_C values and described the constant term A in terms of flux flow process. The solution to f(I) is obtained by adjusting the free parameters, the average I_C and the distribution width, of the Gaussian until the second integral of f(I) produced a best fit to the experimental V-I data.

Warnes and Larbalestier proposed a different method which does not rely on the assumption of the shape of the critical current distribution[26]. With computer technology it is possible to use the approach of Baixeras and Fournet and directly

manipulate the V-I data. One can apply a numerical differentiation technique to the digitized V-I trace and arrived directly at the f(I) distribution. This can be done by differentiating the digitized V-I trace twice and then smoothing the data to obtain the f(I) distribution. The differential smoothing technique used is that of Savitsky and Golay[31]. The advantage of this technique is that the shape of the f(I) distribution is obtained directly from the V-I data. The smoothing consists of selecting m data points (window size) on both sides of a data point and the second derivative is then calculated at this point. By shifting the 2m + 1 data points stepwise through the whole data set the complete d^2V/dI^2 curve can be obtained .

Figure 3.4 is an example of the critical current distribution of a 7-core Ag-sheathed BSCCO(2223) measured at 4.2 K and 8 Tesla. The curve is obtained using the differential analysis with different window sizes(m). When applying the differential analysis method reasonable window sizes have been chosen so as not to lose some of the important features while keeping the signal to noise ratio high[26]. The choice of three window sizes are included in the figure to indicate undersmoothing (m=7), reasonable smoothing (m = 17) and oversmoothing (m = 25) where some of the basic features are lost. The onset of the d^2V/dI^2 curve indicates the lowest critical current in the sample and it drops to zero again at the maximum critical current density. The peak value of the critical current (I_{CP}) then lies between these two regimes. To establish flux flow the current applied has to be several times greater than I_C until a linear region of the V-I trace is reached. This can result in a broad distribution of the critical current as shown in figure 3.4. The distribution of the critical current can be related to the variation of the flux-pinning within the material[25,32].

3.6 Critical current and strain dependence

The critical current is very sensitive to the applied strain and the effect is even greater at high fields. The irreversible strain limit ϵ_{irr} specifies the strain beyond which the conductor is permanently damaged and J_C is irreversibly degraded[33]. This parameter is important because it sets a safe limit that the conductor can tolerate for any mechanical design. When a superconductor is cooled from its fabrication temperature

the thermal contraction of the different materials of the composite are different. This places the superconducting material under prestrain. Kovak calculated the strain caused by different thermal contractions of BSCCO(2223) and Ag on cooling down from room temperature to 77 K by using the following formula[34]:

$$\epsilon_{contr} = \left(1 + \frac{V_{Bi}E_{Bi}}{(1-V_{Bi})E_{Ag}}\right)^{-1} \Delta\epsilon_{therm} \qquad (3.13)$$

where ϵ_{contr} is the strain from thermal contraction, V_{Bi} is the volume fraction of BSCCO(2223) in the composite, E_{Bi} and E_{Ag} are the Young's moduli of bulk BSCCO(2223) and Ag, respectively, and $\Delta\epsilon_{therm}$ is the difference in thermal contraction between the BSCCO(2223) and the Ag matrix on cooling down to liquid nitrogen temperature. Using the values of E_{Bi}=10GPa, E_{AG}=77GPa, $\Delta\epsilon_{therm}=2.1\times10^{-3}$ and V_{Bi}=0.33, equation 3.13 gives a value for ϵ_{contr} of 0.2%[34].

When an external strain is applied to the superconductor, such as Nb_3Sn, the critical current will start at a degraded value, then pass through a maximum at zero `intrinsic strain ' where the prestrain is relieved, and decreases again at some higher strains[35]. Figure 3.5 shows a typical result of a critical current versus axial strain measurements. Here ϵ_{max} represents the position where the applied axial strain, ϵ_a , cancels the prestrain. The axial strain where the critical current is irreversible is different for different conductors. For LTS the typical values range from (ϵ_{irr} - ϵ_{max}) = 0.2 to 0.4% [36].

3.6.1 Types of strain

a. Bending strain

Figure 3.6 is an illustration of bending strain introduced into a conductor by bending[37]. The arc CD represents the neutral plane of the conductor. The maximum tensile strain is along the outermost plane and is represented by arc AB. The maximum strain along the innermost plane is compressive and has the same absolute magnitude

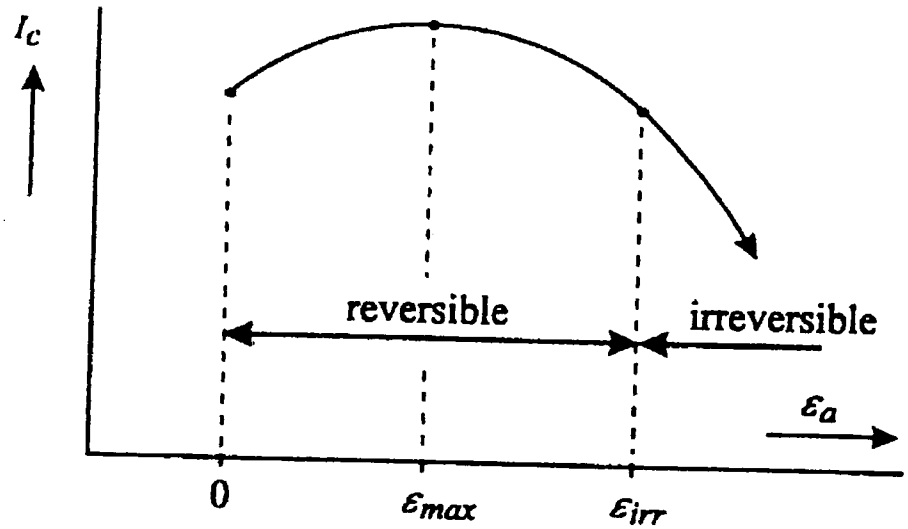

Figure 3.5: A typical result of a critical current versus axial strain for a Nb_3Sn superconductor.

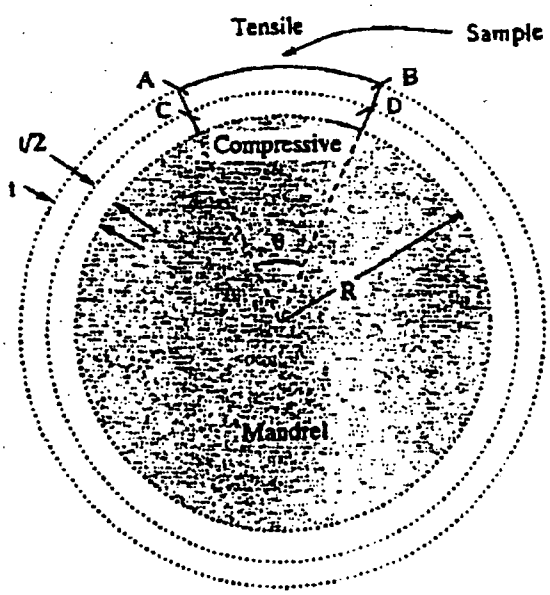

Figure 3.6: An illustration of bending strain introduced into a conductor by bending[37].

as tension. Assuming that the change in thickness due to bending is negligible the bend strain ϵ is given by

$$\epsilon = \frac{L}{L_0} = \frac{t}{(2R+t)} \tag{3.14}$$

where L_0 is the original length, L is the elongation, t is total thickness of conductor and R is radius of curvature. In the simplest model of bend effects for HTS tape one can assume that the superconducting oxide filaments on the tensile side of the tape fracture in tension at some strain and that the zero-strain plane is on CD. In a Nb_3Sn conductor where the superconducting filaments are twisted to reduce ac losses each filament sees alternate tensile and compressive strain. The strain effect is much more severe in a brittle conductor such as Nb_3Sn than that of NbTi[6]. During bending a shift in the conductor's neutral axis can occur as a consequence of plasticity in the tensioned part of the bronze matrix[38]. The usual method of a bending test is to simply bend the conductor with or without a specially made mandrel[37,39].

b. Uniaxial strain

In uniaxial strain all filaments in the superconductor are uniformly affected. The critical current degradation is more severe in uniaxial strain compared to the bending strain. Uniaxial strain can be either tensile or compressive and both degrade the critical current. The standard uniaxial strain experiment is to pull the ends of the superconductor using special tensile test apparatus[33,41,42].

3.6.2 Effect of strain on the critical current in LTS

Figure 3.7 is a J-B-ϵ critical surface for a commercial multifilamentary Nb_3Sn superconductor at 4.2 K showing the reversible degradation of critical current at either tensile or compressive strain as a function of magnetic field[43]. Line AB represents the maximum (strain-free) value of the critical current as a function of the magnetic

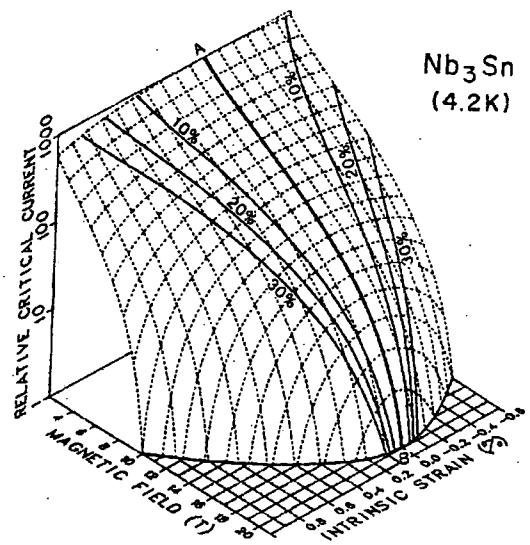

Figure 3.7: A J-B-ϵ critical surface for a commercial multifilamentary Nb_3Sn superconductor at 4.2K. Line AB represents the maximum (strain-free) value of the critical current as a function of the magnetic field[43].

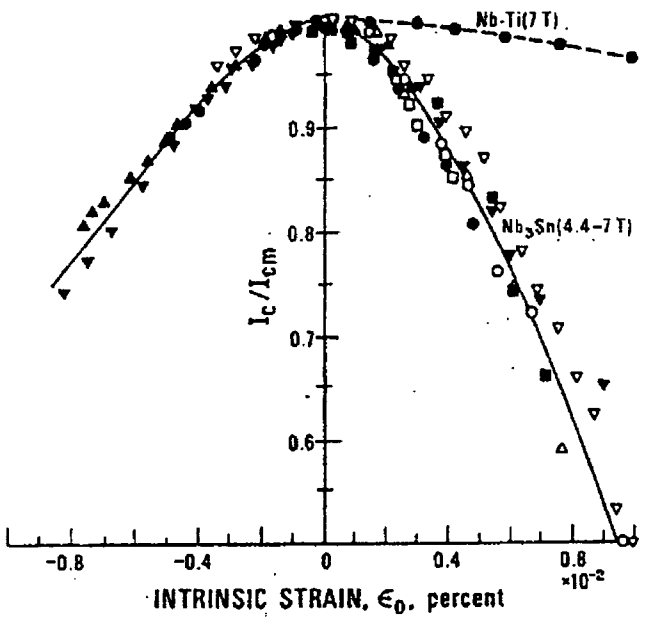

Figure 3.8: The effect of uniaxial strain on the critical current of both ductile(NbTi) and brittle(Nb_3Sn) superconductors at low fields[6]: ▲-Rupp[45]; ○,△, □,▽ -Ekin[46,47]; ●-Ekin, Fickett and Clark[47]; ■-Easton and Schwall[48].

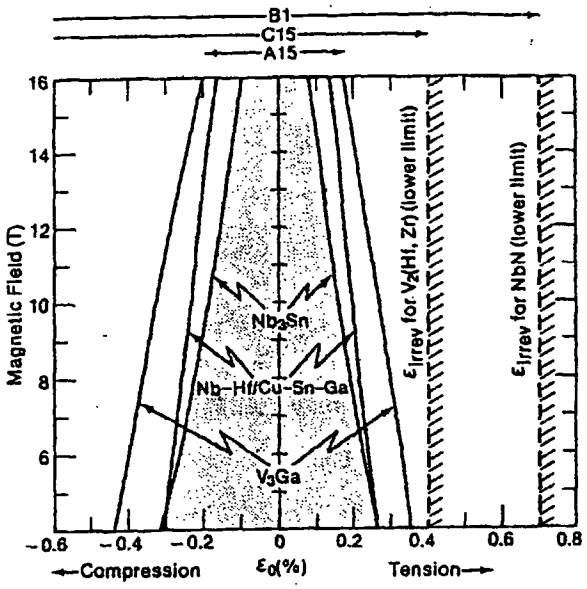

Figure 3.9: A compressive-tensile strain window as a function of magnetic field for limiting critical current degradation to 5% or less in A15, B1 and C15 superconductors[51].

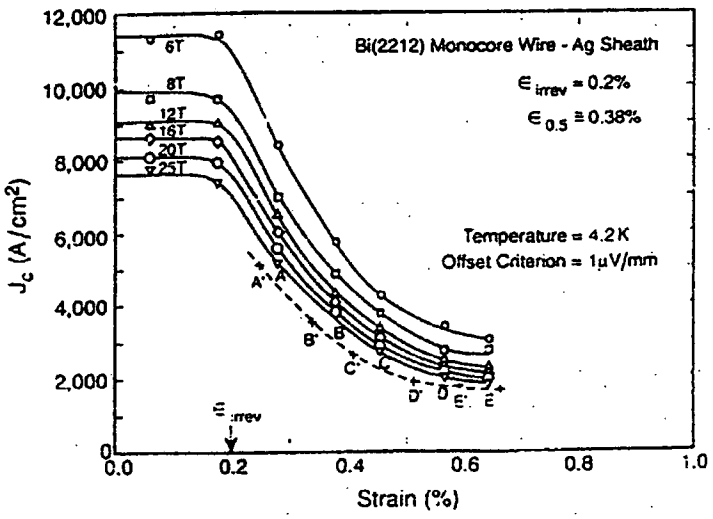

Figure 3.10: A typical J_c against strain curve[55].

field. The lines on either sides of line AB show how much the critical current has degraded from its maximum value at line AB.

The effect of uniaxial strain on the critical current of both ductile (NbTi) and brittle (Nb_3Sn) superconductors at low magnetic fields is shown in figure 3.8[6,44,45,46,47,48]. The strain effect on Nb_3Sn is significantly larger than that of NbTi. In magnet designs NbTi is not as problematic as Nb_3Sn. Ekin suggested that the source of critical current degradation in NbTi and Nb_3Sn is not due to the peripheral effects such as matrix degradation, heat generated by plastic deformation and area reduction, but is associated with the superconductor itself[43]. In Nb_3Sn, where degradation is mostly irreversible at high strains, cracks $\geq$ 1000 nm are observed in the reaction layer. In the region where degradation is mostly reversible the effect is likely from a shift in the intrinsic critical temperature and field, or by an alteration of the vortex-pinning structure[49,50]. Ekin also suggested that in the reversible region, defect size variations on the order of a coherence length(~ 5nm) could be playing an important role.

Figure 3.9 shows a compressive-tensile strain window as a function of magnetic field for limiting current degradation to 5% or less in A15, B1 and C15 superconductors[51]. The strain window sets a safe strain limit for the mechanical design of superconducting devices. Ideally, the superconductor should operate just on the compressive side, where J_C is near maximum, so that there is a safety margin for additional strain. In figure 3.7 the corresponding curves on either side of line AB show the strain window for Nb_3Sn. Experimental evidence shows that the elastic strain effect appears to be strongly dependent on the type of superconductor crystal structure[51].

3.6.3 Effect of strain on critical current in HTS

If strain is applied to a HTS tape or wire there exists a region where the critical current remains almost constant before degradation occurs. Bulk sintered $YBa_2Cu_3O_7$ superconductors fracture at a very low tensile strain of about 0.05%[52]. The Ag-sheathed BSCCO superconductors have a strain tolerance in the range of 0.1 to

0.35%[53,54]. A typical I_C against strain curve is shown in figure 3.10[53]. The sharp reduction in the critical current occurs at ϵ_{irr} , the irreversible strain limit. The constant region before ϵ_{irr} is due to the compressive thermal prestrain within the conductor[36]. This is a result of the differential contractions between the superconducting elements and the silver matrix. However Haken also showed that in this constant region there is indeed a small reduction in I_C with a constant slope of about 1%. The normalised critical current reduction due to small axial strain can be described by:

$$i_C = 1 - C_m \epsilon_a \tag{3.15}$$

where i_C is the normalised critical current, ϵ_a is the applied axial strain and C_m is a constant slope having a value of 4 ± 1 [36]. For Bi-2212 wires Haken also showed that the I_C reduction occurs at strain less than 0.05%. Figure 3.11 illustrates the normalised critical current, i_C for compressive and tensile axial strains for a BSCCO conductor. It consists of three parts: I - the compressive region, II- the flat small axial strain region and III - the large critical current reduction[36,55].

The reduction in the critical current is probably due to transverse cracking of the BSCCO filaments[53,55,56]. The strain tolerance of HTS tapes wires can be improved by increasing the number of filaments [57], subdividing the superconductor material into fine filaments and adding Ag to the superconductor powder prior to processing[53], reinforcing the tapes with aligned-MgO whiskers[58] and decreasing the fill factor (defined as the ratio of the superconductor to the total cross-section)[59]. Kovak et al observed time-dependent recovery of critical current in Ag-sheathed BSCCO(2223) tape in a cyclic bending experiment[34].

3.6.4 Lorentz force and its effect on strain

When transport current passes through a wire in a magnetic field, the wire experiences an additional strain arising from the Lorentz force. The value of $F_L(Nm^{-1})$ is given by

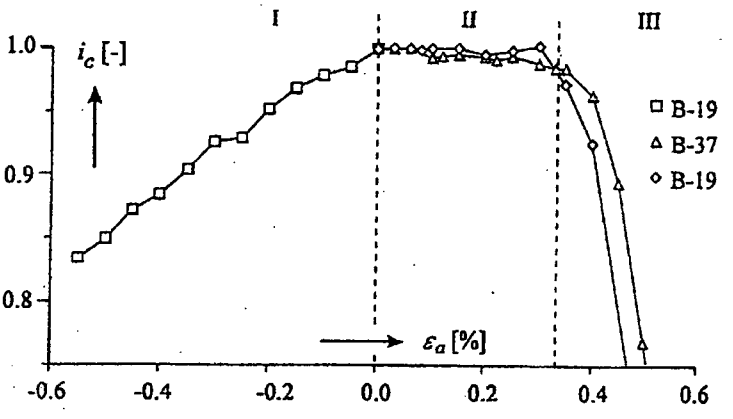

Figure 3.11: A typical I_c against strain curve. This figure was taken from reference 53 showing the normalised I_c for compressive and tensile axial strains at 4.2K for 3 different BSCCO Ag-sheathed samples.

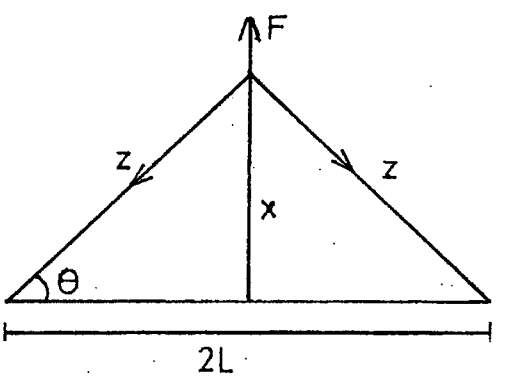

Figure 3.12: Diagram showing the force(F) acting on the wire.

$F_L=I_CB$, where I_C is the critical current and B the applied magnetic field. An approximate calculation for the effect of the Lorentz force is as follows:

Let's assume that the force (F) acting on the wire is shown in figure 3.12, where 2L is the length of the wire and 2z is the new length of the wire after straining by the Lorentz force. From the relation:

$$\tau = G\gamma \tag{3.16}$$

(where τ is shear stress, G the shear modulus and γ the shear strain), we have

τ = F/A (where A is the cross-sectional area)

and

γ = tan θ = x/L for small θ

From 3.16:

$$\frac{F}{A}=G\frac{x}{L} \tag{3.17}$$

$$x=\frac{FL}{AG} \tag{3.18}$$

$$\tan\theta=\frac{x}{L}=\frac{F}{AG} \tag{3.19}$$

so

$$\Delta\epsilon=\frac{(z-L)}{L} \tag{3.20}$$

where $z=\frac{L}{\cos\theta}$

But $\cos\theta\approx 1-\frac{\theta^2}{2}$,

so $\frac{1}{\cos\theta}=\left(1-\frac{\theta^2}{2}\right)^{-1}=1+\frac{\theta^2}{2}$

$\Delta\epsilon$ then can be expressed as:

$$\Delta\epsilon \approx \frac{1}{2}\left(\frac{F}{AG}\right)^2 \qquad (3.20a)$$

But $F_L = \frac{F}{2L}$; so

$$F_L = \frac{1}{\sqrt{2}}\left(\frac{AG}{L}\right)\Delta\epsilon^{\frac{1}{2}} \qquad (3.20b)$$

Equation 3.20b can also be expressed as

$$\frac{F_L}{(\Delta\epsilon)^{\frac{1}{2}}} = \frac{1}{\sqrt{2}}\left(\frac{AG}{L}\right) \qquad (3.20c)$$

Using the values of $L=5\times10^{-3}$m, $A=1.07\times10^{-7}m^2$ and $G_{Nb3Sn}=17$ GPa[60] , gives a value for

$$\frac{F_L}{\Delta\epsilon^{\frac{1}{2}}} \approx 2.6\times10^5 Nm^{-1}.$$

This result will be used in section 4.10.

3.6.5 The strain scaling law

The usual way of estimating the upper critical field is by doing a Kramer plot, $J^{1/2}B^{1/4}$ versus B, based on J_C measurements. The Kramer plots are then extrapolated linearly to zero. The intersection of these lines at $J^{1/2}B^{1/4} = 0$ gives the upper critical field, B_{C2}. These plots give an approximate value of B_{C2} which is useful in determining relative changes of the upper critical field when some of the parameters, eg temperature or strain, are changed.

The measurements of the J_C-ϵ characteristics have shown that the strain effects on J_C are highly field dependent. Ekin found a strain scaling law which describes the $J_C(B,\epsilon)$ dependence of practical high field superconductors.[33]. This relation can be used to scale limited data to obtain a complete $J_C(B,\epsilon)$ curve. Figure 3.13 shows the J_C-ϵ

characteristics for a Nb_3Sn conductor in magnetic fields. The peaks of the critical current occur at the same strain ϵ_M, independent of the magnetic fields. In figures 3.14a and 3.14b, the data of figure 3.13 have been replotted as the pinning force density($F=J_CB$) versus magnetic fields. It shows that the curves are parallel to one another. This means that the entire set of curves can be derived from any one curve simply by scaling. In figure 3.15 the data of figures 3.14a and 3.14b are replotted using normalised coordinates. All the curves superimposed over the entire range of field for both tensile and compressive strains. It can be shown that for any applied strain, F can be expressed as some universal function of the reduced field $b=B/B_{C2}$:

$$F=K(\epsilon)f(b) \tag{3.26}$$

For each conductor there is a unique function f(b) which can be scaled by the prefactor $K(\epsilon)$ to obtain the entire set of curves. For Nb_3Sn, $K(\epsilon)$ and $B_{C2}(\epsilon)$ was found to be directly proportional to one another[33]. This leads to a scaling-law of the form[33,61,62]:

$$F=[B_{C2}(\epsilon)]^n f(b) \tag{3.27}$$

where B_{C2} is the strain dependent upper -critical field, n is a constant and f(b) is a function of the reduced magnetic field $b= B/B_{C2}$. For Nb_3Sn, $n\approx1.0 \pm 0.3$, for V_3Ga, $n\approx1.4$, for Nb_3Ge, $n\approx1.6$ and for NbTi, $n\approx4$. Equation (3.27) allows one to predict F at other strain values by scaling the results by $[B_{C2}(\epsilon)]^n$. The shape of f(b) depends on the superconducting material and reaction conditions. The value n is nearly constant for a given type of superconductor. An expression for J_C/J_{CM} (where J_{CM} is the maximum value of J_C) can be obtained by dividing equation 3.27 by itself at the strain ϵ_M, where the critical current is maximum and using $F=J_CB$. The expression obtained is:

$$\frac{J_C}{J_{CM}}=\left[\frac{B_{C2(\epsilon)}}{B_{C2M}}\right]^n \frac{f(b)}{f(b_m)} \tag{3.28}$$

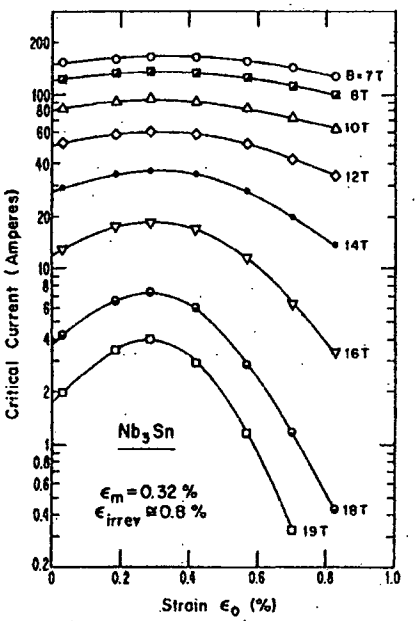

Figure 3.13: The J_c-ϵ characteristics for a Nb_3Sn conductor in magnetic fields[33].

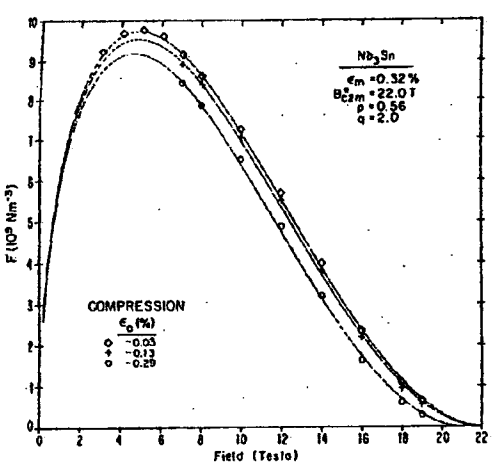

Figure 314a: The data of figure 3.13 have been replotted as the pinning force density versus B for compressive strain[33].

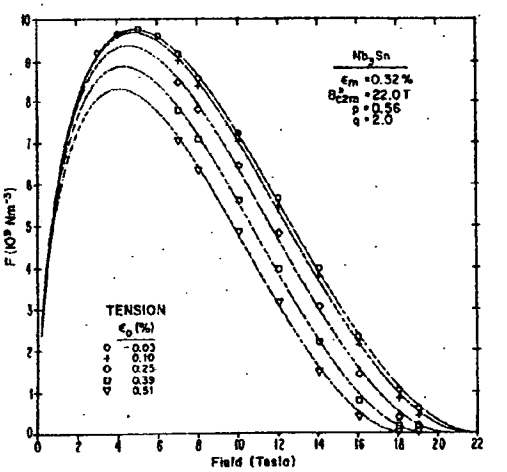

Figure 3.14b: The data of figure 3.13 have been replotted as the pinning force versus B for tensile strain[33].

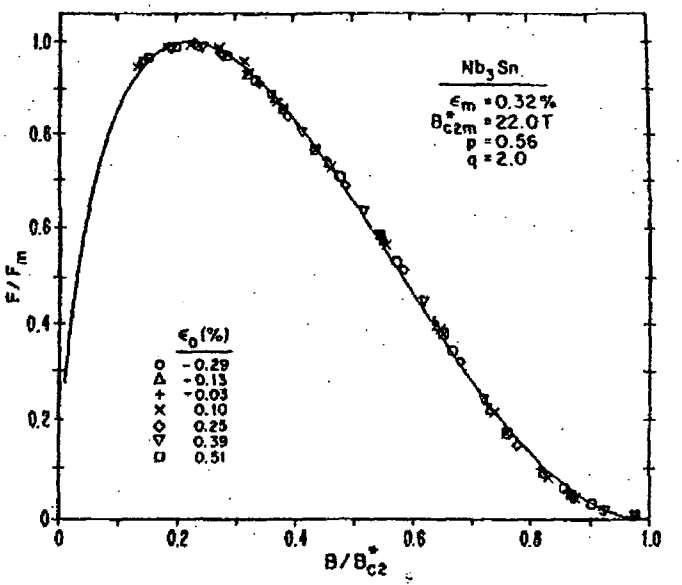

Figure 3.15: The data of figure 3.14a and 3.14b are replotted using normalised coordinates which demonstrates strain scaling.

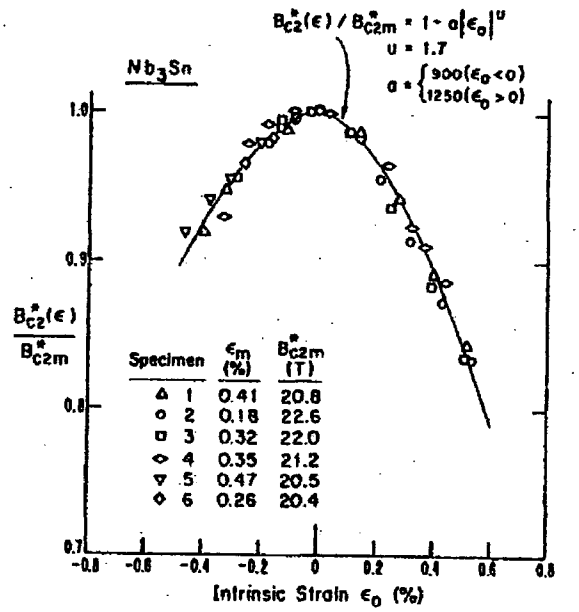

Figure 3.16: The normalised upper critical field as a function of intrinsic strain for six different Nb_3Sn superconductors[33].

The function f(b) is proportional to $b^p(1-b)^q$, where p and q are exponents whose values depend on the type of the pinning model used[13,61]. Substituting this form of f(b) into equation 3.28, we have:

$$\frac{J_C}{J_{CM}} = \left[\frac{B_{C2(\epsilon)}}{B_{C2M}}\right]^{n-p}\left[\frac{1-B/B_{C2}(\epsilon)}{1-B/B_{C2M}}\right]^q \tag{3.29}$$

For Nb_3Sn, $n \approx 1$, $p \approx 0.5$ and $q \approx 2.0$.

Figure 3.16 shows the normalised upper critical field as a function of intrinsic strain $\epsilon_0 (= \epsilon - \epsilon_M)$ for several Nb_3Sn superconductors. By fitting the data with the expression:

$$B_{C2}(\epsilon) = B_{C2M}(1-a|\epsilon_0|^u) \tag{3.30}$$

we have the strain dependence of the upper critical field. Equation 3.30 is evaluated with u=1.7 and a=900 for compression and a= 1250 for tension.

Combining the strain scaling law with the temperature scaling of Fietz and Webb[13], one can obtain an expression for $J_C(B,\epsilon,T)$. The temperature scaling law of Fietz and Webb may be written as:

$$F = [B_{C2}(T)]^v f(b) \tag{3.31}$$

where f(b) is a function of the reduced field $b=B/B_{C2}$ and the exponent v is about 5/2. The strain dependence of B_{C2} is proportional to $(1-a|\epsilon_0|^u)$ and the temperature dependence of B_{C2} is given by $(1-t^2)$, where $t=T/T_C$. Combining equations 3.27 and 3.31 gives:

$$F(T,B,\epsilon) = (1-a|\epsilon_0|^u)^n(1-t^2)^v f(b) \tag{3.32}$$

where n ≈1, v≈ 2.5, t=T/$T_C(\epsilon)$ and b=B/$B_{C2}(T,\epsilon)$.

By dividing equation 3.32 by itself and taking f(b) to be proportional to $b^p(1-b)^q$ one can get the following expression:

$$\frac{J_C}{J_{CM}} = (1-a|\epsilon_0|^u)^{n-p}\left[\frac{1-t^2}{1-t_M^2}\right]^{v-p}\left[\frac{1-b}{1-b_M}\right]^q \tag{3.33}$$

where for Nb_3Sn, v≈ 2.5, n≈ 1, p≈0.5 and q≈2.0.

The strain dependence of $T_C(\epsilon)$ in Nb_3Sn was found to be

$$T_C(\epsilon) = T_{CM}(1-a|\epsilon_0|^u)^{1/w} \tag{3.34}$$

where w≈3. For $B_{C2}(T,\epsilon)$ the proposed equation is

$$B_{C2}(T,\epsilon) \propto (1-a|\epsilon_0|^u)(1-t^2) \tag{3.35}$$

Besides axial strain, one of the first strain components that was studied was the hydrostatic strain/pressure. The difference in the slope (dT_C/dP) in the T_C versus P(Pressure) curve for single crystals and polycrystalline layers of Nb_3Sn superconductors suggests that the deviatoric strain is the most important strain component that determines the critical properties of the Nb_3Sn in a uniaxial strain experiment[63,64]. A deviatoric strain is a measure for the change in shape instead of the change in volume(hydrostatic pressure). A small deviatoric strain can cause a severe decrease of T_C of the material[36]. Although Ekin's scaling law has been quite successful there remains some uncertainties. First, is the uncertainty in determining the exact position of the maximum current. Second, is the influence of the applied compressive strain. The compressive part of Ekin's scaling law comes from the thermal compression of the material(pre-strain). The applied compressive strain has a larger influence on J_C than the compressive thermal pre-strain.

ten Haken showed that the assumption that the maximum in B_{C2} occurs when the superconductor is in the 'strain free' state may not be necessarily correct. Actually there is no state where the strain components are zero. In the axial strain experiment the zero strain state is when the thermal pre-strain is completely relieved. However, one can also consider the axial strain where the minimum in deviatoric strain occurs. Easton showed good agreement between the thermal strain and the measured ϵ_{max} if the yielding of the matrix is taken into account[65]. Figure 3.17 shows the reduced critical current as a function of the applied axial strain[36]. ten Haken showed that the minimum in the deviatoric strain appears at an applied axial strain of $\frac{d\epsilon_{dev}}{d\epsilon_a}=0$ where

$$\epsilon_a=-\frac{\delta}{2}\frac{(1-\nu_b)(1+\nu_b)^2}{(1-\nu+\nu^2)(1+\nu_b+\nu_b^2)-3\nu\nu_b}\approx-1.05\delta \qquad (3.36)$$

In the above equation δ is the thermal strain, ν is the Poisson's ratio of Nb_3Sn and ν_b is the Poisson's ratio for the brass spring that was used in the experiment. The result shows that the minimum in the deviatoric strain can coincide with the zero axial strain inside the Nb_3Sn layer using an appropriate Poisson's ratio. The influence of large applied axial compressive strain on the superconducting properties of Nb_3Sn has been investigated by ten Haken[36]. Figure 3.18 shows an example of $I_C(\epsilon_a,B)$ for a Nb_3Sn tape sample. The applied strain, ϵ_a , is from -0.4%(compression) to 0.7%(tension). Figure 3.19 is the Kramer plot for the same measurements. A variation of B_{C2} in the sample causes a non-linearity in the Kramer current if B approaches B_{C2}. The best Kramer fit is for small axial strains($\approx$ 0.1%). The largest deviation of the Kramer fit is when B approaches B_{C2}. Figure 3.19 shows that at high compressive strains there is a non-linear $I_K(B)$ dependence.

Figure 3.20 shows a comparison of the extrapolated B_{C2} for two different Nb_3Sn samples. The $B_{C2}(\epsilon_a)$ dependence can be fitted to strain scaling law:

$$B_{C2}(T,\epsilon_a)=B_{C2}(T,0)(1-a|\epsilon_a|^u) \qquad (3.37)$$

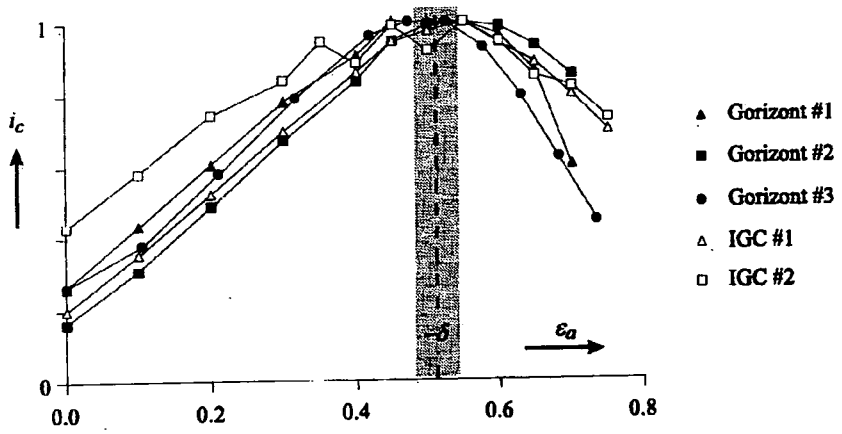

Figure 3.17: The reduced critical current as a function of applied strain for five different Nb_3Sn samples. The estimated point where the thermal pre-strain is cancelled($-\delta$) is indicated with a dotted line. The grey band shows the accuracy for this estimated point[36].

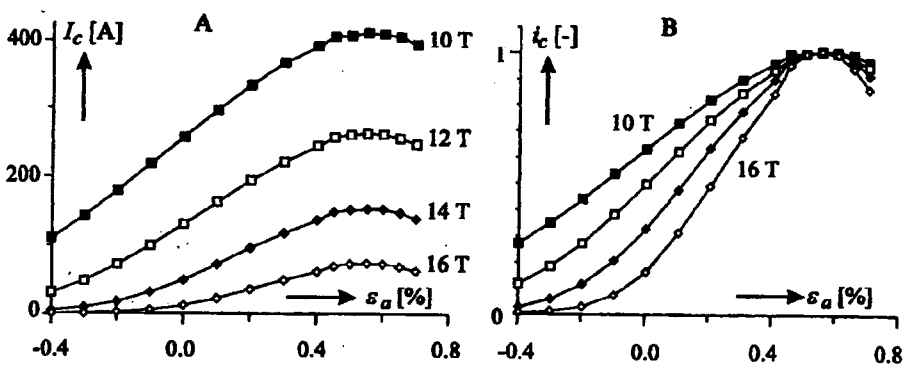

Figure 3.18: An example of $I_C(\epsilon_a,B)$ for a Nb_3Sn tape sample. Left: Measured I_C values. Right: Normalised critical current[36].

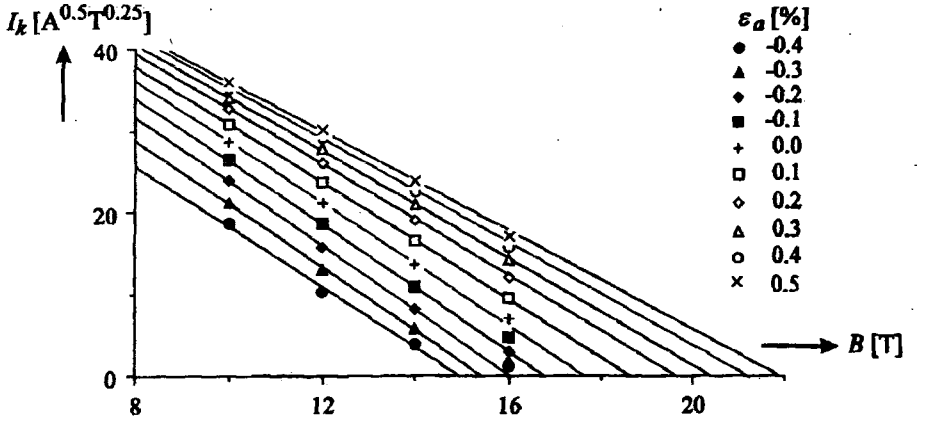

Figure 3.19: A Kramer plot for the data of figure 3.18[36]

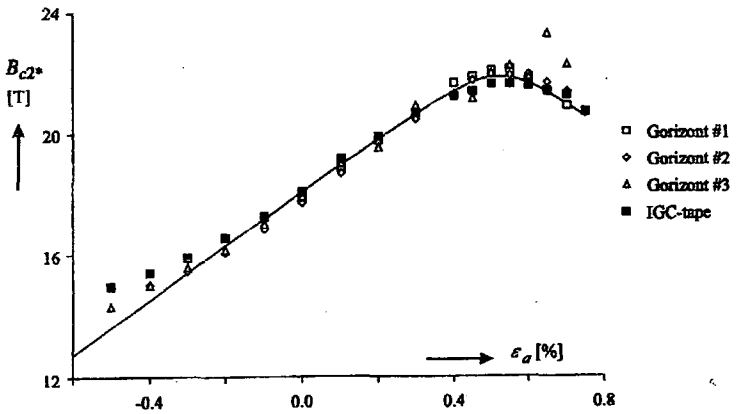

Figure 3.20: A comparison of the extrapolated B_{C2} for two different Nb_3Sn samples[36].

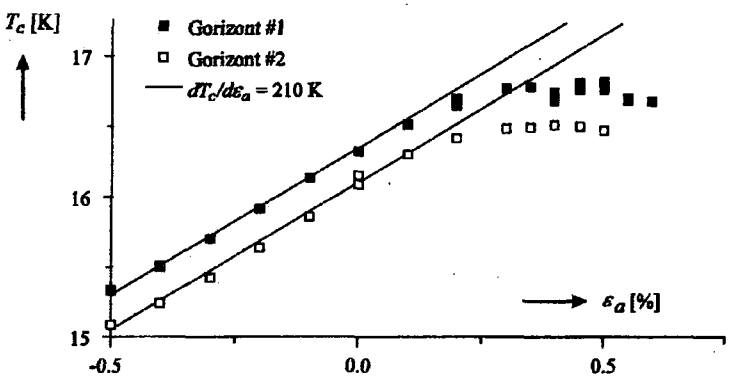

Figure 3.21: The T_C versus axial strain for two different Nb_3Sn samples[36].

The fit is made with u ≈1.7. However, the B_{C2} reduction for the compressive strains is nearly proportional(u≈1) to strain. Considering the change from a power of ≈1.7 to a power of 1, B_{C2} can be expressed as

$$B_{C2}(\epsilon_a)=B_{0,a}-C_a\sqrt{(\epsilon_a+\delta)^2+(\epsilon_{0,a})^2} \tag{3.38}$$

where C_a is the slope $dB_{C2}/d\epsilon_a$.

ten Haken showed that the above equation can be generalised in terms of B_{C2} that depends on deviatoric strain[36],

$$B_{C2}(\epsilon_{dev})=B_{0,d}-C_d\sqrt{(\epsilon_{dev})^2+(\epsilon_{0,d})^2} \tag{3.39}$$

Figure 3.21 shows the T_C versus axial strain for two different Nb_3Sn samples. The strain dependence of T_C is similar to the strain dependence of B_{C2}. There is a maximum in T_C when the applied strain is increased. However, the maximum T_C was shown to be slightly lower than the maximum for B_{C2}. Figure 3.22 is a comparison of T_C, B_{C2} and I_C versus strain for a Nb_3Sn tape. The shape of the curves is quite symmetrical.

Figure 3.23 shows the Kramer plot for two different Nb_3Sn wires. For high compressive strains, there is a difference between the two samples. Figure 3.24 is the B_{C2} versus applied strain for a set of Nb_3Sn wires. The VAC-NS sample is compared to Ekin's scaling law. The $B_{C2}(\epsilon_a)$ dependence was fitted using u=1.7. Figure 3.24 shows that the $B_{C2}(\epsilon_a)$ dependence is slightly asymmetric with respect to the position of the maximum. To account for this asymmetry a new expression is proposed by adding an extra term that is linear in ϵ_a:

$$B_{C2}=B_{0,a}-C_a\sqrt{(\epsilon_a-\delta)^2+\epsilon_{0,a}^2}+C_{2,a}\epsilon_a \tag{3.40}$$

where C_a and C_2 are constant.

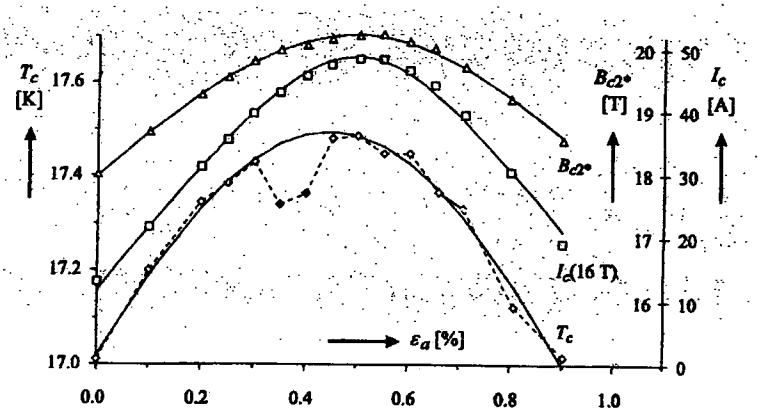

Figure 3.22: A comparison of T_C, B_{C2} and I_C versus strain for a Nb_3Sn tape[36].

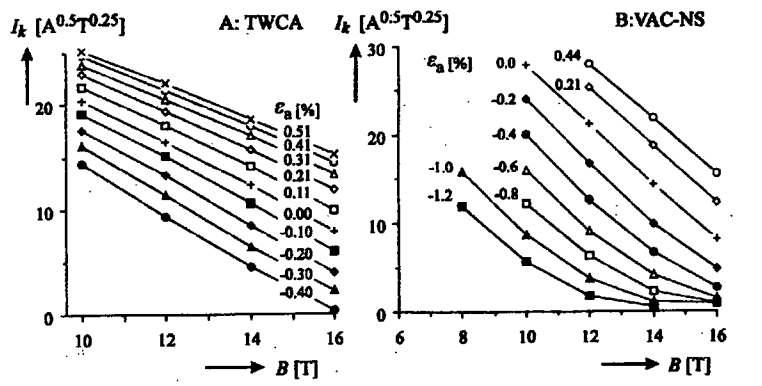

Figure 3.23: The Kramer plot for two different Nb_3Sn wires[36].

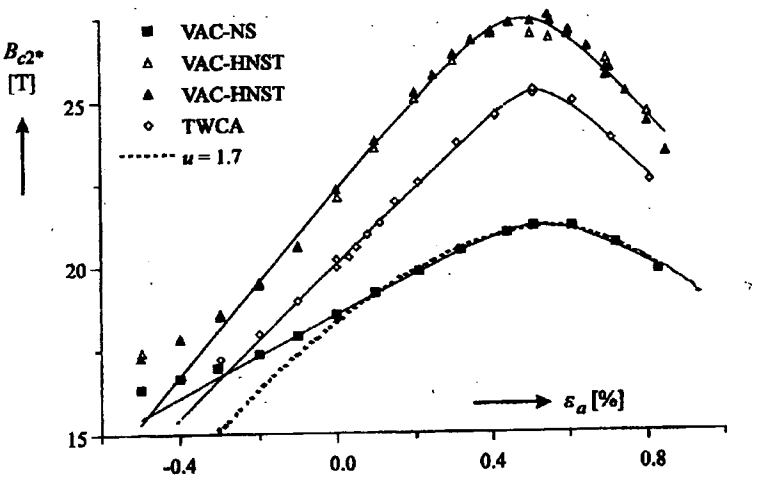

Figure 3.24: The B_{C2} versus applied strain for a set of Nb_3Sn wires[36].

The above equation can be generalised by means of the hydrostatic strains:

$$B_{C2} = B_{0,d} - C_d\sqrt{(\epsilon_{dev})^2 + \epsilon_{0,d}^2} + C_h\epsilon_{hyd} \tag{3.41}$$

where C_d and C_h are constants.

A general expression for B_{C2} that includes transverse pressure was also proposed by ten Haken[36] for a Nb_3Sn structure with a current flowing in the z-direction. The form of the equation is

$$B_{C2} = B_0 - C_B\sqrt{\epsilon_z^2 + \left(\frac{\sigma_x}{E_B}\right)^2 + \left(\frac{\sigma_y}{E_B}\right)^2} \tag{3.43}$$

where σ is the transverse stress, C_B is a constant and E_B is related to Young's modulus of Nb_3Sn(E).

3.7 Summary

This chapter has covered some aspects of the critical current and its relation to superconductivity. The critical current is the most important parameter for industrial applications. In defining critical currents from V-I characteristics different criteria has been used namely, the superconducting-to-normal transition, resistivity, voltage, electric field and power criteria. The most commonly used is the voltage or the electric field criteria. The critical current in type I and type II superconductors has also been considered. The critical current in type I superconductor is explained in terms of Silsbee's rule. In type II the basic idea is that the Lorentz force acts on flux lines in the presence of a transport current. These flux lines are supported by pinning centres up to a certain critical threshold after which flux-line motion occurs. The different types of pinning interactions have been considered. This leads to the problem of determining the bulk volume pinning force of the material. Fietz and Webb showed that for most materials the volume pinning curves obey a scaling law. Generally, the volume pinning

force is found to scale with temperature.

The microstructural distribution of pinning centres in a material can be related to the distribution of the critical current. One method of getting the distribution is to postulate a normal distribution and adjusting several free parameters until a fit is obtained to the experimental V-I data. The other method is to directly manipulate the V-I data and take its second derivative. This method is made possible recently by the use of computers.

Apart from high J_C the material must have good mechanical properties. The effect of strain on the critical current has been discussed. It is interesting to know that the pinning force obeys a strain scaling law. The strain scaling law can be extended and combined with the temperature-scaling relation of Fietz and Webb to obtain a general scaling law for the dependence of F on both strain and temperature. The strain dependence of B_{C2} on the deviatoric strains has also been discussed.

Reference

1. Powell R L and Clark A F., *Cryogenics* **20** 140 (1978).
2. Jones H and Jenkins R G., *High-Temperature Superconducting Materials Science and Engineering:* ed. Donglu Shi (Pergamon) p.260 (1995).
3. Bussiere J F, Garber M and Shen S., *Appl. Phys. Lett.*, **25** 756 (1974).
4. Clark A F and Ekin J W., *IEEE Tran. Magn.* **MAG-13** 38 (1977).
5. Silsbee F B., *J. Wash. Acad. Sci.* **6** 597 (1916).
6. Reed R P and Clark A F., *Materials at Low Temperatures* (American Society for Metals, USA) (1983)
7. Evettes J E, Campbell A M and Dew-Hughes D., *J. Phys. C* **1** 715 (1968).
8. Campbell A M, Evetts J E and Dew-Hughes., *Phil. Mag* **18** 313 (1967).
9. Dew-Hughes D., *Philos. Mag.* **30** 293 (1974).
10. Campbell A M and Evetts J E., *Adv. in Phys.* **20** 199 (1972).
11. Larkin A I and Ovchinnikov Yu N., *J. Low Temp. Phys.* **34** 409 (1979).
12. Kes P H., *IEEE Trans. Magn.* **23** 1160 (1987).
13. Fietz W A and Webb W W., *Phys. Rev.* **178(2)** 657 (1969).
14. Kramer E J., *J. Appl. Phys.* **44** (3) 1360 (1973).
15. Hampshire R G and Taylor M T., *J. Phys. F* **2** 89 (1972).
16. Yeshurun Y and Malozemoff A P., *Phys. Rev. Lett.* **60** 2202 (1988).
17. Suenaga M, Ghosh A K, Xu Y and Welch D O., *Phys. Rev. Lett.* **66** 1177 (1991).
18. Suenaga M, Welch D O and Budhani R., *Supercond. Sci. Technol.* **5** S1 (1992).
19. Sulpice A, Jonnard P and Giordanega B., *Proc. EUCAS 1993 - Applied Superconductivity* **Vol 1**, ed. Freyhardt H C ., 697 (DGM -1993).
20. Zheng D N., *PhD Thesis,* Christ's College, Cambridge (1994).
21. Brandt E H., *Intl. J. Mod. Phys. B* **5**(5) 751 (1991).
22. Zheng D N, Campbell A M, Johnson J D, Cooper J R , Blunt F J, Porch A and Freeman P A., *Phys. Rev. B* **49** 1417 (1994).
23. Czurda C and Weber H W., *Proc. EUCAS 1993 - Applied Superconductivity* **Vol 1**, ed. Freyhardt H C., 795 (DGM 1993).

24. Wisnieski A, Brandstatter G, Czurda C, Weber H W, Morawski A and Lada T., *Physica C* **220** 181 (1994).
25. Warnes W H and Larbalestier D C., *Appl. Phys. Lett.* **48** 1403 (1986).
26. Warnes W H and Larballestier D C., *Cryogenics* **26** 643 (1986).
27. Baixeras J and Fournet G., *J. Chem. Solids* **28** 1541 (1967).
28. Hampshire D P and Jones H., *Cryogenics* **27** 608 (1987).
29. Hampshire D P and Jones H., *J. Phys. C: Solid State Phys.* **20** 3533 (1987).
30. Plummer C J G and Evetts J E., *IEEE Trans. Magn.* **MAG-23** 1179 (1987).
31. Savitsky A and Golay M J E., *Anal. Chem.* **36** 1627 (1964).
32. Kusevic I, Babic E, Prester M, Dou S X and Liu H K, *Solid State Comm.* **88** 241 (1993).
33. Ekin J W., *Cryogenics* **20** 611 (1980).
34. Kovac P, Husek I and Cesnak L., *Supercond. Sci. Technol.* **7** 583 (1994).
35. Evetts J., *Concise Encyclopedia of Magnetic and Superconducting Materials*, Pergamon Press UK (1992).
36. ten Haken B., *PhD Thesis*, University of Twente, Netherlands (1994).
37. Yau J F K, Saviddes N and Sorrell C C., *Physica C* **266** 223 (1996).
38. Luhman T, Welch D O and Suenaga M., *IEEE Trans. Magn.* **MAG-17** 662 (1981).
39. Kovac P, Kopera L, Husek I and Cesnak L., *Supercond. Sci. Technol.* **9** 792 (1996).
40. Li Q, Ostenson J E and Finnemore D K., *J. Appl. Phys.* **70**(8) 4392 (1991).
41. Otto A, Masur L J, Gannon J, Podtburg E, Daly D, Yurek G J and Malozemoff A P., *IEEE Tran. on Appl. Supercond.* **3**(1) 915 (1993).
42. Summers L T, Walsh R P Miller J R., *IEEE Tran. on Appl. Supercond.* **5**(2) (1995).
43. Ekin J W., *J. Appl. Phys* **54**(1) 303 (1997).
44. Ekin J W., *Advances in Cryogenic Engineering* **24** 306 (1978).
45. Rupp G., *IEEE Trans. Magn.* **MAG-13** 1565 (1977).
46. Ekin J W., *Appl. Phys. Letts.* **29** 216 (1976).
47. Ekin J W, Fickett F R and Clark A F., *Advances in Cryogenic Engineering* **22** 449 (1976).

48. Easton D S and Schwall R E., *Appl. Phys. Lett* **29** 319 (1976).

49. Buehler E and Levinstein H J., *J Appl. Phys.* **36**(12) (1965).

50. Ekin J W., *IEEE Tran. on Magn.* **MAG-13** 127 (1977).

51. Ekin J W., *IEEE Tran. on Magn.* **MAG-19** 900 (1983).

52. Ekin J W, Braginski A I, Panson A J, Janocko M A, Capone II D W, Zaluzec, Flandemeyer B, de Lima O F, Hong M, Kwo J and Liou S H., *J. Appl. Phys.* **62**(12) 4821 (1987).

53. Ekin J W, Finnemore D K, Li Q, Tenbrink J., *Appl. Phy. Lett.* **61**(7) 858 (1992).

54. Miller T A, Ostension J E, Li Q, Schwartzkopf L A, Finnemore D K, Righi J, Gleixner R A and Zeigler D., *Appl. Phys. Lett.* **58**(19) 2159 (1991).

55. ten Haken B and ten Kate H J ., *IEEE Tran. on Appl. Supercond.* **5**(2) 1298 (1995).

56. Richens P E, Jones H, Van Cleemput M and Hampshire D P., *IEEE Tran. on Appl. Supercond.* **7**(2) 1315 (1997).

57. Sato K, Hikata T, Mukai H, Ueyama M, Shibuta N, Kato T, Masuda T, Nagata M, Iwata K and Mitsui T., *IEEE Tran. on Magn.* **27**(2) 1232 (1991).

58. Selvamanickam V, Mamberger C, Martin P M and Kroeger D M., *IEEE Tran. on Appl. Supercond.* **5**(2) (1995).

59. Martini L, Bigoni L, Varesi E, Zanella S, Gherardi L, Caracino P and Spreafica S., *Proc. EUCAS 1995 - Applied Superconductivity* **Vol 1**, ed. Dew-Hughes D., Edinburgh (1995).

60. Poirer M, Plamondon R, Cheeke J D N and Bussiere J F., *J. Appl. Phys.* **55**(9) 3327 (1984).

61. Ekin J W., *IEEE Tran. on Magn.* **MAG-17**(1) 658 (1981).

62. Ekin J W., *Filamentary A15 Superconductors*: ed. M. Suenaga and AF Clark p. 187 (1980).

63. Lim K C and Thompson J D., *Phys. Rev. B* **27** 2781 (1983).

64. Chu C W and Vieland L J., *J. of Low Temp. Phys.* **17** 25 (1974).

65. Easton D S, Kroeger D M and Koch C C ; *J. Appl. Phys. 51*(**5**) 2748 (1980).

Chapter 4

A Probe for Measuring the Critical Current Density of Superconductors as a Function of Strain in Magnetic Fields

4.1 Introduction

The effect of strain on the current carrying capacity, J_C, is an important factor in the technological use of superconducting tapes and wires. Superconducting magnet applications, for example, subject the conductor to strain on the order of 0.2% during the process from winding the conductor to forming a magnet[1]. For Nb_3Sn a tensile strain of only 0.5% at 12 T can reduce its J_C by 50%[2]. Therefore it is important to understand the strain tolerance or the ability of these superconducting tapes and wires to withstand mechanical strain without significant deterioration of J_C[3]. Most work on how J_C depends on strain is either tensile or bending tests. The J_C versus strain measurements in high magnetic fields that combine tension and compression are rare because they need specialised equipment.

The Durham probe is designed to measure tensile and compressive strains on short samples in our 17 Tesla superconducting magnet system. Since it is leak-tight, variable temperature measurements can also be made by pumping on the cryogen-bath of the magnet system. The J(B,ϵ) probe can be used to measure J_C(B,ϵ) on low temperature superconductor(LTS) and high temperature superconductor(HTS) wires and tapes. We have successfully used this probe to measure strains on a BiSCCO tape and a Nb_3Sn wire. This chapter describes the design and operation of the J(B,ϵ) probe. Data obtained can then be used to determine the relationship between J_C and strain of the superconducting material.

Section 4.2 describes the principle of operation of the J(B,ϵ) probe. Section 4.3 describes the construction of the probe. This includes a discussion on some design considerations, how the probe works and its general design features. Section 4.4 is a discussion on sample mounting and its development. Section 4.5 is about the probe's wiring system. Section 4.6 describes external circuitry. Section 4.7 outlines the experimental procedure to take data. Section 4.8 describes how strain is measured. Section 4.9 describes what happens to a wire when strain is applied. Section 4.10 is about strain changing with the Lorentz force during V-I measurement. In section 4.11 results are presented for strain measurements on a BiSCCO tape and a Nb_3Sn wire. These measurements were done in field at 4.2 K. This is followed by a short discussion in section 4.12. Section 4.13 concludes this chapter with a short summary of some of the main conclusions.

4.2 Principle of operation

The measurements consist of attaching a strain gauge to the sample which is situated at the bottom of the probe. Current leads are then attached to the sample along with two voltage taps at a distance of 3-5 mm apart. The strain gauge lies between the voltage taps. The probe is then inserted into a high field magnet. Strain is then applied to the sample via a gear system located at the top of the probe. The value of the strain is calculated from the change in resistance of the strain gauge. Then current against voltage(I-V) traces are taken as a function of strain and magnetic field. The I-V measurements are repeated at all the required strains and magnetic fields.

4.3 The J(B,ϵ) probe

4.3.1 Design considerations of the J(B,ϵ) probe

The probe is to be used for tensile and compressive measurements. Strain up to 1.0% can be applied on short samples(~ 10 mm long). However, the upper limit of the applied strain also depends on the type of sample that is being measured. Because high field superconductors are brittle, the applied strain can rarely exceed 1.0% before sample

breakage occurs. Other design considerations included:

(a) Size of the bore of the magnet system.

The size of the bore of the high field magnet is 40 mm. This restricts the overall dimensions of the probe.

(b) Applying strain to the sample.

An important design consideration is how to apply strain to the sample. For tensile measurements the standard method is to pull the sample at both ends by using some sort of an axial pulling machine[4,5]. These may involve using a split-pair magnet system to generate a field transverse to the sample axis. The Durham J(B,ϵ) probe uses a gear system to transfer the driving force from top of the probe down to the sample. The probe works like a 'car-jack'.

4.3.2 How the probe works

Figure 4.1 shows the overall construction of the J(B,ϵ) probe. The driving force is applied manually by turning a knob located at top of the probe. For tensile measurements the knob is turned clockwise. By turning the knob the upper stainless steel rod rotates via a gear system. When the upper rod rotates the lower rod also rotates. The threaded end of the lower rod then moves deeper into the screwthread housing and lifts the screwthread housing towards the lower collar. This causes the upper brass struts at the bottom section of the probe to move upwards. This upward movement causes the top part of the lower brass struts to close. The lower brass struts are fixed at the pivot. When the top part of the lower brass struts closes, the bottom part of the lower brass struts opens up. This movement will stretch the sample. For compressive measurements, the knob is turned anticlockwise and the reverse happens.

4.3.3 Top section of the probe

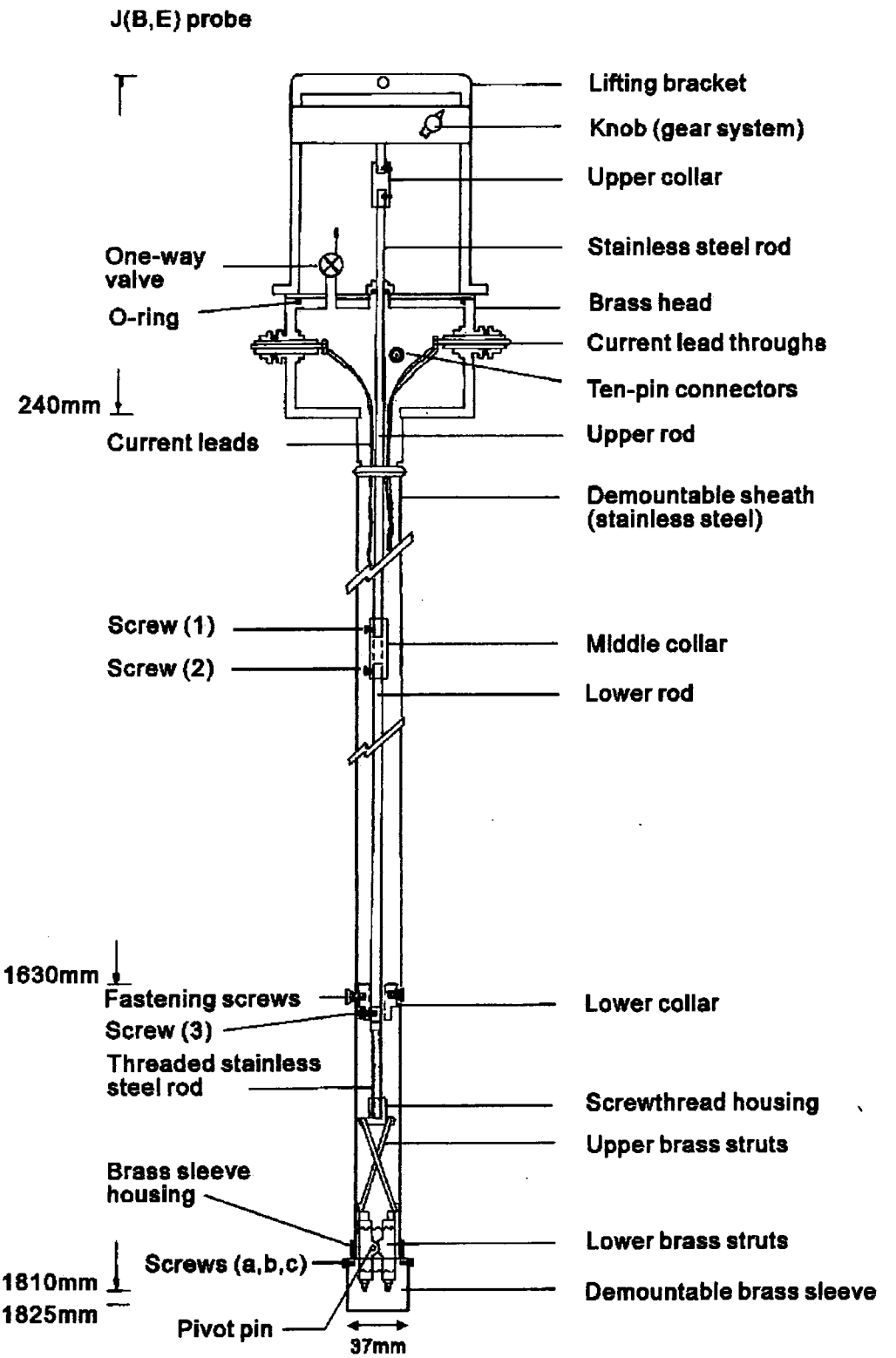

Figure 4.1: The J(B,ϵ) probe (drawn to scale).

The overall length of the probe is 1825 mm. The diameter of the probe is limited to 37 mm so that it can be inserted in the 40 mm bore of our Oxford Instruments 17 Tesla magnet. The top brass head consists of two electrical leadthroughs for current leads, two ten-pin connectors for instrumentation leads, a one way valve and a gear system attached to an aluminium lifting bracket. A thin-walled demountable stainless steel sheath protects the instrumentation leads. It also helps to reduce heat loss and the overall weight of the probe. The whole system is leak-tight.

A 6 mm diameter stainless steel upper rotating rod is attached to the gear system at the upper collar. This rod runs through the middle of the probe to the stainless steel middle collar. A slot(7mm long, 3 mm wide and 1.5 mm deep) is made 2 mm above the bottom end of this rod. This rod is attached to the middle collar by screw (1). The end of this screw sits in the slot of the rod. The rod is free to move axially in the middle collar. When the rod rotates, screw(1) also rotates relative to the rod. The screw prevents the rod from slipping out of the middle collar.

Another 6 mm diameter stainless steel lower rotating rod, with an equivalent slot at one end and a threaded part at the other end, is attached to the stainless steel middle collar. The slotted end of the rod is attached to the middle collar by screw (2). This section serves the same purpose as described in the above paragraph.

From the middle collar, the lower rotating rod runs through another stainless steel collar(lower collar) located near the bottom of the probe. A small horizontal groove(2 mm wide) is made around the lower part of the rod. The position of the groove is 8 mm above the top end of the threaded part. The rod is attached to the lower collar at the groove with a small stainless steel screw(screw 3). The purpose of the lower collar is to centralise the rod and hold it in place when strain is applied. This is one of the fixed points of the probe. The end of screw 3 sits in the groove. This screw prevents the lower collar from slipping along the rod. The lower collar is anchored to the demountable stainless steel sheath by three stainless steel fastening screws. The lower

rod is free to rotate inside the lower collar. When the rod rotates, screw 3 does not move with the rod. The threaded end of this rod is connected to the bottom section of the probe at the screwthread housing.

4.3.4 Bottom section of probe

Figure 4.2 represents the bottom section of the probe. The bottom section of the probe consists of a pair of upper brass struts and a pair of lower brass struts. The upper brass struts are connected to the screwthread housing by two stainless steel pins. The upper brass struts are also connected to the lower brass struts by two stainless steel pins. These pins are insulated from the screwthread housing and the lower brass struts using PTFE. The PTFE also reduces friction when the upper brass struts moves relative to the screwthread housing and the lower brass struts.

The bottom part of each lower brass struts has two brass posts for sample mounting. These brass posts are insulated with Tufnol(Carp Brand). The lower brass struts are attached to the demountable stainless steel sheath by inserting the stainless steel pivot pin through the stainless steel sheath and the pivot point, and hence prevent the bottom section of the probe from rotating when strain is applied. The pivot pin is insulated from the lower brass struts by PTFE. The PTFE also helps to reduce friction when the lower brass struts moves relative to the pin. The two halves of the lower brass struts are connected to each other by two springs. The purpose of these springs is to return the position of the lower brass struts to their normal position when tension is removed.

4.4 Sample mounting

Before mounting the sample ,the demountable stainless steel sheath is first attached to the probe. The purpose for removing the demountable stainless steel sheath after each set of measurements is to check the instrumentation leads inside the probe. Two brass plates of thickness 1.5 mm each are made that fit onto the posts. The sample is soldered at both ends on to the brass plate across the lower brass struts. The demountable brass sleeve is then attached to the stainless steel sheath at the brass sleeve housing by three

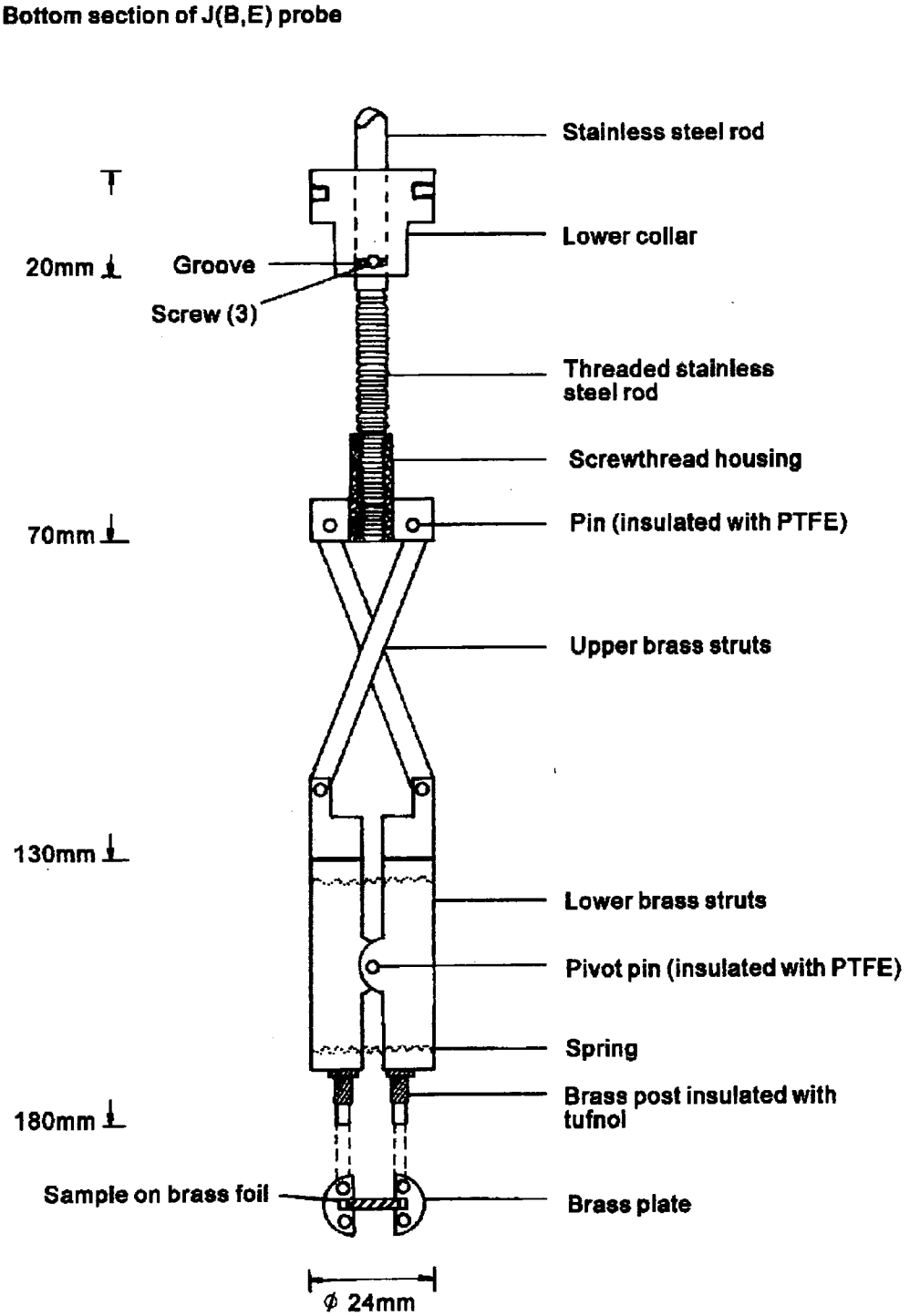

Figure 4.2: The bottom section of the J(B,ϵ) probe (drawn to scale).

screws(a,b,c). This is to protect the sample during handling the probe. The probe is then slowly immersed into the high field magnet. When everything has cooled down the strain reading is noted to see the effect of mounting the sample on the probe. A detailed description of how to mount a HTS BiSCCO tape and a LTS Nb_3Sn wire on the probe is given below.

4.4.1 Sample mounting development

Initial experiments on strain measurements met with limited success. The major obstacle was sample mounting. The procedure outlined in section 4.4.2 is the final procedure that was successful. This section is a short historical account of sample mounting development.

(a) Mounting HTS BiSCCO tape

The first measurements were made by simply soldering the tape on to the brass plates of the J(B,ϵ) probe. Because the tape was brittle it had to be handled carefully. It can also break suddenly after a tensile strain of about 0.15 - 0.2%. To overcome this the tape was then soldered onto a brass foil. Soldering the tape onto a brass foil also helped to eliminate handling problems. At first only the ends of the tape were soldered on the brass foil. But when tensile strain was applied, the ends of the tape usually came-off from the solder joints. The next step was to solder entirely the back of the tape on the brass foil. PbSnAg solder(Fibra-Sonics S-100A-10) was used for sample mounting. The PbSnAg solder has a melting point of 305°C and is ductile at low temperatures[6]. Ordinary PbSn solder was not used because it is less ductile than the PbSnAg solder. The additions of 0.5 wt % silver to ordinary PbSn solder can significantly improve its creep resistance[7]. Creep is the time-dependent deformation of a material when subjected to an applied stress.

Even though the level of strain could now be increased beyond 0.2% the problem of sudden tape breakage still existed. If sudden breakage occurs the gradual change in J_C of the tape cannot be detected. To solve this an SWG 26 (0.45 mm diameter) copper

wire was soldered parallel to the tape. The wire was insulated from the tape and the high current leads to prevent it from acting as a shunt. This `wire and foil ' method enabled strain in excess of 0.3% to be applied to the sample. This was enough to get the desired result.

Brass foil of different thickness were tried and it was found that a brass foil of thickness 0.1 mm gave the best result. A foil of thickness less than 0.1 mm may break earlier than the tape. This can also break the tape prematurely since the tape was soldered entirely to the brass foil. If a thicker than 0.1 mm foil is used extra driving force has to be applied to the probe and this may ruin the gear system. The same reasoning also applies to the choice of the copper wire. For compressive measurements the copper wire was not used.

(b) Mounting Nb_3Sn wire

The first measurements on wires were also made by simply soldering the ends of the wire on to the brass plates of the probe. When tensile strain was applied the wire broke at about 0.1% strain. The entire length of the wire was then soldered onto a brass foil of thickness 0.1 mm. The ends of this foil were then soldered on to the brass plate. Even though the mechanical strength of the wire was slightly increased it was not enough to detect the gradual change in J_C of the wire.

Mounting a Nb_3Sn wire is more complicated than mounting a tape. Since the probe is designed to measure short samples the current transfer length of the wire is an additional problem. If the transfer length is not enough the applied current will not flow through the superconductor region of the wire but is shunted through an alternative path. This problem did not arise with the tape because the ratio of the superconducting material to matrix of the tape is higher than that of the wire.

The wire should be straight so that when strain is applied the force is transmitted uniformly to the wire. A special stainless steel mandrel has been designed for this purpose. The mandrel was designed such that a straight section of the wire (~ 9 mm)

can be obtained. The wire is then reacted in argon atmosphere for 64 hours at 700° C.

A new pair of brass plates of thickness 1.0 mm were also made(fig. 4.3). Each of these brass plates has an additional 1.5 mm hole. Into each hole was fitted a 1.5 mm steel screw. These brass plates were then fitted into the brass posts of the probe. The reacted Nb_3Sn wire was then soldered on to the 0.1 mm thick brass foil. Details for mounting the wire on probe is given in section 4.4.2. The V-I traces taken indicated a large resistive base-line.

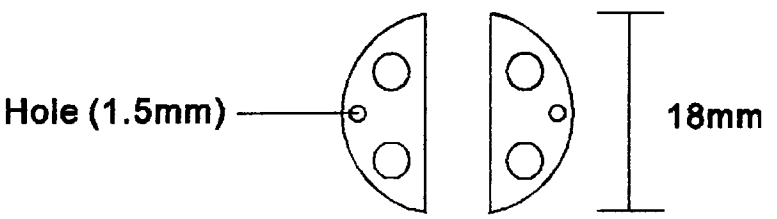

Figure 4.3: Brass plates of thickness 1.0 mm with an additional 1.5 mm hole

The stainless steel screws were then replaced by 1.5 mm copper posts. By doing so the large resistive base-line was markedly reduced since the electrical conductivity of copper is about four orders of magnitude higher than that of stainless steel[8]. The ends of the wire were twisted about three times around the post to increase the transfer length.

The amount of solder used was crucial when soldering the Nb_3Sn wire to the brass foil. The wire has to be entirely soldered to the brass foil. A strain in excess of 0.6% can be applied if the wire was soldered properly. For a 0.37 mm Nb_3Sn wire the thickness of the solder applied should be about 0.2 mm. If the soldering was too thick the V-I traces would give a very large resistive base and made data analysis difficult. Also one may not be able to apply any strain to the wire since it needs a large driving force. If the soldering is too thin then it would not add any mechanical strength to the wire.

4.4.2 A step-by-step procedure on sample mounting.

(a) Mounting a HTS tape on the probe

- A section of the HTS tape is cut to about 9 mm length.

- The tape is then cleaned with M-Prep Conditioner A and M-Prep Neutralizer 5A from Micro-Measurements.

- Next the size of a strain gauge(Micro-Measurements, type: WK-06-062AP-350) is reduced to about 4.5 mm x 2 mm by cutting away the backing material. This reduction in size is necessary so that the strain gauge can fit on the tape. The number 350 represents the resistance of the strain gauge at room temperature.

- The back of the strain gauge is then covered with a bonding epoxy(Micro-Measurements, type: M-Bond 43-B). The epoxy is also applied on the tape where the strain gauge is to be placed.

- The strain gauge is pasted directly onto the tape.

- The sample(tape and strain gauge) is then sandwiched between two rubber pads. The size of each rubber pad is 2.5 mm x 13 mm x 32 mm. The sample and rubber pads are then placed between two metal backup plates. The size of each plate is 3 mm x 13 mm x 32 mm. Pressure is then applied to the sample by clamping the metal plates using a spring clamp. This is to remove any air bubbles trapped in the epoxy.

Two different types of clamps were tested on two different samples; a cloth peg and a spring clamp(type HSC-1 from Micro-Measurements). After curing, V-I traces were taken to check the effect of applying pressure to the samples. The V-I traces indicate that the samples were not damaged. The HSC-1 spring clamp is preferred because it has a larger contact area so that pressure can be evenly distributed on the sample. The force from the spring clamp(about 80N) is higher than from the cloth peg.

- The tape and strain gauge is cured in a furnace at 100°C for 4 hours.

‣After curing, the sample is soldered on to a 3.5 mm x 10 mm x 0.1 mm brass foil.

‣ The stainless steel demountable sheath is first attached to the probe.

‣ A pair of brass plates are fitted to the brass posts at the bottom of the probe as shown in figure 4.2.

‣The sample is mounted onto the probe by soldering the ends of the tape/brass foil onto the brass plates.

‣For tensile measurements a 0.45 mm copper wire is soldered parallel to the sample. The wire is insulated from the tape.

‣High current leads are then soldered directly to the ends of the sample. Voltage taps are also soldered directly on the tape. The strain gauge lies between these voltage taps.

‣Current leads and voltage taps are also connected to the strain gauge terminals.

‣Finally the demountable brass sleeve is attached to end of the probe.

(b) Mounting a Nb_3Sn wire on the probe.

‣For strain measurements a strain gauge (Micro-Measurements, type: EA-06-015DJ-120) with a flexible backing material is used. The number 120 represents the resistance of this strain gauge at room temperature.

‣The size of the strain gauge is reduced to 2.5 mm x 0.6 mm by cutting away some of its backing material.

‣The strain gauge and the wire are then cleaned with the same chemicals as in (a).

- The back of the strain gauge is then covered with a bonding epoxy(same type as in(a)). The epoxy is also applied on the wire where the strain gauge is to be placed.

- The strain gauge is pasted directly onto the wire. The strain gauge is pasted such that it partially wrapped the wire.

- The strain gauge is then tied down to the wire using dental floss. This is to apply pressure to prevent any air bubbles getting trapped in the epoxy.

- Voltage taps are then soldered onto the wire. The strain gauge lies between these voltage taps.

- The strain gauge and wire are cured in a furnace at 100°C for 4 hours.

- Next a 0.1 mm thick brass foil is cut to 3 mm x 20 mm size. A 1.6 mm hole is drilled at both ends of the brass foil.

- The two brass plates (fig. 4.3) are bridged together by inserting the 3 mm x 20 mm brass foil onto the copper posts.

- The Nb_3Sn wire is then carefully inserted into the copper posts until it rests on the brass foil. The entire length of the wire is soldered to the brass foil.

- The ends of the brass foil/wire are soldered to the copper posts.

- The stainless steel demountable sheath is first attached to the probe.

- The sample(and the brass plates) are fitted to the brass posts at the bottom of the probe as shown in fig. 4.2.

- High current leads are soldered directly to the copper posts.

▸Current leads and voltage taps are also connected to the strain gauge terminals.

▸Finally the demountable brass sleeve is attached to the probe to protect the sample.

4.5 Current and instrumentation leads

The high current leads enter the middle section of the brass head via two vacuum-tight current leadthroughs as shown in figure 4.1. At this point they each consists of 5 pairs of twisted copper wires of 0.71 diameter. Travelling down the probe the number of wires in the lead is reduced until there is only a single pair attached to the sample. Reduction begins at about 400 mm down the probe at approximately 300 mm intervals. This is to reduce helium consumption. The current leads are electrically isolated from the main body of the probe by wrapping them with mylar tape. Instrumentation leads are connected to two-ten pin connectors at the middle of the brass head. All instrumentation leads are twisted pairs to minimize electrical noise in high fields. Since the central rod rotates during strain measurements, enough slack is given to the instrumentation leads and the high current leads to cater for these rotations.

When high sample currents flow, the Joule heat produces cold helium gas. Some of this gas flows past the current leads through several holes in the stainless steel demountable sheath and out through the one-way valve at the brass head. These holes are placed below the line of the cryostat baffles. The gas flow prevents the current leads from overheating and helps reduce helium consumption.

4.6 External circuitry

Figure 4.4 represents external circuitry and equipment for strain measurements. The strain is set manually by turning the knob of the gear system at the top of the probe. The constant current through the strain gauge is supplied from a Lakeshore 120 current source. The voltage across the strain gauge is detected by a Keithley DMM (voltmeter 1).

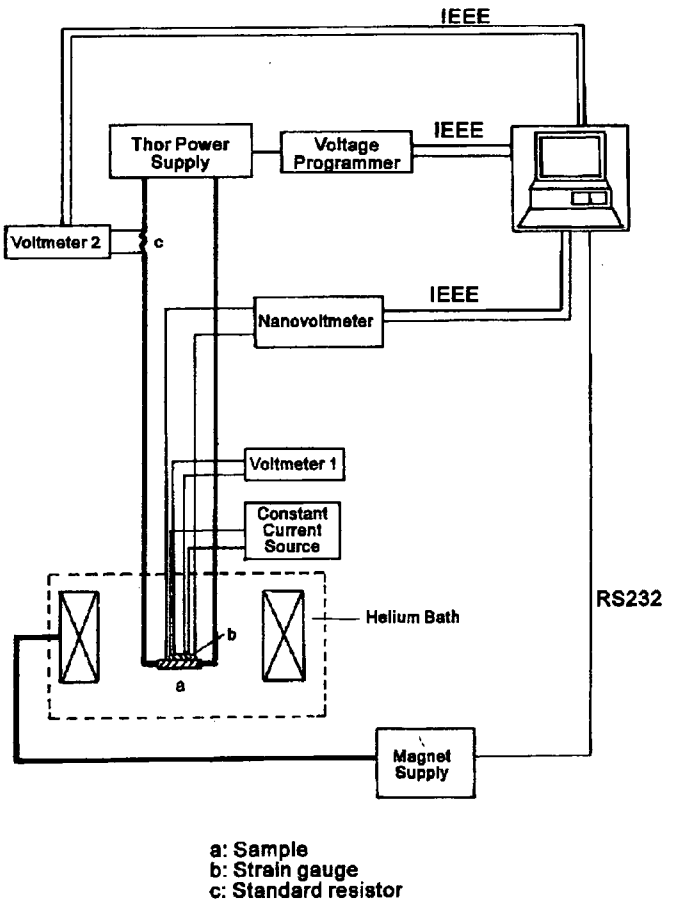

Figure 4.4: External circuitry and equipment for strain measurements.

The system is computer controlled by interactive, real time graphical software written using ASYST (Keithley). A **VITRACE#.PRO** program measures the V-I trace of a sample at a field set manually by the user[9]. The character # stands for number 1 or 2 depending on the type of power supply used. Another program, **VIFIELD#.PRO**, is similar to VITRACE#.PRO but includes control of the superconducting magnet.

The sample current is generated either by a 100 Amp Thor Power Supply or by a 500 Amp Power Supply built in-house. The sample current is ramped by a Kepco voltage programmer and measured by a Keithley digital multimeter (voltmeter 2) with a standard resistor (c) in series. The Keithley DMM has a 6.5 digit resolution and can measure DC voltage from 100nV to 300V. The sample voltage is measured using a Keithley 182

digital nanovoltmeter. It has a high resolution of 1nV. Communication is by the IEEE bus for all instruments except for the magnet power supply which is connected by the RS232 bus.

4.7 Experimental Procedure

Before any strain is applied to the sample a Voltage-Current (V-I) trace is taken to test the quality of the sample. Because PbSn solder becomes superconducting at 4.2 K in zero applied field the initial measurement is made with an applied field of 2 Tesla. This eliminates any possibility that the solder contributes to the V-I trace[6]. The increment in strain is in the range from 0.02% - 1.0%, depending on the sample. V-I traces are then taken for a range of applied fields at a particular strain. The direction of the applied field is perpendicular to the direction of transport current. The strain in the sample is then increased and V-I traces are again taken for a range of applied fields. This procedure is repeated until the sample is damaged.

Measurements can also be made at temperatures below 4.2 K. This can be done by pumping on the helium bath to a particular pressure. One has to make sure that the probe is leak-tight before pumping down. For J_C versus strain measurements the procedure is the same as above.

4.8 Measuring strain

The strain on the sample is measured by a resistance strain gauge pasted on the sample. An electrical resistance strain gauge is a thin metal-foil grid that can be adhesively bonded to the surface of the sample[10]. The resistance of the metal-foil grid changes in proportion to the applied strain. If L is the length of the conductor and R is its resistance then the equation relating the change in resistance to strain is

$$\frac{\Delta R}{R} = G\epsilon \tag{4.1}$$

where

$\epsilon = \frac{\Delta L}{L}$, is the strain

G is the gauge factor or a calibration constant for the strain gauge.

The output of $\frac{\Delta R}{R}$ of the strain gauge is detected as a voltage signal by the DMM. This is done by passing a constant current of 1 mA through the strain gauge. The change in resistance is calculated from the change in voltage shown by the DMM. The sensitivity of the measurement is 1 mΩ. For a strain gauge having an initial resistance of 350 Ω and G=2 , this translates to 1.4 x 10^{-4}% strain.

When a strain gauge is cooled down from room temperature to 4.2 K , four effects occur that influence the signal $\frac{\Delta R}{R}$ from the strain gauge:

a. The resistance of the strain gauge changes.

b. The metal grid of the strain gauge undergoes contraction.

c. The gauge factor, G, changes with temperature.

d. The sample to be measured contracts.

When the sample is mounted on the probe, the contraction of the probe when cooled down to 4.2 K can strain the sample. This means that the sample is already strained relative to an unattached sample suspended at the same temperature. The magnitude of this strain can be deduced by taking the difference between the resistance reading of the sample on the probe and the resistance reading of an unattached sample suspended at the same temperature.

Two sets of 'free' strain gauges (WK-06-062AP-350 and EA-06-015DJ-120) are first immersed into liquid nitrogen (77 K) and then into liquid helium (4.2 K) to get the effect of temperature on these strain gauges. Table 4.1 shows the results for the WK-06-062AP-350 type strain gauges . Table 4.2 are the results for the EA-06-015DJ-120 type strain gauges. The symbols R_T represents room temperature, $\Delta\epsilon$ is the change in strain due to change in temperature and $\overline{\Delta\epsilon}$ are the average values. The negative sign

indicates contraction of these strain gauges.

Strain Gauge (WK-06-062AP-350)	$\Delta\epsilon_{SG1}(\%)$ $R_T \rightarrow$ 77 K	$\Delta\epsilon_{SG1}(\%)$ $R_T \rightarrow$ 4.2 K
a.	-0.265	-0.241
b.	-0.302	-0.287
c.	-0.281	-0.253
d.	-0.287	-0.260
e.	-0.291	-0.267
	$\overline{\Delta\epsilon_{SG1}}$=-0.285	$\overline{\Delta\epsilon_{SG1}}$=-0.262

Table 4.1: The effect of temperature on 'free' strain gauges. Type : WK-06-062AP-350 (SG1).

Strain Gauge (EA-06-015DJ-120)	$\Delta\epsilon_{SG2}(\%)$ $R_T \rightarrow$77K	$\Delta\epsilon_{SG2}(\%)$ $R_T \rightarrow$4.2K
a.	-1.130	-4.45
b.	-1.129	-4.48
c.	-1.126	-4.50
d.	-1.131	-4.46
	$\overline{\Delta\epsilon_{SG2}}$=-1.129	$\overline{\Delta\epsilon_{SG2}}$=-4.473

Table 4.2: The effect of temperature on ' free' strain gauges. Type of strain gauges: EA-06-015DJ-120(SG2).

A simple 'dunk' test is also performed on a set of freely suspended BiSCCO and Nb_3Sn samples to get their resistance readings. These resistance readings are defined as the zero-strain values of the samples. The resistance readings are converted to strain values using equation 4.1. Table 4.3 gives the strain readings for several freely suspended BiSCCO tapes at 77 K and 4.2 K. These samples are from different sections

of the same tape. The symbol ϵ_S represents the strain effect on the sample.

Sample (BiSCCO)	$\Delta\epsilon_{TAPE}(\%)$ $R_T \rightarrow$ 77 K	$\Delta\epsilon_{TAPE}(\%)$ $R_T \rightarrow$ 4.2 K
1.	-0.284	-0.261
2.	-0.252	-0.227
3.	-0.269	-0.252
4.	-0.279	-0.245
5.	-0.238	-0.220
6.	-0.255	-0.241
	$\overline{\Delta\epsilon_{TAPE}}$=-0.263	$\overline{\Delta\epsilon_{TAPE}}$=-0.241

Table 4.3 : The effect of temperature on strain for several freely suspended samples of BiSCCO tapes at 77 K and 4.2 K.
Type of strain gauge: WK-06-062AP-350(SG1)

From Tables 4.1 and 4.3 the difference in strain between the 'free' strain gauges and the freely suspended samples at 4.2 K is about 0.021 %. The results also show that the 'free' strain gauges seem to contract more than that of the unattached samples. The samples may have prevented the strain gauges from contracting further since the strain gauges are pasted directly onto the samples. However, the difference is not that significant.

Table 4.4 gives the strain readings for several unattached short sections of Nb_3Sn wires used in the J_C versus strain experiments. The wires are taken from the same batch. The diameter of the wire is 0.37 mm. From Tables 4.2 and 4.4 the contraction of the Nb_3Sn alone is calculated to be about 0.047%.

After the sample has been mounted on the J(B,ϵ) probe, the probe is slowly inserted into the high field magnet. The resistance of the strain gauge on the sample is continuously monitored when cooling down from room temperature to 4.2 K. When

everything has stabilised at 4.2 K, the resistance reading is taken and then converted to strain value using equation 4.1. The values of strain quoted are the difference between those values found for the sample on the probe and the $\overline{\Delta\epsilon}$ values which are used to define zero strain. The $\overline{\Delta\epsilon}$ value is taken from either table 4.3 or 4.4 depending on the type of strain gauge used.

Sample (Nb_3Sn)	$\Delta\epsilon_{WIRE}(\%)$ $R_T \rightarrow 4.2K$
a.	-4.471
b.	-4.561
c.	-4.539
d.	-4.520
e.	-4.507
	$\overline{\Delta\epsilon_{WIRE}} = -4.520$

Table 4.4 : The effect of temperature on strain for several freely suspended samples of Nb_3Sn wires at 4.2 K.
Type of strain gauge: EA-06-015DJ-120(SG2)

4.9 Compression, or tension, for samples

Sometimes when uniaxial strain is applied to a sample the resistance reading indicates that the sample is experiencing compression instead of tension. This is because the short sample is not really straight. The sample may have buckled during heat treatment. When tensile strain is applied to the sample, the sample will straighten-up. The decrease in the resistance reading is because the strain gauge is on the compressive side of the sample. The other side of the sample will be in tension with the same magnitude as the compressive side but with opposite sign. This problem can occur with wires and tapes.

4.10 Strain changing during V-I measurement

Figures 4.5a and 4.5b show the change in strain($\Delta\epsilon$) for transport current passed through a Nb_3Sn sample when the current is equal to J_C. The value of $F_L(Nm^{-1})$ is given by $F_L=I_CB$. The change in strain is noted when $I=I_C$ (ie. when the voltage across the sample is $10\mu V$). In the presence of a magnetic field, the sample experiences an additional strain arising from the Lorentz force. The change in strain is greater at low fields because the J_C is higher. When a V-I trace is completed, ie. when transport current is zero, the strain reading goes back to within 0.03% of its original value for this particular V-I trace. In figure 4.5b the value of $F/(\Delta\epsilon)^{1/2}$ is ~ 5.8×10^4 Nm^{-1}. An expression for $F/(\Delta\epsilon)^{1/2}$ has been derived in chapter 3. In chapter 3 the value obtained for $F_L/(\Delta\epsilon)^{1/2}$ is 2.6×10^5 Nm^{-1}. The experimental value is about a factor of 4.5 lower than the value calculated in chapter 3. In the calculation it is assumed the Lorentz force acts on a free wire whereas in the experiment the wire is soldered (and restrained) to a brass plate. We suggest that this explains why the experimental value is lower than the theoretical value.

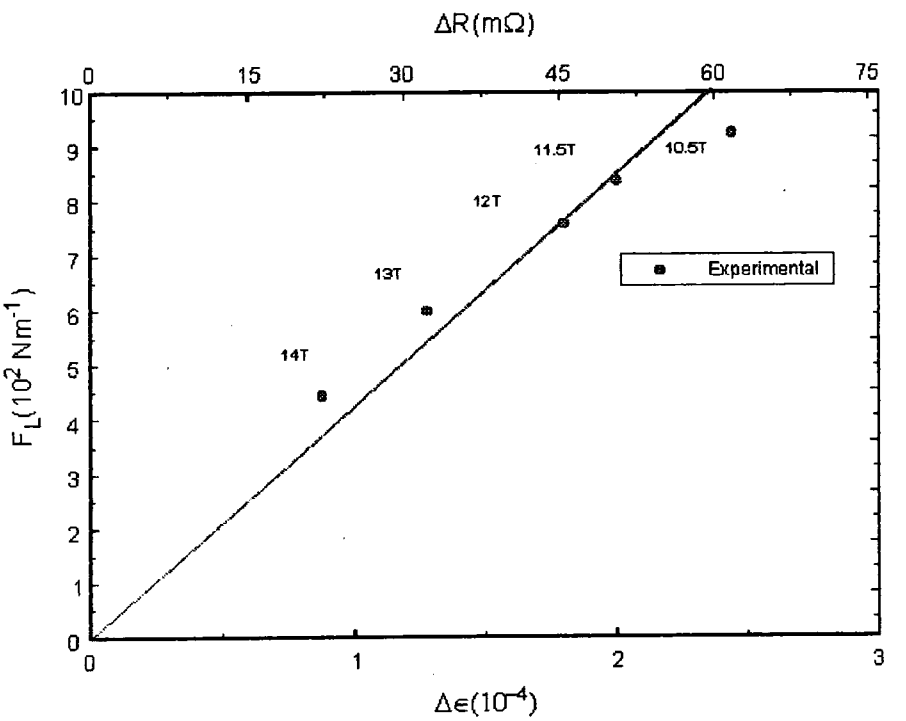

Figure 4.5a: The change in strain ($\Delta\epsilon$) caused by the Lorentz force.

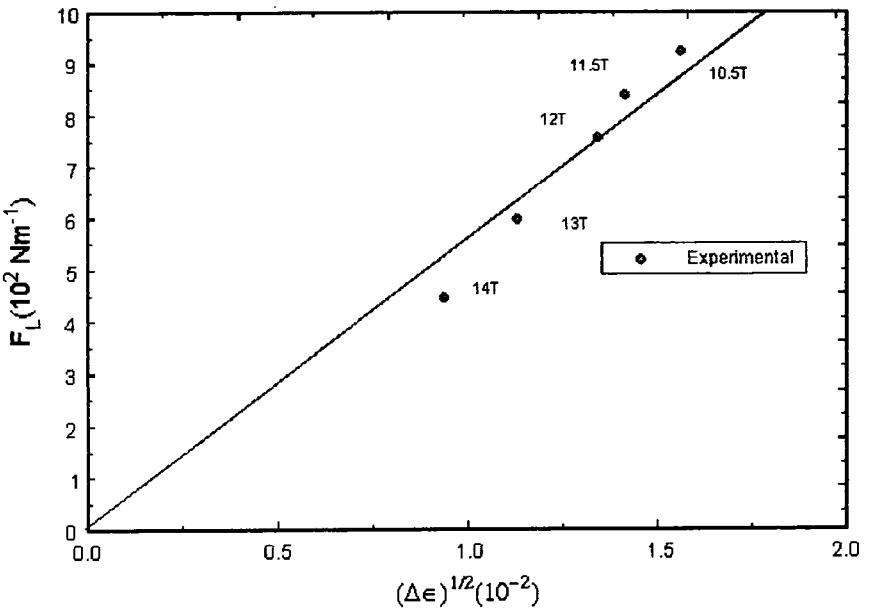

Figure 4.5b: The change in strain$(\Delta\epsilon)^{1/2}$ caused by the Lorentz force.

4.11 Critical current measurements

Figure 4.6 shows J_C against tensile strain for a Nb_3Sn wire. The J_C data were obtained from V-I traces using a 10 μV voltage criteria. Measurements were done in field at 4.2 K. The graph peaks at about 0.3% strain. Data below the 0.3% strain clearly show compressive on the Nb_3Sn wire. The strain value starts at about 0.1% indicating that the wire was already strained by the cool-down of the probe prior to measurements. The strain has been calculated as described in section 4.8.

Figure 4.7 shows a J_C against tensile strain for a multifilamentary BiSCCO tape at 4.2 K. These data were deduced from V-I traces using a 1.0 μV criteria. The data start at about 0.05% strain again indicating that the tape was strained on cool-down by the probe. The figure shows a flat region from 0.05% to about 0.25%. Above 0.25% strain J_C starts to decrease drastically.

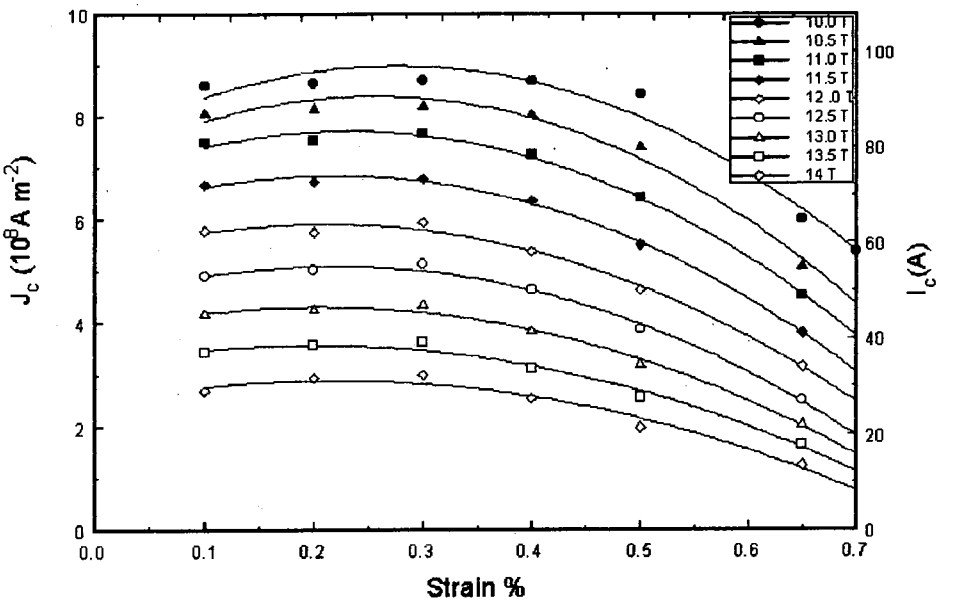

Figure 4.6: J_C against tensile strain for a Nb_3Sn wire.

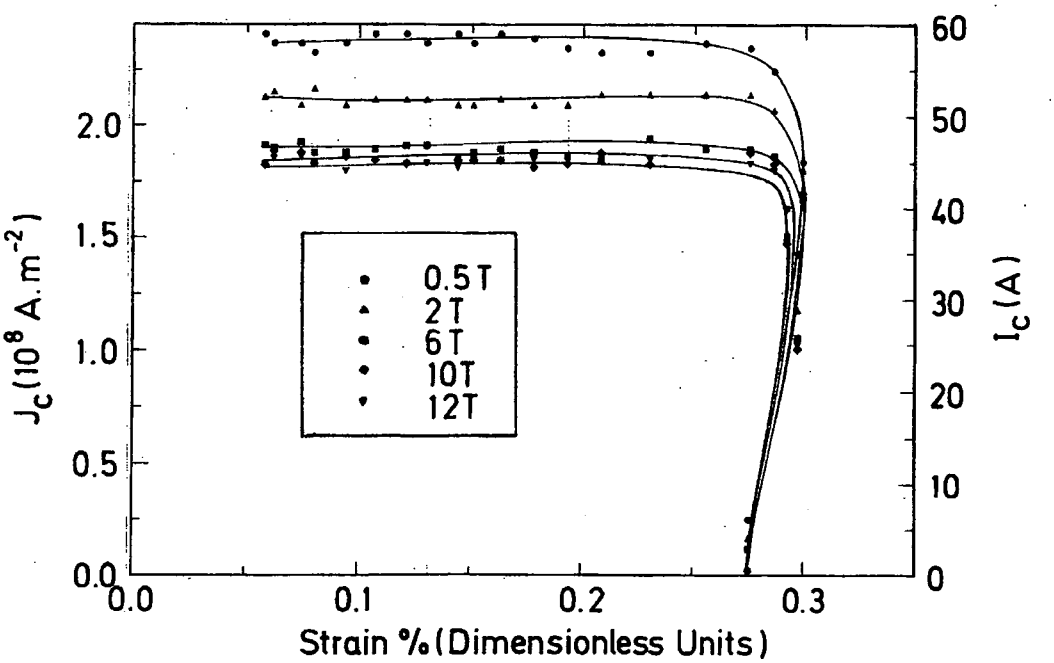

Figure 4.7: J_C against tensile strain for BiSCCO tape.

4.12 Discussion

4.12.1 The Durham Strain Probe

The J(B,ϵ) probe has been designed to measure J_C versus strain on superconducting wires and tapes from 2 K to 4.2 K in high magnetic fields up to 17 Tesla. It can also be used to measure J_C versus strain at 77 K(liquid nitrogen). Strain up to $\pm 1.0\%$ can be applied to short samples. The sensitivity of the strain measurement detected by the DMM is $1.4 \times 10^{-4}\%$ for the tape and $4.0 \times 10^{-4}\%$ for the wire. However, the control for changing the strain is typically 0.01% for the wire and 0.005% for the tape. We attribute this to a slipage in the gearbox system when the sample is subjected to high strains, friction in the joints in the probe, or cracking in the solder.

The J(B,ϵ) probe in this work has limitations as well as advantages. These limitations include:

(a) only short samples can be measured. This leads to the current transfer length problem.

(b) the success of the measurements depends on how well the sample is soldered to the probe.

(c) the rotation of the stainless steel rod can cause the current and instrumentation leads to get entangled.

Some of the advantages of these measurements are:

(a) the probe can fit into any magnet of bore size less than 40 mm.

(b) one can apply both tensile and compressive strain.

(c) very small strain can be applied to the sample by use of the gear system.

(d) it is possible to detect the change in strain on the sample during measurements resulting from the Lorentz force.

4.12.2 Probes used by other workers

As mentioned in section 4.3.1 the simplest technique to apply tensile strain is to pull

the sample at both ends by using some sort of an axial pulling machine. The limitation of this technique is that it is necessary to use a split-pair magnet to generate a field orthogonal to the sample axis. Superconducting magnets that give the highest possible fields are solenoids with radial access that generate fields that are directed axially. Thus using a split-magnet system limits the maximum field that can be applied.

One of the earliest apparatus' designed to simultaneously apply tensile strain, current and a perpendicular magnetic field to a short wire superconductor was reported by Ekin[11]. The magnetic field was produced by a 19T solenoidal Bitter magnet. The length of the sample that was measured was approximately 16.5 mm. The specimens were gripped at either ends by soldering onto two copper blocks. Uniaxial tensile strain is applied by moving one of the copper blocks attached to a complicated pull-rod system. Strain is measured by using a 4-strain gauge extensometer. Uniaxial tensile strain in excess of 1% can be applied to the samples. However this system was not designed to measure both tensile and compressive strains. Also there was no report on the change in strain on the sample because of the Lorentz force during measurements.

An elaborate description of a spiralled bending spring method was given by Walters[12]. This system was designed for tensile and compressive strains. When a torque is applied at the ends of the spring an axial strain is induced in the sample. The strain is then calculated from the angular displacement. The system requires quite a large bore size magnet, approximately 55 mm. Since the sample is supported by a spring, the spring material must have a greater elastic limit than the maximum required for the measurements. With the exception of 318 titanium alloy most materials do not meet this requirement and are non-linear beyond 0.5% strain. The disadvantage of this alloy is that it is difficult to solder the sample onto it.

ten Haken proposed the use of U-shaped bending springs[4], also designed to measure tensile and compressive strains. Strain is applied by exerting a force to the legs of a U-shaped spring. The springs were made from brass because it has a low Young's modulus(95 -100 GPa), is simple to machine and easy to solder the sample to it. However, these brass springs are massive and one needs a large driving force to apply

strain. The strain range for this system is ±1.2%. Since the samples are soldered directly on the springs the change in strain from the Lorentz force acting on the sample has little effect during measurements.

Richens et. al have developed a strain probe that enable the $J_C(B,T,\epsilon)$ characterisation of a < 40 mm diameter single loop HTS tape[13]. The probe consists of an aluminium alloy cylinder with a 1° tapered bore that is slit longitudinally at regular intervals around its circumference. The sample is mounted around the circumference of the cylinder. Strain is applied to the sample by forcing a conical brass plug into the bore of the cylinder which expands evenly as a consequence. The applied strain is measured by a strain gauge glued directly to the surface of the tape. The probe can be inserted into a magnet with a bore size of less than 40 mm. Another advantage of this technique is that the strain on the superconductor can be approximated by counting the number of turns given to the tensioning nut on top of the probe

4.13 Concluding Remarks

Real progress in the application of superconducting materials depends on the understanding of their mechanical properties such as the effect of strain on J_C of these materials. Experiments on the effect of strain on J_C ranges from simple bending tests to those involving complicated strain apparatus. The design and construction of a $J(B,\epsilon)$ probe capable of measuring tensile and compressive strain and its effect on J_C has been presented. The $J(B,\epsilon)$ probe can measure strains up to ± 1.0% on LTS and HTS wires and tapes. The probe can be inserted into any magnet system with a bore size greater than 40 mm. The maximum current that can be passed through the probe is about 150 Amps. J_C versus strain measurements can be made at 4.2 K and 77 K. The probe is leak-tight so that variable temperature measurements can also be made by pumping on the cryogen-bath of the magnet system. Strain is measured via a strain gauge pasted directly on the sample. The sensitivity of the strain measurement detected by the DMM is $1.4\text{x}10^{-4}$% for the tape and $4.0\text{x}10^{-4}$% for the wire. For the BiSCCO tape it has been found that the permanent change in the strain state after each V-I measurement is less than 0.03%. A section on sample mounting development has been presented. Success

in using this probe depends heavily on the sample mounting techniques.

The following two chapters are dedicated to strain measurements using the $J(B,\epsilon)$ probe described here. The influence of strain on J_C and other fundamental properties of the superconducting material is analysed.

References

1. Ekin J W, Finnemore D K, Li Q, Tenbrink J and Carter W., *Apply. Phys. Lett.* **61**(7) 858 (1992).
2. Ekin J W., *IEEE Trans. Magn. MAG-19* **3** 900 (1983).
3. Saviddes N and Yau J., *Physica C* **235** 3457 (1994).
4. ten Haken B., *PhD Thesis* University of Twente Enchede The Netherlands (1994).
5. Martini L, Bigoni L, Varesi E, Zanella S, Gherardi L, Caracino P and Spreafico S., *Inst. Phys. Conf. Series No.* **148** *EUCAS'95* 435 (1995).
6. Warren W H Jr and Bader W G., *Rev. Sci. Instrum.* **40** 180 (1969).
7. Kirk-Othmer, *Encyclopedia of Chemical Technology*(John Wiley & Sons,USA) (1995)
8. Reed R P and Clark A F., *Materials at Low Temperatures* (American Society for Metals, USA) (1983)
9. Friend C F., *PhD Thesis* Hatfield College University of Durham U.K.(1994).
10. Dally J W, Riley W F and McConnelK G., *Instrumentation for Engineering Measurements* (John Wiley & Sons Inc, USA) (1993).
11. Ekin J W., *Cryogenics* **20** 611 (1980).
12. Walters C R , Davidson I M and Tuck G E., *Cryogenics* **26** 406 (1986)
13. Richens P E, Jones H, Von Cleemput M and Hampshire D P., *IEEE Trans. on Appl. Supercond.* **7**(2) 1315 (1997).

Chapter 5

Critical Current of Nb_3Sn Wire as a Function of Strain and Magnetic Field at 4.2 K and 2.9 K

5.1 Introduction

Nb_3Sn has a transition temperature of 18.3 K and an upper critical magnetic field(B_{C2}) of about 22 T at 4.2 K[1]. Nb_3Sn is commercially used to construct stable superconducting magnets operating at fields above 11 T. Below 11 T the ductile material NbTi is widely used. Nb_3Sn is very brittle and can fracture under tensile strains of 0.2 -0.5%, thus causing critical current degradation[2]. The dependence of the critical current(I_C), of Nb_3Sn on uniaxial strain plays an important role in the design and construction of superconducting magnets. When constructing a magnet, external support and reinforcement must be provided to limit the total strain on this material to prevent critical current degradation.

In practical applications, the Nb_3Sn superconductor is divided into fine filaments and embedded in a matrix. This results in a differential thermal contraction between the matrix and the Nb_3Sn filaments as the composite is cooled from its fabrication temperature[3]. The matrix contracts more than the Nb_3Sn filaments and places the superconductor under an initial compressive pre-strain. The presence of this compressive pre-strain is important because it can extend the strain range of the superconductor before fracture. The maximum critical current occurs when the compressive pre-strain is compensated and the superconducting filaments are in the strain-free state[3,4].

This chapter presents J_C versus strain measurements made on a commercial Nb_3Sn wire under axial strain. Section 5.2 describes the Nb_3Sn wire used in these measurements.

Section 5.3 briefly outlines the experimental technique used. The experimental results are presented in section 5.4. In section 5.5 the experimental results are analysed. The findings are discussed in section 5.6. Section 5.7 concludes this chapter with a short summary of some of the main conclusions.

5.2 The Nb_3Sn wire

The samples measured are the VACRYFLUX NS 4500 made by Vacuumschmelze, Germany. The J_C dependence on strain were measured on two samples. One measurement was done at 4.2 K and the other at 2.9 K. The diameter of the Nb_3Sn wire is 0.37 mm. These Nb_3Sn are non-stabilised superconductors containing Nb filaments in a CuSn bronze matrix. The Nb_3Sn conductors are produced by using the solid-state diffusion method[5]. Figures 5.1 and 5.2 show the micrograph pictures of this material. It consists of 4500 Nb filaments in a CuSn bronze matrix. The Nb filaments are arranged in a regular pattern in the CuSn bronze matrix. The superconducting Nb_3Sn layer is formed by applying heat treatment at 700°C for 64 hours. These samples are heat treated in an argon atmosphere. During heat treatment the Sn atoms diffuse from the CuSn matrix into the Nb filaments to form the superconducting Nb_3Sn layers. The process is known as the bronze route.

5.3 Experimental technique

The sample, with a strain gauge attached to it, was mounted on the $J(B,\epsilon)$ probe as described in chapter 4. Two sets of measurements, tensile and compressive, were made on two different samples(sample 1 and sample 2). The V-I characteristics sample 1 were measured at 4.2 K(tensile) and for sample 2 at 2.9 K (compressive) in our high field magnet system. The magnetic field is applied orthogonal to the transport current.

5.3.1 Tensile measurements at 4.2 K

First, the resistance reading of sample 1 on the probe is taken to get the strain value relative to an unattached sample. Details of how this is done is described in section 4.8.

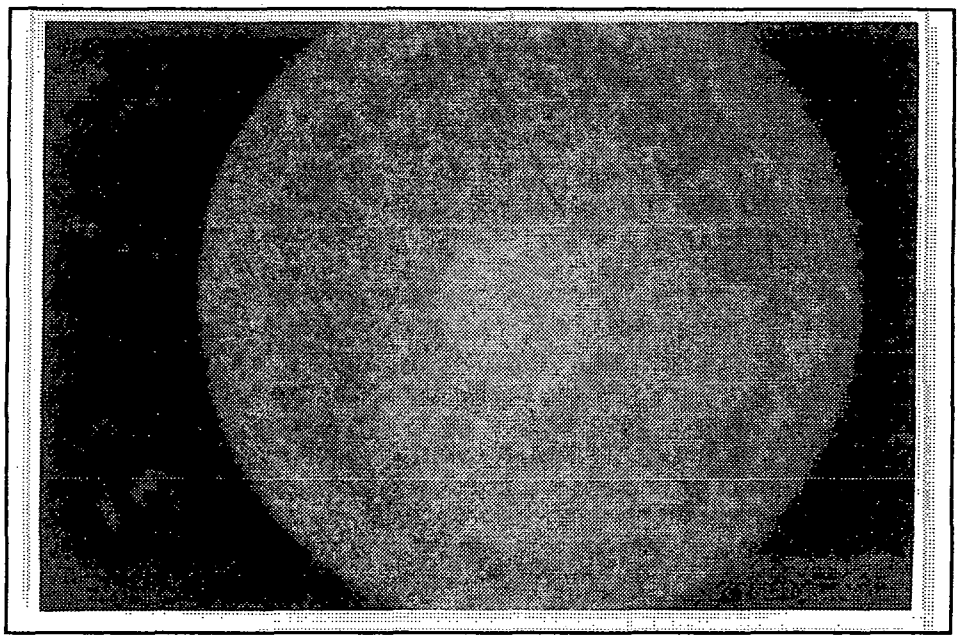

Figure 5.1: The optical micrograph of the Nb_3Sn wire(scale 1mm:4.1μm).

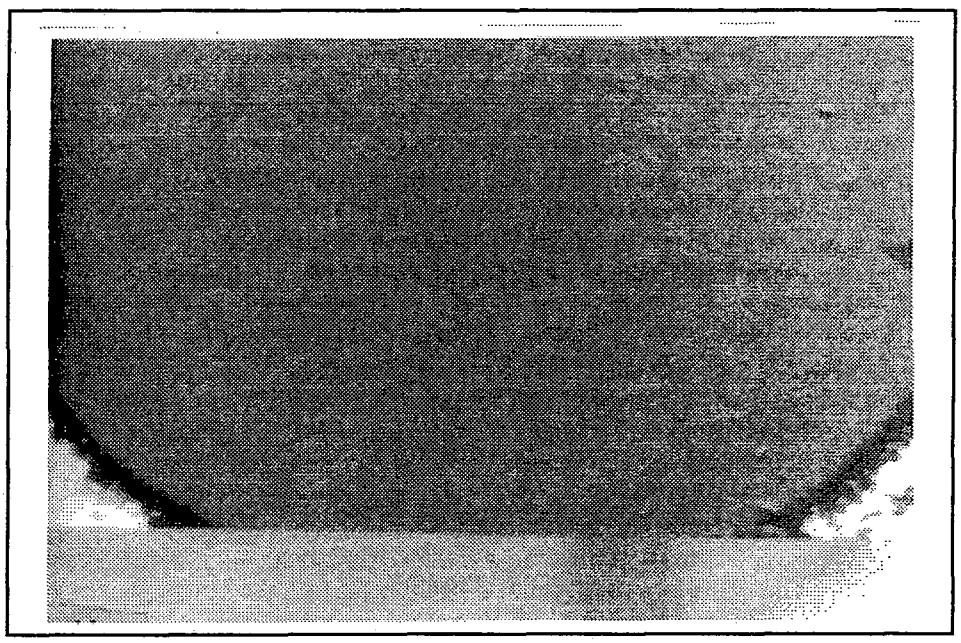

Figure 5.2:The SEM micrograph of the Nb_3Sn wire(scale 1mm:2.7μm).

Before applying any strain V-I traces are taken from 10 T up to 14 T. Then strain is applied to the sample and its V-I traces taken from 10 T up to 14 T. The applied strain is increased in steps of 0.1% until no J_C can be detected.

5.3.2 Compressive measurements at 2.9 K

The resistance reading of sample 2 on the probe is taken to get the strain value relative to an unattached sample. Then a V-I trace is taken at 4.2 K at 10 T to check the quality of the sample. The temperature of cryogen-bath of the magnet system is reduced to 2.9 K by pumping it down to 225 Torr. Before applying any strain V-I traces are taken from 10 T up to 14 T. Then tensile strain is applied to the sample and its V-I traces taken from 10 T up to 14 T. Strain is applied to the sample until no J_C can be detected. The applied strain is increased in steps of 0.1%. When taking a V-I trace at 10 T the pressure of the cryogen bath changes by about 15 Torr near I_C. The pressure went back to 225 Torr before the next V-I trace. At 14 T the pressure of the cryogen-bath changes by about 1 Torr near I_C. This is because at low fields the transport current is higher than at high fields. Thus the Joule heat that is produced at low fields is higher than that at high fields.

When tensile strain is applied to the sample the resistance readings of the strain gauge on the sample shows that the sample undergoes compression. This phenomena has been discussed in section 4.9. The sample undergoes compression until no J_C can be detected.

5.4 Results

Figure 5.3 shows an E-J characteristics for sample 1 at 10 T for different strains. The slope of the E-J characteristics below J_C shows the effect of current transfer problem. The slope of the E-J characteristics in this linear region is referred to as the current-transfer resistivity[6]. From 0.1% strain to 0.5% strain the current transfer resistivity dominates up to about 90 Amps. Above 90 Amps the flux-flow resistivity dominates. For the 0.65% strain the current transfer resistivity dominates to about 50 Amps. The E-J characteristics show the usual curvature as the current approaches the critical

current. There are no marked differences in the E-J characteristics for the 0.1% strain to 0.5% strain. However, at 0.65% strain the E-J characteristics show that J_C is reduced by about 30%. The slope ($\partial V/\partial I$) above J_C are similar for different strains.

Figure 5.4 shows the E-J characteristics for sample 1 at 14 T for the same strain values as in figure 5.3. The slope of the E-J characteristics below J_C is markedly reduced at 14 T. By increasing the applied magnetic field the critical current density is lowered. The slope($\partial V/\partial I$) above J_C are similar for different strains. The J_C values at 0.2% and 0.3% strains are about 12% higher than at 0.1% strain. This indicates that the compressive pre-strain is compensated and the superconducting filaments are in the strain-free state. The J_C values for the 0.45%, 0.5% and 0.65% strains are lower than at 0.1% strain. The J_C value at 0.65% strain is about 60% lower than at 0.1% strain.

Figure 5.5 shows the E-J characteristics for sample 2 at 2.9 K for four different compressive strains. All the curves overlap and the slopes of the E-J characteristics below J_C extend up to about 100 Amp. At 100 Amp the sample quenches probably due to heating of the sample. The E-J characteristics for sample 2 at 14 T is shown in figure 5.6. J_C decreases as strain increases. The J_C value at -0.52% strain is about 43% lower than the J_C value at -0.08% strain. The slope of the E-J characteristics below J_C is markedly reduced and the region where flux-flow resistivity dominates is achieved for all the strains. The E-J characteristics show the non-linear upturn as the current approaches the critical current.

Figure 5.7 shows J_C versus strain for sample 1 using 1μV criteria at 4.2 K. The J_C value is determined by extrapolating the linear region of the current-transfer resistivity to high currents, and using this extrapolated baseline as the reference, the J_C value is read-off at 1μV[6,7]. The strain value starts at 0.1% indicating that the wire was already strained prior to measurements. The strain numbers were adjusted to account for the zero-strain value as described in section 4.8. The maximum J_C occurs at 0.3% strain. Data below 0.3% strain clearly shows the compressive pre-strain region of the sample. Above 0.3% strain J_C decreases as the applied strain increases. Thus the magnitude of the compressive pre-strain is 0.3%. The data points at 0.1% strain for the 11 T and 11.5

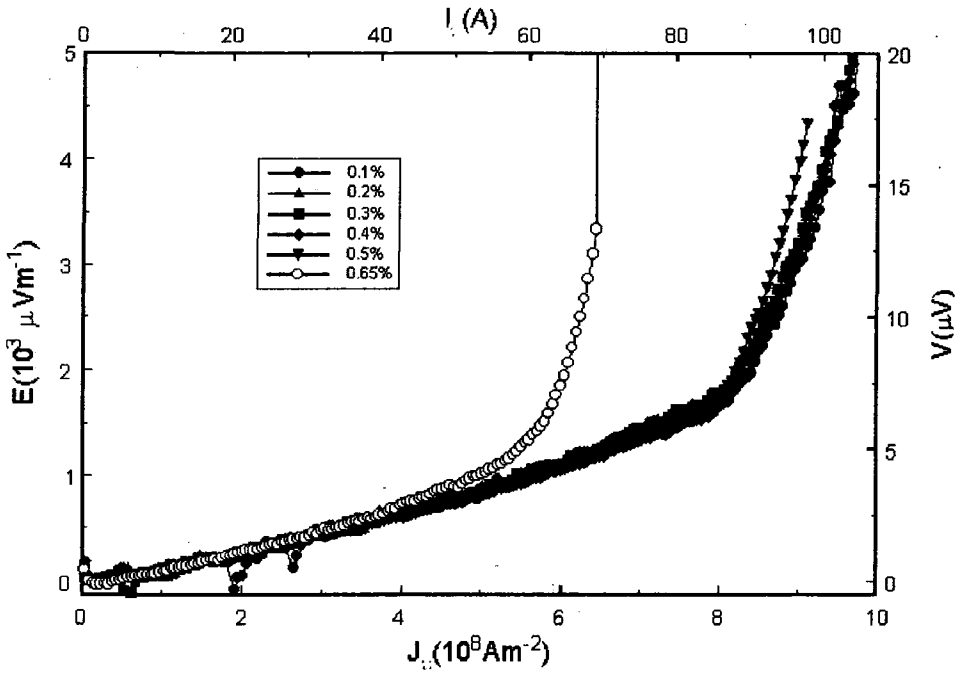

Figure 5.3: E-J characteristics for sample 1 at 10 T for different strains at 4.2 K.

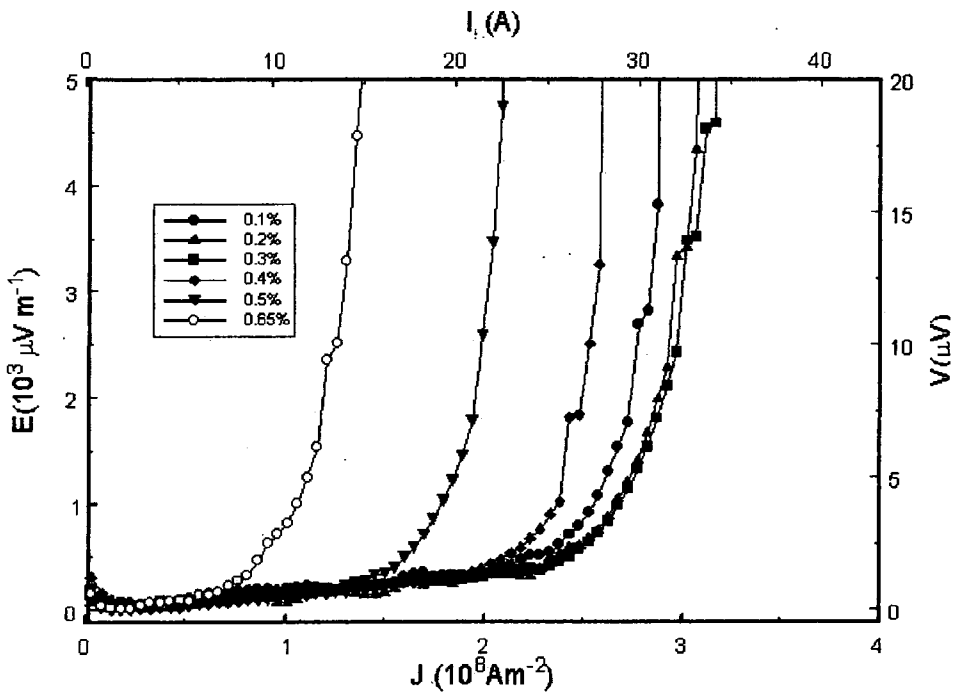

Figure 5.4: E-J characteristics for sample 1 at 14 T for the same strains as in figure 5.3 at 4.2 K.

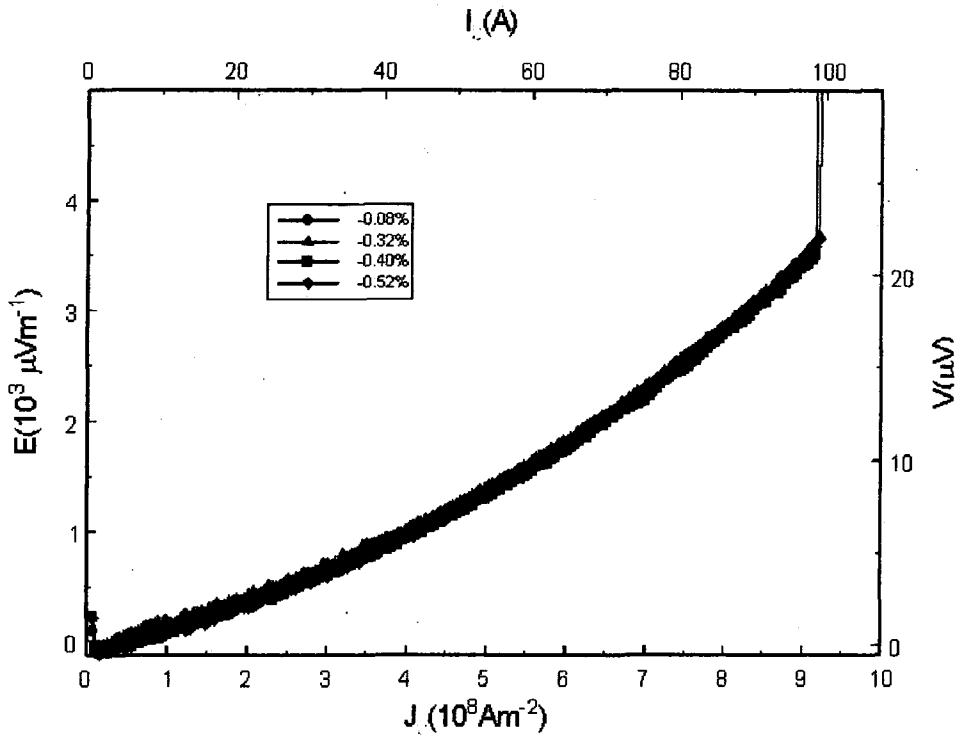

Figure 5.5: E-J characteristics for sample 2 at 10 T for different strains at 2.9 K.

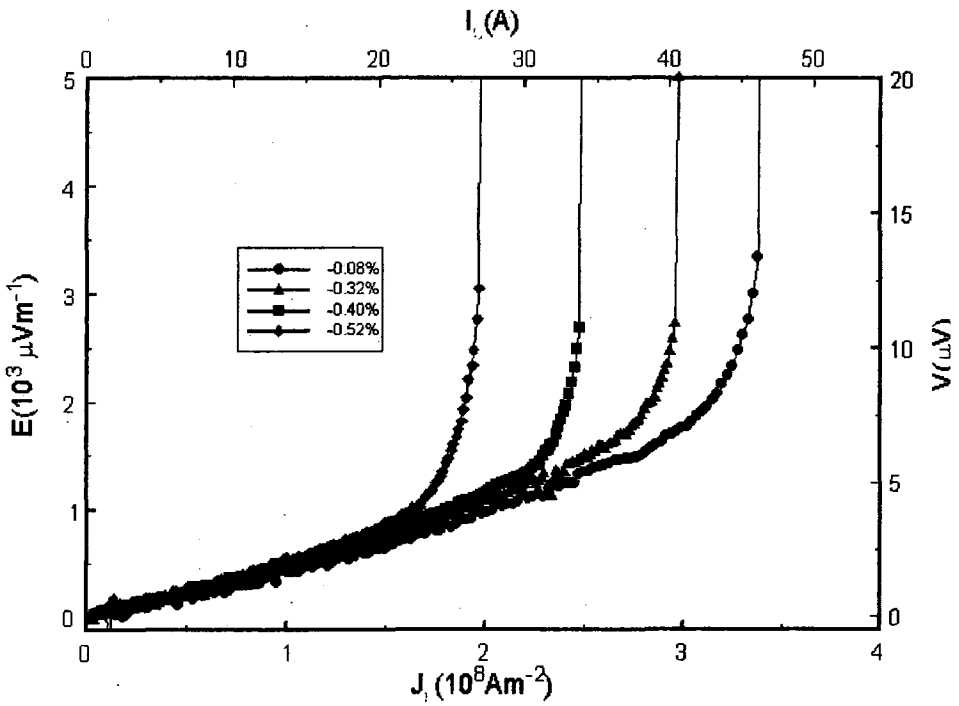

Figure 5.6: E-J characteristics for sample 2 at 14 T for the same strains as in figure 5.4 at 2.9 K.

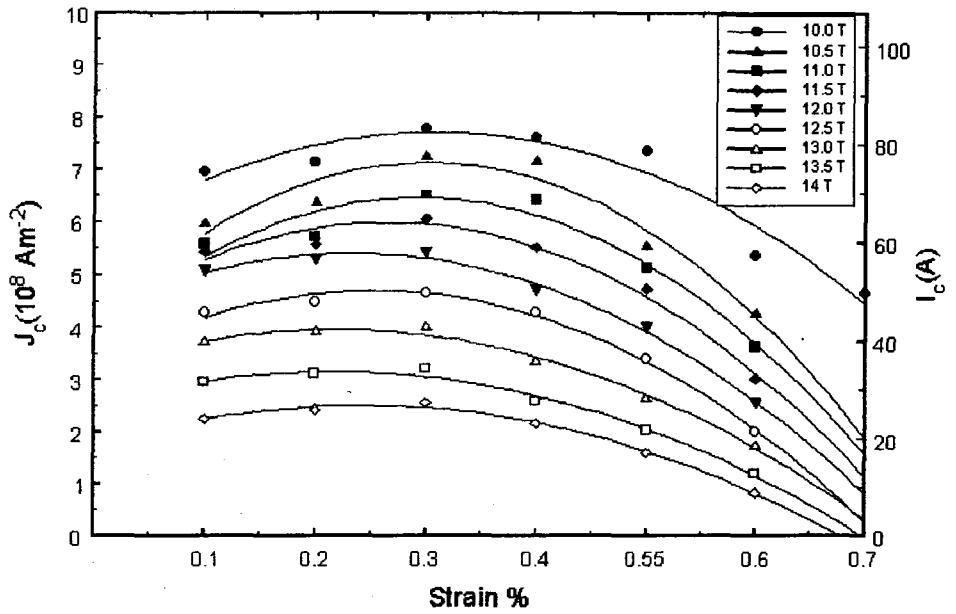

Figure 5.7: J_c versus strain for sample 1 using 1μV criteria at 4.2 K.

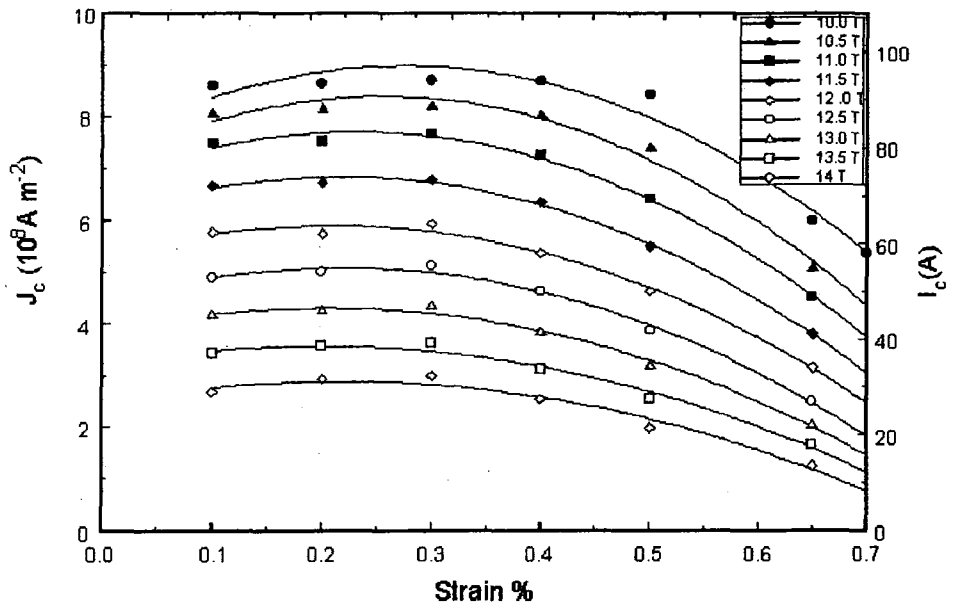

Figure 5.8: J_c versus strain for sample 1 using 10μV criteria at 4.2 K.

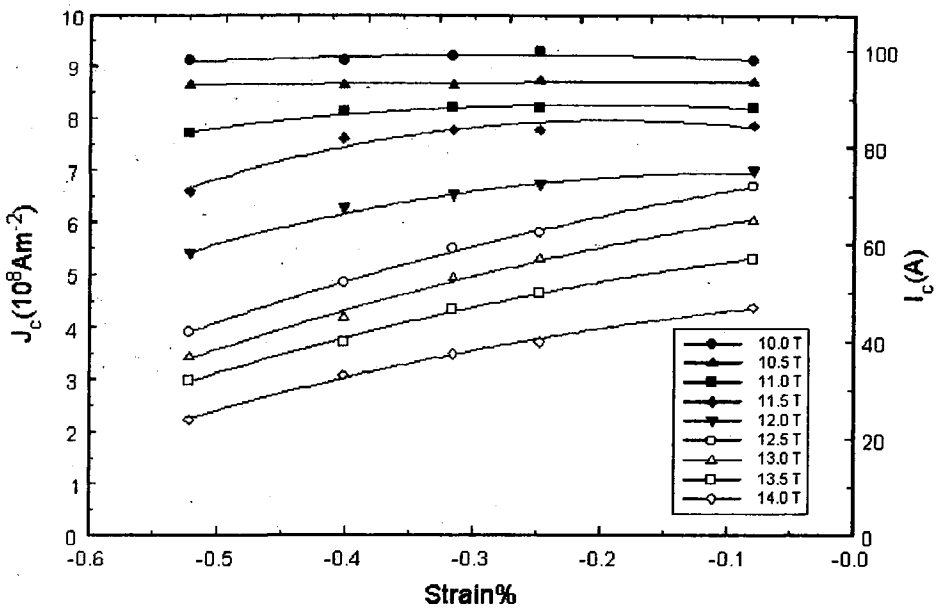

Figure 5.9: J_c versus strain for sample 2 using $1\mu V$ criteria at 2.9 K.

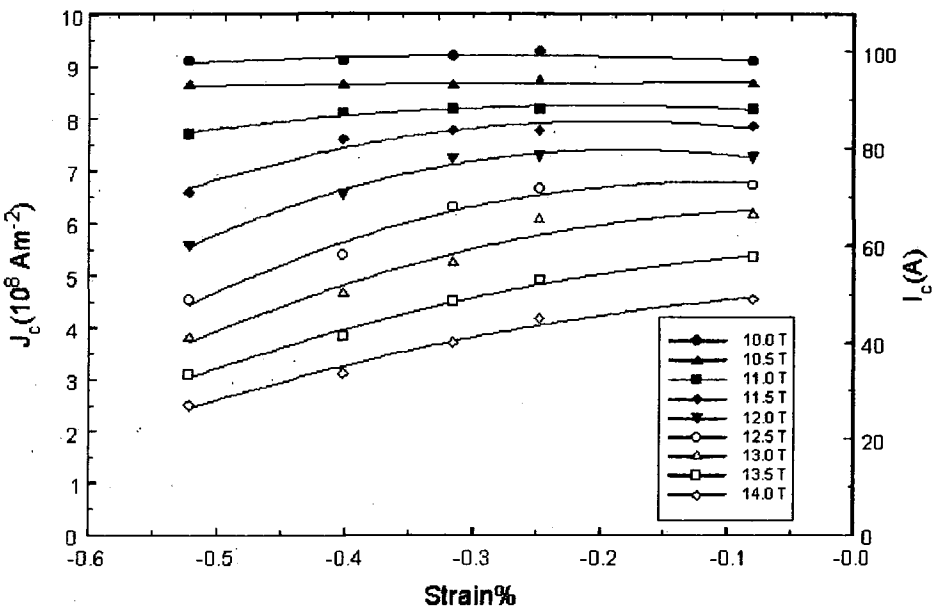

Figure 5.10: J_c versus strain for sample 2 using $10\mu V$ criteria at 2.9 K.

T seems to overlap one another. This is because of the difficulty in determining J_C using a small criteria. Figure 5.8 shows J_C versus strain for sample 1 using a higher criteria of 10μV. The J_C value is determined by the same method as in figure 5.7. The graph shows similar trends as in figure 5.7. The J_C values are higher than that of figure 5.7 because of the higher voltage criteria used. The maximum J_C value occurs at 0.3% strain. Here no data points overlap one another.

Figure 5.9 shows J_C versus strain for sample 2 using 1μV criteria. The strain values starts at -0.1% indicating that the sample has been compressed prior to measurements. The J_C versus strain curve for the 10 T, 10.5 T and 11.0 T fields are flat because these are quench currents. The flux-flow resistivity is achieved for higher fields. The J_C values are determined as in figure 5.7. The J_C values decrease as the applied strain increases. For the 14 T field, J_C is reduced by about a factor of 2 at -0.52% strain from the J_C value at -0.1% strain. Since the sample is initially in compressive pre-strain which degrades the initial critical current, further compression will reduce the critical current. Figure 5.10 shows J_C versus strain for sample 2 using a higher criteria of 10μV. It shows similar trends as in figure 5.9. The values of J_C are higher because of the higher voltage criteria.

5.5 Analysis

Figure 5.11 shows the critical current distribution for sample 1 at 0.3% strain for three different fields. The method for getting the critical current distribution has been described in section 3.5.2. At 13 T a peak occurs at about 48 Amp. As the field increases to 13.5 T the peak is shifted to about 40 Amps with a shoulder at about 37 Amps. At 14 T the main peak is shifted to about 31 Amp and the shoulder has developed into a peak at about 29 Amp. This indicates that parts of the sample are field dependent. We note that the appearance of the double peaks has been attributed to inter-grain J_C which has a strong field dependence, and intra-grain J_C which has a weak field dependence[8].

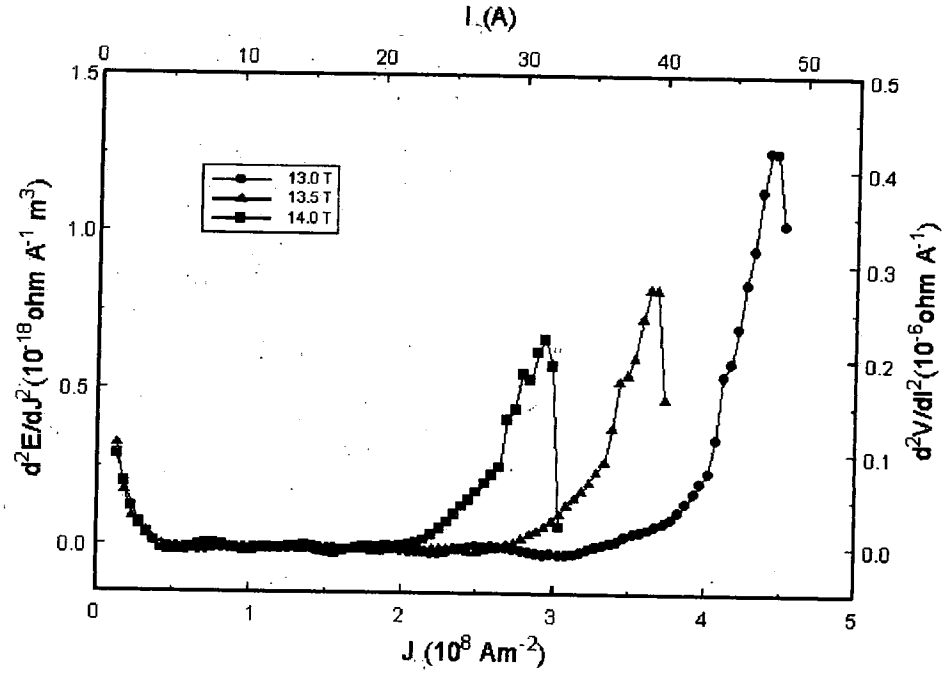

Figure 5.11: The critical current distribution for sample 1 at 0.3 % strain for three different fields.

Figure 5.12 shows J_C versus B for sample 1 for three different strains at 4.2 K. The J_C values are taken using the 10μV criteria. Data points for the 0.4% strain at low fields that do not lie on the curve are quench currents. J_C decreases as the applied field and strain increases. J_C also decreases gradually as the applied field increases. At 14 T J_C has dropped by about a factor of 4 from the J_C value at 10 T. Figure 5.13 shows the J_C versus B for sample 2 for three different compressive strains at 2.9 K. The J_C values are taken using the 10μV criteria. J_C decreases gradually as the applied field increases. At 14 T J_C has also dropped by a factor of 4 from the J_C value at 10 T.

Figure 5.14 shows the Kramer plot (ie . $J^{1/2}B^{1/4}$ versus B) for sample 1[9]. The Kramer plot lines are fairly straight and parallel to each other. However, at low strains and low fields the lines seems to overlap on one another. This is because of the quench currents at these strains and fields. The upper magnetic field at each strain can be obtained by extrapolating linearly the Kramer plots to $J^{1/2}B^{1/4} = 0$. The straight lines suggest that the pinning force, F_P, can be described by the relation[10], $F_P = J \times B = \alpha(B_{C2})^n b^{1/2}(1 - b)^2$, where b is the reduced field ($b=B/B_{C2}$).

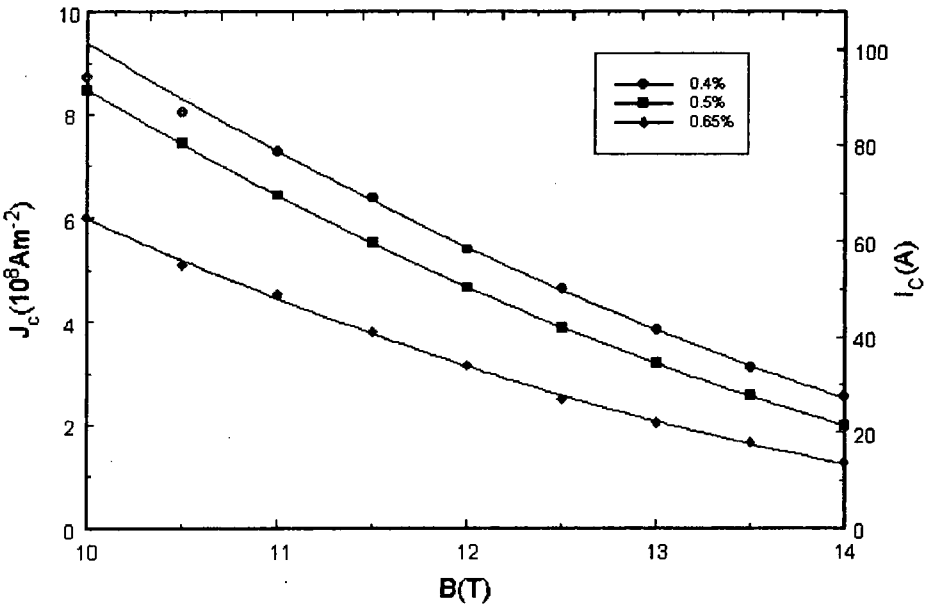

Figure 5.12: J_c versus B for sample 1 for three different strains at 4.2 K.

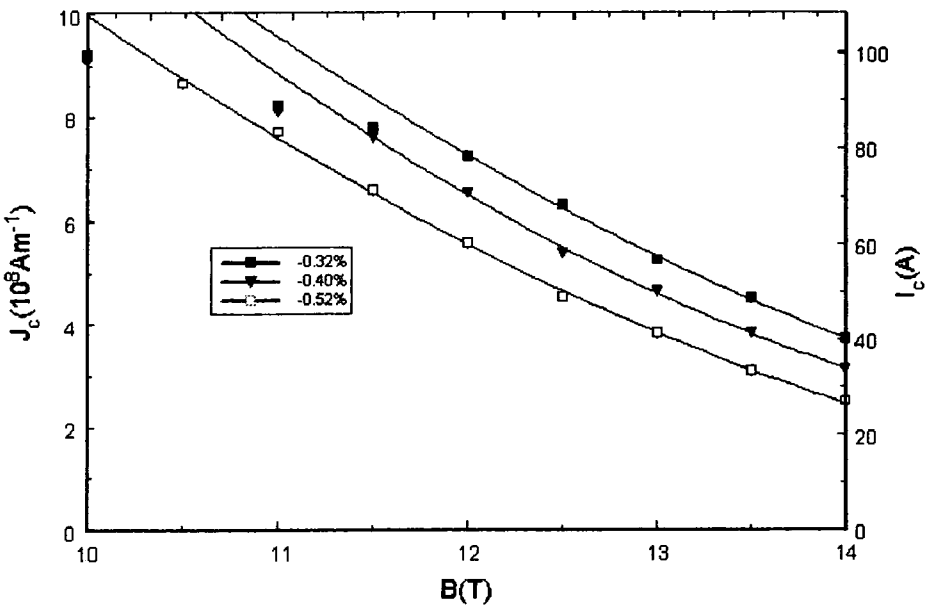

Figure 5.13: J_c versus B for sample 2 for three different compressive strains at 2.9 K.

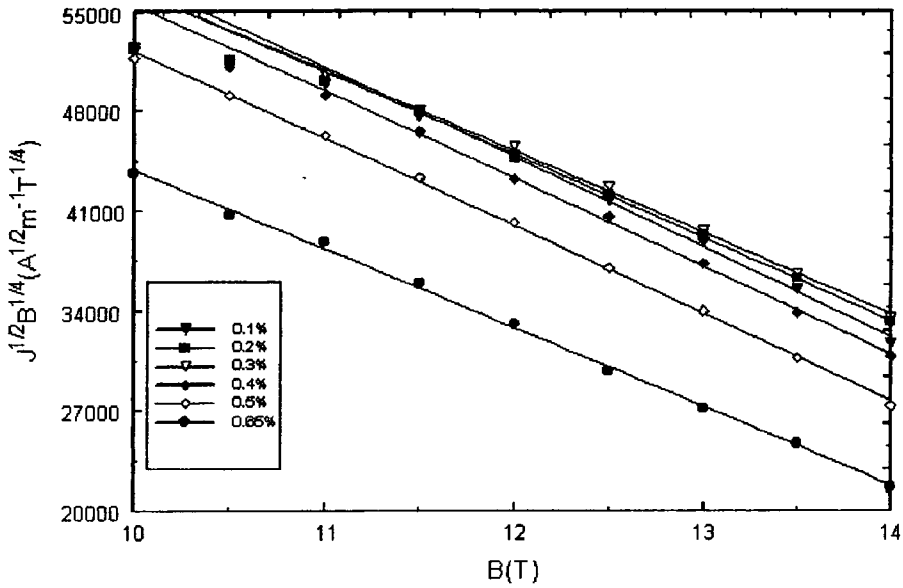

Figure 5.14: Kramer plot for sample 1 at 4.2 K.

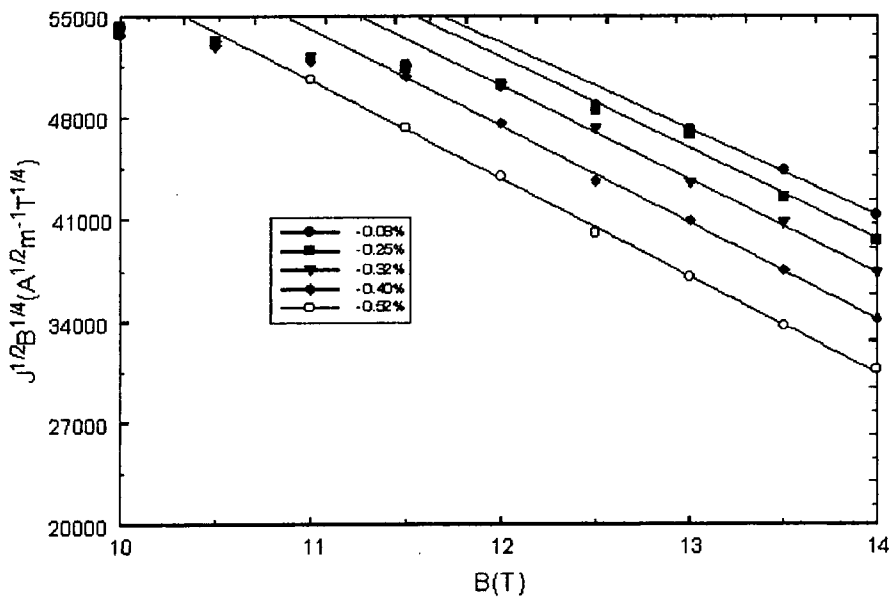

Figure 5.15: Kramer plot for sample 2 at 2.9 K.

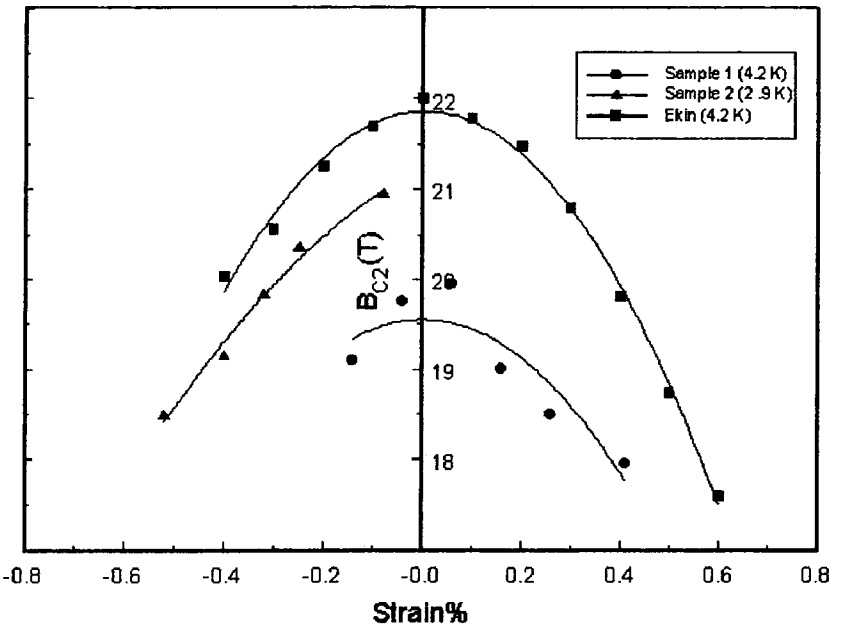

Figure 5.16: B_{c2} versus strain (where the peak is by definition taken to be zero strain) for samples 1 and 2 compared to Ekin's data[ref.12].

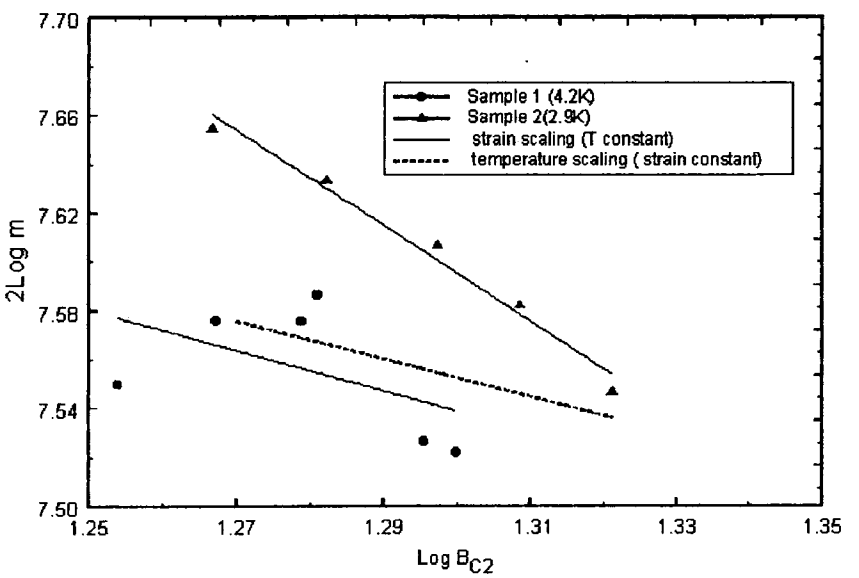

Figure 5.17: A plot of 2logm versus log B_{c2} for samples 1 and 2.

Figure 5.15 is the Kramer plot for sample 2. The Kramer lines are also fairly straight and parallel to each other. The Kramer plots of figures 5.14 and 5.15 also suggest that J_C is limited by a single pinning mechanism.

Figure 5.16 shows B_{C2} versus strain for samples 1 and 2. On the same graph is plotted the values of B_{C2} versus strain obtained by Ekin at 4.2 K on a 0.69 mm diameter Nb_3Sn wire[11]. The 0.69 mm sample was chosen because it has almost the same compressive pre-strain value(0.32%) as sample 1. The strain axis of figure 5.16 has been adjusted so that the strain-free state(ie., when the compressive pre-strain is completely relieved) is referred as the 0% strain. The values of B_{C2} at 0% strain obtained by Ekin on a set of 6 different samples range from 20.4 T to 22.6 T. The values of B_{C2} at 0% strain for sample 1 is 19.6 T and for sample 2 is 21.2 T. The graph also shows that B_{C2} increases as temperature decreases.

From the gradient in the Kramer plots one can calculate m where $m = \frac{\partial(J^{1/2}B^{1/4})}{\partial B}$

$= \left(\alpha B_{C2}^{\,n-\frac{5}{2}}\right)^{\frac{1}{2}}$.

Figure 5.17 shows a plot of 2log m versus log B_{C2} for samples 1 and 2. From the slope of 2log m versus log B_{C2} one can calculate the values of α and n where

$$F_P = \alpha(B_{C2}(\epsilon))^n b^{1/2}(1-b)^2 \qquad (5.1)$$

The values of α are found to be 4.20 ± 0.57 x 10^8 $Am^{-2}T^{-1}$ and 1.37 ± 0.05 x 10^{10} $Am^{-2}T^{-1}$ for samples 1 and sample 2, respectively. The values of n are found to be 1.67± 0.7 and 0.54± 0.16 for sample 1 and sample 2, respectively. It shows that the index, n, of the sample has decreased by about a factor of 3 when the temperature is reduced from 4.2 K to 2.9 K.

The Kramer plots($J^{1/2}B^{1/4}$ versus B) for sample 1 and sample 2 from figures 5.14 and 5.15 are replotted together in figure 5.18.

In figure 5.17 the two solid lines represent strain scaling(ie., when T is constant and ϵ varies). The dotted line represents temperature scaling(ie., ϵ constant and T varies). The B_{C2} values for samples 1 and 2 for the temperature scaling is taken from figure 5.16 at about -0.15% strain. Here the three B_{C2} values used are assumed to be at constant strain. The functional form of the temperature scaling law has the form:

$$F_P = \alpha[B_{C2}(T)]^n b^{1/2}(1-b)^2 \tag{5.2}$$

The new values of α and n from temperature scaling are found to be $3.63\pm0.62 \times 10^8$ $Am^{-2}T^{-1}$ and 1.72 ± 1.3, respectively.

5.6 Discussion

The peaked shape of the J_C versus B plot for uniaxial tensile strain can be explained in terms of compressive pre-strain. The maximum J_C occurs at about 0.32% strain. As seen

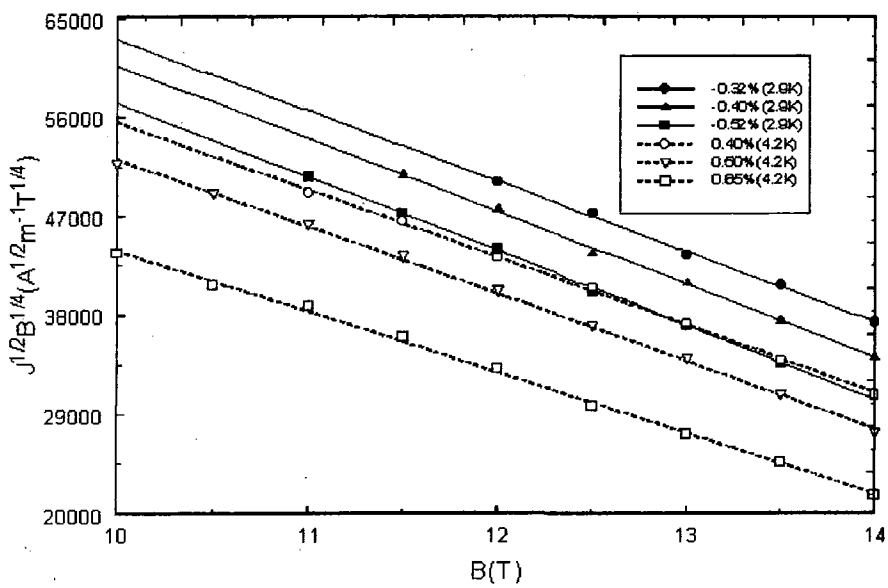

Figure 5.18: The Kramer plots for samples 1 and 2 are replotted together.

in figure 5.8 the peak value where J_C is maximum is independent of the applied field. The compressive pre-strain tends to degrade the J_C. When tensile strain is applied to Nb_3Sn, the initial effect is to relieve the compressive pre-strain on the Nb_3Sn. As the compressive pre-strain is relieved, J_C increases until the Nb_3Sn reaches its strain-free state. At the strain-free state J_C reaches its maximum. Haken showed that the maximum J_C occurs when the deviatoric strain is minimum[10]. If tensile strain is further applied to Nb_3Sn, J_C starts to degrade. The amount of strain needed to bring the Nb_3Sn to its strain-free state varies from specimen to specimen, depending on how the specimen is prepared. For some specimens, J_C may decrease monotonically as strain increases[11,12,13,14,15]. When selecting conductors for practical purposes, the critical currents should be compared at the peak in order to set the useful strain limits on the conductors.

Ekin showed that the pinning force density, F, in Nb_3Sn obeys a simple uniaxial strain scaling law of the form[12]

$$F_P = \alpha[B_{C2}(\epsilon)]^n b^{1/2}(1-b)^2 \tag{5.3}$$

where b is the reduced field $b=B/B_{C2}$. The values of n for sample are found to be 1.67 ± 0.68 and 0.54 ± 0.16 for sample 1 and sample 2, respectively. Ekin showed that the index n has values 1 ± 0.3[12]. Using the values of α and n obtained above, the functional form for sample 1 can be written as

$$F_P = 4.20\pm0.57\times10^{8}[B_{C2}(\epsilon)]^{1.67\pm0.68} b^{1/2}(1-b)^2 \tag{5.4}$$

For sample 2, the functional form can be written as

$$F_P = 1.37\pm0.05\times10^{10}[B_{C2}(\epsilon)]^{0.54\pm0.16} b^{1/2}(1-b)^2 \tag{5.5}$$

When ϵ is constant and T varies, the functional form can be written as

$$F_P = 3.63\pm0.62\times10^{8}[B_{C2}(T)]^{1.72\pm1.28} b^{1/2}(1-b)^2 \tag{5.6}$$

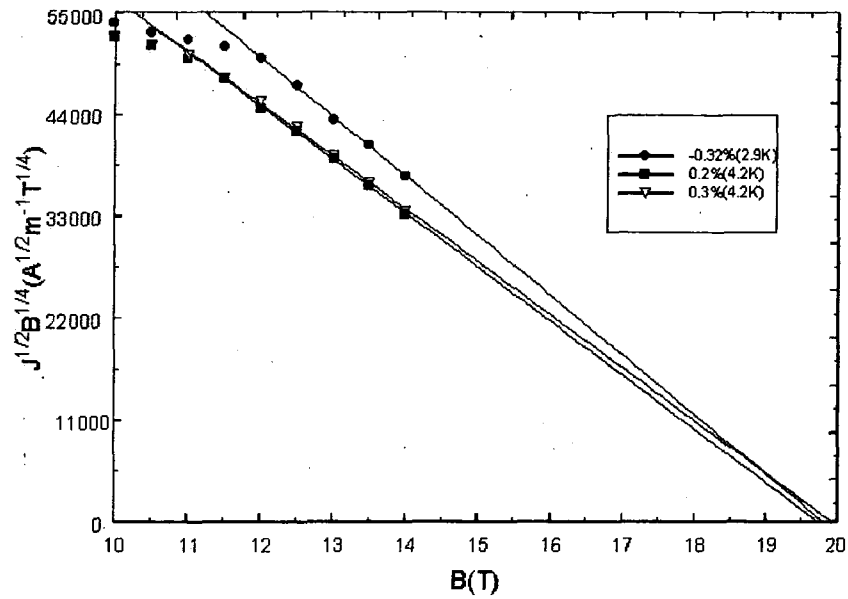

Figure 5.19: $J^{1/2}B^{1/4}$ versus B for sample 1(at 0.2% and 0.3% strain) and sample 2(at -0.32% strain) extrapolated to $J^{1/2}B^{1/4} = 0$.

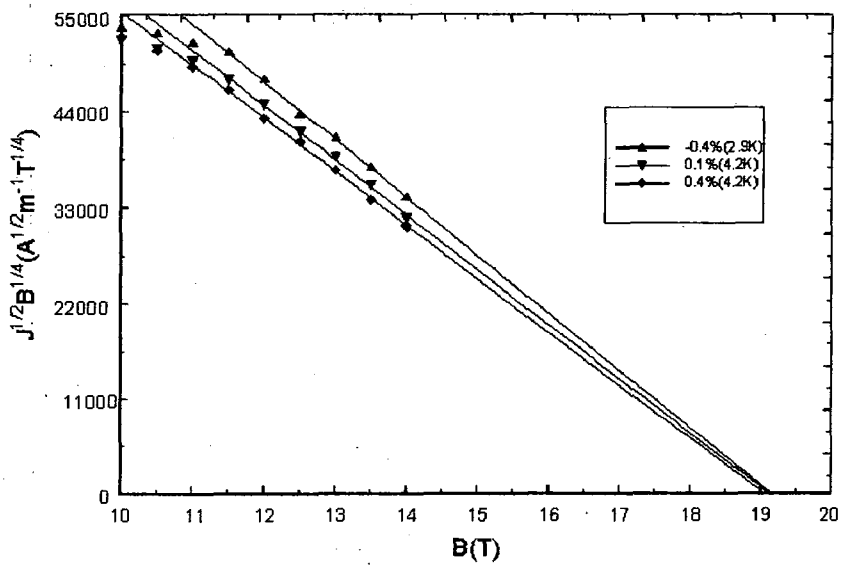

Figure 5.20: $J^{1/2}B^{1/4}$ versus B for sample 1(at 0.1% and 0.4% strain) and sample 2(at -0.4% strain) extrapolated to $J^{1/2}B^{1/4}=0$.

The difference in the values of n given by equation 5.4(and 5.5) and 5.6 demonstrate that the index n only parameterises the change in J_C with change in strain or temperature. According to Scaling Laws (H-S-T)[16,17] there should be a unique value for n which characterizes the pinning mechanism. The empirical law is a simplification so the pinning mechanism cannot be identified by these Scaling Laws. This is demonstrated in figures 5.19 and 5.20. Within each of these figures the values of B_{C2} for the different measurements is the same. The Scaling Laws would suggest that these Kramer lines should all have the same gradient and hence should superimpose on one another. Experimentally we do not find superposition and hence explicitly demonstrate the break-down of the Scaling Laws.

The width of the J_C versus strain at 10 T of figure 5.8 shows that J_C degrades by about 8% at ±0.2% strain on both sides of the peak. Ekin showed similar results where the width of the I_C versus strain indicates that at 10 T there is a ±0.2% strain margin of error around the maximum before I_C degrades by more than 5%[12]. ten Haken showed a decrease of about 10% in J_C at 10 T at ±0.2% strain from the peak[10]. ten Haken also showed that there is shift in the maximum of the J_C versus strain as the applied field increases. He showed that at 10 T the maximum occurs at about 0.4% strain and is shifted to about 0.5% strain at 16 T. The reduction of J_C and the shift in maximum is attributed to `cracking'. Cracking causes mechanical damage that reduces of the cross-section of the superconducting path in the Nb_3Sn layer or filaments.

Figure 5.16 shows that when the temperature is reduced the value of B_{C2} at 0% strain(ie., when the compressive pre-strain is completely relieved) increases by about 8%. The maximum value of B_{C2} occurs when J_C is maximum. For sample 1, B_{C2} decreases by about 9% from its maximum value at +0.4% strain. For sample 2, B_{C2} decreases by about 8.5% from its maximum at -0.4% strain.
Ekin's data showed that B_{C2} decreases by about 7% from its maximum value at +0.4% strain.

5.7 Conclusions

This chapter is an attempt to investigate the effect of strain on the critical current density, J_C, on a Nb_3Sn wire. Uniaxial strain does not only affect J_C but also the upper critical field, B_{C2}. From the data the following observations and conclusions have been drawn:

a. The compressive pre-strain of the sample measured at 4.2 K is found to be about 0.3%.

b. Maximum J_C occurs when the deviatoric strain is a minimum.

c. If strain is applied to the sample beyond its strain-free state, J_C decreases.

d. J_C also decreases if compressive strain is applied to the sample. This is because the sample is initially in compressive pre-strain which degrades the initial critical current, thus further compression will reduce the critical current even more.

e. The decrease in J_C at the very highest strains is attributed to fracture in the superconducting filaments.

f. The maximum values for B_{C2} occurs where J_C is maximum.

g. At 4.2 K , the value of B_{C2} maximum is 19.6 T. At 2.9 K, the value of B_{C2} maximum is 21.2 T. The values of B_{C2} is thus affected by temperature.

h. The values of B_{C2} decreases as strain is increased beyond the strain-free state.

i. The value of α is found to be $4.20 \pm 0.57 \times 10^8$ $Am^{-2}T^{-1}$for sample 1. For sample 2, α is found to be $1.37 \pm 0.05 \times 10^{10}$ $Am^{-2}T^{-1}$. It shows that α changes when strain is applied to the sample.

j. The values of n are 1.67 ± 0.7 and 0.54 ± 0.16 for sample 1 and sample 2, respectively.

k. The values of α and n from temperature scaling are found to be $3.63 \pm 0.62 \times 10^8$ $Am^{-2}T^{-1}$ and 1.72 ± 1.3, respectively.

The strain scaling law can be expressed as:

$$F_P = \alpha[B_{C2}(\epsilon)]^n b^{1/2}(1-b)^2$$

The temperature scaling law can be expressed as:

$$F_P = \alpha[B_{C2}(T)]^n b^{1/2}(1-b)^2$$

The importance of the scaling law is that it is possible to measure F_P at one strain or temperature, and then be able to predict F_P at another strain or temperature by simply scaling the results by $[B_{C2}]^n$. The index n is a constant which determines the strain or temperature dependence of the pinning. The difference in the values of n between strain scaling and temperature scaling shows that n only parameterises the change in J_C with change in strain or temperature. So the value of n(~2.0) from temperature scaling need not necessarily mean planar pinning. The empirical law is a simplification so the pinning mechanism cannot be identified by these Scaling Laws.

These measurements demonstrate that it is important to understand the effect of strain on J_C in determining the strain limits for mechanical designs. Even though B_{C2} and to some extent temperature[18] are affected by strains, another key factor dictating the mechanical design is the effect of strain on J_C.

References

1. Reed R P and Clark A F., *Materials at Low Temperatures* (American Society for Metals, USA) (1983).
2. Foner S and Schwartz B.,*Superconductor Materials Science: Metallurgy, Fabrication and Applications*(Plenum Press, New York) (1981).
3. Ekin J W., *IEEE Trans. Magn. MAG-19* **3** 900 (1983).
4. Rupp G., *IEEE Trans. Magn. MAG-13* **5** (1977).
5. Kunzler J E., *Rev. Mod. Phy.* 33(4) 501 (1961).
6. Ekin J W., *J. Appl.Phys.* **49**(6) 3406 (1978).
7. Ekin J W, Clark A F and Ho J C., *J. Appl. Phys.* **49**(6) 3410 (1978).
8. Babic E, Prester M and Biskup N., *Solid State Comm.*, **77**(11) 849 (1991).
9. Kramer E J., *J. Appl. Phys.* **44**(3)(1973).
10. ten Haken B ., *PhD Thesis*, University of Twente, Netherlands (1994).
11. Fietz W A and Webb W W., *Phys. Rev.* **178(2)** 657 (1969)
12. Ekin J W., *Cryogenics* **20** 611 (1980).
13. Ekin J W., *Mechanical Properties and Strain Effects- Superconductor Materials Science: Metallurgy, Fabrication and Applications;* ed: Foner S and Schwartz B(Plenum Press, New York) (1981).
14. Ekin J W., *Appl. Phys. Letts.* **29** 216 (1976).
15. Easton D S and Schwall R E., *Appl. Phys. Lett* **29** 319 (1976).
16. Hampshire R G, Sutton J and Taylor M T., *Proc. British Cryogenics Council Conf. on Low Temp. and Electric Power*, Royal Society, London 251(1969).
17. Hampshire R G and Taylor M T., *J. Phys. F: Metal Phys.*, **2** 89 (1972).
18. McEvoy J P., *Physica C* **55** 540 (1975).

Chapter 6

Critical Current of BiSCCO Tape at 4.2 K as a Function of Strain and Magnetic Field Up to 12 Tesla

6.1 Introduction

Among the high-T_C superconductors, the Bi-based cuprates (BiSCCO) are at present the most promising candidates for industrial applications. These applications will require tapes or wires with high critical current densities, J_C, in long lengths and good mechanical properties. These materials must also be able to sustain a high critical current density when subjected to a considerable strain. Multifilamentary BiSCCO tapes have been shown to exhibit enhanced strain tolerance over mono-core tapes, and there is a world-wide effort to optimise these materials[1]. A useful tape should be able to maintain a current density of the order of 10^8 Am^{-2} under operational strain.

This chapter is about the effect of strain on the current densities of an Ag-sheathed BiSCCO(2223) tape. Section 6.2 describes the tape used for the J_C versus strain experiments. Section 6.3 is a brief description of the experimental technique for getting the data. The experimental results are presented in section 6.4. The findings are discussed in section 6.5. Section 6.6 concludes this chapter.

6.2 The BiSCCO/Ag tape.

The tape used in these measurements is a multifilamentary IGC BiSCCO/Ag tape. Five samples(Sample 1, 2, 3, 4 and 5) of the tape were measured. The samples measured were short sections($\approx$ 9 mm) from a tape of total length of about 400 mm. The thickness of the tape is 0.18 mm and the width is 3.40 mm. Figures 6.1(a) and 6.1(b) show the micrograph pictures of the same tape taken at two different magnifications.

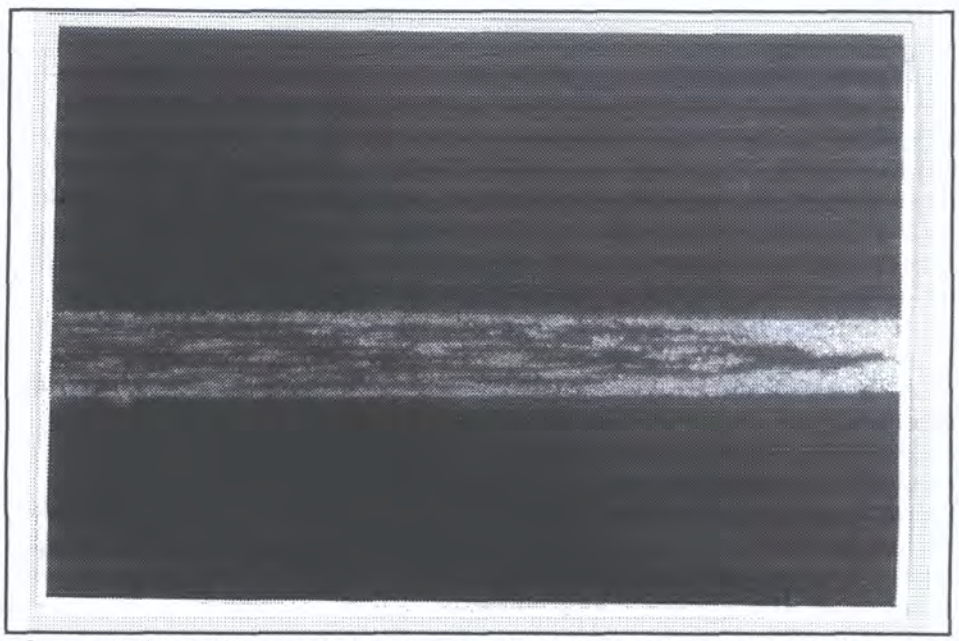

Figure 6.1(a): The optical micrograph of the cross-section of the tape (scale is 1mm:15.7μm)

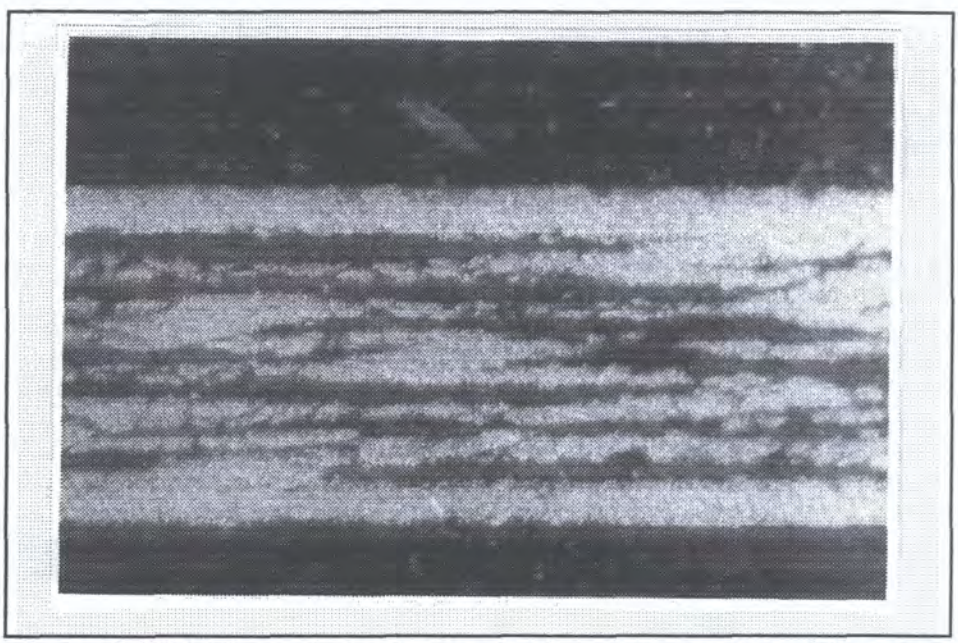

Figure 6.1(b):The optical micrograph of the cross-section of the tape (scale 1mm:4μm).

The cross-section is taken so that the direction of the macroscopic transport current and the applied strain were perpendicular to the plane of the paper. The tape consists of 40% of superconducting material. The superconducting material is covered by a silver sheath which is represented as the `white' part of the picture. The tape was made using the standard oxide powder-in-tube(OPIT) method[2]. According to IGC a critical current of about 29 A has been measured on a short sample($\approx$ 4 cm) at 77 K in zero field. A quick check by taking a V-I trace on a 9 mm sample at 77 K (0 T) gives a critical current of 31 A at 0.5 μV criteria. Transport current was applied along the length of the tape and perpendicular to the c-axis. The c-axis is defined as the direction perpendicular to the plane of the tape.

6.3 Experimental technique.

The sample, with a strain gauge pasted on it, was mounted on the J(B,ϵ) probe as described in chapter 4. The V-I characteristics of the tape were measured at 4.2 K in our high field magnet system. For samples 1, 4 and 5 data were taken from 0.5 T up to 12 T with increasing and decreasing field to see the effect of hysteresis. Data were taken from 0.5 T up to 10 T for samples 2 and 3. The field was applied perpendicular to the direction of transport current and parallel to the c-axis. The V-I characteristics are measured for each sample and the critical current density calculated using a 1.0μV(0.3 x 10^3 μVm^{-1}) criteria. The experimental technique has been described in detail in chapter 4. The critical current distribution is obtained by taking the second derivative of the experimental V-I values. Details for obtaining the critical current distribution has been described in section 3.5.

6.3.1 Uniaxial tensile strain measurements

Tensile strain were applied on samples 1 and 2 up to about 0.3%. For sample 3, when tensile strain was applied to the sample, the resistance readings of the strain gauge on the sample showed that the sample was compressed up to 0.3% strain. This phenomena was discussed in section 4.9. After being compressed to 0.3% strain, the sample then went into tension up to 0.2%. The sample is then recompressed to 0.16% strain.

6.3.2 Bending(compression and tension) measurements

A tape will bend after being compressed to a certain extent. A bent tape has both a tensile side and a compressive side. For sample 4, the strain gauge was on the compressive side of the tape. Sample 4 was compressed up to -0.66% strain. For sample 5, the strain gauge was on the tensile side of the tape. The tensile strain on sample 5 was up to 0.33%.

6.4 Experimental results

6.4.1 Sample 1

Figure 6.2 is an example of an E-J characteristics taken at 6 T for three different strain values. The baselines are rather flat indicating that good contacts have been achieved. The gradient($\partial V/\partial I$) above J_C at 0.062% strain is steeper than that at 0.292% and 0.297%. This shows at low strain the pinning is stronger. Between 0.292% and 0.297% strains, a slight increase in strain decreases J_C significantly compared to that between 0.062% and 0.297%.

Figure 6.3 shows J_C versus B(ascending and descending fields) at the same strain values as above (ie., 0.062%, 0.292% and 0.297%). J_C decreases as strain and applied field increase. The graph also shows hysteresis for all three strains. The J_C values for the descending fields are higher than for ascending fields. The magnitude of the hysteresis for the 0.062% strain is about 37% at 0.5 T and decreases as the field increases. The difference at 0.5T for each strain also decreases as strain increases.

Figure 6.4 is J_C versus strain for ascending fields. There is a flat region from 0.06% strain to about 0.25% strain. After 0.25% strain J_C gradually drops by about 20% at 0.28% strain. Then J_C drops sharply indicating that the sample has been damaged. The slight decrease in strain observed at low J_C values is probably due to cracks in the solder. This causes the tape to slip from the brass posts at the solder joints. Figure 6.5 shows J_C versus strain for descending fields. There is a flat region from 0.06% to

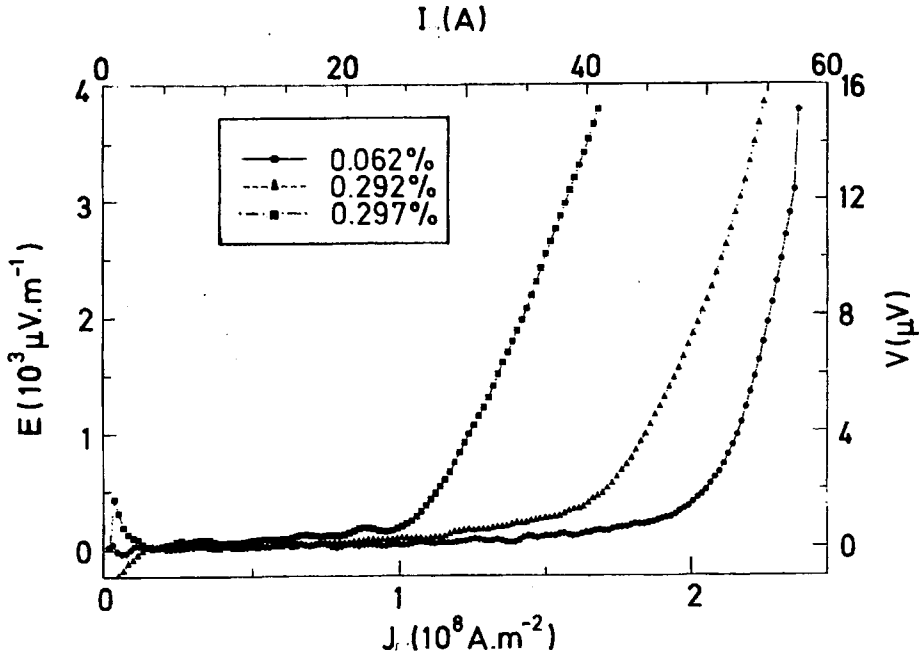

Figure 6.2: E-J characteristics taken at 6 T for three different strain values (sample 1).

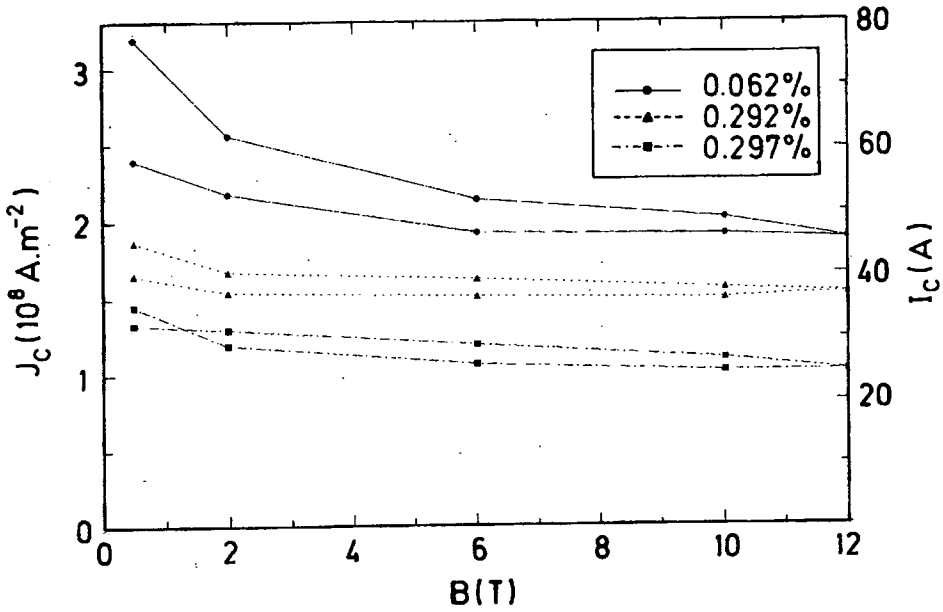

Figure 6.3: J_c versus B (ascending and descending fields) at the same strain values as in figure 6.2 (sample 1).

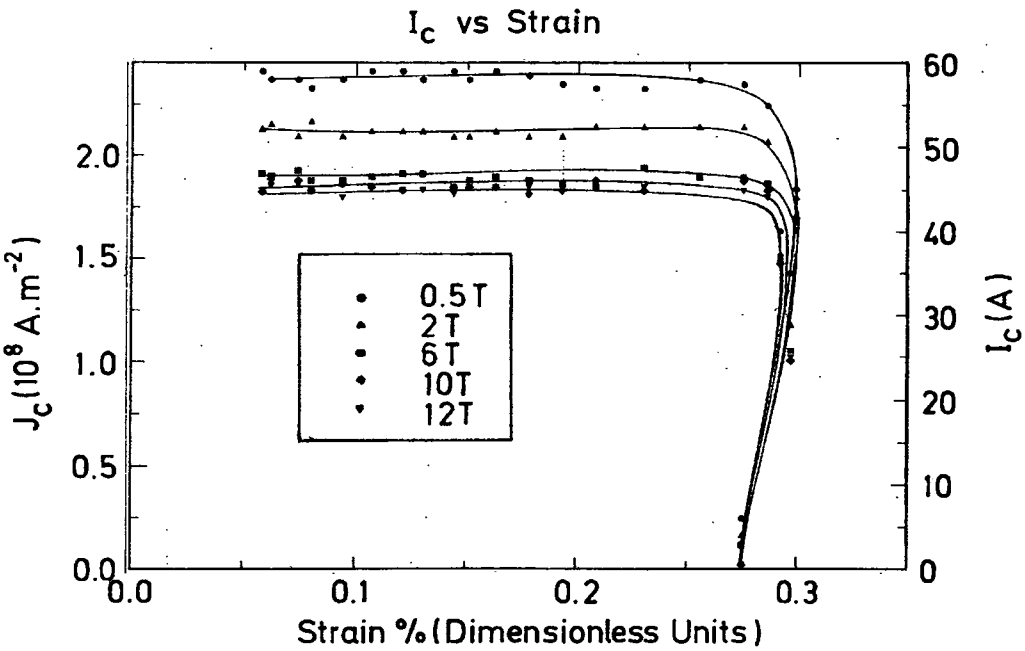

Figure 6.4: J_c versus strain for ascending fields (sample 1).

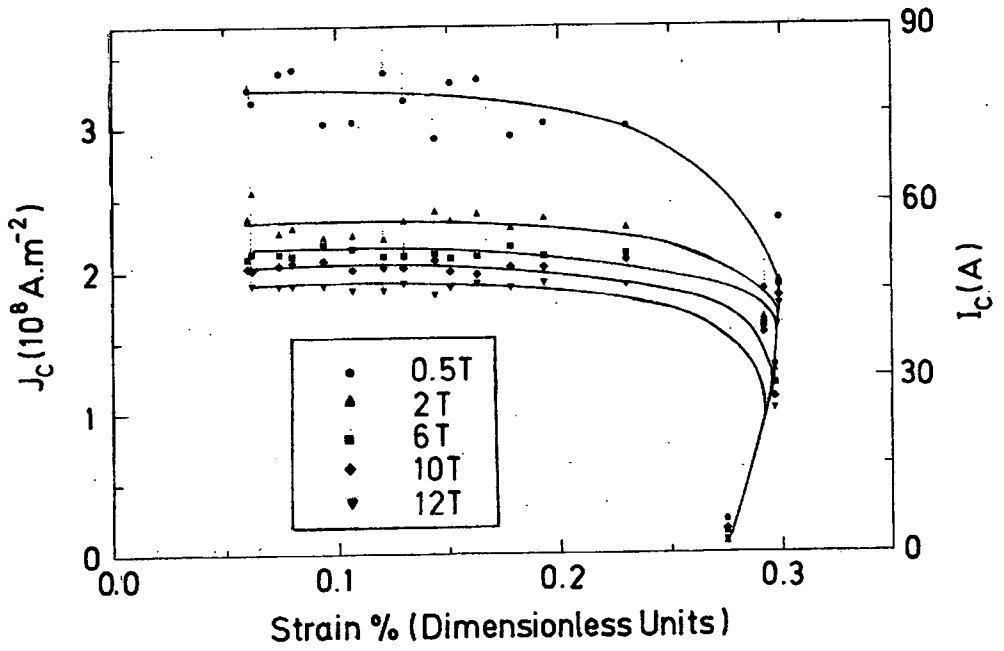

Figure 6.5: J_c versus strain for descending fields (sample 1).

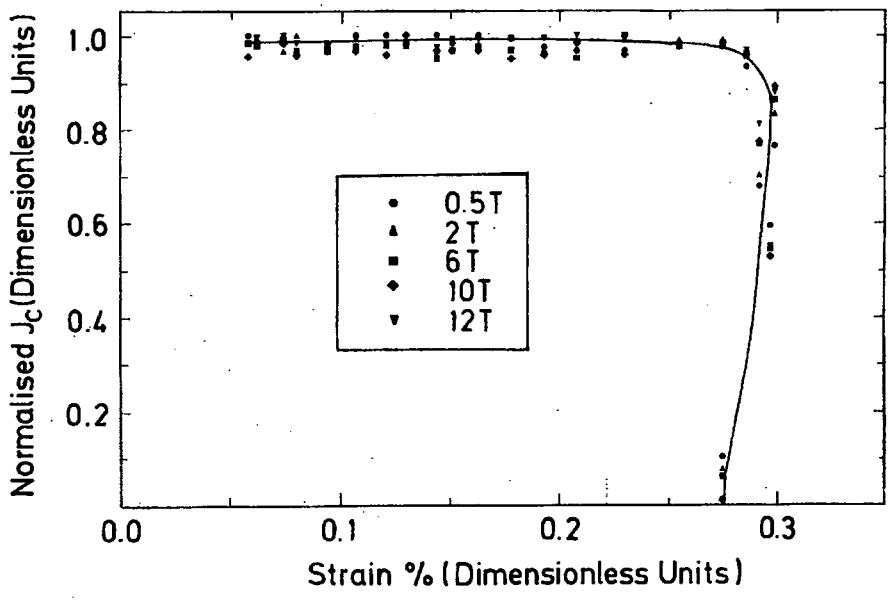

Figure 6.6: Normalised J_c versus strain for ascending fields (sample 1).

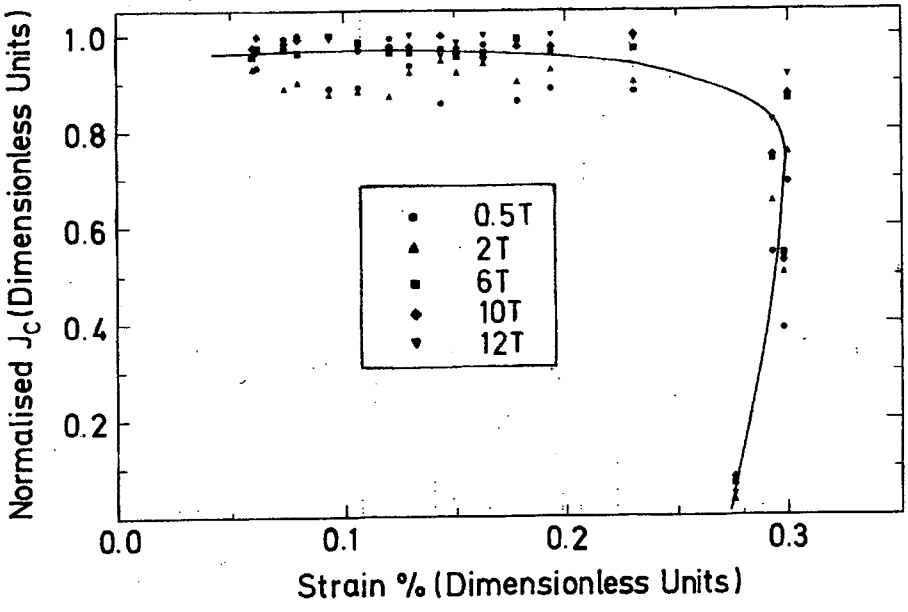

Figure 6.7: Normalised J_c versus strain for descending fields(sample 1).

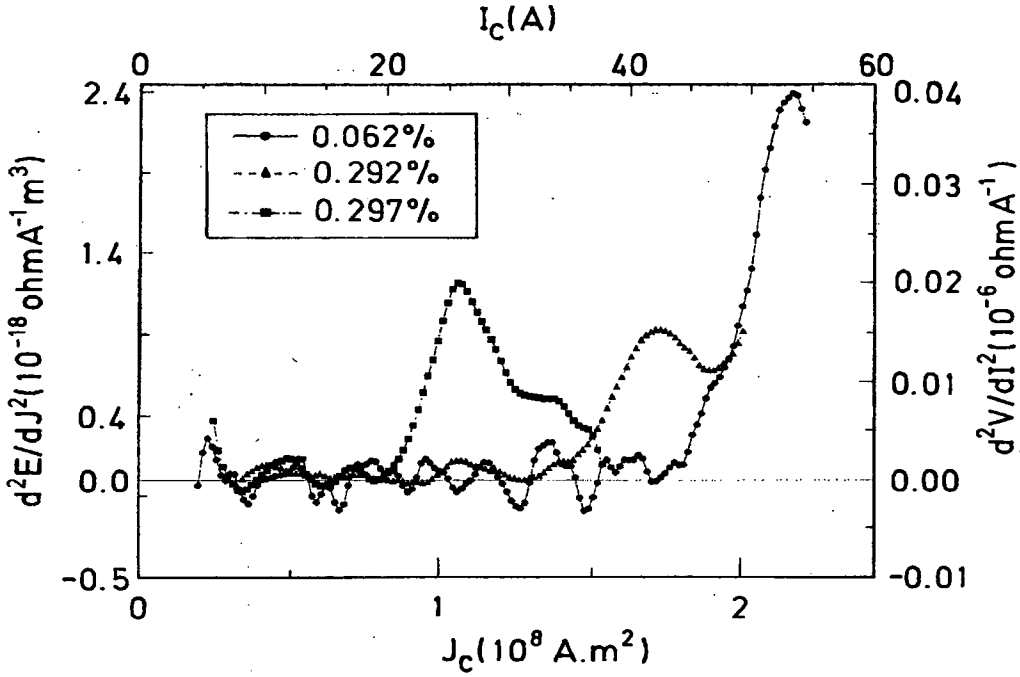

Figure 6.8: The critical current distribution at 6 T for three different strains (sample 1).

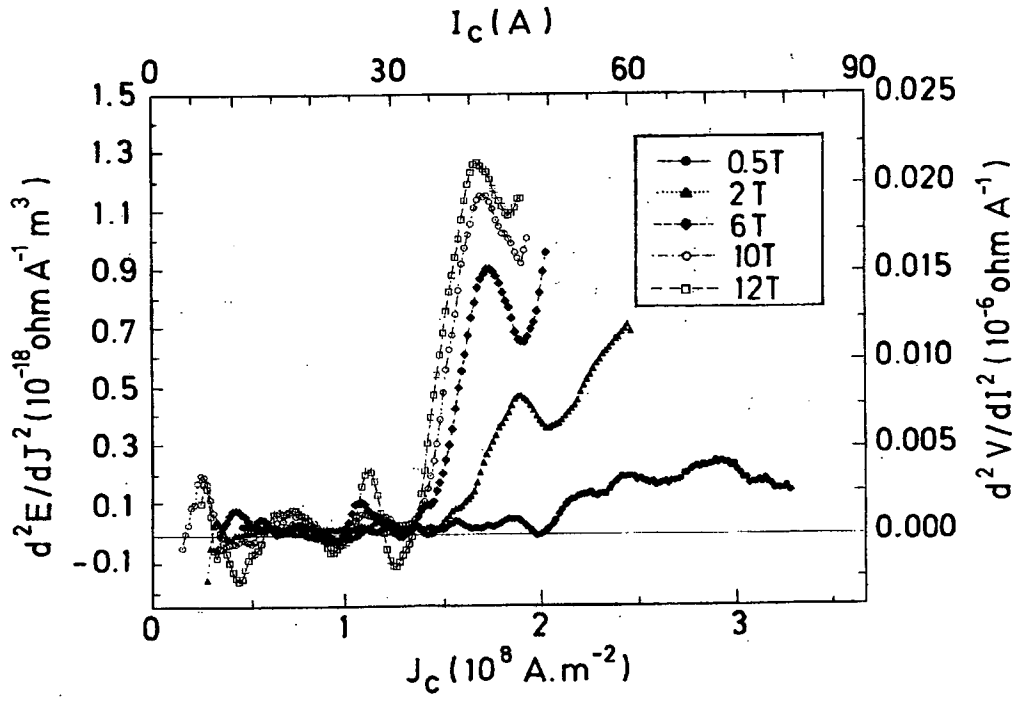

Figure 6.9: The critical current distribution at 0.292% strain for five different magnetic fields(sample 1).

about 0.25% strain.

Figure 6.6 shows the normalised J_C versus strain for ascending fields. The curves superimpose on one another. This shows that the strain properties are broadly field independent. There is a gradual drop in J_C at about 0.26% before the sharp drop occurs. The gradual section of the drop in J_C occurs because cracks do not propagate the entire section of the filaments[3]. The normalised J_C versus strain for B descending is shown in figure 6.7. The 6T, 10 and 12 T curves superimposed on one another. The lower field curves, 0.5 T and 2 T, also seems to superimposed on one another. The gaps between these two curves is quite large at low strain values.

Figure 6.8 shows the critical current distribution at 6 T for three different strains. There is one sharp peak at 55 Amp at 0.062% strain. At 0.292% strain, the peak is lowered to about 42 Amps. This peak is broader compared to the peak at 0.062% strain. At 0.297% strain, the peak reduces to about 25 Amps but is sharper than at 0.297% strain. A secondary peak seems to appear at about 25 Amps.

Figure 6.9 shows the critical current distribution at 0.292% strain for five different magnetic fields. At 0.5 T there is no obvious peak. However, at 2 T , the peak is more obvious. The current at which the peaks occur decrease as field increases.

6.4.2 Sample 2

Figure 6.10 is an E-J characteristic taken at 10 T for three different strain values. The features of the E-J characteristics are similar to figure 6.2. The baselines are rather flat and the gradient($\partial V/\partial I$) above J_C at lower strains are steeper than at higher strains. J_C decreases by a factor of 0.4 from 0.028% strain to 0.340% strain. In figure 6.2(sample 1), J_C decreases by a factor of 1 from 0.062% strain to 0.297% strain. It shows that when strain is applied, the damage to the superconducting filaments for sample 2 is more gradual than that of sample 1.

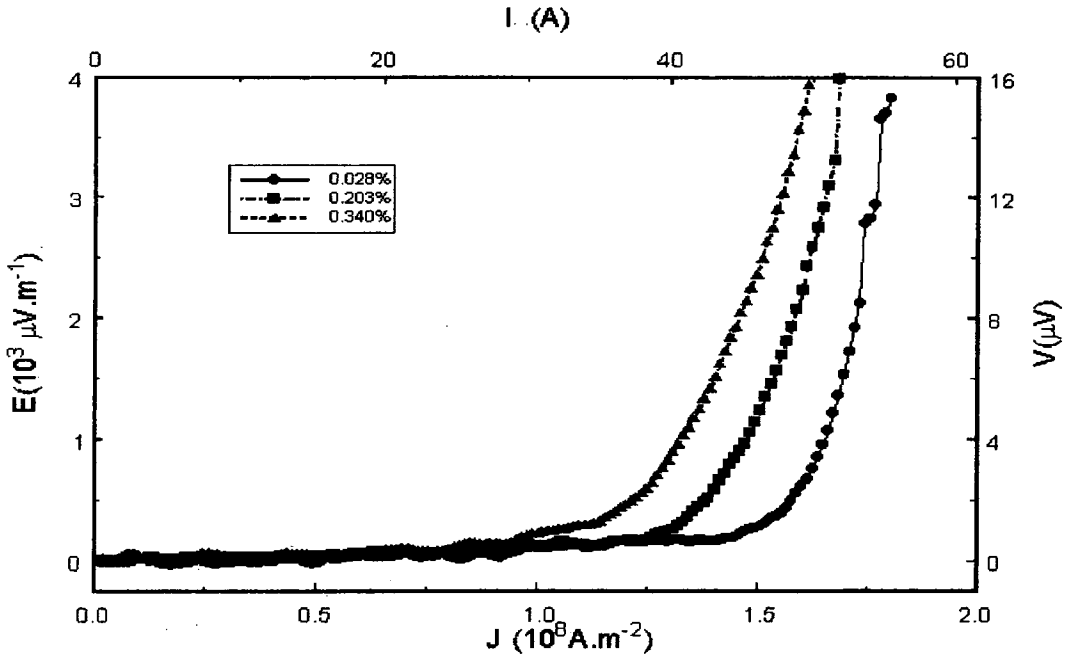

Figure 6.10: E-J characteristics at 10 T for three different strain values(sample 2).

Figure 6.11 is J_C versus strain for ascending fields. There is a flat region from 0.028% strain to about 0.18% strain. The sample is able to withstand strain up to 0.340%, after which no J_C can be detected. The J_C degradation begins at about 0.18% and occurs stepwise. The stepwise degradation of J_C was not observed in sample 1. The stepwise degradation of J_C was also observed in the work of Keβler et al[4]. Figure 6.12 shows the normalised J_C versus strain for ascending fields. The curves superimpose on one another indicating that the strain properties are broadly field independent. However cracks appear to be more deleterious to J_C at higher fields.

Figure 6.13 shows the critical current distribution at 0.5 T for two different strains. The trends of the critical current distribution is similar to figure 6.8(sample 1). There is one pronounced peak at about 65 Amp. At higher strain a secondary peak appears at about 50 Amp and the distribution is much broader. Hence the critical current distribution data allows one to find an intrinsic J_C (ie. the second peak) even if the sample is damaged. Figure 6.14 shows the critical current distribution at 10 T for two different strains. It shows similar trends as figure 6.13. There is one pronounced peak at low strain. At higher strain a secondary peak appears and the distribution is much broader.

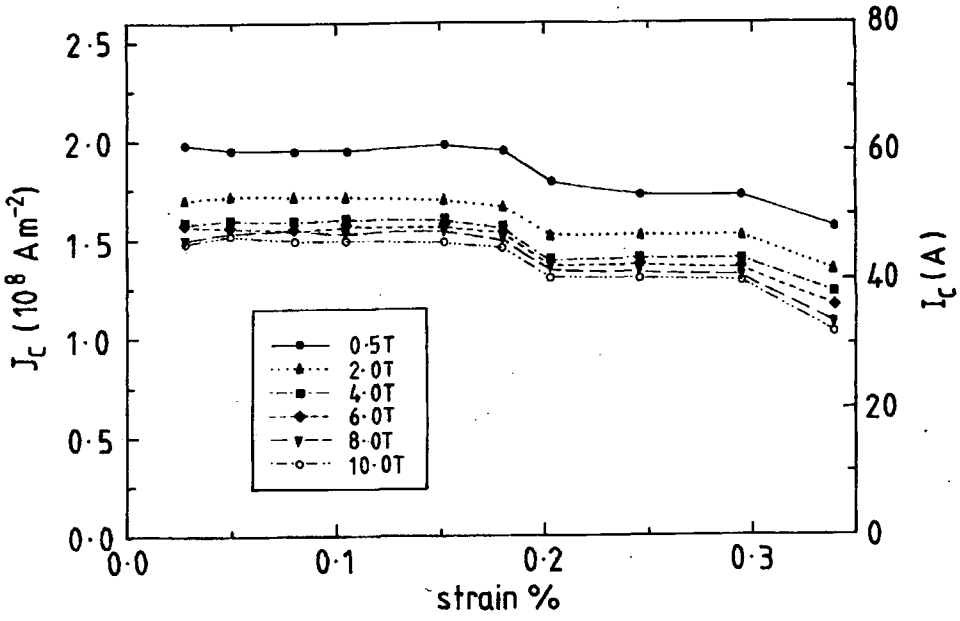

Figure 6.11: J_c versus strain for ascending fields(sample 2).

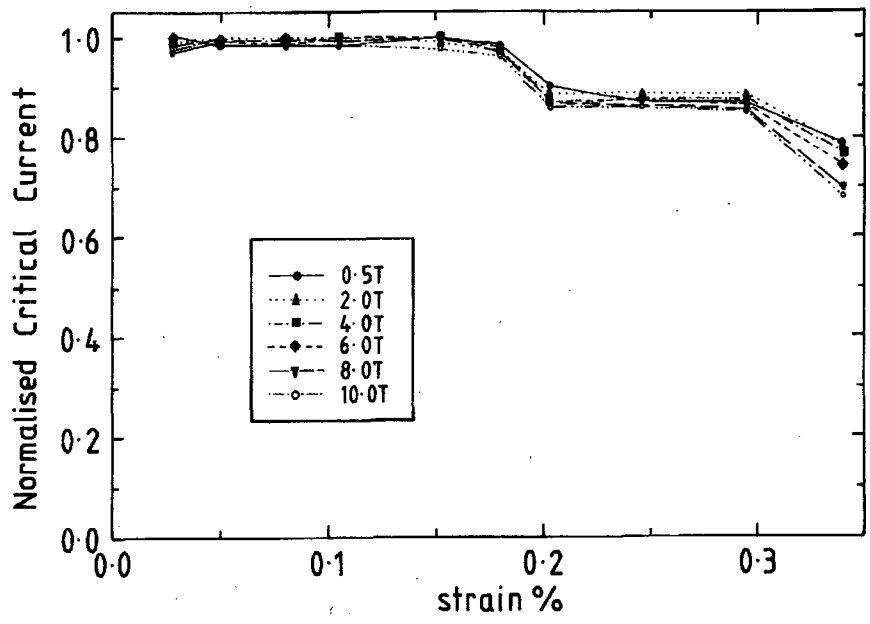

Figure 6.12: Normalised J_c versus strain for ascending fields(sample 2).

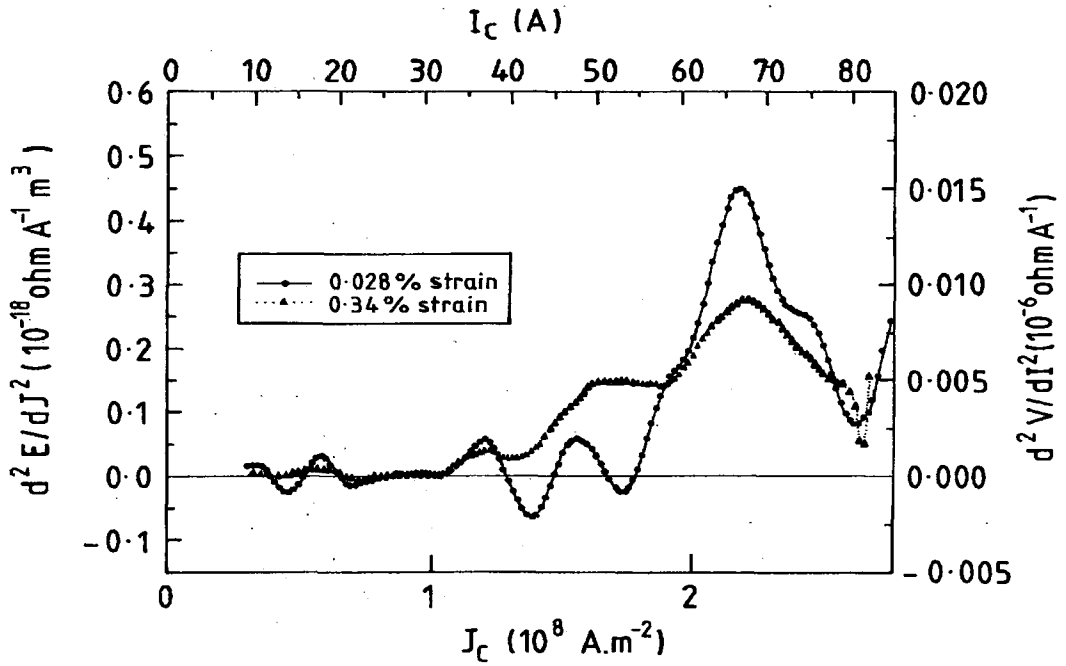

Figure 6.13: The critical current distribution at 0.5 T for two different strains (sample 2).

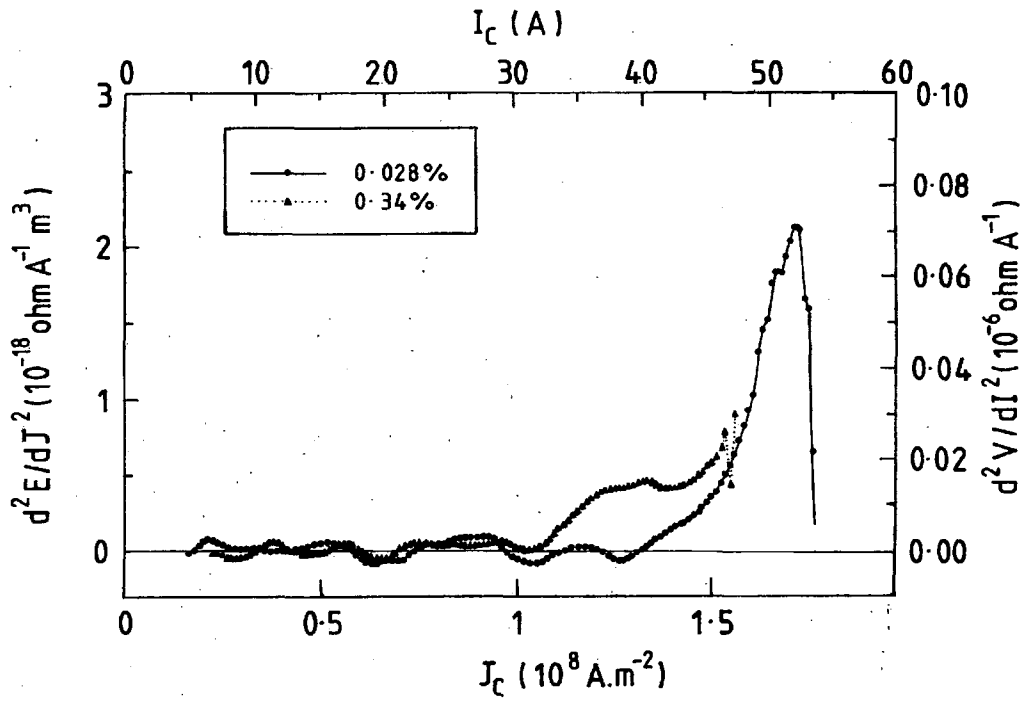

Figure 6.14: The critical current distribution at 10 T for two different strains (sample 2).

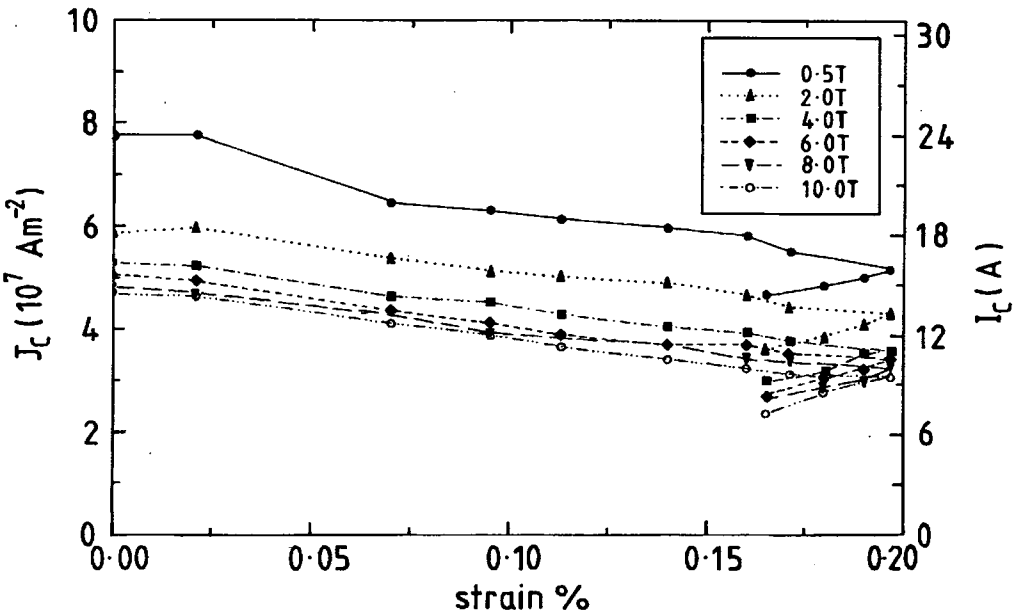

Figure 6.16: J_c versus strain for ascending fields(sample 3).

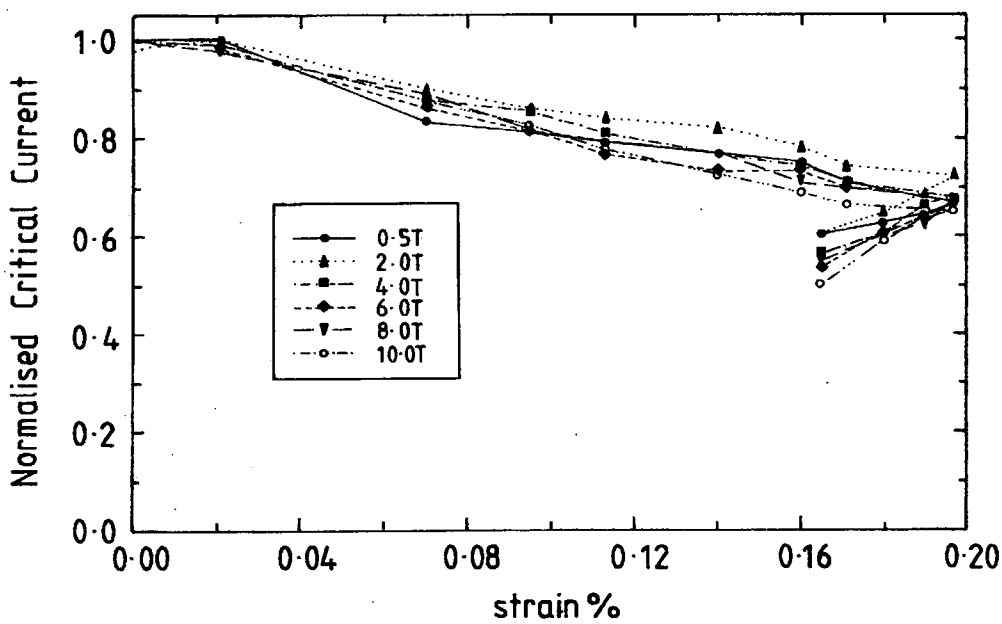

Figure 6.17: Normalised J_c versus strain(sample3).

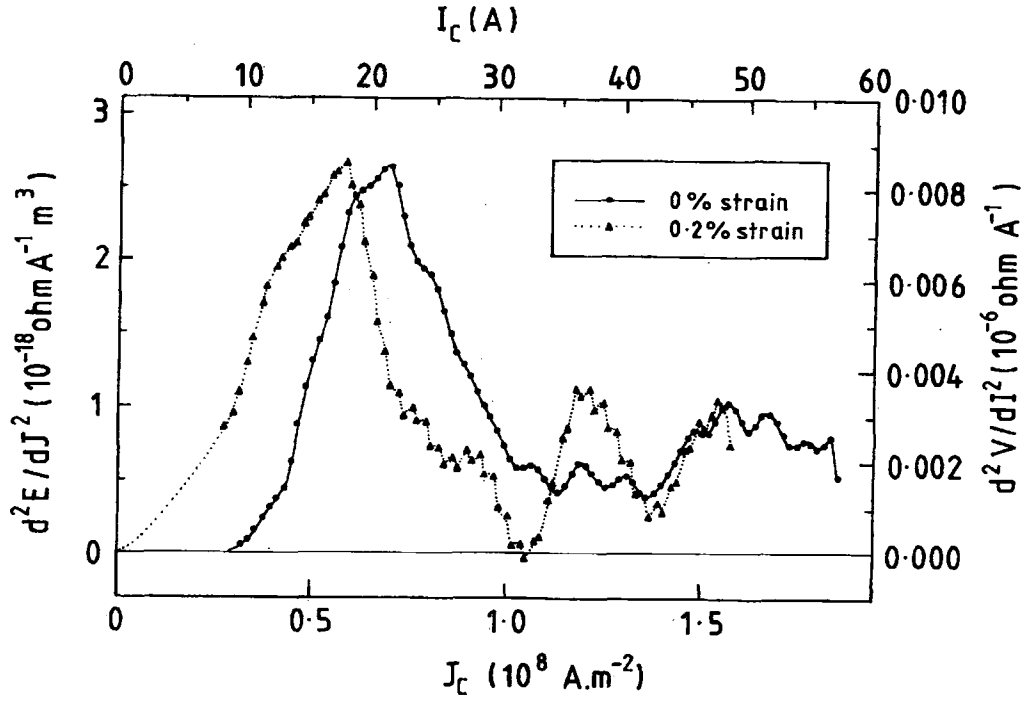

Figure 6.18: The critical current distribution at 0.5 T for two different strains (sample 3).

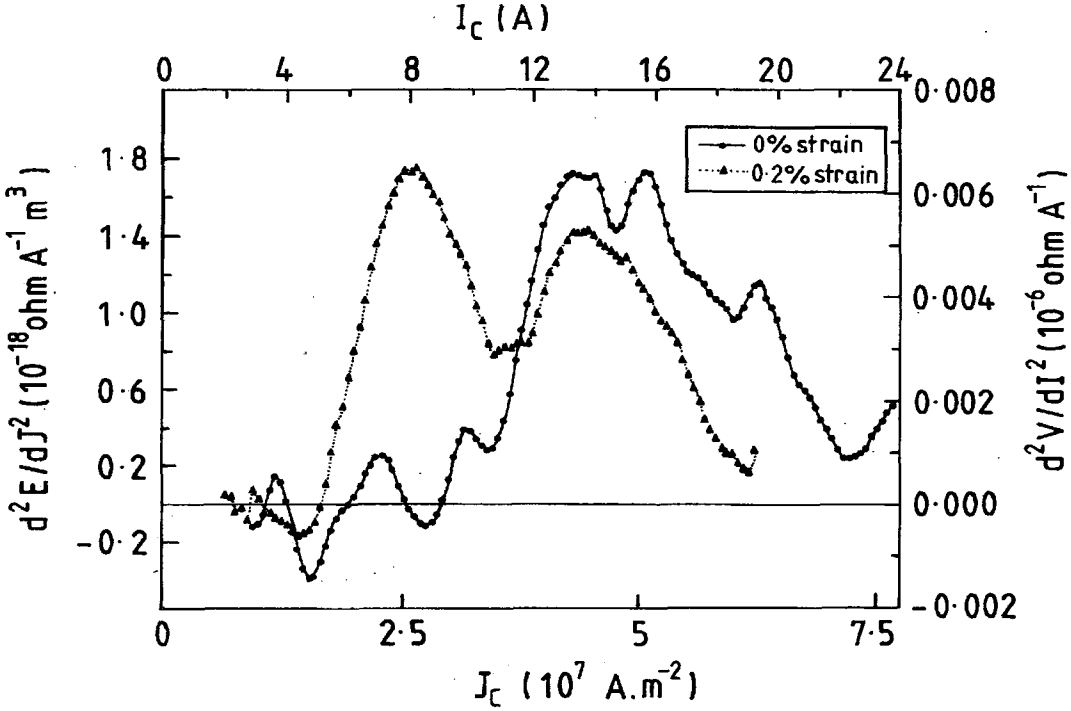

Figure 6.19: The critical current distribution at 10 T(sample 3).

However, the secondary peak at low strain is not easily distinguishable as that of figure 6.13.

6.4.3 Sample 3

Figure 6.15 is an E-J characteristic taken at 10 T for three different tensile strain values. The baselines are rather flat, similar to samples 1 and 2. However, the gradients($\partial V/\partial I$) above J_C are almost parallel for the three strains. The J_C value at low strain is about a factor of 3 lower than that for sample 2. This is because the sample has been damaged when it undergoes compression.

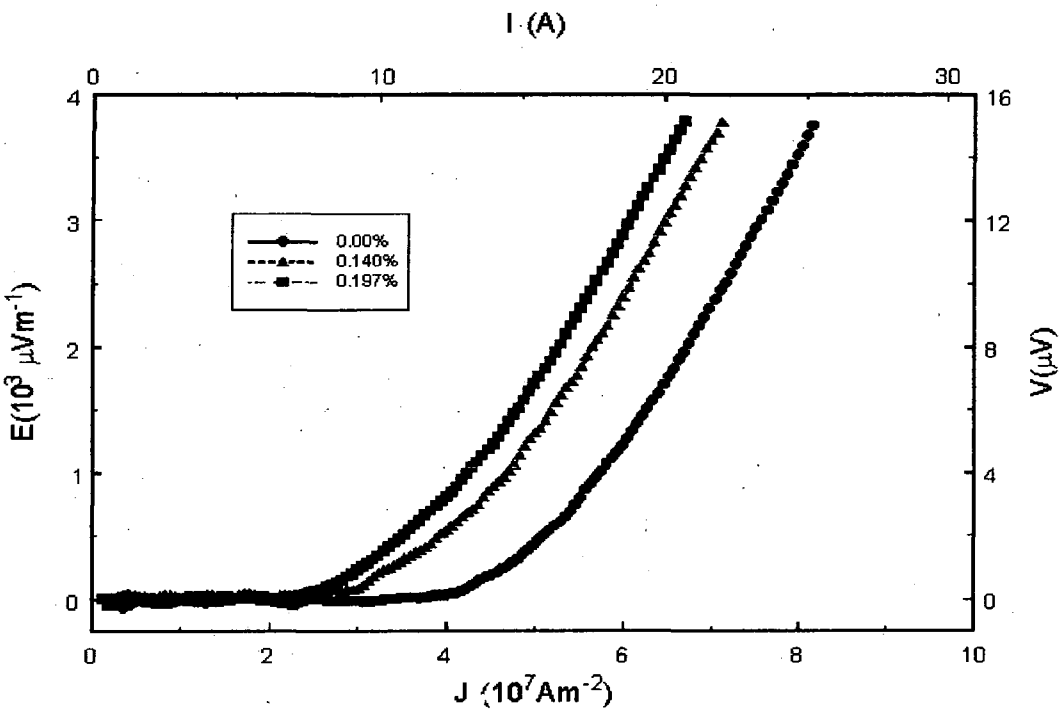

Figure 6.15: E-J characteristics at 10 T for three different strains(sample 3).

Figure 6.16 shows the J_C versus strain for ascending fields. It shows a stepwise degradation of J_C, similar to sample 2. Further J_C reduction is observed when the tape is recompressed to 0.16% strain. Cracks occur as strain changes and the decrease in J_C is determined by the history of the mechanical deformation. The normalised J_C versus strain is shown in figure 6.17. The curves do not superimpose on one another at high

strains. After J_C reduction to 50% the grains/grain boundaries/current paths are more susceptible to magnetic fields.

Figure 6.18 shows the critical current distribution at 0.5 T for two different strains. It shows similar trends as the samples 1 and 2. At higher strain the main peak is shifted to lower J_C. In addition to the main peak subsidiary peaks appear at higher strain. The critical current distribution at 10T is shown in figure 6.19. The critical current distribution at low strain clearly shows a double peak. One peak is at 16 Amp and the other is at about 14 Amp. As strain increases the peaks are shifted to lower J_C. The 16 Amp peak is shifted to about 13 Amp and the 14 Amp peak is shifted to 8 Amp. It shows that one peak is more susceptible to strain. The peaks at higher strain is broader than at lower strain.

6.4.4 Sample 4

Figure 6.20 shows an E-J characteristics for sample 4 taken at 6 T for four different bending(compressive) strain values. The baselines and the gradients($\partial V/\partial I$) above J_C are similar to sample 1. Figure 6.21 is J_C versus B (ascending and descending) for three different strains. All curves shows hysteresis, similar to figure 6.3. The J_C for descending fields are higher than for ascending fields. The J_C versus strain for three different fields are shown in figure 6.22. The 2 T curve are plotted for both ascending and descending fields. The flat region extends from -0.012% strain to about -0.5% strain. Above 0.5% strain J_C drops gradually by about 23% at -0.66%. Figure 6.23 shows the normalised J_C versus strain for the three different fields. The curves superimpose on one another. Similar to sample 1, the strain properties are broadly field independent. The strain goes beyond -0.6% before the sample is damaged; ie when no J_C can be measured. The strain limit for this sample before being damaged is twice as high compared to sample 1 and 2. The grains are probably compressed together, thus increasing the contact area. However, at above -0.66% strain the additional force from the applied strain will cause slippage between grains. This will affect the contact areas between grains and leads to cracks formation.

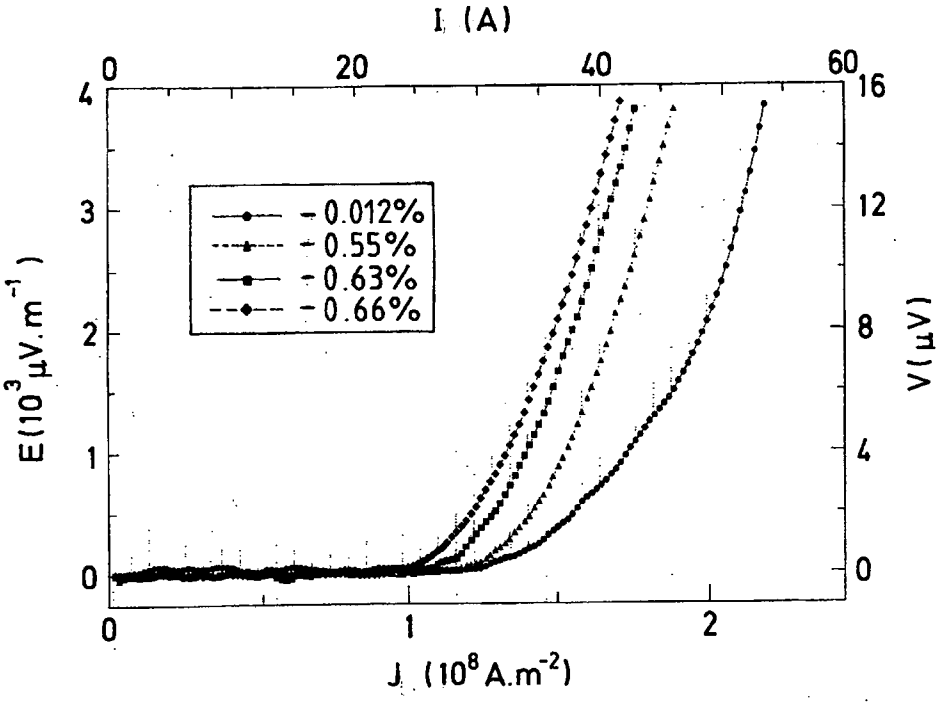

Figure 6.20: E-J characteristics at 6 T for four different bending (compressive) strain values(sample 4).

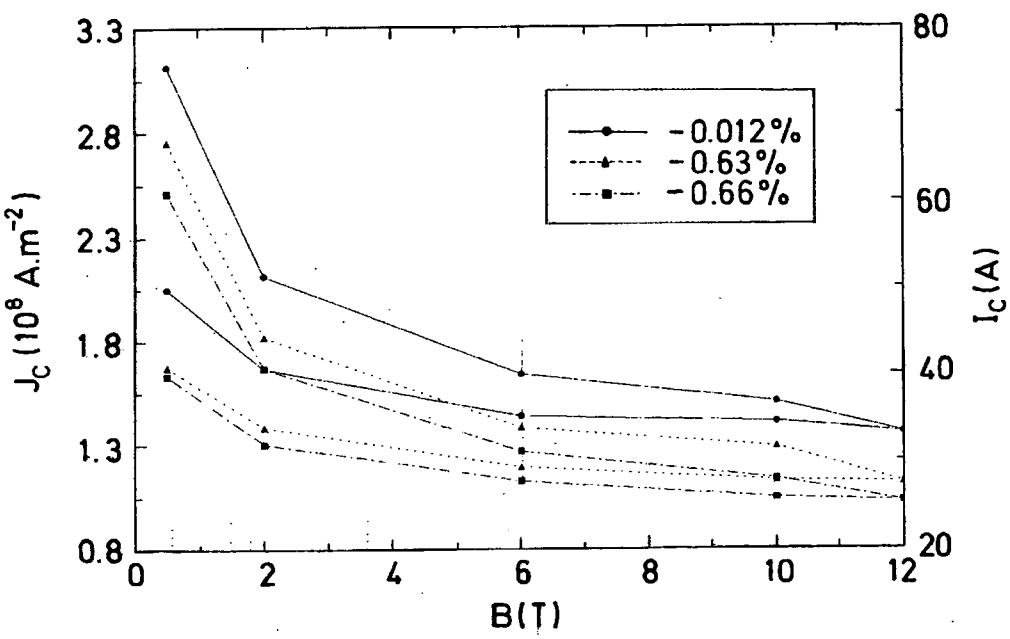

Figure 6.21: J_c versus B (ascending and descending) for three different strains (sample 4).

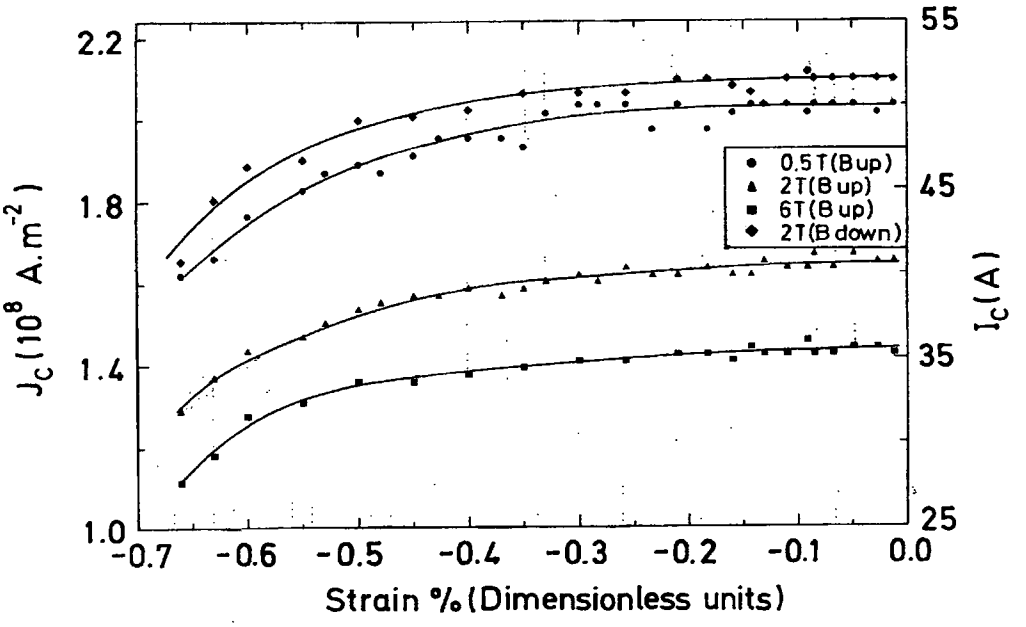

Figure 6.22: J_c versus strain for three different fields(sample 4).

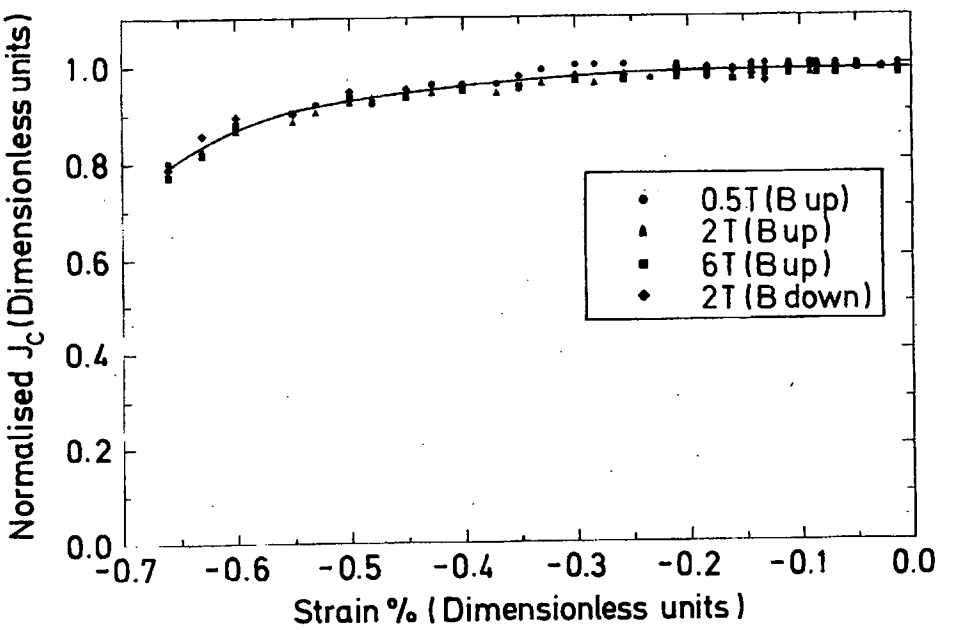

Figure 6.23: Normalised J_c versus strain for three different fields(sample 4).

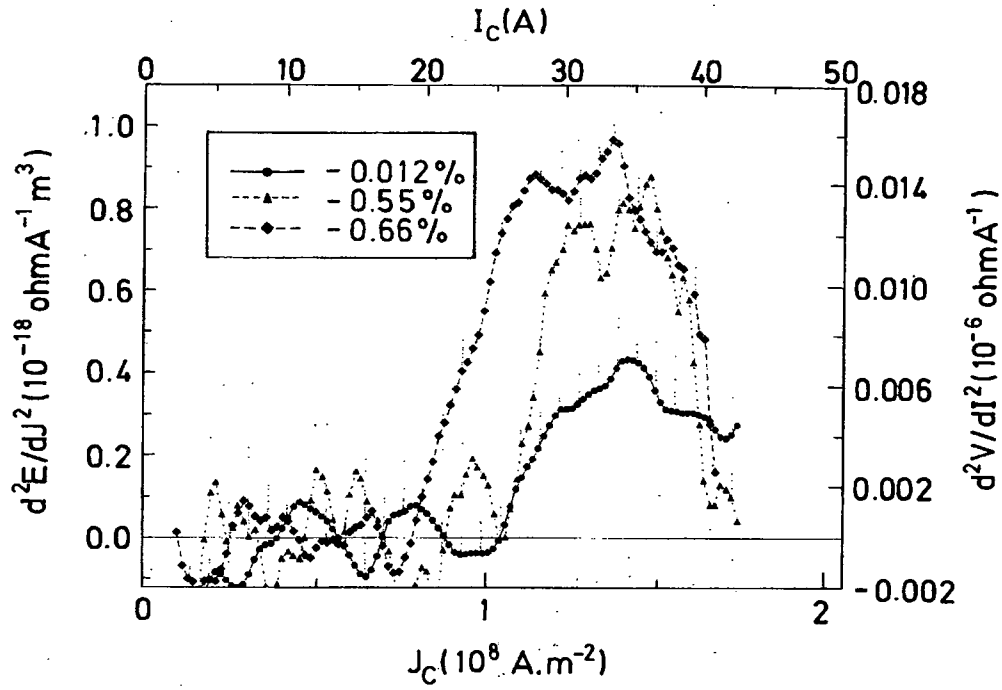

Figure 6.24: The critical current distribution at 6 T for three different strains (sample 4).

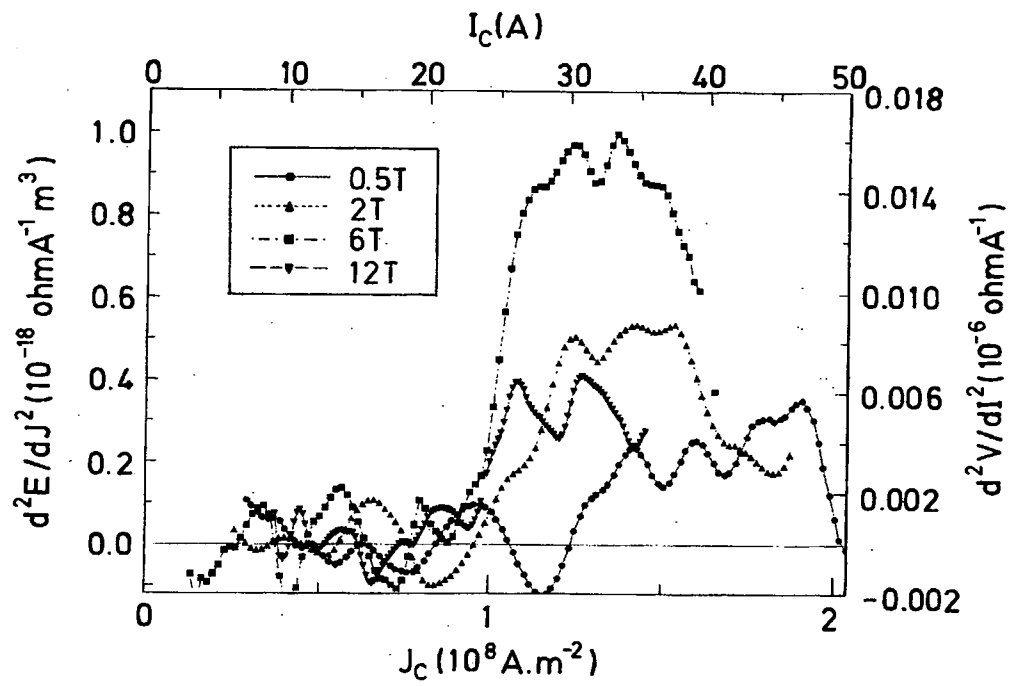

Figure 6.25: The critical current distribution at -0.63% strain for four different fields(sample 4).

Figure 6.24 shows the critical current distribution at 6 T for three different strains. At -0.55% strain the graph shows two peaks. Similar to the previous samples, the peaks start to separate and shifted to lower J_C as strain is increased. Figure 6.25 shows the critical current distribution at -0.63% strain for four different fields. As the field increases the two peaks start to develop.

6.4.5 Sample 5

Figure 6.26 shows an E-J characteristics of the bent(tensile) tape at 6 T for three different strain values. The features of the E-J characteristics are similar to those of sample 1. At 0.333% strain, J_C has dropped by about 16% from that at 0.026% strain. Figure 6.27 shows J_C versus B for ascending and descending fields for three different strain values. All curves show hysteresis and are similar to figures 6.3 and 6.21. Figure 6.28 shows J_C versus strain for ascending fields and figure 6.29 shows J_C versus strain for descending fields. The flat regions occur from 0.026% strain to about 0.21% strain. At 0.333% strain J_C has dropped by about 23% from its original value. The normalised J_C versus strain for ascending and descending fields are shown in figures 6.30 and 6.31, respectively. The curves superimpose on one another at the flat region. But for strains above 0.2% the normalised J_C values are do not fall on the single curve. This indicates that parts of the tape are field dependent.

Figure 6.32 shows the critical current distribution at 6 T for two different strains. It shows a pronounced peak at about 47 Amp with a shoulder at about 42 Amps. When strain increases the two peaks separate and moves to lower J_C values. The critical current distribution at 0.333% strain is shown in figure 6.33. It shows a broad peak at 0.5 T which indicates that I_C is evenly distributed throughout this region. As the field increases the peak becomes narrower and a secondary peak starts to appear. The peaks are also shifted to lower J_C as the field increases.

6.5 Discussion

The above figures on J_C versus tensile strain show that J_C degradation starts to occur

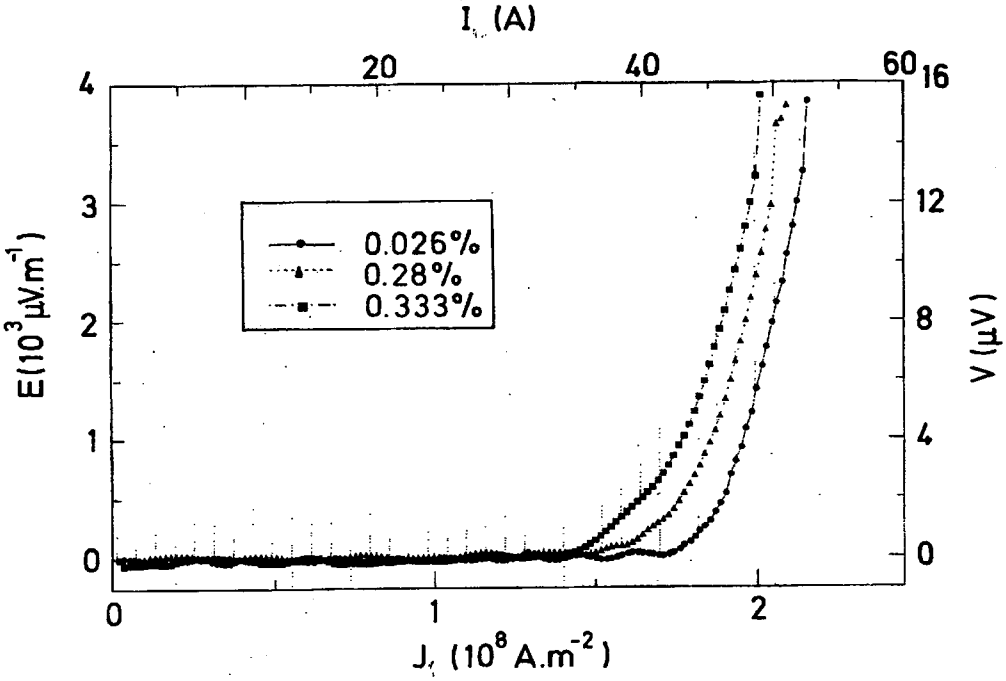

Figure 6.26:E-J characteristics of the bend(tensile) tape at 6 T for three different strain values(sample 5).

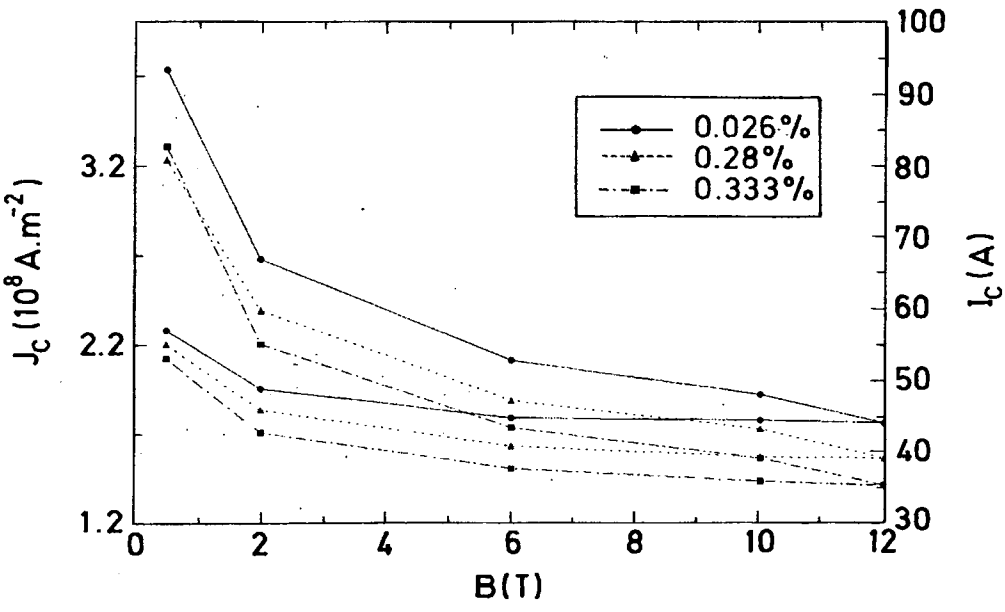

Figure 6.27: J_c versus B (ascending and descending) for three different strain values (sample 5).

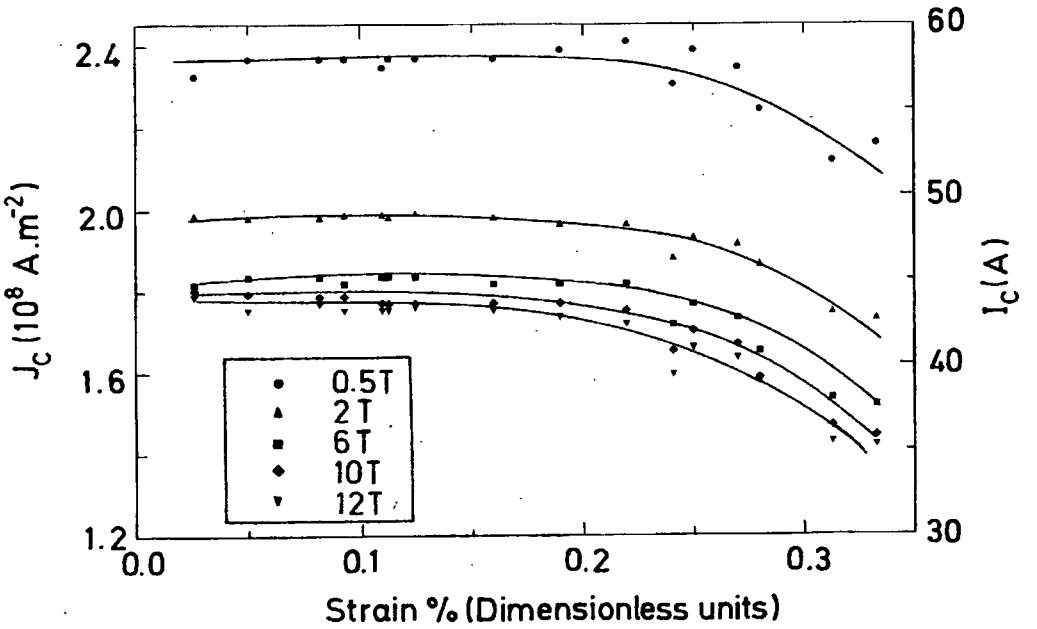

Figure 6.28: J_c versus strain for ascending fields (sample 5).

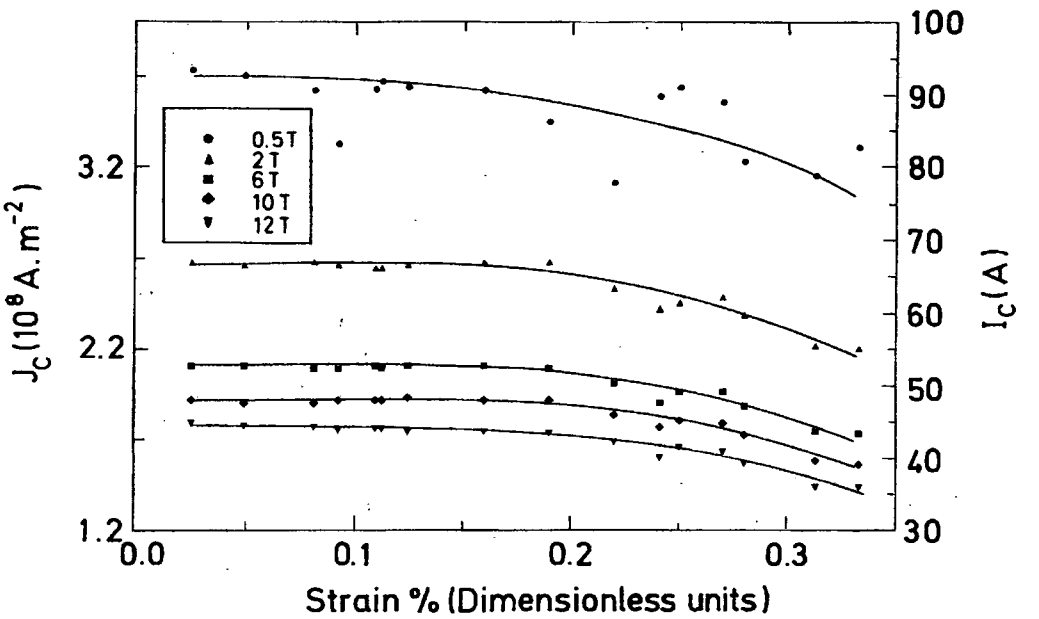

Figure 6.29: J_c versus strain for descending fields(sample 5).

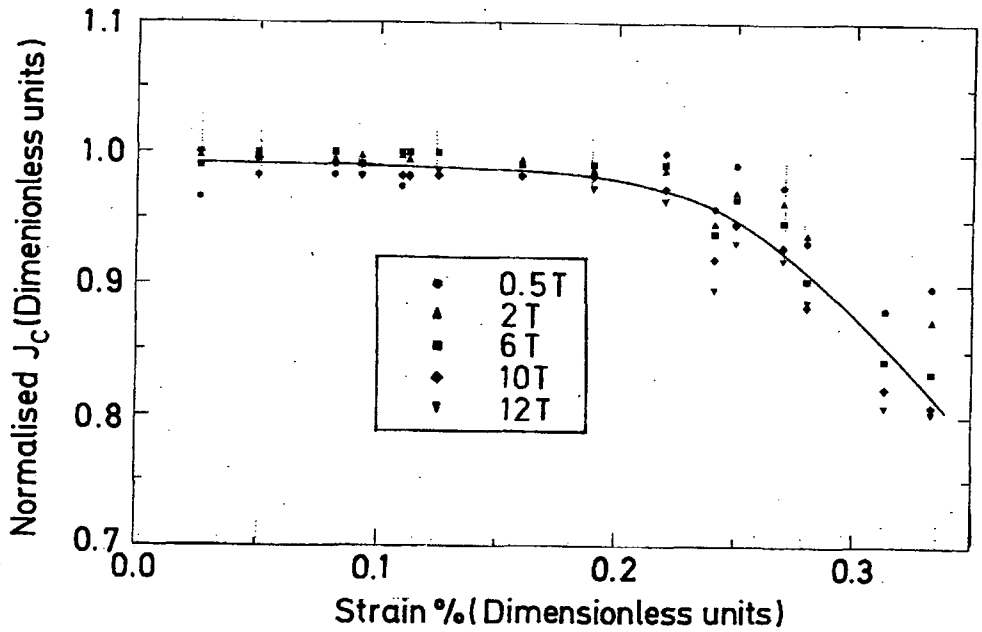

Figure 6.30: Normalised J_c versus strain for ascending fields(sample 5).

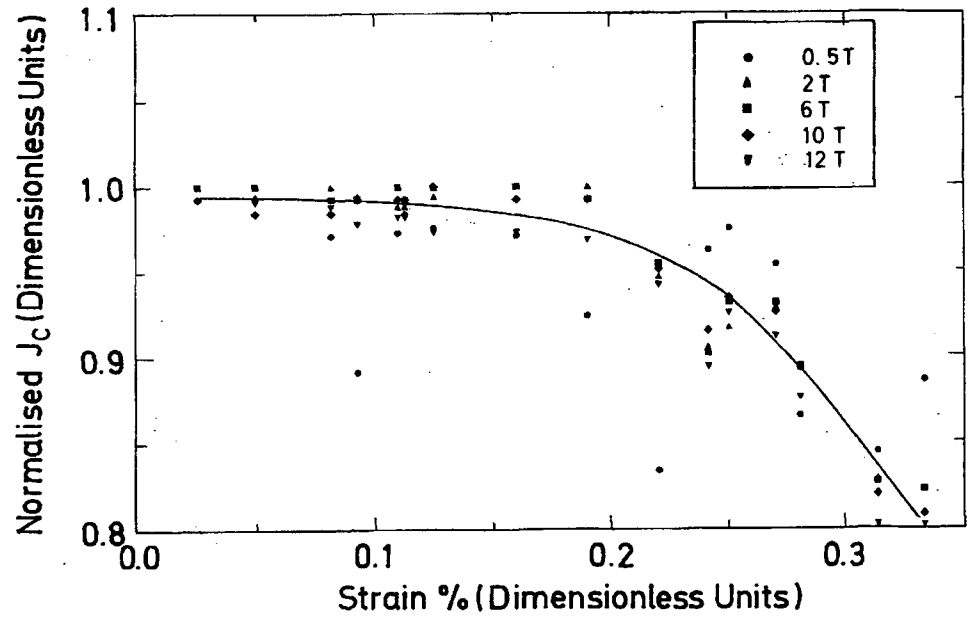

Figure 6.31: Normalised J_c versus strain for descending fields (sample 5).

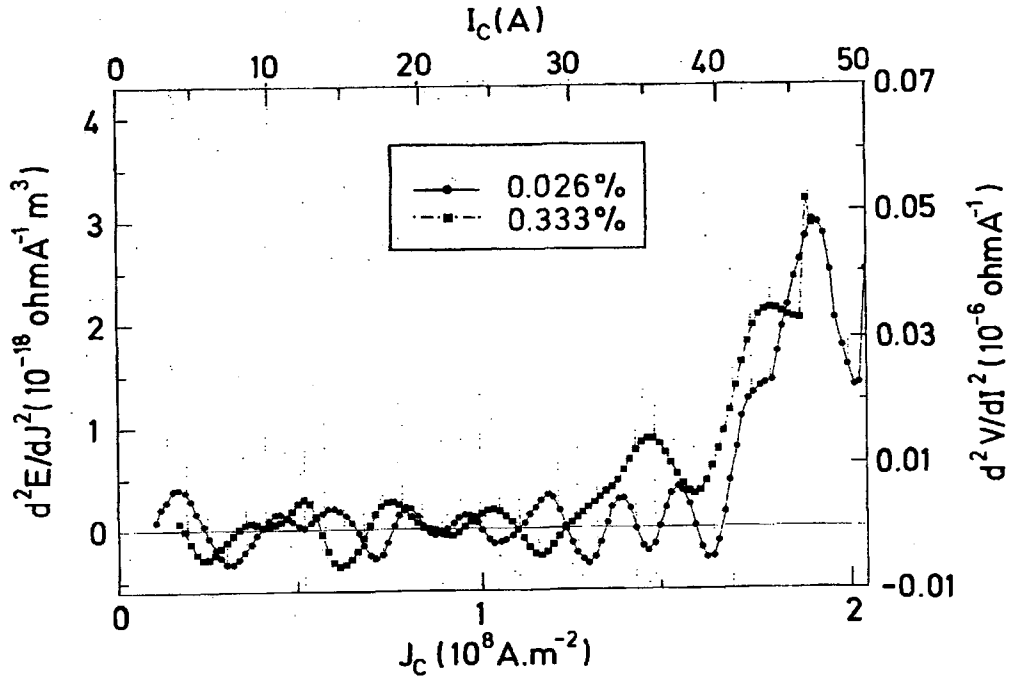

Figure 6.32: The critical current distribution at 6 T for two different strains (sample 5).

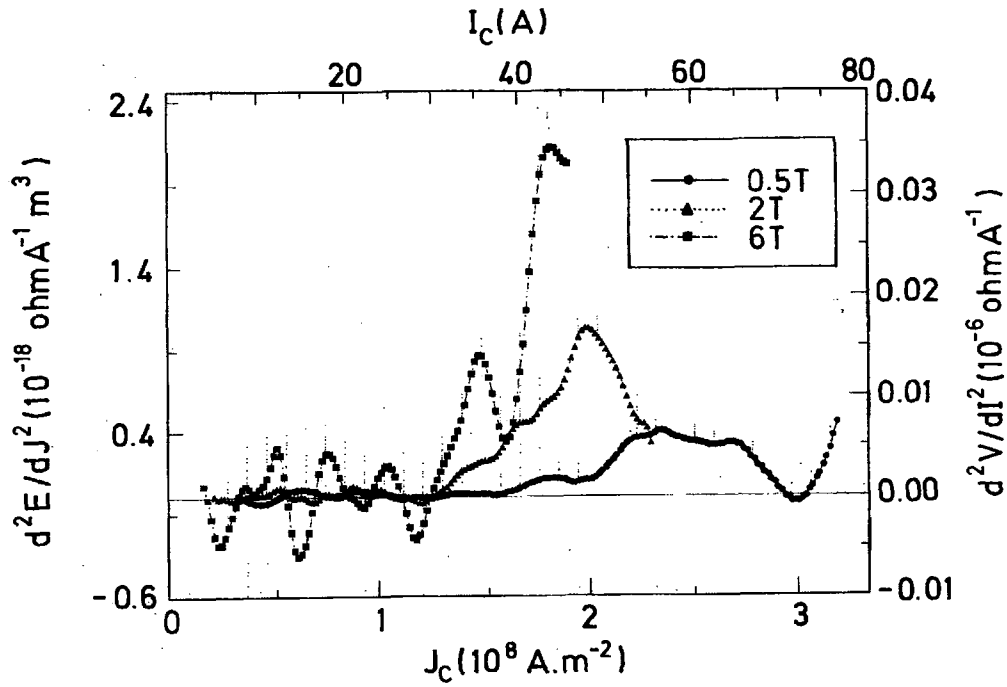

Figure 6.33: The critical current distribution at 0.333% strain (sample 5).

between 0.18%-0.25% strain. Sekine et al showed that for BiSCCO(2223)/Ag sheathed multifilamentary tape J_C degradation starts below 0.1%[5]. Sekine also showed that at about 0.08% strain J_C drops rapidly with increasing strain. He suggested that the onset of decreasing J_C with the onset of yielding in the sample. The degradation is irreversible which further suggests that a correlation between mechanical deformation and degradation of J_C exists.

Yau and Saviddes showed that the onset of J_C degradation is between 0.3%-0.5% strains for a BiSCCO(2223) monofilament tape and about 1.5% for a 49-filament tape[6]. Sato, Zhang and Yau showed that for BiSCCO(2223)/Ag the strain tolerance can be increased by using multifilamentary configurations[7,8,9]. For BiSCCO(2223) monofilamentary tapes with a filament thickness of approximately 20 μm, cracks start to occur at a strain value of about 0.2%[7]. For multifilamentary BiSCCO(2223) tapes with filament thickness less than 5 μm, cracks occur at about 1% strain.

Keβler et al showed that the use of dispersion-hardened AgMn instead of pure Ag as matrix material leads to an improvement of J_C versus strain properties of BiSSCO(2223) tapes. The stepwise degradation of J_C shows that the mechanism responsible for this type of behaviour is attributed to the formation of cracks in the filaments which is statistically distributed in the tape section[4]. Keβler also showed that for two sections of the same tape the onset of J_C degradation occurs at two different strains. This may be attributed to the inhomogeneity of the sample.

Otto et al showed that the gradual decrease in the critical current beyond the critical strain in the tensile measurements suggests that the superconducting filaments are damaged nonuniformly by applied strain, with some filaments remaining intact or partially intact up to a much larger strain[3]. He also showed that voids are formed at the ends of the sheared grains as the grains slide past each other when strain is applied. Another method to improve the strain tolerance of the BiSCCO tapes is to coprocess the Bi powder compound with Ag powder to provide a ductile matrix within the superconductor core. The Ag matrix acts a crack arrestor and relieves some of the stress[10].

Kovac et al showed the interesting effect of critical current recovery in the Ag-sheathed BiSCCO(2223) tapes after bending and straightening[11]. The effect is explained by compression of the BiSCCO(2223) cores from the Ag-sheath after cooling down. When the tape is bent and then straightened the contacts between grains are disturbed. The compression causes gliding of the BiSCCO grains and thus the recovery of these contacts.

For the BiSCCO tapes, unlike Nb_3Sn, there is no increase in J_C at low strains. This may indicate that the differential thermal contraction between the Ag matrix and the superconducting material does not play a large role[5]. However, Keβler showed that the filament pre-compression for pure Ag-sheath is about 0.04-0.05% and for the AgMg sheath is about 0.12-0.15%[4]. Richens et al suggested that the flat region before J_C degradation is due to the thermal pre-strain in the superconductor[12].

The hysteresis observed in the J_C versus B for ascending and descending fields may be attributed to weak-links between the superconducting grains. Noto et al also pointed out that hysteresis of J_C with increasing and decreasing fields is due to trapped flux in the superconducting grains[13]. Sato et al showed that J_C for descending fields are higher than for ascending fields and the hysteresis decreases as the magnetic field increases[7]. The magnitudes of the hysteresis at low fields at 4.2 K varies between about 20% to 50%. The magnitudes of the hysteresis can be lowered by improving the grain boundary characteristics of the superconductor.

Babic et al suggested that the distribution of the grain size leads to a similar distribution of inter-grain junctions, resulting in the observed critical current distribution[14]. The appearance of the double peaks may be attributed to inter-grain J_C and intra-grain J_C[15]. The inter-grain J_C has a strong field dependence and the intra-grain J_C has a small field dependence. Babic also suggested that the critical current may redistribute to 'stronger' inter-grain junctions within the superconductor. This may explain the change in shape of the critical current distribution when there is change in strain and magnetic field. ten Haken showed that the critical current distribution for a BiSCCO(2212) at low strains is broader than at high strains[16]. The critical current distribution obtained by ten

Haken does not show any secondary peaks. This is in contrast to the results obtained in our experiments. At higher strains secondary peaks appear and the distribution is much broader. The appearance of secondary peaks suggests that these peaks are more susceptible to strain.

The critical current distribution may be used to determine the intrinsic J_C of a sample. Figure 6.13 shows that there is a high current peak at low strain. This high current peak does not shift to lower J_C when strain is increased, even though the height of this peak is lower than the height of the peak at low strain. The high current peak may be due to the undamaged regions of the tape, and hence be used to determine the intrinsic J_C of the sample. The low current peak may be due to the damaged parts of the sample. Thus if one is given a damaged sample, there is still a possibilty of determining the intrinsic J_C of the sample by investigating its critical current distribution. The critical current distribution method is also a useful tool in assessing the quality of the sample.

6.6 Conclusion

The effect of strain on the current densities has been measured on five short sections($\approx$ 9mm) of an Ag-sheathed BiSCCO(2223) tape. Measurements were done at 4.2 K and in magnetic fields up to 12 Tesla. Tensile strain was applied on samples 1, 2 and 3. Bending(compression and tension)strains were applied on sample 4 and 5. The following conclusions have been drawn:

a. J_C degradation starts to occur between 0.18%-0.25% strain. The decrease in J_C is attributed to crack formation in the superconducting filaments.

b. The hysteresis observed in the J_C versus B for ascending and descending fields may be attributed to weak-links between the superconducting grains. The magnitude of the hysteresis decreases as the applied field increases.

c. The appearance of secondary peaks may be attributed to inter-grain J_C (strong field dependence) and intra-grain J_C(small field dependence). Alternatively the

low current peak may be due to cracks and the high current peak may be due to undamaged regions.

d. When the applied field increases the peaks of the critical current distribution are shifted to lower J_C values.

e. Secondary peaks develop as strain is increased.

f. For a damaged sample the critical current distribution is broader. The appearance of two peaks suggests the presence of damaged and undamaged parts of the tape.

g. The double differential analysis is a useful tool to assess the quality of a sample. It can be used to find the J_C in undamaged regions.

The Ag-sheathed BiSCCO(2223) wires and tapes are the most promising for industrial applications operating at liquid nitrogen temperature. There is a world-wide effort to increase the strain tolerance of these materials and results have been encouraging.

References

1. Selvamanickam V, Bamberger C, Martin P M and Kroeger D M., *IEEE Trans. Appl. Supercond.* **5**(2) 1826 (1995).
2. Jones H and Jenkins R G., *Chapter 6 in High-Temperature Superconducting Materials Science and Engineering - New Concepts and Technology*; ed: Shi D(Pergamon,UK) p.393 (1994).
3. Otto A, Masur L J, Gannon J, Podtburg E, Daly D, Yurek G J and Malozemoff., *IEEE Trans. Appl. Supercond.* **3**(1) (1993).
4. Keβler J and Goldacker W., *EUCAS 1993-Applied Superconductivity Vol.1*, Ed. Freyhardt H C (DGM,1993) p. 213.
5. Sekine H, Schwartz J, Kuroda T, Maeda H and Numata K., *J. Appl. Phys.* **70**(3) (1991).
6. Yau J and Saviddes N., *Appl. Phys. Lett.* **65**(11) (1994).
7. Sato K, Hikata T, Mukai H, Ueyama M, Shibuta N, Kato T, Masuda T, Nagata M, Iwata K and Mitsui T., *IEEE Trans. Magn. MAG-27* **2** 1231 (1991).
8. Zhang H, Zhou E Y, Yu H G and Wu H., *IEEE Trans. Appl. Supercond.* **3**(1) (1993).
9 Yau J F K, Saviddes N and Sorrell C C., *Physica C* **266** 223 (1996).
10. Ekin J W, Finnemore D K, Li Q, Tenbrink J., *Appl. Phy. Lett.* **61**(7) 858 (1992).
11. Kovac P, Husek I and Cesnak L., *Supercond. Sci. Technol.* **7** 583 (1994).
12. Richens P E, Jones H, Von Cleemput M and Hampshire D P., *IEEE Trans. on Appl. Supercond.* **7**(2) 1315 (1997).
13. Noto K, Morita H, Watanabe K, Murakami Y, Obi Y, Fujimori H, Kobayashi N and Muto Y., *Jpn. J. Appl. Phys.* **26**(Suppl. 26-3) 1195 (1987).
14. Babic E, Prester M and Biskup N., *Solid State Comm.*, **77**(11) 849 (1991).
15. Seeber B, Cheggour N, Perenboom JAAJ and Grill R., *Physica C* **234** 343 (1994).
16. ten Haken B ., *PhD Thesis*, University of Twente, Netherlands (1994).

Chapter 7

Transport critical current measurements of a HIP'ed and unHIP'ed bulk samples of $PbMo_6S_8$ in magnetic fields up to 12 Tesla

7.1 Introduction

The Chevrel phase $PbMo_6S_8$ (PMS) is a potential candidate for the next generation of high field applications because its upper critical field can exceed 50 T at 4.2 K [1]. Magnetic studies on bulk PMS samples have shown that the critical current density of PMS can be markedly increased by fabricating the material using a hot isostatic press (HIP) [2,3].

In this work, transport critical current measurements (J_C) are presented on a HIP'ed bulk sample of $PbMo_6S_8$ as a function of magnetic field and temperature and compared to those of bulk PMS prepared at ambient pressure (unHIP'ed). These data are used to calculate the functional form of the volume pinning force (F_p) for each sample from J_C and the effective upper critical field B^*_{C2}. We determine the effect of HIP'ing PMS on J_C in high magnetic fields.

Section 7.2 describes a detailed outline for preparing unHIP'ed and HIP'ed samples. Section 7.3 explains the experimental techniques used to measure the critical currents. The results of these measurements are presented in section 7.4. In section 7.5 the experimental data is analysed and the values of the upper critical fields (B^*_{C2}) are calculated. Section 7.6 discusses the findings and the values of B^*_{C2} obtained are compared with magnetic measurements. Section 7.7 finishes the chapter with a summary that includes the main conclusions.

7.2 Sample Fabrication

The HIP'ed $PbMo_6S_8$ sample preparation involved a two step reaction procedure in a controlled environment. Initially 10 g of the starting materials, Pb (99.9999% purity), Mo (99.95% purity, 4-8 μm grain size) and S (99.999% purity) were mixed in a glove box in the atomic ratio 1:6:8. The material was then sealed under vacuum in a pre-cleaned silica tube. The tube was then heat treated at 450 °C for 4 hours in an Argon atmosphere. The furnace temperature was slowly increased to 650 °C at a rate of 33° $C.hr^{-1}$ and held constant at this temperature for 8 hours. After this the sample was air quenched by allowing it to cool to room temperature. Before the next heat treatment, the sample was ground thoroughly in a glove box using a mortar and pestle. The sample was then pressed into 10 mm diameter pellets and sealed in a pre-cleaned silica tube under vacuum. This procedure was done in a glove box to ensure that the sample was not exposed to oxygen which can degrade its superconducting properties[4,5,6]. The oxygen level in the glove box can be kept at < 5 ppm and the moisture level at < 10 ppm. The sample was given further heat treatment at 1000 °C for 44 hours in Argon atmosphere to form the $PbMo_6S_8$ phase.

The sample was then HIP'ed for several hours as follows[7]: The sintered sample was again ground into powder in the glove box and pressed under vacuum into pellets. The pellets were then wrapped with molybdenum (Mo) foil (99.95% purity, 0.25 mm thick) and sealed in a stainless steel tube under vacuum using hot-spot welding. Wrapping the sample with Mo foil eliminates the probabilty of the sample reacting with the container. The sample was then HIP'ed at 1300 bar for 8 hours at 900 °C. The HIP'ed sample was then extracted from the Mo foil and cut to the desired shape.

Figure 7.1 shows the x-ray diffraction pattern of the unHIP'ed PMS. It indicates that the samples are predominantly single phase where all the major peaks can be attributed to the PMS. HIPing similarly prepared samples but HIP'ed at 800°C has been shown to increase the density of the material by more than 20%, ie. from about 70% dense in the unHIP'ed sample to more than 90% in the HIP'ed sample[8].

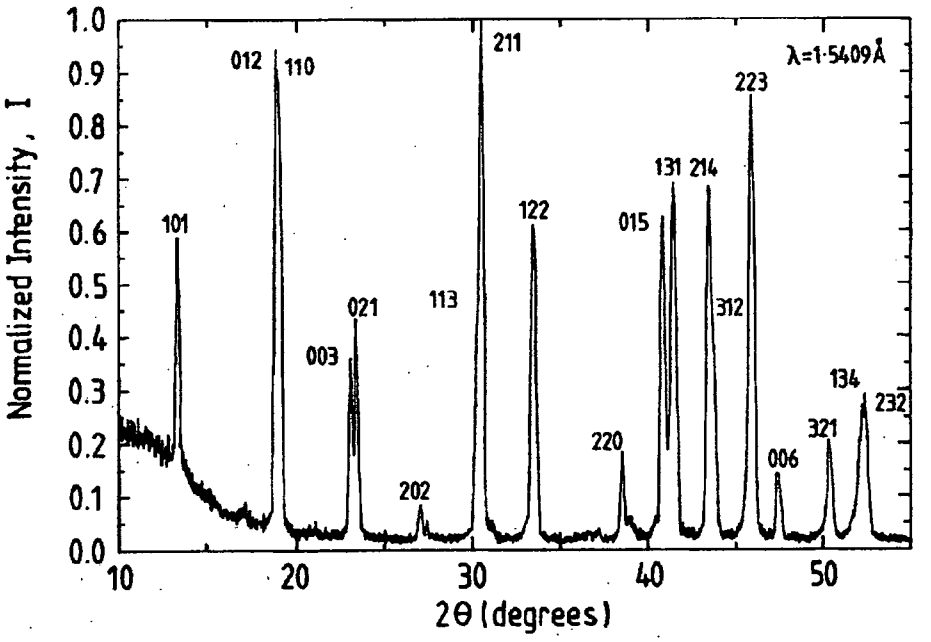

Figure 7.1: The x-ray diffraction pattern for the unHIPed sample of $PbMo_6S_8$.

7.3 J_C measurements

The samples were carefully cut into rectangular shapes with dimensions 6.0 x 2.4 x 0.5 mm^3 (unHIP'ed) and 6.0 x 1.9 x 0.8 mm^3 (HIP'ed). The unHIP'ed sample was very brittle compared to the HIP'ed sample, so extra care was taken when cutting the unHIP'ed sample. These samples were trimmed using a 240 grit AL/OX cloth roll (glasspaper). Trimming is made easier by using a pair of tweezers. Current contacts on both samples were made as follows: First, silver paint was deposited on both ends of a sample. Once the silver paint has dried to room temperature it was annealed in a furnace for about 2 hours at 50° C. The sample was then taken out of the furnace and mounted on a small Tufnol(Carp Brand) board for mechanical protection. After that the sample was mounted on the sample bed of a J(B,T) probe[9]. Current contacts were made by soldering the ends of the sample to the probe's current leads using Pb/Sn/Ag solder. Silver paint was also used for voltage contacts. The distance between the voltage taps is 2 mm.

The four terminal measurements were made using a J(B,T) probe that can measure critical current densities as a function of temperature in high magnetic fields to an accuracy of ±70 mK at 10 K [9,10]. Figure 7.2 shows the experimental set-up for the measurements. The set-up is similar to that described in chapter 4 except that here the J(B,ϵ) probe is replaced by a J(B,T) probe. Here the temperature is controlled by a Lakeshore DRC 91A Temperature Controller. Before the voltage-current(V-I) traces were taken a resistance versus temperature measurement shows that the T_C for unHIP'ed and HIP'ed samples were about 13.5 K and 13 K, respectively. This was done by passing a constant 100mA current through the sample and increasing the temperature until a voltage was detected. For the HIP'ed sample, data were taken from 8.7 K up to 12.9 K and for the unHIP'ed sample, from 5 K up to 13 K, in magnetic fields up to 12 T. The critical current densities were measured at a 2μV (10 μVcm^{-1}) criteria. In all measurements, the magnetic field was orthogonal to the transport current.

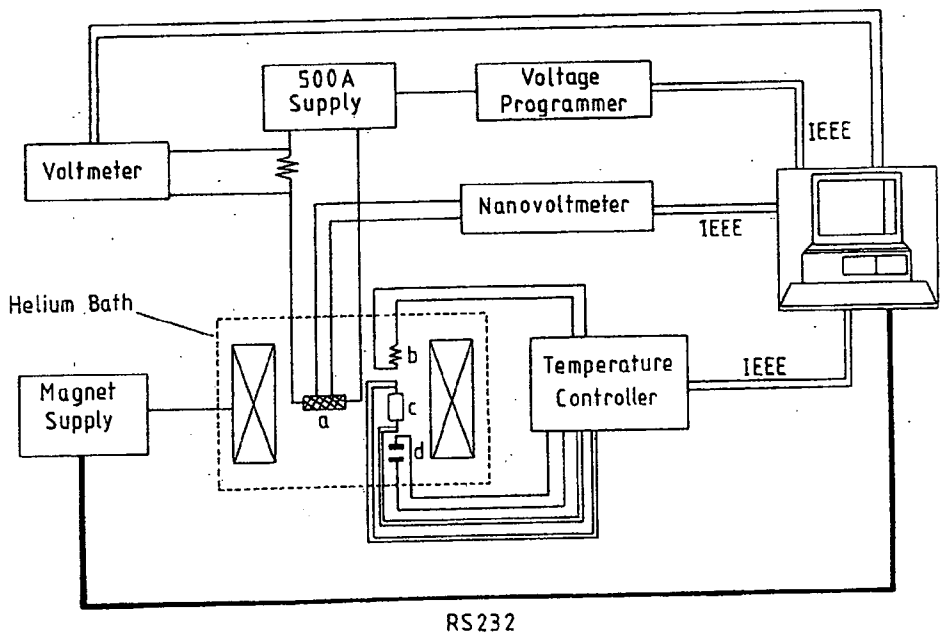

Figure 7.2: The experimental set-up for the J(B,T) measurements.
(a: sample; b: 25 Watt heater; c: RhFe resistance thermometer;
d: Capacitance thermometer)

7.4 Results

At each temperature, as the field is decreased, J_C increases much more rapidly for the HIP'ed sample than the unHIP'ed sample. Figure 7.3 is an example of an E-J characteristics of the HIP'ed sample at 10.5 K for three different magnetic fields. The baseline is rather flat and has a low noise level which demonstrates sufficiently low contact resistances have been achieved for good temperature control over the range of J_C investigated. Figures 7.4 and 7.5 show the J_C data for both samples. Figure 7.6 shows the effective upper critical field B^*_{C2} as a function of temperature for both samples. The B^*_{C2} curve of the unHIP'ed sample lies above that of the HIP'ed sample in this temperature range. On the same figure are magnetic and specific heat[11] data for a similarly prepared sample, HIP'ed at 800 °C. It can be seen that the B^*_{C2} curve of our sample lies close to the B_{irr} line from the magnetic measurements and significantly below the upper critical field data B_{C2}.

7.5 Analysis of the experimental data

The J_C characteristics are linear throughout most of the field range at each temperature in figures 7.3 and 7.4. The effective upper critical fields B^*_{C2} have been calculated at each temperature by linearly extrapolating J_C to zero. The pinning force F_p can then be represented by the relation

$$F_p=\alpha(B^*_{C2})^n(T)b(1-b) \qquad (7.1)$$

where $b=B/B^*_{C2}$ is the reduced magnetic field and $n=1.6 \pm 0.06$ and 1.67 ± 0.06 for the HIP'ed and unHIP'ed sample respectively. The index n which gives the temperature dependence was calculated from a plot of $\log(\partial J_C/\partial B)$ against $\log(B^*_{C2})$. The values of α, a constant depending on the sample microstructure, was found to be $6.0\times10^5\,Am^{-2}T^{-0.6}$ and $0.9\times10^5 Am^{-2}T^{-0.67}$ for the HIP'ed and unHIP'ed sample, respectively.

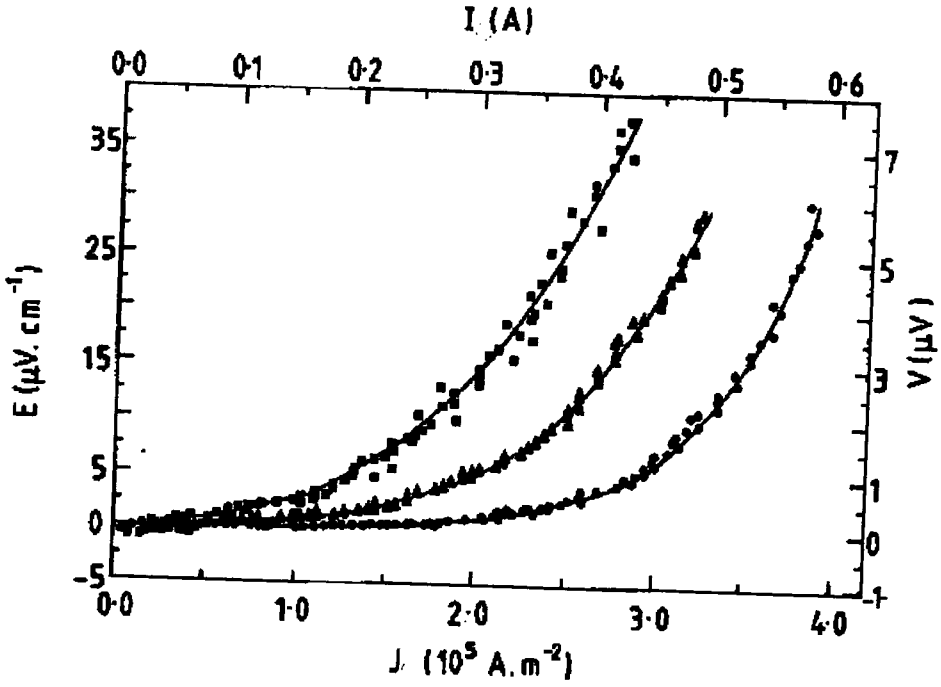

Figure 7.3: The E-J characteristics for the HIP'ed sample at 10.5 K in magnetic fields of (from right to left): 3.6 T, 3.8 T and 4 T.

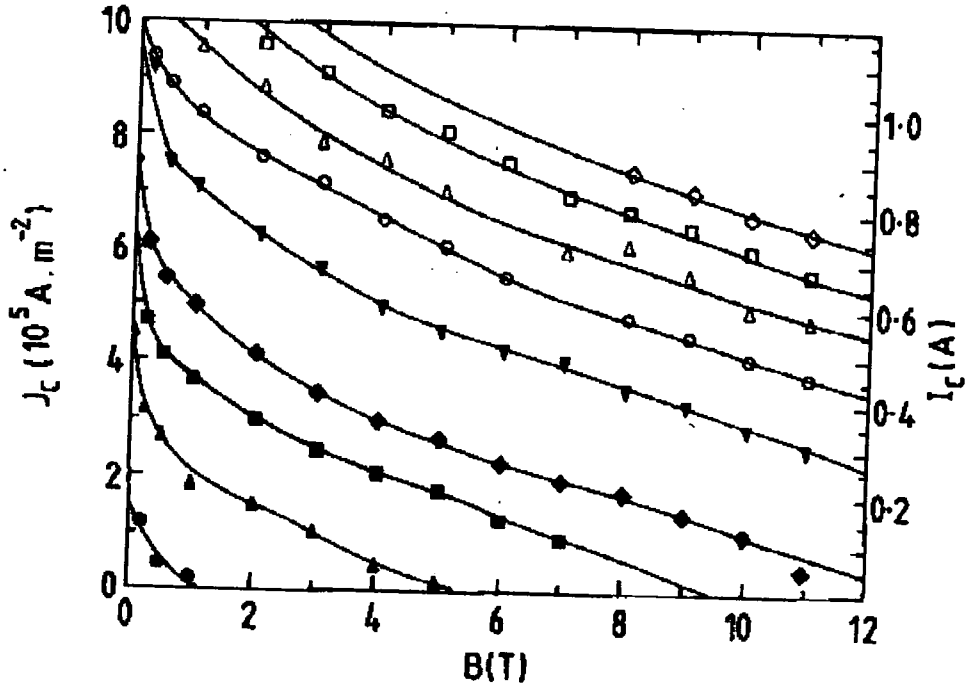

Figure 7.4: J_c of the unHIP'ed sample as a function of field and temperature (from top to bottom): 5, 6, 7, 8, 9, 10.5, 11, 12, 13 K)

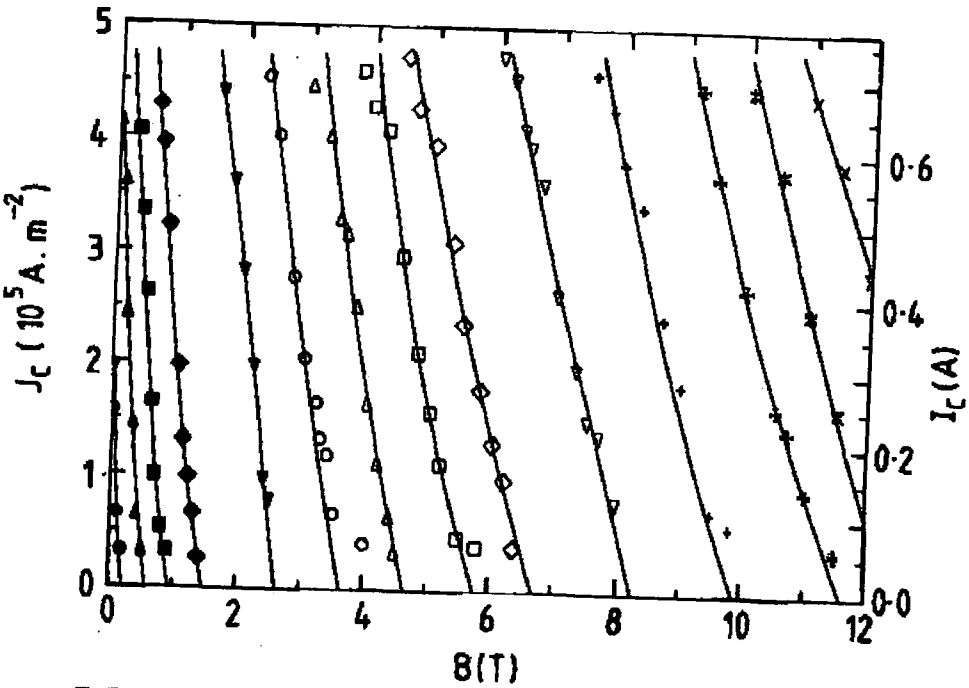

Figure 7.5: J_c of the HIP'ed sample as a function of field and temperature (right to left: 8.7, 8.9, 9.1, 9.9, 10.2, 10.5, 11, 11.4, 11.7, 12, 12.3, 12.5, 12.7 and 12.9 K)

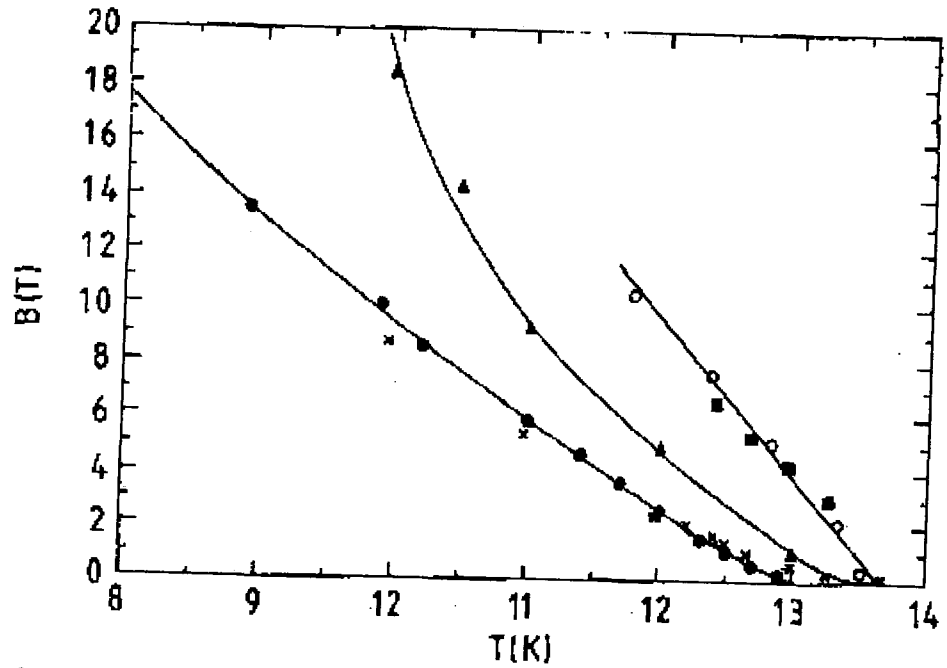

Figure 7.6: The B^*_{c2} line for the HIP'ed (●) and unHIP'ed (▲) sample. (HIP'ed: ×: B_{irr}, ■:B_{c2}-magnetic measurements[3]; ○: B_{c2}- specific heat measurements[5])

7.6 Discussion

The functional form of F_P, more specifically the reduced field dependence and the values of n, are similar for both samples. This suggests that the mechanism that determines J_C in both samples is the same. However the value of α, and hence the magnitude of J_C for the HIP'ed sample is larger by a factor of ≈ 7 than that of the unHIP'ed sample. We expect that the primary reason for the improvement in the HIP'ed sample is due to an increase in the density and the contact area between the grains, although the results are also consistent with stronger pinning. These results agree with complementary magnetic data on similar samples[8].

In contrast to most transport measurements on wires that show a Kramer dependence, we have found a functional form for F_P that is most commonly found in systems where core pinning dominates [12]. The transport measurements presented here are very sensitive to the intergranular current density. This may possibly be due to the regions of contact between the grains in these bulk samples are off-stoichiometric or highly defective.

The comparison between these transport measurements and the magnetic and specific heat data support the conclusion that the irreversibility line of bulk HIP'ed and unHIP'ed PMS is markedly less than the upper critical field. The similarity between the B^*_{C2} curve from the transport measurements and the B_{irr} line from magnetic measurements suggests that the difference in HIP'ing temperature does not significantly affect these parameters. We attribute the lower values of B^*_{C2} and T_C found in the HIP'ed sample to some oxygen contamination during processing [5].

Most work to determine the J_C on bulk samples comes from magnetic measurements which are sensitive to intragranular J_C. We have completed transport current measurements which are particularly sensitive to intergranular transport J_C.

7.7 Summary

Transport critical current measurements have been made on bulk $PbMo_6S_8$ (PMS) samples from 5 K up to T_c in magnetic fields up to 12 T. The properties of hot isostatically pressed (HIP'ed) PMS fabricated at $1.3x10^8$ $N.m^{-2}$(1300 bar) at 900°C are compared with those of PMS fabricated at ambient pressure.

We have found that the critical current density increased by a factor of ≈7 when the sample was hot isostatically pressed.

Both samples can be described by a single functional form $F_p = \alpha B^n_{c2}(T)b(1-b)$ which suggests that the same pinning mechanism determines J_c. For the HIP'ed sample the pinning force F_P can be represented as:

$$F_P = 6.0x10^5(B^*_{C2})^{1.6}(T)b(1-b) \tag{7.2}$$

The expression for the unHIP'ed is then :

$$F_P = 0.9x10^5(B^*_{C2})^{1.67}b(1-b) \tag{7.3}$$

The B^*_{c2} for the HIP'ed sample lies close to the irreversibility line derived from complementary magnetic measurements on a HIP'ed sample. However it is significantly lower than the unHIP'ed sample over the same temperature range.

The B^*_{c2} values for the HIP'ed sample extrapolate to above 30 T at 4.2 K . Our results demonstrate that the critical current density of HIP'ed $PbMo_6S_8$ in high magnetic fields is sufficiently large that this material is a potential candidate for the next generation of high field applications operating in magnetic fields up above 25 Tesla.

References

1. Odermatt R, Fisher Ø , Jones H and Bongi G., *J. Phys. C: Solid State Phys* **7** L13 (1974).
2. Alekseevskii N E, Dobrovol'skii N M, Eckert D and Tsebro V I., *J. Low Temp. Phys.* **29** 565 (1977).
3. Zheng D N, Ramsbottom H D and Hampshire D P., *Phys. Rev B* **52** (17) 12931 (1995).
4. Capone II D W, Guertin R P, Foner S, Hinks D Gand Li H C., *Phys. Rev. B* **29**(11) 6375 (1984).
5. Foner S, McNiff Jr. E J and Hinks D J., *Phys. Rev. B* **31** 6108 (1985).
6. Hinks D G, Jorgensen J D and Li H C., *Phys. Rev. Lett.* **51**(20) 1911 (1983).
7. Le Lay L, Willis T C and Larbalestier D C., *Appl. Phys. Lett.* **60**(6) 775 (1992).
8. Ramsbottom H D., *PhD Thesis University* of Durham U.K. (1996).
9. Friend C M and Hampshire D P., *J. Meas. Sci. Tech.* **6** 98 (1994).
10. Friend C F., *PhD Thesis* Hatfield College University of Durham U.K.(1994).
11. Ali S, Zheng D N and Hampshire D P., *Proc. EUCAS 1995 - Applied Superconductivity* **Vol 1**, ed. Dew-Hughes D., Edinburgh (1995).
12. Dew-Hughes D ., *Philos. Mag.* **30** 293 (1974).

Chapter 8

Transport Critical Current Measurements of HIP'ed Gd-doped Bulk Samples of $PbMo_6S_8$ in Magnetic Fields Up to 14 Tesla

8.1 Introduction

In chapter 7 it was shown that HIPping can increase the critical current density, J_C of $PbMo_6S_8$(PMS). Critical current density that exceeds 10^8 Am^{-2} at 20 Tesla (1.9 K) have been reported on HIP'ed $PbMo_6S_8$ wires[1]. This relatively high J_C value, in addition to the high B_{C2} value, demonstrates that this material is a promising candidate for high field applications. Fisher et. al discovered that doping $PbMo_6S_8$ with Gadolinium(Gd) increases T_C, dB_{C2}/dT and B_{C2}[2,3]. The B_{C2} of Gd-doped PMS extrapolates to about 60 Tesla at 0 K.

In this study, transport critical current measurements have been made on the HIP'ed $Pb_{1-x}Gd_xMo_6S_8$ bulk samples. The values of x (0, 0.1, 0.2 and 0.3) represents the nominal concentration of Gd. Data obtained are used to calculate the irreversibility field(B_{irr}) and the functional form of the volume pinning force(F_P). Complementary resistivity and ac susceptibility measurements have also been made on these samples.

Section 8.2 describes sample fabrication. Section 8.3 gives an outline of the experimental techniques for J_C measurements. In this section current contacts for bulk PMS were improved compared to those used on samples in chapter 7. The J_C results are presented in section 8.4. Section 8.5 is devoted to the analysis of the experimental data. The B_{irr} data from transport measurements are compared to those obtained from specific heat(C_P) and vibrating sample magnetometer(VSM) measurements. The findings are discussed in section 8.6. Section 8.7 concludes this chapter.

8.2 Sample Fabrication

The HIP'ed $Pb_{1-x}Gd_xMo_6S_8$ samples prepared involved a two step reaction procedure in a controlled environment. The starting materials, pure elements of Pb, Gd, Mo and S were mixed in the atomic ratio 1-x:x:6:8. The samples were pressed in a glove box under Argon to reduce contamination. The samples were heat treated in Argon atmosphere at 450°C for 4 hours, then at 650°C for 8 hours. The samples were then ground, pressed into discs and heat treated at 1000°C for 44 hours in Argon atmosphere to form the $Pb_{1-x}Gd_xMo_6S_8$ phase. Finally the samples were HIP'ed at 2×10^8 $N.m^{-2}$ (2000 bar) for 8 hours at 800°C. The detailed procedure for sample fabrication has already been described in chapter 7.

X-ray diffraction pattern on a $Pb_{0.7}Gd_{0.3}Mo_6S_8$ shows that most of the peaks can be identified as PMS. Other peaks are identified as MoS_2, Mo_2S_3 and small traces of Gd_2S_3[4]. TEM measurements on $Pb_{0.9}Gd_{0.1}Mo_6S_8$ and $Pb_{0.7}Gd_{0.3}Mo_6S_8$ show that the grain sizes are 0.30-0.93μm and 0.24-1.02 μm, respectively[5]. The grain boundaries appear to be clean and narrow. The distribution of Gd is not uniform and is clustered in small areas as Gd_2S_3[6].

8.3 Experimental Technique

The samples were carefully cut into rectangular shapes using a 240 grit AL/OX clothroll(glasspaper). The cross-sectional areas of the samples are given in Table 8.1:

Sample	Cross- sectional area (mm^2)
$PbMo_6S_8$	1.9 x 0.5
$Pb_{0.9}Gd_{0.1}Mo_6S_8$	2.2 x 0.7
$Pb_{0.8}Gd_{0.2}Mo_6S_8$	1.0 x 0.5
$Pb_{0.7}Gd_{0.3}Mo_6S_8$	1.0 x 0.5

Table 8.1: The cross-sectional area for each sample.

The length of each sample is about 6-7 mm. The high current contacts on the samples were made by soldering Indium at each end of the sample. Soldering was done by using a Fibre-Sonics Ultrasonic Soldering System. The reasons for using ultrasonic soldering are:

a. No flux is needed when applying the solder. The ultrasonic energy is able to remove surface oxides, grease, dirt and other contaminants from area being soldered.

b. The solder can be forced into tiny pores and crevices, thus giving better contacts. A short current lead (1.0 mm dia. Cu wire) is then soldered to the ends of the sample.

Silver paint is used for voltage contacts. The distance between the voltage contacts is about 1.5 mm. Each sample is then mounted on a piece of Tufnol(Carp Brand) board (~ 10 x 10 x 10 mm^3) using GE varnish for mechanical strength.

Initial tests show that when transport currents pass through the samples in the presence of magnetic fields the samples cracked easily and were damaged with the Lorentz force. The samples were then covered with Stycast epoxy (type 2850 FT Grace Speciality Polymers) to structurally support the samples. The Stycast epoxy was allowed to dry at room temperature for at least 24 hours before mounting on the probe. The purpose for using Stycast epoxy was to prevent the samples from damage at high fields because of the Lorentz force. The four terminal measurements were made using the $J_C(B,T)$[7]. The magnetic fields were applied orthogonal to the transport current. V-I traces were taken from 0 T up to 14 T and from 9.3 K up to T_C. This time , with Stycast on, the samples quenched when transport current was above 10 A. So the transport current was limited up to 10 A to avoid quenching and the possibility of damaging the samples. The pressure inside the probe was maintained at less than 20 Torr. The critical current density, J_C was measured at 0.5 μV(3.3 μVcm^{-1}).

Resistivity and ac susceptibility measurements were also made using a home-made probe that simultaneously measures resistivity and ac susceptibility. Measurements were taken

from 0 T up to 12 T. The T_C for each sample is determined from these measurements.

8.4 Results

Figure 8.1 is an example of a V-I characteristics from measurements made on the $Pb_{0.8}Gd_{0.2}Mo_6S_8$ sample at 11 K with an applied field of 5, 6 and 8 T. The baseline is rather flat and the noise level is about ±65 nV. This shows that sufficiently low contact resistances have been achieved for good temperature control over the range of J_C investigated. The noise on these traces may have originated from the sample current supply. The slope(dE/dJ) of the curve above J_C at 5 T and 6 T is steeper than that at 8 T. The shape of the curve also indicates strong pinning.

Figures 8.2- 8.5 show the J_C data as a function of field and temperature for four different doping levels. At each temperature, as the field is increased, J_C decreases. The drop in J_C is slower at higher fields. For example, at 11 K and 8 T the J_C values are as follows (Table 8.2):

Sample	J_C (Am^{-2})
$PbMo_6S_8$	2.3×10^6
$Pb_{0.9}Gd_{0.1}Mo_6S_8$	3.8×10^6
$Pb_{0.8}Gd_{0.2}Mo_6S_8$	4.1×10^6
$Pb_{0.7}Gd_{0.3}Mo_6S_8$	1.0×10^6

Table 8.2: J_C values at 11K and 8 T

The value of J_C for x=0.3 is approximately half that for the undoped sample(x=0). This result agrees with that obtained from magnetic measurements [4]. The J_C value at 10.2 K and 5 T for the $Pb_{0.7}Gd_{0.3}Mo_6S_8$ sample is about 0.2×10^8 Am^{-2}. The J_C value from magnetic measurements on a similar sample($Pb_{0.7}Gd_{0.3}Mo_6S_8$) at 10 K and 5 T is also about 0.2×10^8 Am^{-2}[4]. Table 8.2 also shows that there seems to be an optimum level of doping for J_C. The J_C value for x=0.2 is twice the value of J_C for the undoped

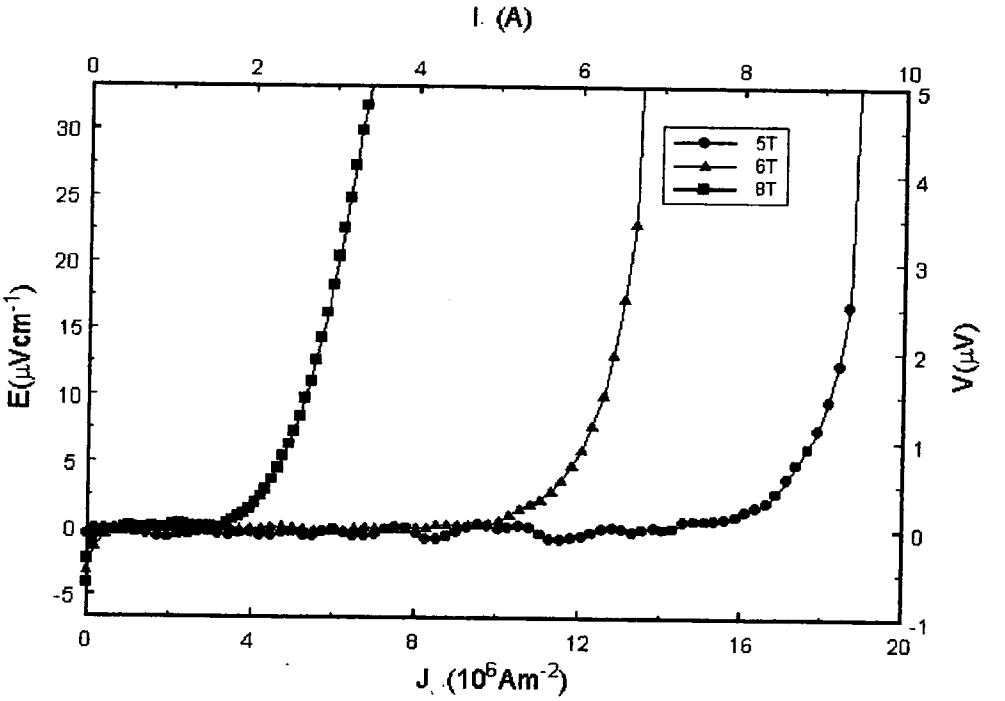

Figure 8.1: V-I characteristics of $Pb_{0.8}Gd_{0.2}Mo_6S_8$ at 11 K with an applied field of 5, 6 and 8 T.

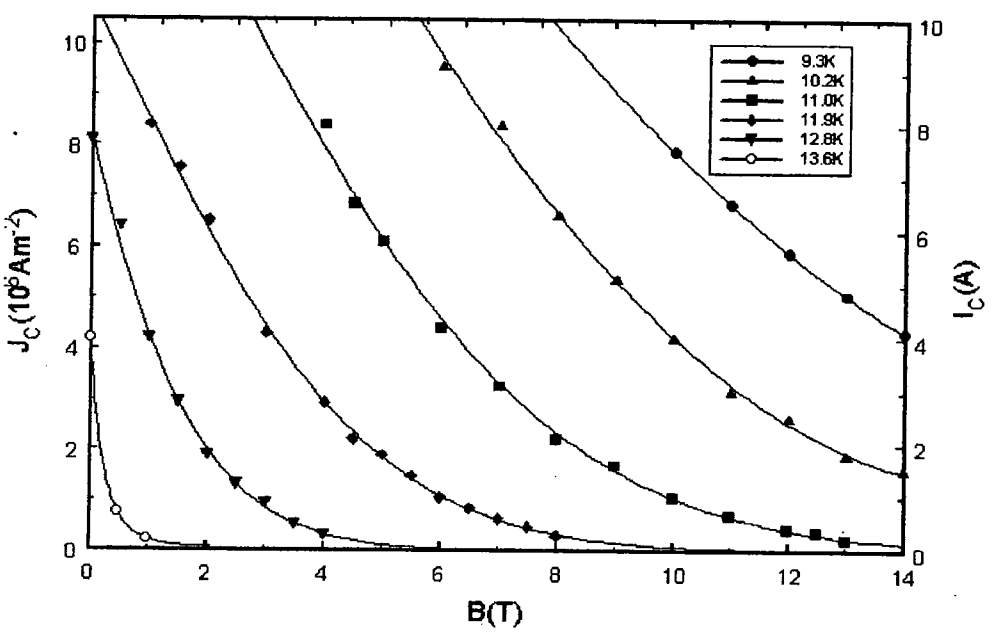

Figure 8.2: The critical current density of $PbMo_6S_8$ as a function of field and temperature.

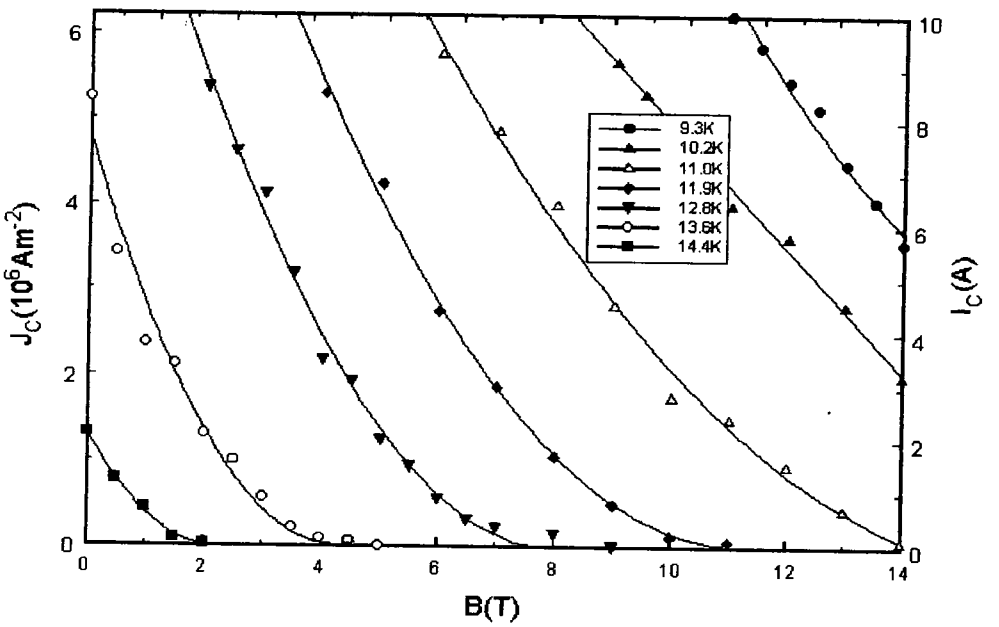

Figure 8.3: The critical current density of $Pb_{0.1}Gd_{0.9}Mo_6S_8$ as a function of field and temperature.

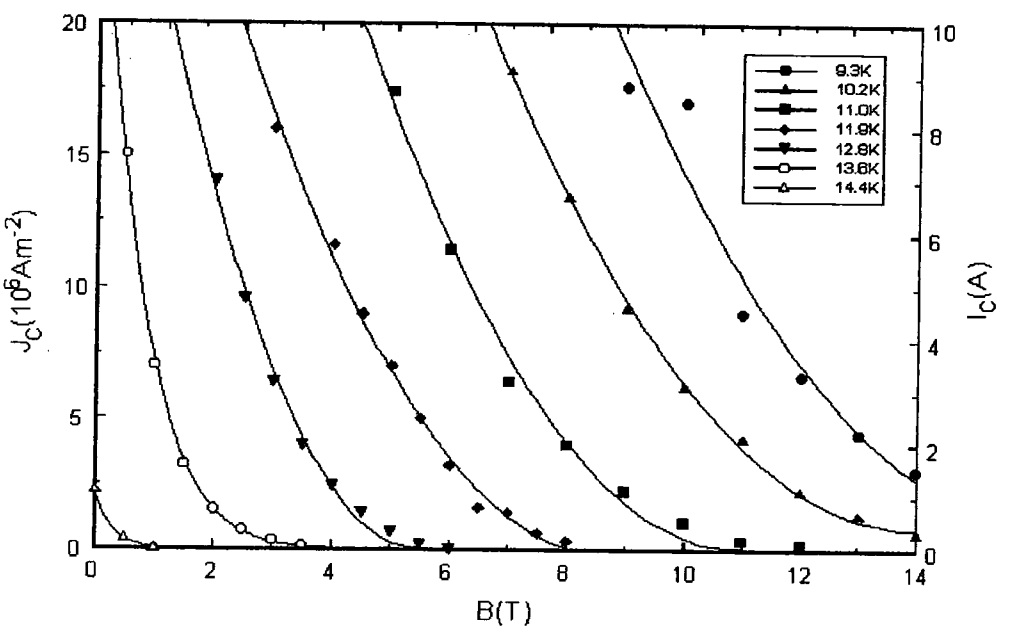

Figure 8.4: The critical current density of $Pb_{0.8}Gd_{0.2}Mo_6S_8$ as a function of field and temperature.

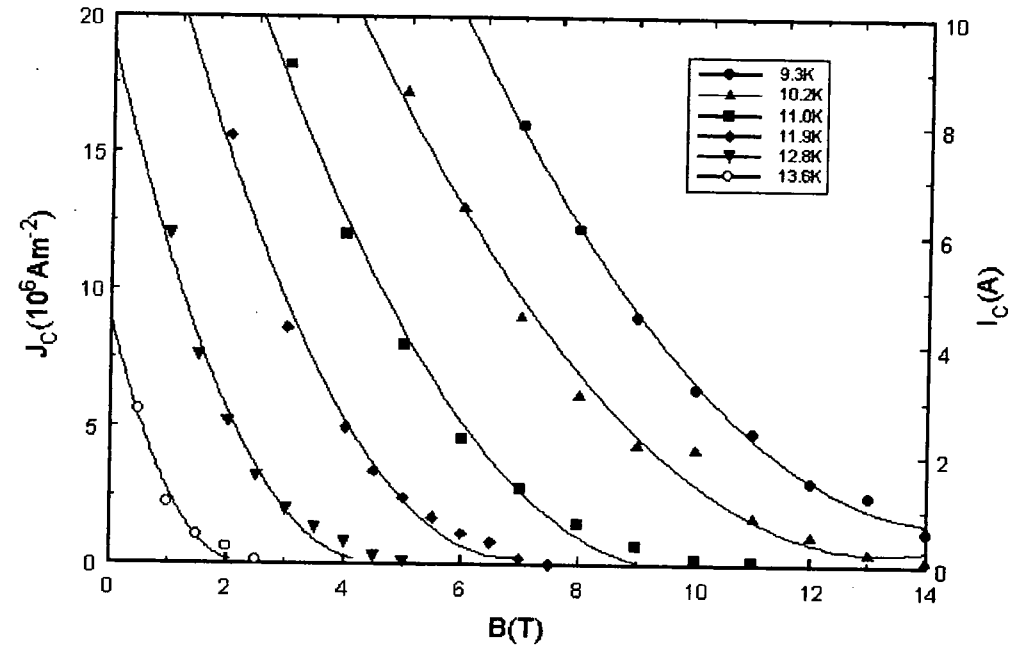

Figure 8.5: The critical current density of $Pb_{0.7}Gd_{0.3}Mo_6S_8$ as a function of field and temperature.

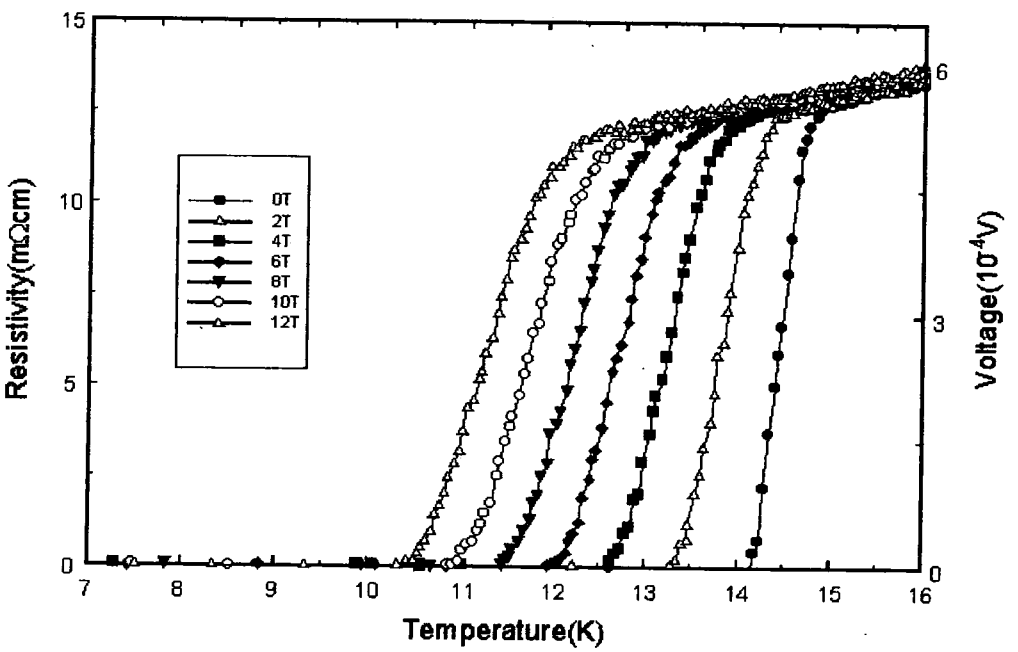

Figure 8.6a: The resistivity measurement for $Pb_{0.8}Gd_{0.2}Mo_6S_8$ sample.

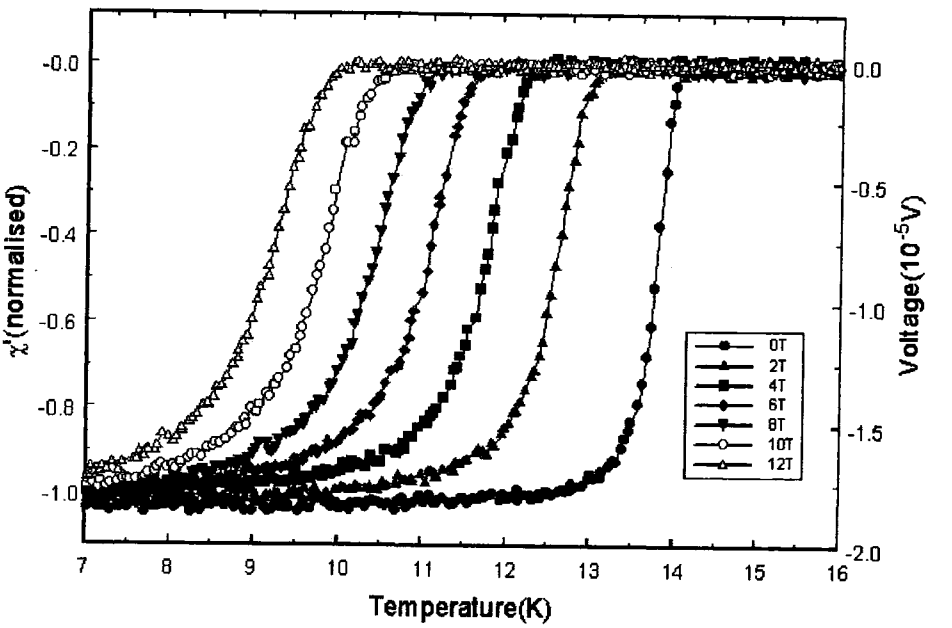

Figure 8.6b: The lossless component of the ac susceptibility measurement for $Pb_{0.8}Gd_{0.2}Mo_6S_8$ sample.

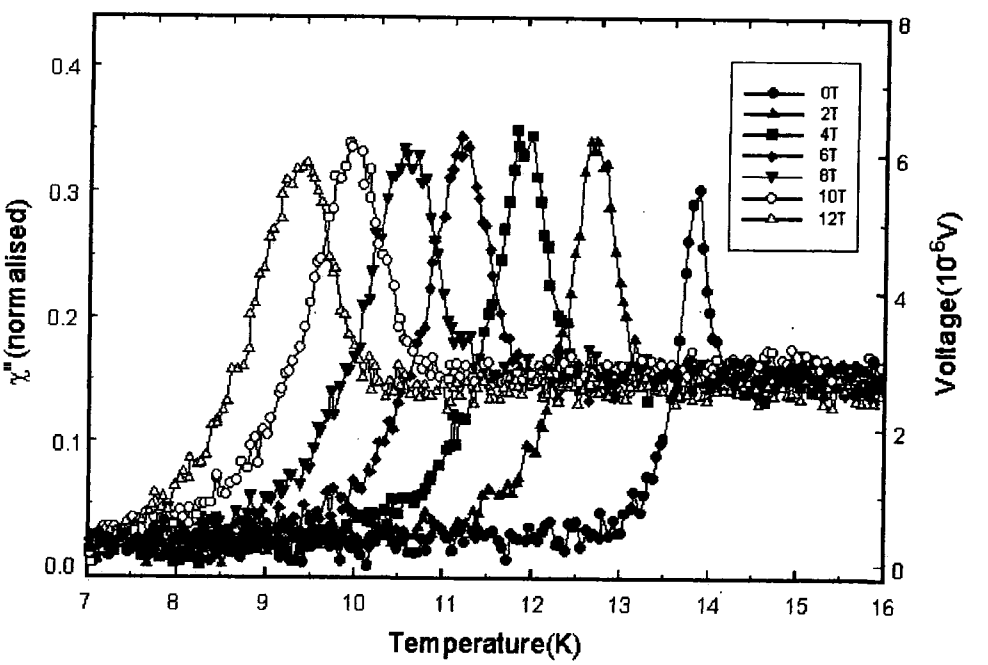

Figure 8.6c: The loss component of the ac susceptibility measurements for $Pb_{0.8}Gd_{0.2}Mo_6S_8$ sample.

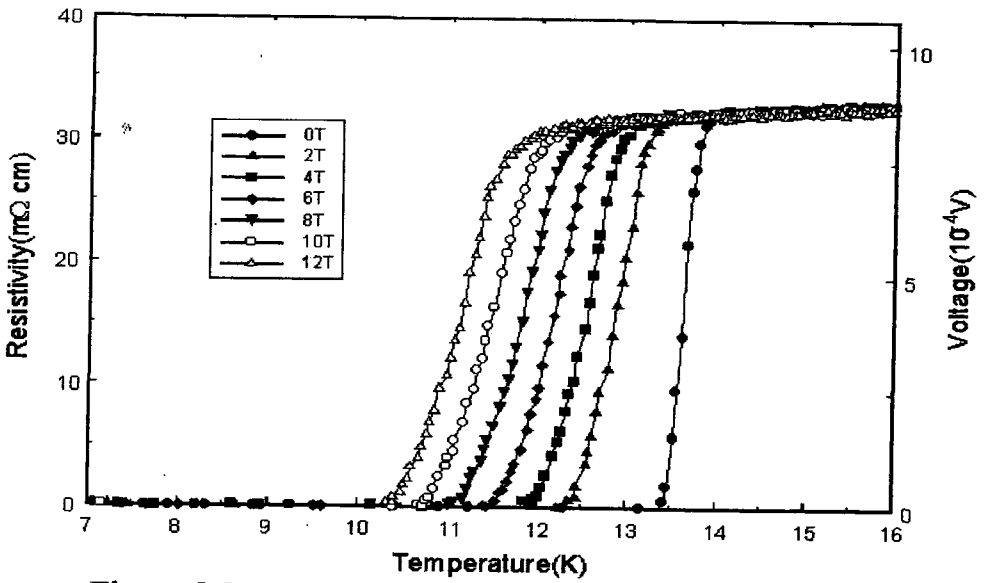

Figure 8.7a: The resistivity measurement for $PbMo_6S_8$ sample.

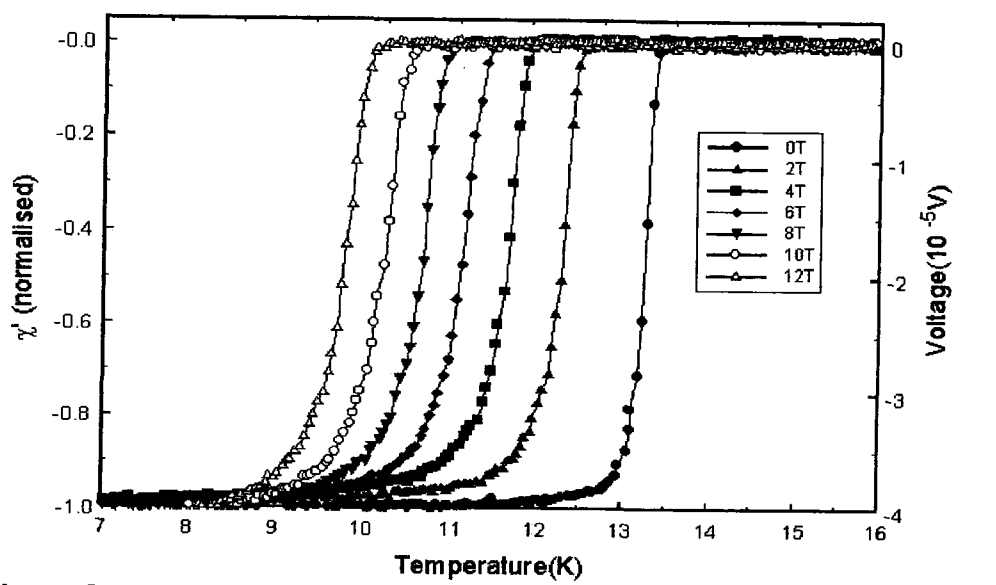

Figure 8.8a: The lossless component of the ac susceptibility measurements for $PbMo_6S_8$ sample.

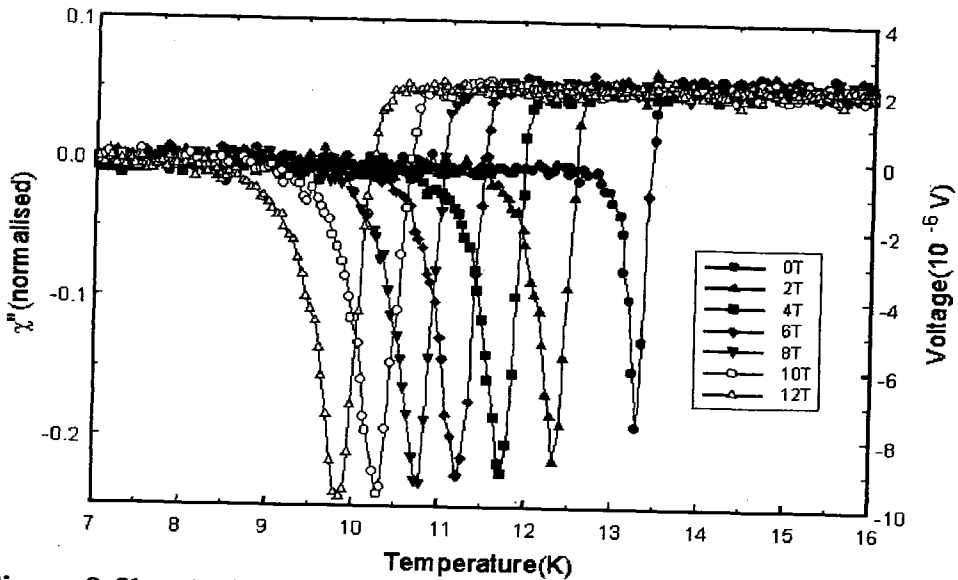

Figure 8.8b: The loss component of the ac susceptibility measurements for $PbMo_6S_8$ sample. A problem with phasing the lock-in amplifier has lead to an inversion of the data.

sample.

Figure 8.6a shows the resistivity measurement for the x=0.2 sample. The $T_{C\,(onset)}$ for this particular sample is about 14.8 K. The transition broadens as field increases. The broadening may be due to flux creep (thermal activation).

Figure 8.6b shows the lossless component of the ac susceptibility measurement for x=0.2 sample. The $T_{C\,(midpoint)}$ is about 14.8 K at 0 T. T_C decreases as the field increases. The loss component of the ac susceptibility measurement for the same sample is shown in figure 8.6c. The peak at 0 T occurs at about 13.9 K.

Figure 8.7a shows the resistivity measurement for the x=0 sample. The $T_{C(onset)}$ for this sample is about 13.9 K at 0T. Figure 8.8a shows the lossless component of the ac susceptibility measurement for the x=0 sample. The $T_{C(midpoint)}$ at 0 T is about 13.8 K.

The loss component of the ac susceptibility measurement for the same sample is shown in figure 8.8b. A problem with phasing the lock-in amplifier has lead to an inversion of the data.

The transition temperatures from resistivity and ac susceptibility measurements are summarised in Table 8.3 and 8.4, respectively:

Gd⇒	x = 0	x = 0.1	x = 0.2	x = 0.3
R(onset)	13.94 K	14.89 K	14.83 K	14.81 K
R(midpoint)	13.80 K	14.55 K	14.50 K	14.40 K
R(0)	13.50 K	14.24 K	14.14 K	14.22 K

Table 8.3: Transition temperature from resistivity measurements for $Pb_{1-x}Gd_xMo_6S_8$. R(0) indicates zero resistance transition temperature.

Gd⇒	x = 0	x = 0.1	x = 0.2	x = 0.3
χ(onset)	13.41 K	13.97 K	13.91 K	13.88 K
χ(midpoint)	13.24 K	13.82 K	13.76 K	13.74 K
χ(peak)	13.29 K	13.83 K	13.88 K	13.90 K

Table 8.4: Transition temperature from ac susceptibility measurements for $Pb_{1-x}Gd_xMo_6S_8$.

Initially T_C increases as the sample is doped with Gd. Further increases in Gd above x=0.1 does not show any significant effect on T_C. The χ(onset) corresponds to the R(0) values, ie., when the sample is superconducting.

8.5 Analysis

Figures 8.9- 8.12 are Kramer plots (i.e., $J^{1/2}B^{1/4}$ versus B) for each sample. The lines

shown have been obtained by least-squares straight line fits to the data (n.b. 10.2K in figure 8.10 is an exception and provides a guide to the eye). The Kramer plot lines are fairly straight and parallel to each other. The irreversibility field, B_{irr} at each temperature can be obtained by extrapolating linearly the Kramer plots to $J^{1/2}B^{1/4} = 0$. The straight lines suggest that the pinning force F_P can be described by the Kramer relation [8], $F_P = J_C \times B = \alpha(B_{irr})^m b^{1/2}(1 - b)^2$ where b is the reduced field($b=B/B_{C2}$). The B_{irr} for each sample are compared in figure 8.13. At low temperatures the x=0 and x=0.1 lines lie above the x=0.2 and x=0.3 lines.

Figure 8.14 compares the effect of Gd-doping on T_C from resistivity and ac susceptibility measurements to those from specific heat, C_P measurements[9]. These measurements show that the peak values occur at x = 0.1.

The B_{irr} for the samples as a function of temperature determined from resistivity and ac susceptibility measurements are shown in figures 8.15, 8.16, 8.17 and 8.18. In figure 8.15 the B_{irr} is determined from R_{onset} of the resistivity measurements, and in figure 8.16 the B_{irr} is determined from the R(0) of resistivity measurements. At high temperatures the B_{irr} lines for the Gd-doped samples lie above the B_{irr} of the undoped sample. In figure 8.17, the B_{irr} is determined from the AC_{onset} of the ac susceptibility measurements, and in figure 8.18 the B_{irr} is determined from the peak of the ac loss component. Figure 8.17 shows that close to T_C the B_{irr} line for the undoped sample lies below the B_{irr} lines of the doped samples. At high temperatures the B_{irr} line for the undoped sample lies above the B_{irr} lines of the doped samples. Figure 8.18 also show similar trends. The loss component of the x=0.3 sample could not be readily obtained because of insufficient data.

In figure 8.19 the B_{irr} line from Kramer plot for x=0.2 is compared to specific heat (C_P), resistivity, ac susceptibility and vibrating sample magnetometer(VSM) measurements made on similar samples. The B_{C2} line from C_P measurements lies above the B_{irr} line from resistivity(R_{onset}) measurements. This is followed by the B_{irr} line from Kramer plot,

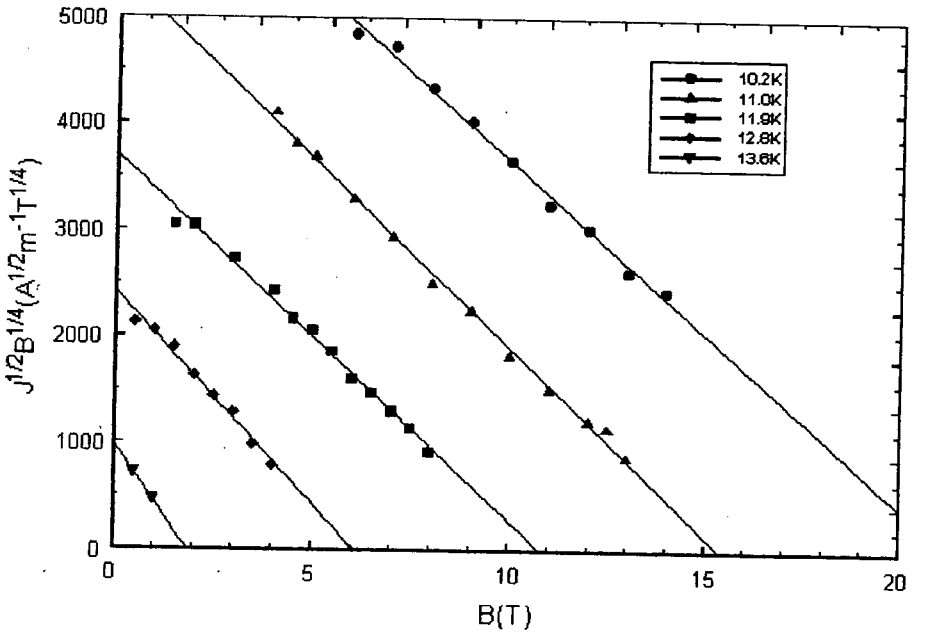

Figure 8.9: $J^{1/2}B^{1/4}$ versus B for $PbMo_6S_8$.

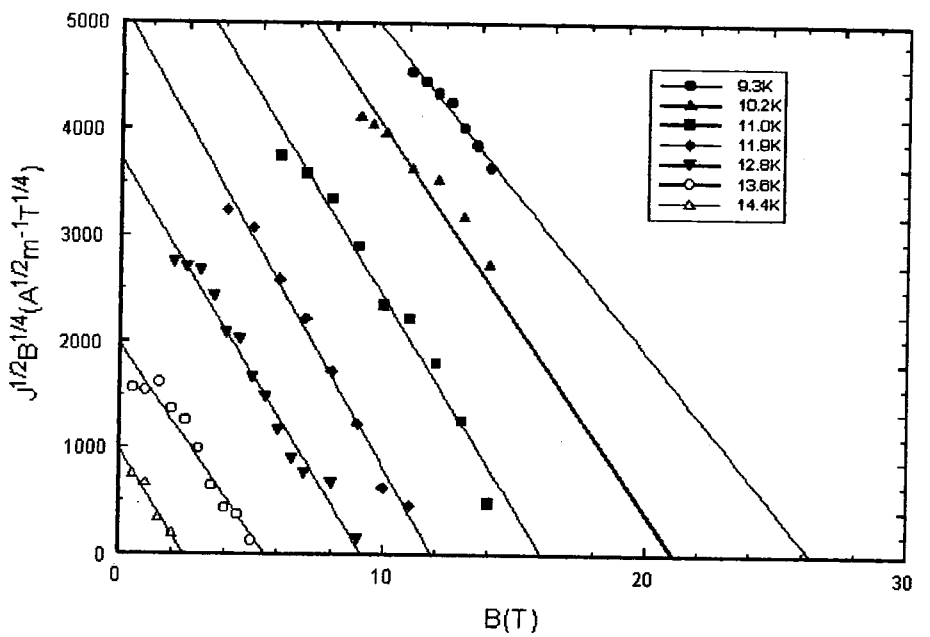

Figure 8.10: $J^{1/2}B^{1/4}$ versus B for $Pb_{0.9}Gd_{0.1}Mo_6S_8$.

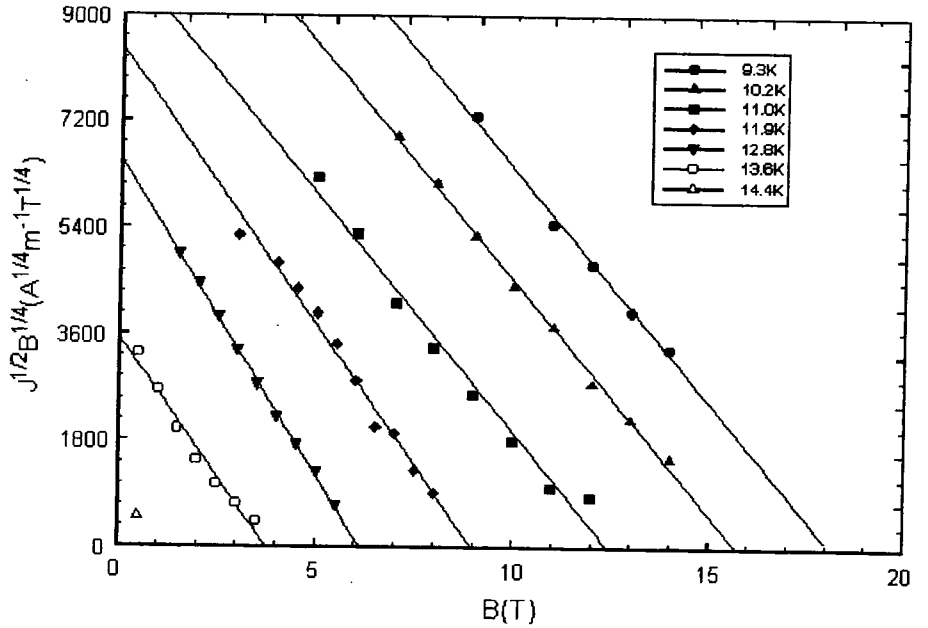

Figure 8.11: $J^{1/2}B^{1/4}$ versus B for $Pb_{0.2}Gd_{0.8}Mo_6S_8$.

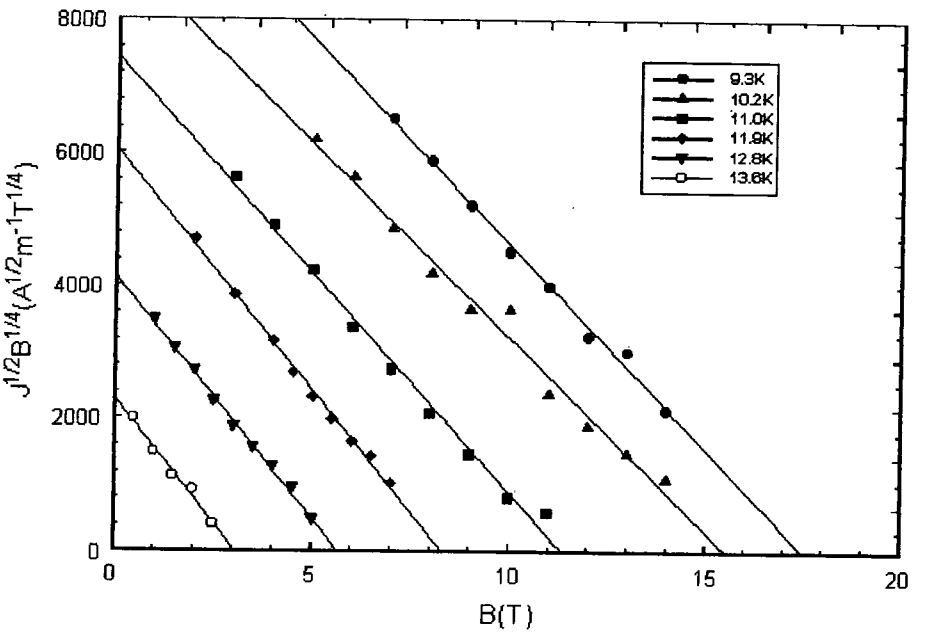

Figure 8.12: $J^{1/2}B^{1/4}$ versus B for $Pb_{0.7}Gd_{0.3}Mo_6S_8$.

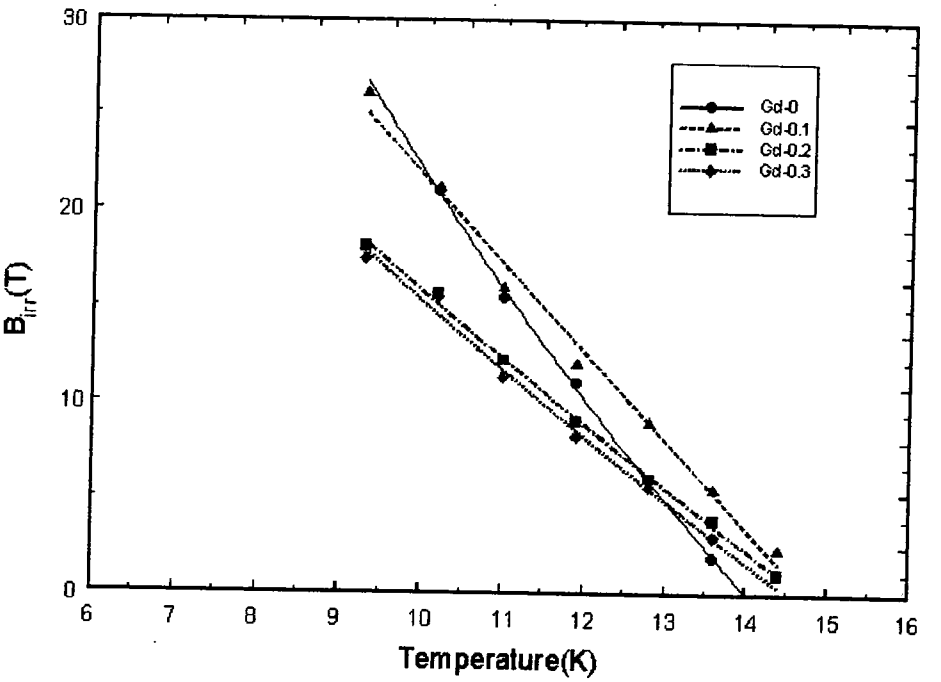

Figure 8.13: The B_{irr} determined from J_c data for the four samples as a function of temperature: $PbMo_6S_8$(Gd-0), $Pb_{0.9}Gd_{0.1}Mo_6S_8$(Gd-0.1), $Pb_{0.8}Gd_{0.2}Mo_6S_8$(Gd-0.2) and $Pb_{0.7}Gd_{0.3}Mo_6S_8$(Gd-0.3).

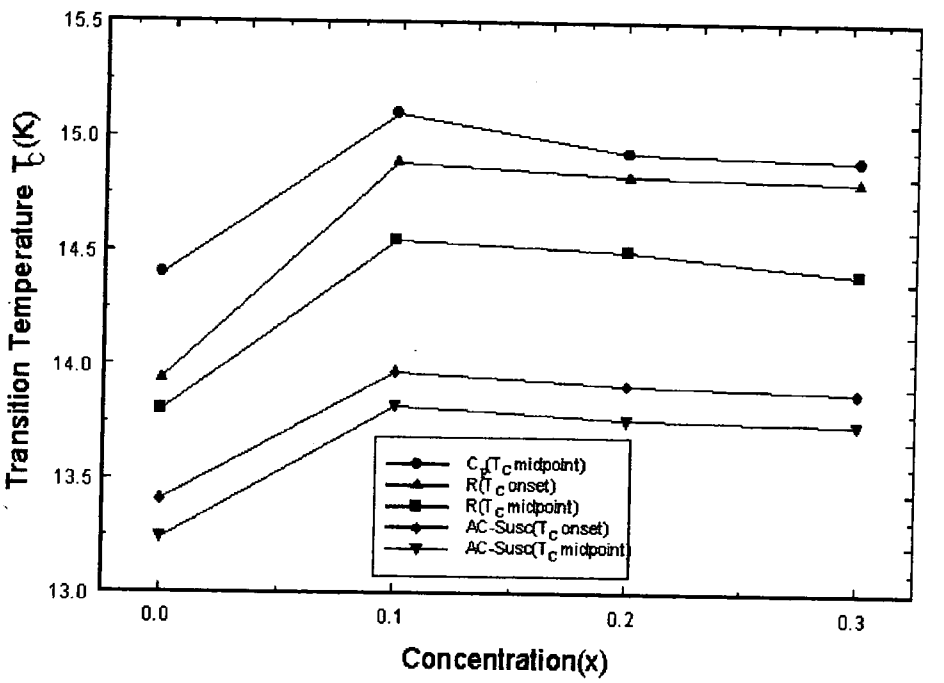

Figure 8.14: The effect of Gd-doping on T_c from resistivity, ac susceptibility and C_p[ref.9] measurements.

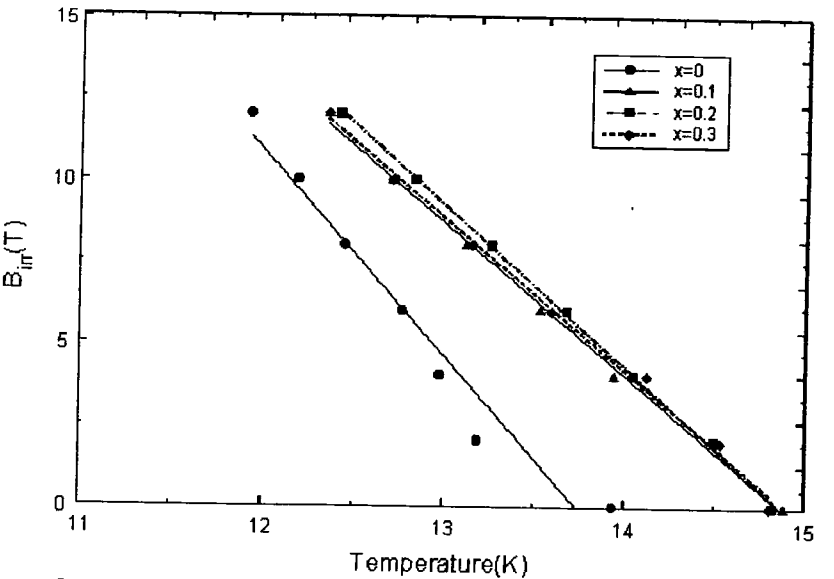

Figure 8.15: The B_{irr} for the four samples as a function of temperature determined from resistivity measurements(R_{onset}).

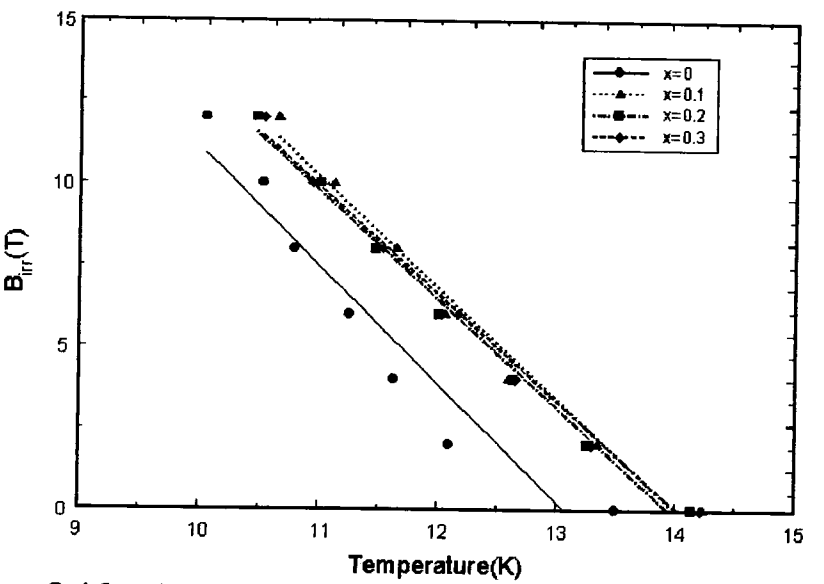

Figure 8.16: The B_{irr} for the four samples as a function of temperature determined from resistivity measurements:R(0)

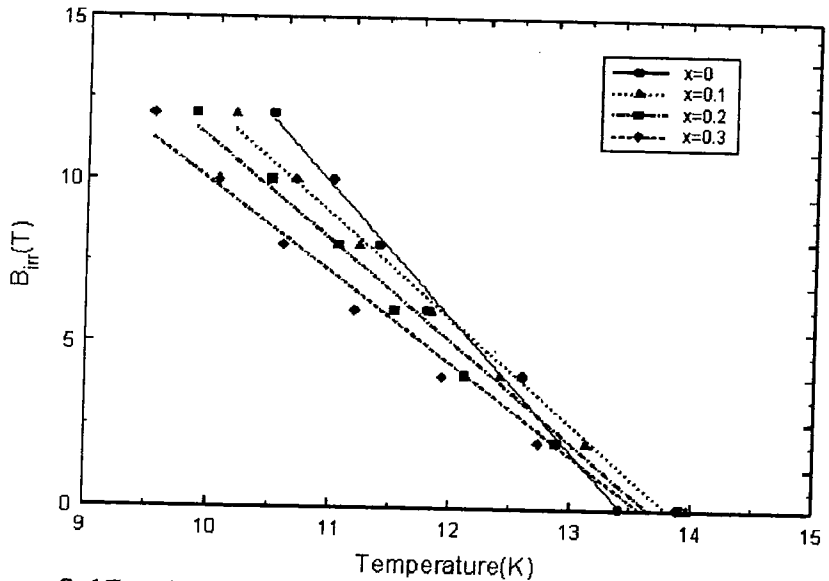

Figure 8.17: The B_{irr} for the four samples as a function of temperature determined from ac susceptibility measurements(AC_{onset}).

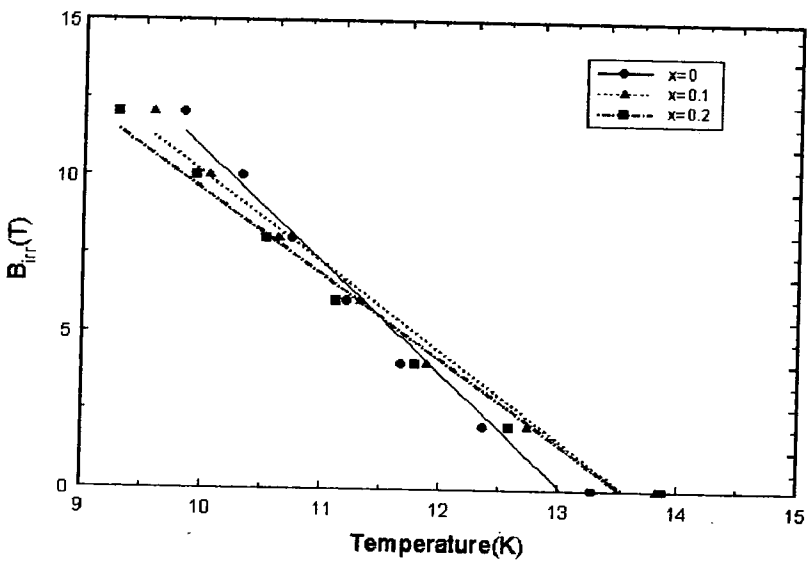

Figure 8.18: The B_{irr} for three samples as a function of temperature determined from ac susceptibility measurements(peak of the AC loss).

the B_{irr} from ac susceptibility measurements and finally the B_{irr} from VSM measurements.

Table 8.5 gives the values of the index n and the constant α calculated from J_C measurements. The temperature dependence(n) of these samples are different from one another. The highest value for α is for x=0.2 sample. Table 8.2 shows that the highest value for J_C is also when x=0.2. The value of α for the x=0.2 sample has increased by about a factor of 3 compared to the undoped sample.

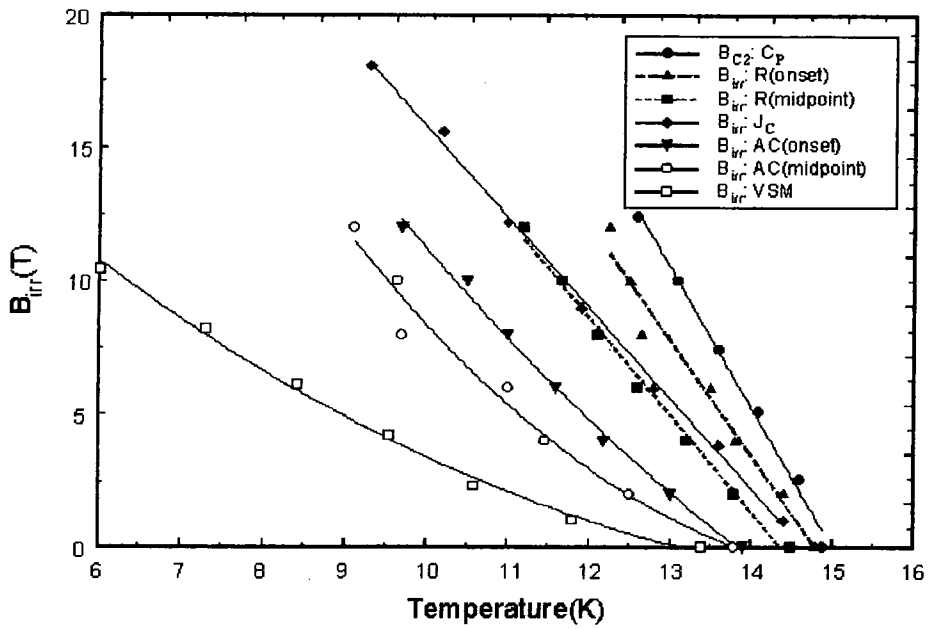

Figure 8.19: The B_{irr} line for the $Pb_{0.8}Gd_{0.2}Mo_6S_8$ sample is compared to C_P[9], resistivity, ac susceptibility and VSM[17] measurements.

Sample	n	α
$PbMo_6S_8$	2.08 ± 0.11	3.5×10^5
$Pb_{0.9}Gd_{0.1}Mo_6S_8$	2.42 ± 0.23	1.66×10^5
$Pb_{0.8}Gd_{0.2}Mo_6S_8$	2.30 ± 0.09	1.04×10^6
$Pb_{0.7}Gd_{0.3}Mo_6S_8$	2.22 ± 0.12	8.36×10^5

Table 8.5: Values of n and α for $Pb_{1-x}Gd_xMo_6S_8$(x= 0, 0.1, 0.2 and 0.3). α is a constant depending on sample microstructure.

The upper critical field at 0 K, $B^*_{c2}(0)$ can be calculated from the relation[10]:

$$B^*_{C2}(0) = -A T_C \left(\frac{dB_{C2}}{dT} \right)_{T=T_C} \qquad (8.1)$$

where A varies between 0.693 for the dirty limit superconductors and 0.726 for the clean limit superconductors. The PMS is a type II superconductor with a high GL-parameter $\kappa \sim 130$ [11], coherence length $\xi_0 \approx 48$ Å and a mean free path $l \sim 23$ Å [12]. Since l is less than ξ_0 we can assume that the sample is in the dirty limit. The calculated values for each sample is tabulated in Table 8.6. These values are calculated by taking the lower estimate for A and the $T_{C(midpoint)}$ from resistivity measurements.

The slope $\partial B_{irr}/\partial T$ for $PbMo_6S_8$ (x=0) is comparable but slightly lower than that obtained from specific heat, C_P measurements[9]. However, the slopes for the Gd-doped sample(x=0.2) is lower than those obtained from C_P measurements. The last column compares $B^*_{C2}(0)$ obtained from C_P and ac magnetisation measurements[4]. The B_{irr} may also be interpreted as the effective upper critical field, B^*_{C2} where the extrinsic parameter, J_C is zero. For the $PbMo_6S_8$ sample , the $B_{irr}(0)$ from J_C measurements is slightly lower than that of C_p but higher than that of ac magnetisation measurements. For the $Pb_{0.8}Gd_{0.2}Mo_6S_8$ sample, the $B_{irr}(0)$ from J_C measurements is about 37% lower than those of C_P measurements. The $B_{irr}(0)$ value for the $Pb_{0.7}Gd_{0.3}Mo_6S_8$ sample determined from J_C measurements is about 13% higher than the $B^*_{C2}(0)$ determined from ac magnetisation measurements. The specific heat measurement is a bulk measurement whereas the J_C and ac magnetisation measurements are sensitive to intergranular and intragranular transport currents, respectively. The J_C measurements also show that adding Gd decreases the B_{irr} of the material. Although adding Gd increases T_C of the sample, the slopes ($\partial B_{irr}/\partial T$) for the Gd-doped samples are lower than $\partial B_{irr}/\partial T$ of the $PbMo_6S_8$ (x=0) sample. The slopes ($\partial B_{irr}/\partial T$) and $B_{irr}(0)$ decrease as the amount ofdoping increases. The $B_{irr}(0)$ for the x=0.3 sample is about 2% lower

Sample	$\partial B_{irr}/\partial T$ (TK^{-1})	$B_{irr}(0)$ (T)	$\partial B^*_{C2}/\partial T$ (TK^{-1})	$B^*_{C2}(0)$ (T)
$PbMo_6S_8$	-5.56	53.9	-5.74[1] -4.00[2]	57.3[1] 38.8[2]
$Pb_{0.9}Gd_{0.1}Mo_6S_8$	-4.44	45.5	-	-
$Pb_{0.8}Gd_{0.2}Mo_6S_8$	-3.33	34.1	-5.21[1]	54.0[1]
$Pb_{0.7}Gd_{0.3}Mo_6S_8$	-3.33	33.5	-3.00[2]	29.1[2]

Table 8.6: Values of $\partial B_{irr}/dT$ and $B_{irr}(0)$ for $Pb_{1-x}Gd_xMo_6S_8$ calculated using equation 8.1 assuming dirty limit(data from J_C measurements).
(1) Data from specific heat measurements[9].
(2) Data from ac magnetisation measurements[4].

Sample	$\partial B_{irr}/\partial T$ (TK^{-1})	$B_{irr}(0)$ (T)	$\partial B_{irr}/\partial T$ (TK^{-1})	$B_{irr}(0)$ (T)
$PbMo_6S_8$	-5.79	55.9	-3.78	35.4
$Pb_{0.9}Gd_{0.1}Mo_6S_8$	-4.79	49.4	-3.41	33.7
$Pb_{0.8}Gd_{0.1}Mo_6S_8$	-4.91	50.4	-3.39	33.2
$Pb_{0.7}Gd_{0.3}Mo_6S_8$	-4.95	50.8	-3.24	31.9

Table 8.7: Values of $\partial B_{irr}/\partial T$ and $B_{irr}(0)$ for $Pb_{1-x}Gd_xMo_6S_8$ determined from resistivity measurements: (i)columns 2 and 3- data from R_{onset}
(ii)columns 4 and 5 - data from R(0)

Sample	$\partial B_{irr}/\partial T$ (TK^{-1})	$B_{irr}(0)$ (T)	$\partial B_{irr}/\partial T$ (TK^{-1})	$B_{irr}(0)$ (T)
$PbMo_6S_8$	-4.36	40.9	-3.38	31.2
$Pb_{0.9}Gd_{0.1}Mo_6S_8$	-3.23	31.3	-2.74	26.3
$Pb_{0.8}Gd_{0.2}Mo_6S_8$	-3.05	29.4	-2.50	24.1
$Pb_{0.7}Gd_{0.3}Mo_6S_8$	-2.70	26.0	-	-

Table 8.8: Values of $\partial B_{irr}/\partial T$ and $B_{irr}(0)$ for $Pb_{1-x}Gd_xMo_6S_8$ determined from ac susceptibility measurements:(i) columns 2 and 3 - data from χ'_{onset}
(ii) columns 4 and 5 - data from χ''_{peak}

than the $B_{irr}(0)$of the x=0.2 sample. It shows that further increases in Gd-doping above x=0.2 has only a slight effect on $B_{irr}(0)$ of the material.

8.6 Discussion

Doping the HIP'ed PMS with gadolinium has been shown to increase the T_C of the material. The resistivity measurements ($R_{midpoint}$) show that the HIP'ed Gd-doped PMS is approximately 0.8 K higher than the undoped HIP'ed PMS. This value of T_C does not change significantly up to x = 0.3. Fisher has also observed the same effect for Chevrel Phase $Sn_{1.2(1-x)}Eu_xMo_{6.35}S_8$[13]. The highest T_C for the Gd-doped PMS is when x=0.1 and this trend is also confirmed by specific heat, C_P and ac susceptibility measurements shown in figure 8.14. The highest reported value for a rare earth doped PMS is about 15 K [9,14]. The T_C values measured with resistivity and ac susceptibility measurements are about 4% and 7%, respectively less than C_P measurements. The variation of T_C may be a result of sample inhomogeneity or the thermometry used in these different methods of measurements or both. Catani, also using resistivity, ac susceptibility and C_P measurements, showed that the different T_C obtained is due to the

quality of the sample and not because of the different techniques used[15]. It is not clear why there are slight improvements in T_C but it is possible that at low concentrations the Gd may act as an oxygen getter, thus improving the T_C of the sample. It is believed that the substitution of Gd onto the Pb lattice sites can affect T_C through a change in charge transfer from the Pb-site to the Mo_6S_8 octahedra[16,17].

Although T_C has increased after adding Gd (Table 8.6), the slopes $[\partial B_{irr}/\partial T]$ of the x=0.1, x=0.2 and x=0.3 samples have decreased by about 20%, 40% and 40%, respectively, from the $\partial B_{irr}/\partial T$ value of the undoped sample. Similar effect has also been observed by Foner et. al.[18].

Table 8.9 is a summary of the $B_{irr}(0)$ determined from C_P[9], resistivity, J_C, ac susceptibility and ac magnetisation measurements. These measurements show that the undoped (x=0) sample has the highest value of $B_{irr}(0)$. The highest $B_{irr}(0)$ values are

Sample	C_P	R_{onset}	R(0)	J_C	AC_{onset}	AC_{peak}	AC Mag
x=0	57.3	55.9	35.4	53.9	40.9	31.2	38.8
x=0.1	-	49.4	33.7	45.5	31.3	26.3	-
x=0.2	54.0	50.4	33.2	34.1	29.4	24.1	-
x=0.3	-	50.8	31.9	33.5	26.0	-	29.1

Table 8.9: The $B_{irr}(0)$ for the $Pb_{1-x}Gd_xMo_6S_8$ samples determined from different measurements. Units are in Tesla.

obtained from C_p measurements. For the x=0 sample, the $B_{irr}(0)$ values obtained from R_{onset}, J_C, AC_{onset} and ac magnetisation measurements are lower than the value obtained from C_P measurements by about 2.5%, 6%, 28% and 30%, respectively. For the x=0.2 sample, the $B_{irr}(0)$ values obtained from R_{onset}, J_C and AC_{onset} are lower than those from C_P measurements by about 7%, 37% and 45%, respectively. The differences in the $B_{irr}(0)$ values obtained from different measurements may be explained in terms of the properties of the grains and grain boundaries. The C_P measurement is a volumetric

measurement, ie. it is sensitive to the properties of the grains but not sensitive to the properties of the grain boundaries. The onset of the resistivity measurement indicates that the properties of the grains have degraded but not the grain boundaries. Thus the R_{onset} is not sensitive the properties of the grain boundaries. However, the R(0) shows that the properties of the grain boundaries have degraded, ie. it is sensitive to grain boundaries. The J_C, ac susceptibility and ac magnetisation measurements are also sensitive to grain boundaries. Since $B_{irr}(0)$ is defined as when J_C equals 0 because of the degradation of the grain boundaries, the real $B_{C2}(0)$ of the grains is higher than the $B_{irr}(0)$. The differences in the values of $B_{irr}(0)$ also arises from the difference in the T_C values used in these measurements. For the J_C measurements the value of T_C depends on the criteria used in determining J_C from the V-I traces.

The functional form of the pinning force, $F_P \propto b^{1/2}(1-b)^2$, suggests that a grain boundary pinning mechanism operates in this material. This functional form is well established in Nb_3Sn where grain boundaries are the major pinning centres[8,19].

The x=0.1 and x=0.2 samples show that adding Gd can increase J_C by about a factor of 1.6 and 1.8, respectively. Rossel and Fisher showed that J_C increases by artificially introducing defects by neutron irradiation on PMS [20]. This suggests the importance of intragranular pinning. However, the x=0.3 sample showed that J_C is significantly reduced by about 50% compared to the undoped sample. The J_C reduction is probably due to the presence of more second phase material. The superconducting volume would then be less than the sample volume, thus lowering J_C[4]. Alternatively, by adding Gd, the reduction in J_C at the grain boundaries is probably due to the alteration of superconducting properties close to the surface of the grains caused by adding Gd[21]. Introducing Gd to PMS significantly reduces the irreversibility field, B_{irr}. The addition of magnetic ions will in general decrease the B_{irr} due to the exchange scattering of the conduction electrons on the magnetic ions[13].

8.7 Conclusions

Transport critical current measurements have been made on a series of HIP'ed Chevrel

Phase $Pb_{1-x}Gd_xMo_6S_8$ bulk samples from 9.3 K up to T_C in magnetic fields up to 14 Tesla. The properties of these Gd-doped samples are compared to those of the undoped sample.

Complementary resistivity and ac susceptibility measurements have also been made on these samples in magnetic fields up to 12 Tesla.

Doping PMS with Gd has improved the T_C of the samples. The highest T_C value is 14.55 K($R_{midpoint}$), ie when x=0.1. The exact reason for such improvements is not clear. Better fabrication techniques or Gd acting as a good oxygen getter, or both maybe responsible for improving the quality of the samples.

We have also found that doping PMS with Gd up to x=0.2 increases the J_C with a maximum at x=0.2(J_C = 4.1 x 10^6 Am^{-2} at 11 K and 8 T). However when x=0.3 the J_C has decreased by about 50% from that of the undoped sample. The highest value for α is also obtained for the x=0.2 sample.

Although T_C has improved, the slopes $[\partial B_{irr}/\partial T]$ from J_C measurements have decreased by about 20% for the x=0.1 and about 40% for the x=0.2 and 0.3 samples. The $B_{irr}(0)$ from J_C measurements has been calculated to be 53.9 T, 45.5 T, 34.1 T and 33.5 T for the x=0, 0.1, 0.2 and 0.3 samples, respectively. The B_{irr} line from J_C measurements lies below that of the upper critical field (B_{C2}) from C_P measurements.

The functional form of the pinning force, $F_P \propto b^{1/2}(1-b)^2$, is similar to that commonly observed in Nb_3Sn. This suggests that a grain boundary pinning mechanism operates in this material.

Our results show that it is possible to increase J_C of Chevrel Phase materials by doping them with rare-earth elements. However much work is needed to fully understand the complexities of these materials to meet the challenges for technical applications.

References

1. Decroux M, Cheggour N, Gupta A, Bouquet V, Chevrel R, Peremboom J A A J and Fisher Ø., *Czec. J. Phys.* **46** Suppl. S5 2757 (1996).
2. Fisher Ø, Jones H, Bongi G, Sergent and Chevrel R., *J. Phys. C: Solid State Phys.* **7** L450 (1974).
3. Fisher Ø., *Appl. Phys.* **16** 1 (1978).
4. Ramsbottom H D, *PhD Thesis* University of Durham U.K. (1996).
5. Zheng D N, Ali S, Hamid H A, Eastell C, Goringe M and Hampshire D P., *The Critical Current of the Chevrel Phase Superconductor Lead-Molybdenum-Sulphur with Gadolinium*, submitted to Physica C (1997).
6. Eastell C, Goringe M J and Hampshire D P., *Private Comminication* (1996).
7. Friend C F., *PhD Thesis* University of Durham U.K. (1994).
8. Kramer E J., *J. Appl. Phys.* **44** 1360 (1973).
9. Ali S., *PhD Thesis* University of Durham U.K. (1996).
10. Cors J, Cattani D, Decroux M, Stettler A and Fischer Ø., *Physica B* **165 & 166** 1521 (1990).
11. Zheng D N, Ramsbottom H D and Hampshire D P., *Phys. Rev. B* **52** (17) 1 (1995).
12. Woollam J A, Alterovitz S A and Luo H-L., in *Superconductivity in Ternary Compounds I, Topics in Current Physics* : eds. Ø Fischer and M B Maple (Springer, Berlin) p.161 (1982).
13. Fisher Ø, Decroux M, Roth S, Chevrel R and Sergent M., *J. Phys. C: Solid State* **8** L474 (1975).
14. Fisher Ø, Decroux M, Chevrel R and Sergent., *in Superconductivity in d-and f-Band Metals:* eds. Douglas DH (Plenum Press, New York) p.175 (1976).
15. Cattani D, Cors J, Decroux M, Seeber B and Fisher Ø., *Physica C* **153-155** 461 (1988).
16. Shelton R N, McCallum R W and Adrian H., *Phys. Lett.* **56A**(3) 213 (1976).
17. Zheng D N and Hampshire D P., *Proc. EUCAS 1995 - Applied Superconductivity* **Vol 1** ed. Dew-Hughes D., Edinburgh (1995).
18. Foner S, McNiff Jr E Jand Hinks D G., *Phys. Rev. B* **31** 6108 (1985).

19. Luhman T, Pande C S and Dew-Hughes D., *J. Appl. Phys.* **47**(4) 1459 (1976).
20. Rossel C and Fisher Ø., *J. Phys. F: Met. Phys.* **14** 473 (1984).
21. Cattani D, Cors J, DeCroux M and Fisher Ø., *Physica B* **165 & 166** 1409 (1990).

Chapter 9

Conclusion

9.1 Introduction

This thesis has given a brief introduction to superconductivity and a review on some aspects of the critical current. This thesis has been divided into two parts. The first part is about the effect of mechanical strain on J_C for both low and high temperature superconductors. A probe has been designed to measure the effect of strain on J_C on short wires and tape samples. Measurements have been made on a commercial BiSCCO Ag-sheath tape and on a Nb_3Sn wire. The Bi-based cuprates(BiSSCO) are one of the most promising high temperature superconductors for practical applications while Nb_3Sn has already been widely used for making magnets. An attempt has been made to understand the effect of strain on J_C on Nb_3Sn at two different temperatures(4.2 K and 2.9 K).

The second part of this work has been on the Pb Chevrel phase superconductor, PMS. This material has a transition temperature, $T_C \approx 15$ K, coherence length, $\xi \approx 40$Å, upper critical field $B_{C2}(0) \approx 60$ T, and has been shown to attain $J_C \approx 2 \times 10^8$ Am^{-2} in a magnetic field of 20 T. This material is a promising candidate for producing high magnetic fields above 20 T. Transport measurements have been made on a HIP'ed and unHIP'ed samples of PMS and their results compared. Transport, resistivity and ac susceptibility measurements have also been made to investigate the effect of doping PMS with gadolinium(Gd). The effect of different levels of doping PMS with Gd on J_C and T_C have been discussed.

This final chapter summarises the main conclusions and suggests some ideas for future work.

9.2 Summary

The J(B,ϵ) probe has been designed and built to measure J_C versus strain on short superconducting wires and tapes from 2K to 4.2 K in high magnetic fields in our 17 T magnet system. The probe can also be used to measure J_C versus strain at 77 K(liquid nitrogen). The probe can be inserted into any magnet system with a bore size greater than 40 mm. One can apply both tensile and compressive strains to the sample when using this probe. The J(B,ϵ) probe can measure strains up to $\pm 1.0\%$. The maximum current that can be passed through the probe is about 150 Amps. The probe is leak-tight so that variable temperature measurements can be made by pumping on the cryogen-bath of the magnet system. The strain on the sample is measured via a strain gauge pasted directly on the sample. The sensitivity of the strain measurement detected by the Digital Multimeter(DMM) is $1.4 \times 10^{-4}\%$ for the tape and $4.0 \times 10^{-4}\%$ for the wire. The control for changing the strain is typically 0.01% for the wire and 0.005% for the tape. Success in using this probe depends heavily on the sample mounting techniques.

The effect of strain on J_C has been made on a commercial Nb_3Sn wire. The compressive pre-strain of the wire measured at 4.2 K is found to be about 0.3%. The maximum J_C occurs when the deviatoric strain is a minimum. If additional strain is applied to the sample J_C decreases. The compressive pre-strain is a result from the differential thermal contraction between the matrix and the Nb_3Sn filaments as the composite is cooled from its fabrication temperature. J_C also decreases when compressive strain is applied to the sample. This is because the sample is initially in compressive pre-strain which degrades the initial critical current, thus further compression will reduce the critical current. The decrease in J_C at the very highest strains is attributed to fracture in the superconducting filaments. The maximum values for B_{C2} occur where J_C is maximum. At 4.2 K, the value of B_{C2} maximum is 19.6 T and at 2.9 K is 21.2 T. The values of B_{C2} decreases as strain is increased beyond the strain free-state. From strain scaling , the constant α is found to be $4.20 \pm 0.57 \times 10^8$ $Am^{-2}T^{-1}$ for the sample measured at 4.2 K(sample 1), and for the sample measured at 2.9 K the value of α is $1.37 \pm 0.05 \times 10^{10}$ $Am^{-2}T^{-1}$(sample 2). The values of n are found to be 1.67 ± 0.7 and 0.54 ± 0.16 for sample 1 and sample 2, respectively. The values of α and n from temperature scaling are found to be

3.63 ± 0.62 x10^8 $Am^{-2}T^{-1}$ and 1.72 ± 1.3, respectively. The difference in the values of n between strain scaling and temperature scaling shows that n only parameterises the change in J_C with the change in strain or temperature.

The effect of strain on J_C has also been measured on five short sections of a IGC Ag-sheathed tape. Measurements were done at 4.2 K and in magnetic field up to 12 Tesla. Tensile strain were applied on samples 1, 2 and 3. Bending(compression and tension)strains were applied on sample 4 and 5. J_C degradation starts to occur between 0.18%-0.25% strain. The decrease in J_C is attributed to crack formation in the superconducting filaments. The critical current distribution of the tape under strain and in magnetic fields has been addressed. The appearance of secondary peaks may be attributed to inter-grain J_C (strong field dependence) and intra-grain J_C(small field dependence). Alternatively the low current peak may be due to cracks and the high current peak may be due to undamaged regions. When the applied field increases the peaks of the critical current distribution are shifted to lower J_C values. Secondary peaks develop as strain is increased. For a damaged sample the critical current distribution is broader. The appearance of two peaks suggests the presence of damaged and undamaged parts of the tape. The double differential analysis is a useful tool to assess the quality of a sample. It can be used to find the J_C in undamaged regions.

Transport critical current measurements have been made on bulk $PbMo_6S_8$(PMS) samples from 5 K up to T_C in magnetic fields up to 12 T. The properties of hot isostatically pressed (HIP'ed) PMS fabricated at $1.3x10^8 Nm^{-2}$(1300 bar) at 900°C are compared with those of PMS fabricated at ambient pressure. X-ray diffraction pattern of the unHIP'ed PMS shows that the sample is predominantly single phase. The critical current density increases by a factor of ≈7 when the sample was hot isostatically pressed. Both samples can be described by a single functional form $F_p = \alpha B^n_{C2}(T)b(1-b)$ which suggests that the same pinning mechanism determines J_C. The B^*_{C2} for the HIP'ed sample lies close to the irreversibility line derived from complementary magnetic measurements on a HIP'ed sample. However it is significantly lower than the unHIP'ed sample over the same temperature range.

Transport critical current measurements have been made on a series of HIP'ed Chevrel Phase $Pb_{1-x}Gd_xMo_6S_8$ bulk samples from 9.3 K up to T_C in magnetic fields up to 14 Tesla. The properties of these Gd-doped samples are compared to those of the undoped sample. Complementary resistivity and ac susceptibility measurements have also been made on these samples in magnetic fields up to 12 Tesla. Doping PMS with Gd may have improved the T_C of the samples. The highest T_C value is 14.55 K($R_{midpoint}$), ie when x=0.1. It is thought that better fabrication techniques or Gd acting as a good oxygen getter, or both maybe responsible for improving the quality of the samples. Doping PMS with Gd increases J_C with a maximum at x=0.2(J_C = 4.1 x 10^6 Am^{-2} at 11 K and 8 T). However when x=0.3, J_C decreases by about 50% from that of the undoped sample. The highest value for α is also obtained for the x=0.2 sample. Although T_C have improved, the slope $[\partial B_{C2}/\partial T]$ has decreased by about 20% for the x=0.1 and about 40% for the x=0.2 and 0.3 samples. The $B_{irr}(0)$ from J_C measurements has been calculated to be 53.9 T, 44.5 T, 34.1 T and 33.5 T for the x=0, 0.1, 0.2 and 0.3 samples, respectively. The B_{irr} line from transport measurements lies below that of the upper critical field (B_{C2}) from C_P measurements. The functional form of the pinning force, $F_P \propto b^{1/2}(1-b)^2$, is similar to that commonly observed in Nb_3Sn. This suggests that a grain boundary pinning mechanism operates in this material.

9.3 Future work

The J(B,ϵ) probe has been designed to measure the effect of strain on J_C at a fixed temperature(eg., at 4.2 K or 77 K). Variable temperature measurements can only be made by pumping on the cryogen-bath. To get a complete understanding of the effect of magnetic field, strain and temperature on J_C, future work should include designing a strain probe that incorporates temperature control. This will avoid pumping on the helium bath which uses a lot of helium. It is recommended that the probe is designed to measure longer samples to avoid the current transfer problem. The new probe should have less moving parts to avoid the instrumentation leads getting entangled and thus ruining the experiment. A complete set of data is required over a wide temperature range to test Ekin's scaling law. However, at present such data do not yet exist for other low temperature and high temperature superconductors.

With regards to PMS, future work should be the effort to increase its J_C. One way is to reduce the grain size of this material. This may involve optimising the HIP'ping and heat treatment process. The role of oxygen, too, is crucial in understanding its effect on J_C. Further investigation on doping PMS with rare-earth elements is needed to understand how it affects T_C and grain boundaries. Thus it may be possible to increase J_C to a level required for practical applications. Effort should also be made to make PMS wires and their mechanical properties could be tested by using the new strain probe. The ultimate aim is to use these wires to make magnets that can generate high magnetic fields.

Appendix 1

In Appendix 1, preliminary results are documented. They are probably not publishable but may be of value for future workers in the area.

Appendix 1a

J_c versus B for a PMS wire

Figure A1 shows J_c versus B for a PMS wire at 4.2K for ascending and descending fields. The diameter of the wire is 0.4mm. J_c was determined at 5 μV criteria. J_c drops rapidly between 0 and 1 T. When it was measured for a second time it showed a resistive trace. This is probably due to the degradation of the material during thermal cycling.

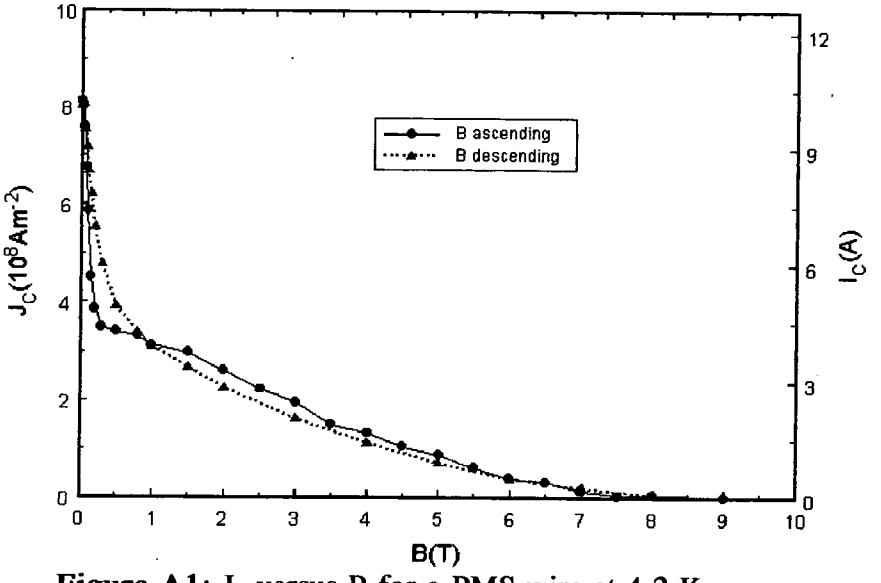

Figure A1: J_c versus B for a PMS wire at 4.2 K.

Appendix 1b

I_c versus B for a $Pb_{1.1}Mo_6S_x$ and $PbMo_6S_8$ bulk samples.

Figures A2a and A2b show I_c versus B for $Pb_{1.1}Mo_6S_x$ and $PbMo_6S_x$ samples bulk samples at 4.2K. The samples were covered with stycast. The I_c values are very high which demonstrates the efficacy of cooling of the current leads. However I_c values are quench currents and therefore unreliable.

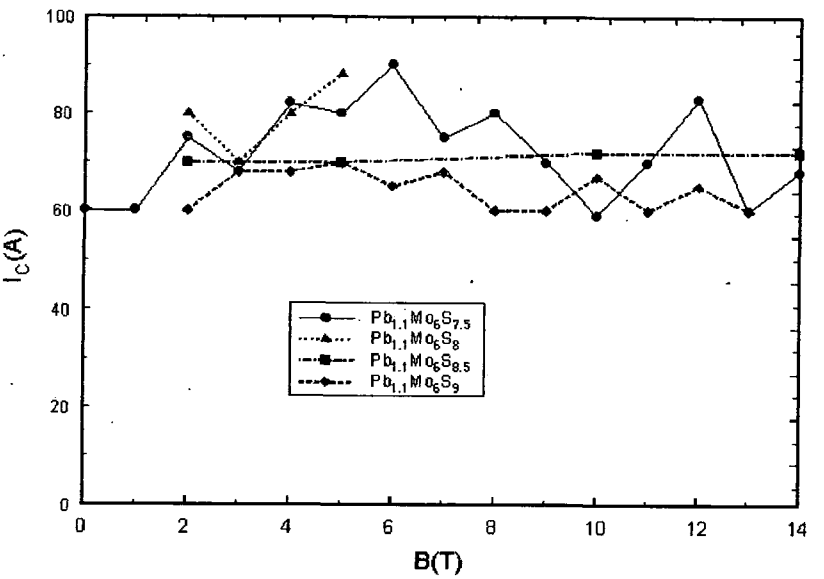

Figure A2a: I_c versus B for $Pb_{1.1}Mo_6S_x$ bulk samples at 4.2K.

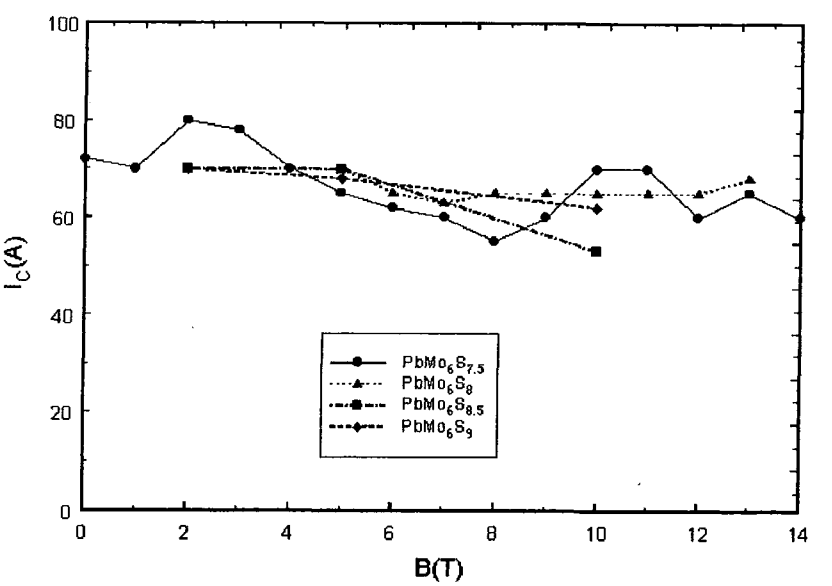

Figure A2b: I_c versus B for $PbMo_6S_x$ bulk samples at 4.2K.

Appendix 2 List of Computer Programs

All the measurements are computer controlled by interactive, real time graphical software written using ASYST(Keithley). All communications are via IEEE interface except for the magnet power supply which uses the RS232 bus. All data are saved in LOTUS file.

DEVICES.PRO

This file contains the IEEE address settings, the initialisation sequences, serial polling and the setup for all the instruments used. This program is first loaded at the beginning of the measurements.

VITRACE#.PRO

This program measures the V-I trace of a sample at a field set manually by the user. The character # stands for number 1 or 2 depending on the type of the power supply used. If the 100A Thor power supply is used the character # is 1, and if the 500 A power supply is used the character # is 2. All program variables are held in ASYST file VITRACE.VAR. The VITRACE#.PRO automatically loads the VITRACE#.VAR file.

VIFIELD#.PRO

This program is similar to VITRACE#.PRO except that it includes control of the superconducting magnet. All variables are held in VIFIELD#.VAR.

RUNRESSU.IJD

This program simultaneously measures the ac susceptibility and the resistance versus temperature of the sample. All program variables are held in ASYST file RUNRESSU.VAR.

RUNRES.PRO

This is an earlier program written to measure the resistance versus temperature of the sample. All variables are held in RES.VAR

Appendix 3 Courses and Conferences

Oct. 93 - June 94	Univ. of Durham	Postgrad. Lecture Course
October 1993	Univ. of Durham	Starting Your PhD.
November 1993	Univ. of Birmingham	Low Temp. Techniques Course
December 1993	Univ. of Leeds	CMMP 93
May 1994	IOP, London	Strongly Correlated Systems
June 1994	Univ. of Durham	Mechanical Workshop Course
October 1994	National Physical Lab. (NPL)	Frontiers of Measurements at Low Temperatures
November 1994	Univ. of Cambridge	Engineering Aspects of HTS
December 1994	Univ. of Warwick	CMMP 94
March 1995	Univ. of Durham	Compressed Gas Safety Awareness
July 1995	Univ. of Edinburgh	EUCAS 95
December 1995	Univ. of Liverpool	CMMP 95
December 1996	Univ. of York	CMMP 96